Advances in Cognitive Neurodynamics

Alessandra Lintas · Paolo Enrico · Xiaochuan Pan · Rubin Wang · Alessandro Villa *Editors*

Advances in Cognitive Neurodynamics (VII)

Proceedings of the Seventh International Conference on Cognitive Neurodynamics – 2019

Springer

Advances in Cognitive Neurodynamics

Series Editor

Rubin Wang, Institute of Cognitive Neurodynamics, East China University of Science and Technology, Shanghai, China

More information about this series at http://www.springer.com/series/11163

Alessandra Lintas · Paolo Enrico · Xiaochuan Pan ·
Rubin Wang · Alessandro Villa
Editors

Advances in Cognitive Neurodynamics (VII)

Proceedings of the Seventh International Conference on Cognitive Neurodynamics – 2019

Springer

Editors
Alessandra Lintas
HEC LABEX & ISI Complexity
Science Group
University of Lausanne
Lausanne, Vaud, Switzerland

Xiaochuan Pan
Institute for Cognitive Neurodynamics
East China University of Science
and Technology
Shanghai, China

Alessandro Villa
NeuroHeuristic Research Group
University of Lausanne
Lausanne, Vaud, Switzerland

Paolo Enrico
Dipartimento di Scienze biomediche
Università degli Studi di Sassari
Sassari, Italy

Rubin Wang
Institute for Cognitive Neurodynamics
East China University of Science
and Technology
Shanghai, China

ISSN 2213-3569 ISSN 2213-3577 (electronic)
Advances in Cognitive Neurodynamics
ISBN 978-981-16-0316-7 ISBN 978-981-16-0317-4 (eBook)
https://doi.org/10.1007/978-981-16-0317-4

This Springer imprint is published by the registered company Springer Nature Singapore Pte Ltd.
The registered company address is: 152 Beach Road, #21-01/04 Gateway East, Singapore 189721, Singapore

Committees

General Chair

Alessandro Villa (University of Lausanne, Switzerland)

General co-Chair

Alessandra Lintas (University of Lausanne, Switzerland)

International Committee

José M. Delgado-García (Pablo de Olavide University, Spain)
Xiaochuan Pan (East China University of Science and Technology, China)
IchiroTsuda (Chubu University, Japan)
Minoru Tsukada (Tamagawa University, Japan)
Alessandro Villa (University of Lausanne, Switzerland)
Rubin Wang (East China University of Science and Technology, China)

Local Organizing Committee

Paolo Enrico (University of Sassari)
Alessandra Lintas (University of Lausanne)

Scientific Committee

José M. Delgado-García (Pablo de Olavide University, Spain)
Daqing Guo (University of Electronic Science and Technology of China, Chengdu, China)
Ichiro Tsuda (Chubu University, Japan)
Yoshikazu Isomura (Tamagawa University, Machida, Japan)
Peiyang Li (Chongqing University of Posts and Telecommunications, China)
Hans Liljenström (SLU and Agora for Biosystems, Sweden)
Alessandra Lintas (University of Lausanne, Switzerland)
Woochang Lim (Daegu National University of Education, S. Korea)
Simona Monaco (Università degli Studi di Trento, Italy)
Xiaochuan Pan (East China University of Science and Technology, Shanghai, China)
Marisa Pedemonte (CLAEH University, Punta del Este, Uruguay)
Barry J. Richmond (NIMH/NIH/ DHHS, Bethesda, MD, USA)
Masamichi Sakagami (Tamagawa University, Machida, Japan)
Minoru Tsukada (Tamagawa University, Machida, Japan)
Alessandro Villa (University of Lausanne, Switzerland)
Rubin Wang (East China University of Science and Technology, Shanghai, China)
Yutaka Yamaguti (Fukuoka Institute for Technology, Japan)

Paper Acceptance and Contact Volume Editor

Alessandra Lintas (University of Lausanne, Switzerland)

Artistic Communication and Design

Arch. Eugenio Lintas (Sassari, Italy)
Prof. Dr. Minoru Tsukada (Tamagawa University, Machida, Japan)

Secretariat

Desk Assistance
Qinyue Zheng (Huazhong University of Science and Technology, Wuhan, China)
Manon Jaquerod (University of Lausanne, Switzerland)

Technical Support
Marco Pisano (University of Sassari)

Home Page

http://icc-n.com/

Preface

Studying cognition from a dynamic point of view has become a trend currently, and rapid developments have taken place in nonlinear dynamics and cognitive science. In order to promote the integration of cognitive science and neurodynamics as a whole, the 7th International Conference on Cognitive Neurodynamics (ICCN 2019) was held in Alghero (Sassari), Italy, from September 29 to October 2, 2019. The conference was hosted in a building of the Università degli Studi di Sassari. It was precisely in this university that the famous anatomist Luigi Rolando dedicated himself to those researches that served as the basis of the neurological studies that would have made him famous: in Sassari he published, in 1809, his fundamental contribution "Saggio sopra la vera struttura del cervello dell'uomo e degli animali, e sopra le funzioni del sistema nervosa" (Essay on the true structure of the human brain and of animals, and above the functions of the nervous system). This scientific work is part of the line of studies that applied the experimental method in neurophysiology, following the path of the Bernese physiologist Albrecht von Haller (1708–1777) who published in 1753–1755 an essay entitled the "Dissertation on the Irritable and Sensitive Parts of Animals" (original title: De partium corporis humani sensibilius et irritabilus). This work was based on numerous experiments of vivisection and on stimulation of organs using the new knowledge offered to physiology by physics, chemistry and natural history. With a rudimentary technique of stimulation, Von Haller classified the parts in irritable, sensible or elastic and noted that the reactions varied between different parts of the brain. This approach resulted in a turnabout in the university environment of the eighteenth century.

Supported by the work of Alessandro Volta, Rolando was struck by the analogy between electric devices and the structure of cerebellum to which he assigned a role in locomotion. In addition, Rolando was able to discern regularities in the morphology of the cerebral cortex and could establish relations between its parts while tracing the map and assigning them a name. Rolando's research was based on the metaphysical assumption that brain organisation had necessarily to be submissive to constant and recognizable laws. His criticisms directed against the organology concepts of Gall, then diffused throughout the Occidental world, were not at all dictated by a priori concepts. Rolando did not underestimate these anatomical studies, but he denounced on several occasions the absence of objective evidence for distinct organs to the tens of

mental functions identified by the phrenologists. The link of the University of Sassari with the neurosciences continued along the twentieth century. Giuseppe Levi, the histologist who mentored the academic education of two Nobel laureates, Rita Levi Montalcini (was awarded the 1986 Nobel Prize in Physiology or Medicine jointly with colleague Stanley Cohen for the discovery of nerve growth factor) and Renato Dulbecco (was awarded the 1975 Nobel Prize in Physiology or Medicine jointly to David Baltimore and Howard Martin Temin for their discoveries concerning the interaction between tumour viruses and the genetic material of the cell), worked and taught in Sassari from 1909 to 1913. Daniel Bovet—who in 1957 had won the Nobel Prize in Physiology and Medicine, for his research on synthetic curaries and their therapeutic application—was nominated chair of pharmacology at the University of Sassari in 1963. He continued his research on the actions carried out by nicotine at the brain level and remained in the chair of pharmacology for 6 years.

These historical premises formed the background to host the top-level international conference in cognitive neurodynamics ICCN 2019. The intrinsic highly interdisciplinary feature of cognitive neurodynamics depends on the fact that it is not a science in itself, but represents one of the developments of the neuroheuristic paradigm. The information processing affected by the brain appears then as a result of an accordance between Nature ("bottom-up") and Nurture ("top-down"). Research strategy based on the "bottom-up" information flow, the preferred view by neurobiologists, seems potentially necessary and sufficient; however, it is not wholly viable to actual experimentation considering the impossibility of simultaneously examining, even in a primitive species, all cellular elements of the brain and all variables that affect those elements. The "top-down" strategy with the assistance of "dark boxes" is easier to bring to fulfillment but insufficient and irrelevant in understanding the mechanisms coordinating the local networks of cellular elements. It seems therefore that a fusion of the "bottom-up" and "top-down" mechanisms is needed, leading to the neuroheuristic (or neuristic) paradigm, borrowed from the Greek terms neuron (nerve) and heuriskein (to find, to discover). Its definition corresponds to that branch of Science aimed at exploring the assumptions of the neurosciences through an ongoing process continuously renewed at each successive step of the advancement towards understanding the brain in its entirety.

The series conferences of ICCN provide very good opportunities for scientists from various fields to review their achievements, to share their ideas and to promote the development of this field. The 2019 conference followed those organized in Carmona, Seville, Spain (August 1–5, 2017), in Sanya, China (June 3–7, 2015), in Sigtuna, Sweden (June 23–27, 2013), in Niseko Village, Hokkaido, Japan (June 9–13, 2011), in Hangzhou, China (November 15–19, 2009) and in Shanghai, China (November 17–21, 2007). Last but not least, this series of conferences has increasingly offered the opportunity to gather and celebrate friendships and promote scientific collaborations by means of a rich set of social activities. In 2019, this tradition started with a performance of traditional music and dances of Sardinia (on Sunday 29th of September) and an archealogical guided tour to ancient Sardinian acropolis Anghelo Rui and complex nuraghe Palmavera (Tuesday 1st of October) and continued all along with gastronomic specialties of Sardinian cuisine. In addition,

we had the great honour to enjoy two performances by the internationally renowned Japanese violinist Tamamo Ange Saito.

ICCN 2019 was organized as a single-track conference which attracted almost 80 participants from 16 countries (Brazil, China, France, Germany, Israel, Italy, Japan, New Zealand, Norway, Russia, Spain, South Korea, Sweden, Switzerland, USA and Uruguay), who made this conference a successful and memorable scientific event. There were 52 presentations overall including 6 plenary lectures and 9 symposia. The plenary speakers were Profs. Drs. Masamichi Sakagami (Brain Science Institute, Tamagawa University, Machida, Japan), Barry J. Richmond (Section on Neural Coding and Computation, Laboratory of Neuropsychology, NIMH/NIH/ DHHS, Bethesda, MD, USA), Hans Braun (Institute of Physiology, Philipps University of Marburg, Germany), Miguel Merchán (Instituto de Neurociencias of Castilla y Leòn-INCyL, Universidad de Salamanca, Spain), Xiaochuan Pan (Institute for Cognitive Neurodynamics, East China University of Science and Technology, Shanghai, China) and Hiromichi Tsukada and Minoru Tsukada (Brain Science Institute, Tamagawa University, Machida, Japan).

The broad span of research in cognitive neurodynamics conferred at ICCN 2019 is presented in this volume organized in the following six sections: (I) Neurophysics and Analysis of NeuroInformation (eight chapters); (II) Functional Interactions in Neural Networks (six chapters); (III) Auditory and Multisensory Processing (five chapters); (IV) Human Brain Dynamics and Motor Control (six chapters); (V) From Neural Dynamics to Executive Functions: Short Papers (12 abstracts); and (VI) Information Processing and Transmission in the Cerebral Cortex: Short Papers (11 abstracts). All submitted papers were peer-reviewed by experts in the field based on originality, significance, quality and clarity, under the coordination of the contact volume editor Dr. Alessandra Lintas (LABEX—HEC Lausanne, University of Lausanne, Switzerland). We thank all the authors for the outstanding contributions to this conference proceedings.

Finally, we wish to express our gratitude to all those who made the 7th International Conference on Cognitive Neurodynamics and this proceedings volume possible. In addition to all the contributing authors, we especially thank Prof. Minoru Tsukada who kindly designed an original logo for the ICCN series of conference. We acknowledge the helpful assistance of the personnel of the University of Sassari along the conference and the contribution of Arch. Eugenio Lintas for the artistic design of the communication material. We gratefully acknowledge sponsorship from the Dipartimento di Architettura, Università degli Studi di Sassari, the European Neural Network Society and the Neuroheuristic Research Group of the University of Lausanne. We thank also the journal "Cognitive Neurodynamics" by Springer for the publication of this book series.

Sassari, Italy — Alessandra Lintas
Lausanne, Switzerland — Alessandro Villa
December 2019

Organizers and Sponsors

This conference is organized by
Dipartimento di Scienze Biomediche, Università degli Studi di Sassari, Italy
Neuroheuristic Research Group, University of Lausanne, Switzerland

Sponsored by
Università degli Studi di Sassari, Italy (Dipartimento di Architettura)
Neuroheuristic Research Group, University of Lausanne, Switzerland

Management and Scientific Support by
European Neural Network Society (ENNS)

Contents

Neurophysics and Analysis of NeuroInformation

Seizure Detection of Epileptic EEG Based on Multiple Phase-Amplitude Coupling Methods

Yao Miao, Toshihisa Tanaka, Shintaro Ito, and Jianting Cao

Abstract For epileptic electroencephalography (EEG) analysis, features extraction is crucial in seizure detection. In this paper, five methods for phase-amplitude coupling (PAC) were employed to analyze epileptic EEG to verify that PAC can be used as a biomarker to detect seizures. Specifically, five algorithms of evaluating PAC were used to compute PAC of seizure activity and seizure-free intervals at nine frequency band combinations. Then PAC of the EEG in a public dataset computed was classified by support vector machine (SVM), where the classification performance was assessed by calculating mean area under curve (AUC) based on receiver operating characteristic (ROC) with k-fold cross-validation (CV). Moreover, phase-amplitude comodulogram was applied to the same dataset to confirm intuitively classification accuracy. Results showed that the classification accuracy at band combination $\theta - \gamma$ was up to 0.96 and 0.99 for identifying seizure-free and seizure intervals both within epileptogenic zone and for classifying seizure-free interval EEG not within epileptogenic zone and seizure EEG within epileptogenic zone separately. Classification results of five different PAC methods were similar to each other. Furthermore, it was shown that there existed significant coupling at band combination $\theta - \gamma$ for EEG of seizure activities by observing from the comodulograms, which were consistent with the classification results.

Y. Miao · T. Tanaka (✉) · S. Ito
Tokyo University of Agriculture and Technology, 2-24-16 Naka-cho, Koganei-shi Tokyo 184-8588, Japan
e-mail: tanakat@cc.tuat.ac.jp

Y. Miao
e-mail: miao@sip.tuat.ac.jp

S. Ito
e-mail: ito17@sip.tuat.ac.jp

J. Cao
Saitama Institute of Technology, 1690 Fusaiji, Fukaya-shi, Saitama 369-0293, Japan
e-mail: cao@sit.ac.jp

A. Lintas et al. (eds.), *Advances in Cognitive Neurodynamics (VII)*, Advances in Cognitive Neurodynamics,
https://doi.org/10.1007/978-981-16-0317-4_1

1 Introduction

Epileptic seizure is defined as a transient occurrence of signs and/or symptoms due to abnormal excessive or synchronous neuronal activity in the brain by the International League Against Epilepsy (ILAE) (Fisher, 2014). Electroencephalography (EEG) is one of the primary diagnostic tools to be used currently in the location and characterization of seizures. Currently, the clinical diagnosis of epilepsy is basically based on the doctor's clinical experience by visually observing the patient's EEG. And due to the predictability of the seizure, long-term detection of the subject is necessary, which leads to disadvantages such as long manual detection and low efficiency for doctors. Therefore, it is necessary to apply signal processing methods for automatic detection of epileptic EEG in the diagnosis of epilepsy.

Many studies have been reported on epileptic EEG. For example, the classifier to detect epileptic seizures was optimized by finding an optimal combination of training sets (Bogaarts et al., 2016). The epileptic seizures were predicted with the autoregressive (AR) model (Chisci et al., 2010). Moreover, a novel index was proposed to predict the epileptic seizure (Aksenova et al., 2007). Another work introduced the measure based on data mining techniques to analyze the epileptic EEG (Exarchos et al., 2006). Furthermore, another study proposed a methodology for nonlinear estimation based on bispectral analyses in localizing the epileptogenic focus side (Villa and Tetko, 2010). However, more features need to be used to analyze the epileptic EEG to obtain more accurate results of detecting epileptic seizures. In this paper, phase-amplitude coupling (PAC) is introduced to detect epileptic seizures. The underlying idea behind using PAC is that PAC may be as a candidate biomarker to characterize the epileptic seizures as it has been proven to be closely associated with cognitive activity in the brain (Canolty and Knight, 2010).

PAC is defined as the coupling on high-frequency amplitude modulated by low-frequency phase. Many studies have shown the differences in coupling between epilepsy zone and normal zone. For example, research has shown that the PAC was elevated in the seizure onset zone for the children with medically intractable epilepsy secondary to focal cortical dysplasia (Ibrahim, 2013). And delta-modulated high-frequency oscillation may provide accurate localization of epileptogenic zone by identifying the regions of interest for extratemporal lobe patients (Guirgis, 2015). Moreover, the PAC in seizure onset zone was higher than normal zone (Mina Amiri et al., 2016).

There are several approaches to evaluate PAC strength. In this paper, five common PAC methods were employed to compute PAC values between low-frequency phase and high-frequency amplitude from different aspects, in order to identify EEG of seizure activity and EEG of seizure-free intervals and compare the performance of five PAC algorithms. Specifically, Bonn EEG data were filtered into three bands of low-frequency oscillation and three bands of high-frequency oscillation, and PAC values for nine groups of band combination were calculated by every PAC method, respectively. Then PAC features for the EEG of seizures activity and for the EEG of seizure-free intervals were classified by using support vector machine (SVM).

Afterward, the classification results were evaluated by calculating mean area under curve (AUC) value based on receiver operating characteristic (ROC) with k-fold cross-validation (CV). Final results showed that there existed obvious coupling features between θ band phase and γ band amplitude for EEG in seizures, with the classification result which was up to 0.99 for the EEG of seizures within epileptogenic zone and the EEG of seizure-free intervals not in epileptogenic zone, as well as the classification accuracy was up to 0.96 for the EEG of seizures and seizure-free intervals within epileptogenic zone. Results also show that the classification accuracy analyzed by five different algorithms of computing PAC was similar to each other. Moreover, the phase-amplitude comodulogram confirms intuitively the classification results.

2 Materials and Methods

2.1 Materials

The epileptic EEG dataset used in this paper is from the Department of Epileptology at the University of Bonn (Andrzejak, 2001). The dataset is publicly available and used widely in the research of epileptic EEG data analysis and classification. There were five sets in the dataset, denoted as set A, set B, set C, set D, and set E. Each of set contained 100 single-channel EEG segments with recording duration of 23.6 s per segment. The sampling rate and band-pass filter were set to 173.61 and 0.5340 Hz. In details, set A and set B were surface EEG recordings taken from five healthy volunteers who were relaxed in an awake state with eyes open (set A) and eyes closed (set B). Set C, set D, and set E were intracranial EEG recordings originated from five patients, in which set C and set D were taken from during seizure-free intervals from the opposite of the hemisphere of the brain (set C) and within epileptogenic zone (set D), set E was taken from epileptic seizure activity. In this paper, set C, set D, and set E were studied.

2.2 Methods of PAC

PAC is explained as that the high-frequency amplitude is modulated by the low-frequency phase. Low-frequency phase time series and high-frequency amplitude time series were computed firstly before computing the PAC strength. In this paper, finite impulse response (FIR) filter and Hilbert transform were used. Take an example, for a single-channel time series $x(n)$ ($n = 1, 2, \ldots, N$), FIR filtered was applied to extract high-frequency oscillation interested $x_h(n)$ and low-frequency oscillation interested $x_l(n)$. Then, the Hilbert transform was used to extract corresponding

instantaneous phase time series and instantaneous amplitude time series of both oscillations. Two analytic signals were obtained as

$$z_l(n) = a_l(n)e^{i\phi_l(n)},\ a_l(n) = |z_l(n)|, \tag{1}$$

$$z_h(n) = a_h(n)e^{i\phi_h(n)},\ a_h(n) = |z_h(n)|,\ (n = 1, 2, \ldots, N), \tag{2}$$

where $\phi_l(n)$ and $\phi_h(n)$ were the instantaneous phase time series, as well as $a_l(n)$ and $a_h(n)$ were the instantaneous amplitude time series of both high-frequency oscillation and low-frequency oscillation. It is shown in Fig. 1 the process of band-pass filtering and Hilbert transform before computing coupling strength.

There were five algorithms to be employed to calculate the PAC strength. The first method was used to estimate PAC strength by taking the mean vector length modulation index (MVL-MI) (Canolty and Edwards, 2006). It firstly defined the complex variable $z(n) = a_h(n)e^{i\phi_l(n)}$ $(n = 1, 2, \cdots, N)$ and then computed the absolute value of the mean vector based on $z(n)$ and defined the MI as

$$M_{\text{raw}} = \left| \frac{1}{N} \sum_{i=1}^{N} z(n) \right|,\ (n = 1, 2, \ldots, N). \tag{3}$$

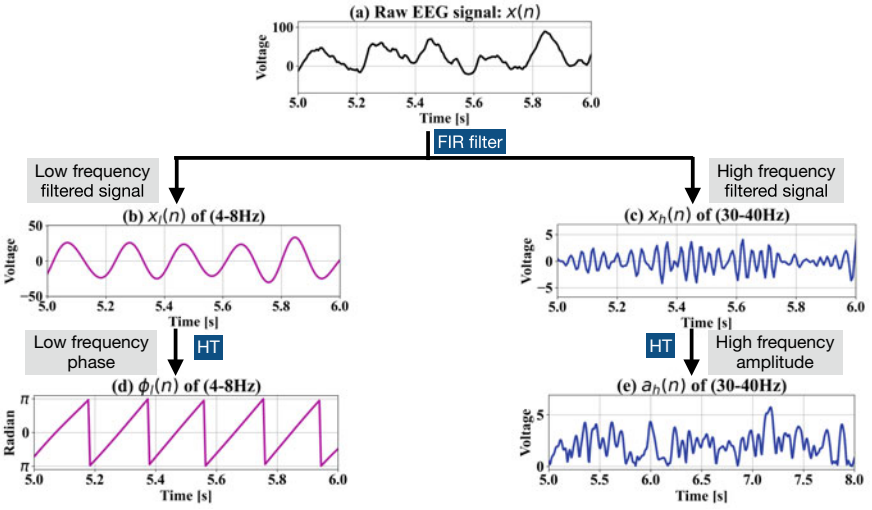

Fig. 1 EEG signal preprocessing process. **a** was one second raw EEG segment $x(n)$ $(n = 1, 2, \ldots, N)$. **b** and **c** were the low-frequency filtered signal $x_l(n)$ of 4–8 Hz and high-frequency filtered signal $x_h(n)$ of 30–40 Hz processed by FIR filter. **d** and **e** were the corresponding low-frequency phase $\phi_l(n)$ and high-frequency amplitude time series $a_h(n)$ calculated by Hilbert transform. HT denotes Hilbert transform. The figure is original.

Then use surrogate data approach to compute the surrogate $z_s(n)$ ($n = 1, 2, \ldots, N$; $s = 1, 2, \ldots, S$) by introducing an arbitrary time lag between $\phi_l(n)$ and $a_h(n)$. And compute the mean vector $M_s = \left| \frac{1}{N} \sum_{i=1}^{N} z_s(n) \right|$ of $z_s(n)$ according to the definition of MI. And repeat the above step for $s = 1, 2, \ldots, S$ times to obtain the surrogate values $M_1, M_2, \ldots, M_S$, and compute the mean μ and standard variance σ of these surrogate values. Finally, compute the normalized MI to evaluate PAC strength which is denoted as M, where

$$M = \left| \frac{M_{\text{raw}} - \mu}{\sigma} \right|. \tag{4}$$

The second method to quantify the PAC is based on phase-locking value (PLV) (Vanhatalo, 2004; Cohen, 2007; Mormann, 2010). The PLV is defined as

$$PLV = \left| \frac{1}{N} \sum_{n=1}^{N} e^{i(\phi_l(n) - \phi_{a_h}(n))} \right|, \tag{5}$$

where Hilbert transform is applied to $a_h(n)$ to get $\phi_{a_h}(n)$.

The third algorithm to measure the PAC strength was based on general linear model (GLM) (Penny and Duzel, 2008). For the algorithm, a new high-frequency amplitude model by introducing a multiple regression is

$$a_h = X\beta + e, \tag{6}$$

where $X = \begin{bmatrix} \cos(\phi_l(1)) & \sin(\phi_l(1)) & 1 \\ \vdots & \vdots & \vdots \\ \cos(\phi_l(n)) & \sin(\phi_l(n)) & 1 \\ \cos(\phi_l(N)) & \sin(\phi_l(N)) & 1 \end{bmatrix}_{N \times 3}$, $(n = 1, 2, \ldots, N)$, β are regression coefficients by using least squares solution, and $\cos(\phi_l(n))$ and $\sin(\phi_l(n))$ are the cosine and sine transform of low-frequency phase time series, respectively. Afterward, the value ${r_{GLM}}^2$ which is defined to quantify the coupling strength is described as

$${r_{\text{GLM}}}^2 = \frac{SS(a_h) - SS(e)}{SS(a_h)}, \tag{7}$$

where $SS(A_h)$ and $SS(e)$ are the sum of squares of high-frequency amplitude time series a_h and the sum of squares of error e.

The fourth method to evaluate the PAC was based on an adaptive of the Kullback–Leibler distance (KL distance) (Tort, 2010). In this algorithm, $\phi_l(t)$ is divided into bins in order, and the mean value of $a_h(t)$ in each phase bin j is computed, where the mean value is expressed by $\langle a_h \rangle_{\phi_l}(j)$. And normalize the mean value $\langle a_h \rangle_{\phi_l}(j)$ as

$$P(j) = \frac{\langle a_h \rangle_{\phi_l}(j)}{\sum_{j=1}^{N_{\text{bins}}} \langle a_h \rangle_{\phi_l}(j)}, \tag{8}$$

where N_{bins} is the number of phase bins. Then the new MI is defined as

$$MI = \frac{D_{KL}(P, U)}{\log(N_{\text{bins}})}, \tag{9}$$

where $D_{KL}(P, U) = \log(N_{\text{bins}}) - H(P)$, $H(P) = -\sum_{j=1}^{N_{\text{bins}}} P(j) \log[P(j)]$.

The fifth method to quantify the PAC strength is by redefining the MVL-MI as (Tolga, 2011)

$$\rho = \frac{1}{\sqrt{N}} \times \frac{|\sum_{n=1}^{N} a_h(n) e^{i\phi_l(n)}|}{\sqrt{\sum_{n=1}^{N} a_h(n)^2}} (n = 1, 2, \ldots, N). \tag{10}$$

2.3 *Method of Classification*

SVM is a supervised learning method based on statistical learning theory (SLT) in machine learning. The basic model is the linear classifier that defines the largest interval in the feature space. It maps the vector to the high-dimensional feature space through nonlinear mapping and then selects the most classified surface to obtain a hyperplane segmentation, which can separate the two types of modes and ensure the interval is maximized as shown in Fig. 2.

The hyperplane segmentation **H** is defined as

$$\mathbf{w}^T x + b = 0. \tag{11}$$

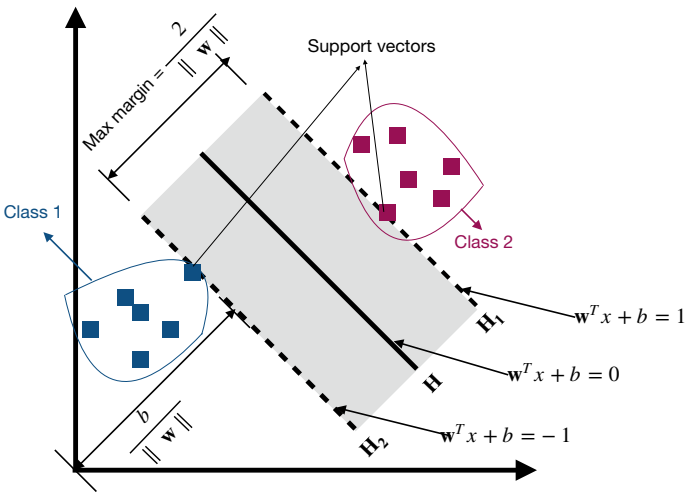

Fig. 2 Principle of binary classification based on SVM. The figure is original.

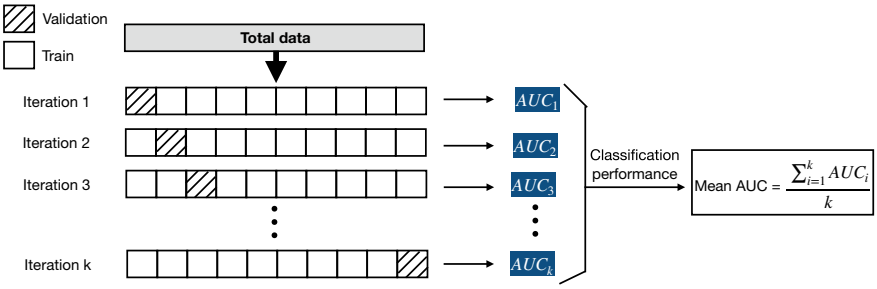

Fig. 3 Process of classification performance evaluation based on SVM and k-fold CV. The figure is original.

Then the problem of finding the max margin can be transformed to the following conditional extreme value problem, defined as

$$\begin{cases} \min \frac{1}{2}\mathbf{w}^T\mathbf{w}, \\ s.t. \quad y_i(\mathbf{w}^T x_i + b) - 1 \geq 0. \end{cases} \tag{12}$$

2.4 Evaluation of Classifier Performance

In this paper, the classification performance of SVM is evaluated by the mean AUC based on ROC with k-fold CV. AUC is defined as the area under the ROC curve, and ROC is the indicator to reflect the relationship between sensitivity and specificity of variables. Especially, the k-fold CV is employed to reduce bias and get more information from limited samples, in which k-fold CV is a resampling procedure that is used to assess machine learning models on limited data samples. The calculation of mean AUC is shown in Fig. 3. Firstly, the dataset is shuffled randomly and partitions the original dataset into k equal subsets. Onefold data are retained as the validation set, and all the remaining $k-1$ folds are kept in the CV training set. Secondly, the CV training set is used to train the machine learning model, and the AUC value of the model is calculated by validating the predicted results against the validation set. Thirdly, repeat the step for k times and k AUC values are calculated. Finally, estimate the accuracy of the model by taking the mean of the AUC derived in all the k cases of CV.

3 Results

In this paper, set C, set D, and set E of Bonn dataset at nine frequency band combinations were processed by five methods of PAC illustrated above, in which nine band combinations were $\delta_l - \alpha$, $\delta_l - \beta$, $\delta_l - \gamma$, $\delta_h - \alpha$, $\delta_h - \beta$, $\delta_h - \gamma$, $\theta - \alpha$, $\theta - \beta$,

and $\theta - \gamma$. Then PAC features were classified using SVM by means of scikit-learn Python module "sklearn.svm.SVC" function with kernel set to linear (Pedregosa and Varoquaux, 2011). And the classification performance was described by computing mean AUC value based on ROC with k-fold CV, in which $k = 10$. The flowchart of process is shown in Fig. 4.

From Tables 1 and 2, it is intuitively observed that the AUC at band combination $\theta - \gamma$ is obviously the highest, that is to say, there exits significant coupling of seizure activity between the phase of θ band and the amplitude of γ band. Specifically, the classify accuracy of detecting seizures is up to 0.96 at band combination $\theta - \gamma$ within an epileptogenic zone by using GLM algorithm. Moreover, the accuracy to detect seizures reaches 0.99 at band combination $\theta - \gamma$ for set C and set E. Furthermore, the classification results processed by five different methods of computing PAC were similar to each other.

Moreover, phase-amplitude comodulogram based on MVL[1] method was used to observe intuitively the differences of PAC features of seizure activity and seizure-free intervals. Phase-amplitude comodulogram is the graphical representation that exhibits coupling strength among multiple bands. When there is no prior assumption of frequency bands phase-modulating and the amplitude-modulated, the comodulogram can be used to locate initially the frequency bands where coupling occurs. We

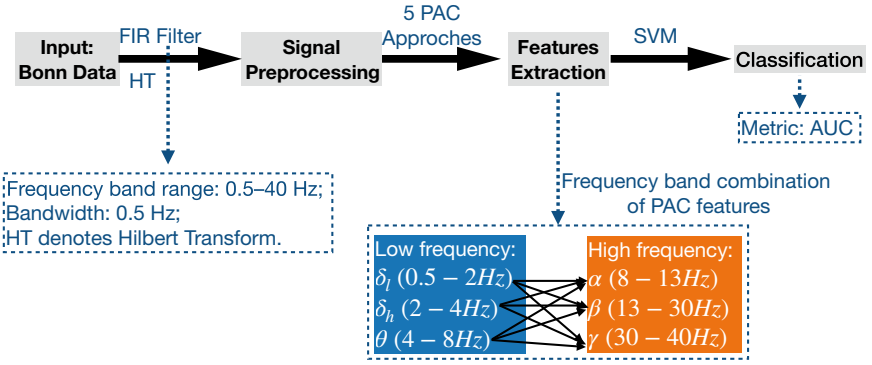

Fig. 4 Flowchart of Bonn data analysis experiment based on five PAC methods. The figure is original.

Table 1 AUC of PAC for set D and set E based on five PAC methods at nine band combinations

Bands	$\delta_l - \alpha$	$\delta_l - \beta$	$\delta_l - \gamma$	$\delta_h - \alpha$	$\delta_h - \beta$	$\delta_h - \gamma$	$\theta - \alpha$	$\theta - \beta$	$\theta - \gamma$
MVL[1]	0.44	0.59	0.63	0.79	0.85	0.84	0.80	0.89	0.92
PLV	0.41	0.72	0.72	0.76	0.85	0.86	0.91	0.93	0.95
GLM	0.54	0.42	0.63	0.77	0.82	0.81	0.91	0.93	0.96
KL-MI	0.44	0.66	0.30	0.73	0.80	0.85	0.92	0.93	0.94
MVL[2]	0.46	0.50	0.47	0.70	0.78	0.80	0.93	0.92	0.94

It is noted that MVL[1] is the first method, and MVL[2] is the fifth method

Table 2 AUC of PAC of set C and set E based on five PAC methods at nine band combinations

Bands	$\delta_l - \alpha$	$\delta_l - \beta$	$\delta_l - \gamma$	$\delta_h - \alpha$	$\delta_h - \beta$	$\delta_h - \gamma$	$\theta - \alpha$	$\theta - \beta$	$\theta - \gamma$
MVL[1]	0.60	0.72	0.78	0.87	0.92	0.90	0.84	0.97	0.97
PLV	0.60	0.80	0.84	0.85	0.94	0.92	0.92	0.98	0.98
GLM	0.60	0.74	0.73	0.85	0.91	0.89	0.91	0.98	0.98
KL-MI	0.53	0.81	0.89	0.89	0.96	0.98	0.95	0.99	0.99
MVL[2]	0.56	0.71	0.74	0.82	0.90	0.89	0.95	0.98	0.99

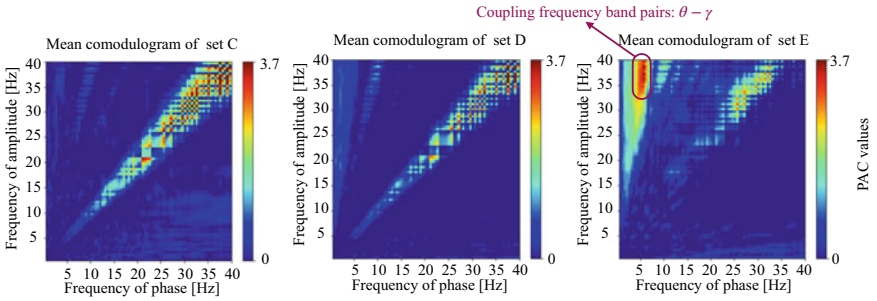

Fig. 5 Results of mean comodulograms of set C, set D, and set E for Bonn dataset based on MVL[1] method. x-axis and y-axis represent frequency of phase and frequency of amplitude, respectively. PAC values are displayed by pseudo-color plot. The part marked by purple denotes there is strong phase-amplitude coupling between the phase of θ and the amplitude of γ. The figure is original.

applied comodulogram measure to analyze set C, set D, and set E. For each single channel of each group, the comodulogram was obtained by representing MI values of multiple $\left[f_A(i),\ f_P(j) \right]$ pairs, with both $f_A(i)$ and $f_P(j)$ being calculated in 0.5 Hz steps with 0.5 Hz bandwidths in frequency range 0.5–40 Hz. Then, 100 comodulograms for each set were obtained. Hereafter, mean values were taken for each set. As shown in Fig. 5, compared with mean comodulograms of set C and set E as well as results of set D and set E, it is significantly shown that there exists strong coupling at band combination $\theta - \gamma$ for set E, which is consistent with the classification results illustrated above (Tables 1 and 2).

4 Conclusions

In this paper, epileptic EEG of Bonn dataset was analyzed by five PAC algorithms at nine different frequency band combinations to evaluate the differences of PAC strength between seizure activities and seizure-free intervals. The coupling strength features at different band combinations computed by different PAC methods were extracted and classified by SVM. Classification results were then denoted by AUC based on ROC with k-fold CV. Final results were shown that the classification accu-

racy was the highest at band combination $\theta - \gamma$, which can be explained as that there existed stronger PAC strength in EEG during seizure activity at the band combination $\theta - \gamma$ compared with EEG during seizure-free intervals. Hereafter, the results processed by five different evaluation methods of computing PAC were similar to each other, which illustrated the coupling results are almost unaffected by the difference of evaluation methods. Moreover, the results were also visually verified via phase-amplitude comodulogram. All these summaries indicate that the PAC feature can be used as a biomarker to detect epileptic seizures. Furthermore, this paper has a potential limitation that only EEG from ten subjects was analyzed, so in the future study, more datasets will be collected to certify the generality of the conclusion that the PAC can be used as one of the biomarkers to detect epileptic seizures.

Acknowledgements This work was supported by JST CREST (Grant No. JPMJCR1784) and JSPS KAKENHI (Grant No. 18K04178, 17K00326).

References

Aksenova, T. I., Volkovych, V. V., & Villa, A. E. P. (2007). Detection of spectral instability in EEG recordings during the preictal period. *Journal of Neural Engineering*,. https://doi.org/10.1088/1741-2560/4/3/001.

Amiri, M., Frauscher, B., & Gotman, J. (2016). Phase-amplitude coupling is elevated in deep sleep and in the onset zone of focal epileptic seizures. *Frontiers in Human Neuroscience*, *10*, 384. https://doi.org/10.3389/fnhum.2016.00387.

Andrzejak, R. G., et al. (2001). Indications of nonlinear deterministic and finite-dimensional structures in time series of brain electrical activity: Dependence on recording region and brain state. *Physical Review E Statistical Nonlinear Soft Matter Physics*, *64*, 061907. https://doi.org/10.1103/PhysRevE.64.061907.

Bogaarts, J. G., Gommer, E. D., Hilkman, D. M. W., van Kranen-Mastenbroek, V. H. J. M., & Reulen, J. P. H. (2016). Optimal training dataset composition for SVM-based, age-independent, automated epileptic seizure detection. *Medical & Biological Engineering & Computing*, *54*, 1285–1293. https://doi.org/10.1007/s11517-016-1468-y.

Canolty, R. T., Edwards, E., et al. (2006). High gamma power is phase-locked to theta oscillations in human neocortex. *Science*, *313*, 1626–1628. https://doi.org/10.1126/science.1128115.

Canolty, R. T., & Knight, R. T. (2010). The functional role of cross-frequency coupling. *Trends in Cognitive Sciences*,. https://doi.org/10.1016/j.tics.2010.09.001.

Chisci, L., Mavino, A., Perferi, G., Sciandrone, M., Anile, C., Colicchio, G., et al. (2010). Real-time epileptic seizure prediction using AR models and support vector machines. *IEEE Transactions on Biomedical Engineering*,. https://doi.org/10.1109/TBME.2009.2038990.

Cohen, M. X. (2007). Assessing transient cross-frequency coupling in EEG data. *Journal of Neuroscience*,. https://doi.org/10.1016/j.jneumeth.2007.10.012.

Exarchos, T. P., Tzallas, A. T., Fotiadis, D. I., Konitsiotis, S., & Giannopoulos, S. (2006). EEG transient event detection and classification using association rules. *IEEE Transactions on Information Technology in Biomedicine*,. https://doi.org/10.1109/TITB.2006.872067.

Fisher, R. S., et al. (2014). ILAE official report: A practical clinical definition of epilepsy. *Epilepsia.*,. https://doi.org/10.1111/epi.12550.

Guirgis, Mirna, et al. (2015). Defining regions of interest using cross-frequency coupling in extratemporal lobe epilepsy patients. *Journal of Neural Engineering*,. https://doi.org/10.1088/1741-2560/12/2/026011.

Ibrahim, George M., et al. (2013). Dynamic modulation of epileptic high frequency oscillations by the phase of slower cortical rhythms. *Experimental Neurology*,. https://doi.org/10.1016/j.expneurol.2013.10.019.

Mormann, F., et al. (2010). Phase/amplitude reset and theta-gamma interaction in the human medial temporal lobe during a continuous word recognition memory task. *Hippocampus*,. https://doi.org/10.1002/hipo.20117.

Pedregosa, F., Varoquaux, G., et al. (2011). Scikit-learn: Machine learning in Python. *Journal of Machine Learning Research*, *12*, 2825–2830.

Penny, W. D., Duzel, E., et al. (2008). Testing for nested oscillation. *Journal of Neuroscience Methods*,. https://doi.org/10.1016/j.jneumeth.2008.06.035.

Tolga, E. Ö., & Schnitzler, A. (2011). A critical note on the definition of phase-amplitude cross-frequency coupling. *Journal of Neuroscience Methods*, *201*(2), 438–43. https://doi.org/10.1016/j.jneumeth.2011.08.014.

Tort, A. B., Komorowski, R., et al. (2010). Measuring phase-amplitude coupling between neuronal oscillations of different frequencies. *Journal of Neurophysiology*, *104*(2), 1195–210. https://doi.org/10.1152/jn.00106.2010.

Vanhatalo, S., et al. (2004). Infraslow oscillations modulate excitability and interictal epileptic activity in the human cortex during sleep. *Proceedings of the National Academy of Sciences*,. https://doi.org/10.1073/pnas.0305375101.

Villa, A. E. P., & Tetko, I. V. (2010). Cross-frequency coupling in mesiotemporal EEG recordings of epileptic patients. *Journal of Physiology - Paris*,. https://doi.org/10.1016/j.jphysparis.2009.11.024.

EEG-Based Emotion Classification Using Entropy Features and Machine Learning Techniques

Jianhua Zhang, Peng Chen, and Rubin Wang

Abstract In recent years, emotion recognition has drawn intense interest from researchers in various fields. Because physiological signals are intrinsically correlated with emotions, emotion recognition method using physiological signals is objective and insusceptible to intentional disguise of the human subject under study. In particular, electroencephalogram (EEG) signals are sensitive to variations in emotional state. In this paper, the 4-class emotion classification problem is investigated. First we employ the data clustering algorithm to determine the actual class label of each physiological data point. Then, nonlinear dynamics analysis is used to extract two entropy features (i.e., sample entropy and approximate entropy) from 32-channel EEG signals. Finally, we compare five feature dimensionality reduction or feature selection algorithms and four types of machine learning classifiers. The comparative results have shown that the combination of Kernel Spectral Regression approach for EEG feature dimensionality reduction and random forest (RF) for multi-class classification leads to promising emotion classification performance.

1 Introduction

Emotion recognition is a principal branch of affective computing. It is an interdisciplinary field that integrates computer science, cognitive psychology, and neuroscience. Human emotional status can be recognized by the use of facial expressions,

J. Zhang (✉)
Department of Computer Science, Oslo Metropolitan University, 0166 Oslo, Norway
e-mail: jianhuaz@oslomet.no

P. Chen
School of Information Science and Engineering, East China University of Science and Technology, Shanghai 200237, People's Republic of China
e-mail: chenpeng0538@qq.com

R. Wang
Institute for Cognitive Neurodynamics, East China University of Science and Technology, Shanghai 200237, People's Republic of China
e-mail: rbwang@ecust.edu.cn

A. Lintas et al. (eds.), *Advances in Cognitive Neurodynamics (VII)*, Advances in Cognitive Neurodynamics,
https://doi.org/10.1007/978-981-16-0317-4_2

acoustic signals, behavioral data (i.e., body gesture, posture, etc.), or psychophysiological data (Petrushin, 1999; Anderson & McOwan, 2006; Pantic & Rothkrantz, 2000; Zhong et al., 2017). Nonetheless, the first three methods are subjective in nature. For example, the experimental subjects might deliberately conceal their true feelings and their disguised facial expressions or behavior may not correspond well to their task performance in the experimental or real-world environments. In comparison, the emotion recognition through physiological signals is more objective and reliable (Wang et al., 2014). EEG signals originate from the central nervous system (CNS) and respond more rapidly to changes of emotion than peripheral neural signals. Furthermore, it has been shown by several studies that EEG signals contain important emotion-relevant features (Petrantonakis & Hadjileontiadis, 2011; Li et al., 2009).

Picard and her associates at the MIT gathered four types of physiological signals (electromyography, pulse rate, galvanic skin response, and respiration) to identify eight classes of emotion (Picard et al., 2001). From those signals, they extracted both time- and frequency-domain features. They performed feature selection using forward floating search method, Fisher projection method and the combination of both. Finally, the KNN algorithm is used to perform classification. The results showed that the 3-class (i.e., anger, sadness, and happiness) classification accuracy achieved 88.3%, demonstrating the feasibility of using the physiological signals for emotional state recognition. In Brady et al. (2016), the authors used visual and auditory cues to trigger emotions, collected four sorts of physiological signals, including temperature, galvanic skin response, blood volume, and electrocardiogram (ECG) signal, and achieved an average classification rate of 61.8%. In Chanel et al. (2006), the authors used the international emotional picture system to arouse emotions, carried out 100 high- and low-arousal emotion-induction using four subjects, and recorded EEG, blood pressure, and skin electric response. They extracted the relevant features from heart rate, temperature, and respiratory signals, and compared the performance of linear discriminant analysis and Naive Bayes methods for emotion classification. A classification rate of around 55% was obtained. In Koelstra et al. (2012), the authors used music videos as the stimuli. Each of the 32 subjects was asked to watch 40 clips of the music video. They measured the subjective rating, facial expressions, EEG, and peripheral physiological signals and reported an overall correct classification rate of 67.7%. In Schmidt and Trainor (2001), the researchers also utilized music to elicit four classes of emotions and observed that when positive musical stimuli were used, the EEG activities in the frontal areas of left hemisphere increased, whereas the EEG activities in the frontal areas of right hemisphere strengthened under the negative music stimuli. Therefore, it was concluded in their paper that there is a strong correlation between the frontal area of brain and the emotions. In Wagner et al. (2005), the authors recorded four physiological signals (i.e., ECG, galvanic skin response, EOG, and respiration). They compared three feature selection algorithms: variance analysis, Fisher projection method, and sequence forward drifting selection. In addition, they adopted three classifiers, namely K-nearest neighbor, linear discriminant analysis, and multi-layer perceptron, to classify the emotions into four states (joy, happiness, anger, and sadness) and obtained promising emotion classification results.

In this paper, we consider the emotion recognition problem using EEG signals and attempt to reveal the complex unknown correlation between EEG signals and emotional states. First, the subjective assessment data were clustered to determine the target emotion classes. Then, we perform feature extraction based on nonlinear dynamics analysis of the EEG signals. We compare the emotion recognition accuracy of five feature reduction algorithms, i.e., Kernel Spectral Regression (KSR), Locality Preserving Projection (LPP), Principal Component Analysis (PCA), minimal-Redundancy-Maximal-Relevance (mRMR), and Relieff, as well as four ML classifiers, including k-Nearest Neighbor (KNN), Naïve Bayes (NB), Support Vector Machine (SVM), and Random Forest (RF).

2 Methods

2.1 Dataset and EEG Data Preprocessing

Emotion Elicitation Experiment. This section will describe the DEAP database used in our emotion classification work. Using the 2D model of emotion, Koelstra et al. (2012) used 40 music videos for emotion elicitation and 32 subjects (half male and half female; age 19–37 with a mean age of 26.9 years old) in their experiments. They measured physiological signals as well as facial expression data. More specifically, they measured 40-channel physiological signals, including 32-channel EEG signals and other 8-channel peripheral physiological signals (including skin electric response, respiration, temperature, ECG, blood volume, EMG, and EOG signals). Figure 1 shows the experimental procedure that they suggested.

There were 40 trials of emotional stimulation experiment for each subject (each trial corresponding to watching one of the 40 music video clips). Each trial consists of four steps:

Step 1: Before each video starts, display the current video number for 2 s.

Step 2: Record the 5 s baseline EEG data.

Step 3: Play the 1-min music video.

Step 4: Collect subjective ratings (i.e., self-evaluation) on four rating scales: arousal, valence, liking, and dominance.

EEG Data Preprocessing. EEG signals respond to the change of emotional state more rapidly than other peripheral physiological signals, therefore in this paper, we focus on using EEG signals for emotion classification. In the data acquisition experiment, the original EEG signals were collected at a sampling rate of 512 Hz and then down-sampled to 128 Hz. The EOG artifact is removed from the EEG recordings by using a 4–45 Hz band-pass filter. The pre-processed EEG consists of the 60 s EEG data (during music video watching) and 3 s baseline data (before the playing of the music video). During the establishment of the DEAP database, subjects were asked to take 2 min break after watching every two videos.

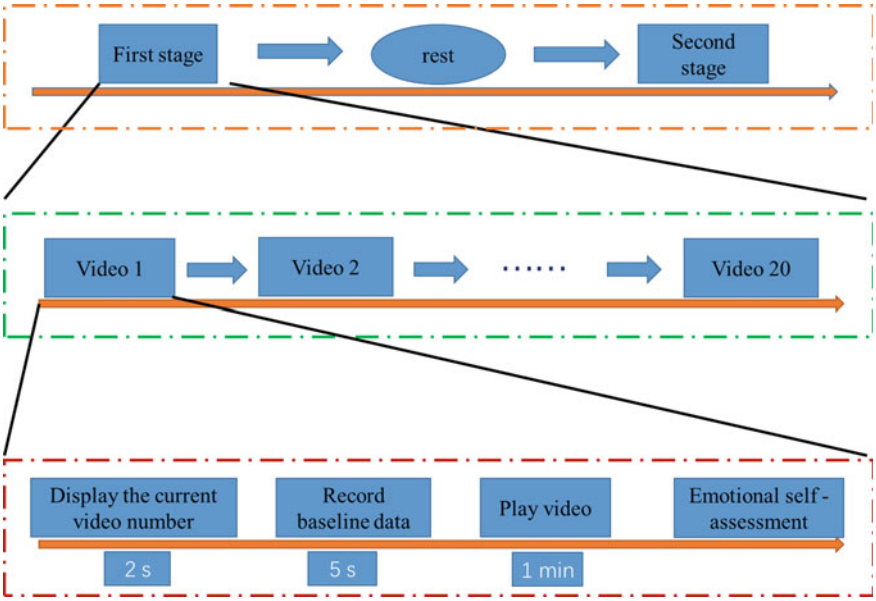

Fig. 1 The emotion-induction experimental procedure

In order to minimize the impact of the previous stimulus on the current emotion and the effect of inter-subject non-stationarity of physiological signals, we subtract the pre-stimulus baseline EEG features from the post-stimulus ones and then normalize the resulting difference (or deviation) to the interval [0, 1]. The 60 s EEG signal is segmented into 15 equal, non-overlapping segments. Here, 4 s is taken as the length of the time window. After such processing, the number of samples is 40*15 = 600 per subject. For 32 subjects, 32*600 = 19,200 samples are available.

Most of the previous studies considered only a usually small number of emotion classes. For example, using the DEAP database, many studies on emotion recognition dealt with the binary emotion (positive vs. negative valence or high vs. low arousal) classification problem and computed the class labels by oversimplified threshold of subjective data (Yin et al., 2017; Petrantonakis & Hadjileontiadis, 2011; Daimi & Saha, 2014; Yoon & Chung, 2013). In order to determine reliably the target emotional classes, we use the following method. By performing *k*-means clustering of subjective ratings on the arousal and valence rating scales, we can determine the target emotion class for each data point on the 2D (arousal and valence) emotion plane. The clustering results are shown in Fig. 2. Figure 3 shows the 2D emotion plane, where LV represents low valence (negative emotion), HV represents high valence (positive emotion), LA represents low arousal, and HA represents high arousal. The cluster centers when $k = 4$ are given in Table 1.

When *k*-means algorithm is used for clustering, it is necessary to set the initial clusters. The setting of the initial cluster centers depends on if the 2D emotion model can be accounted for the obtained class labels. Since the true class labels (i.e.,

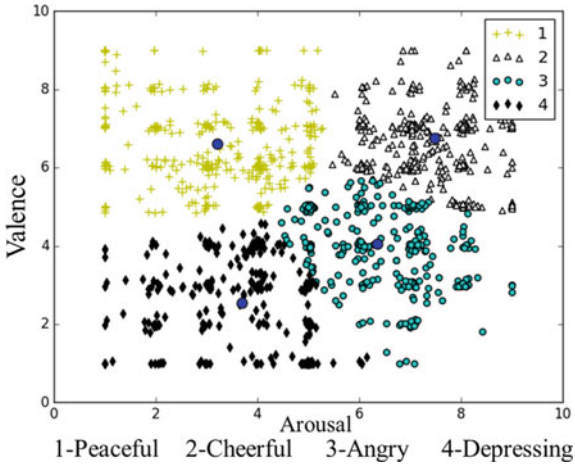

Fig. 2 The *k*-means clustering result

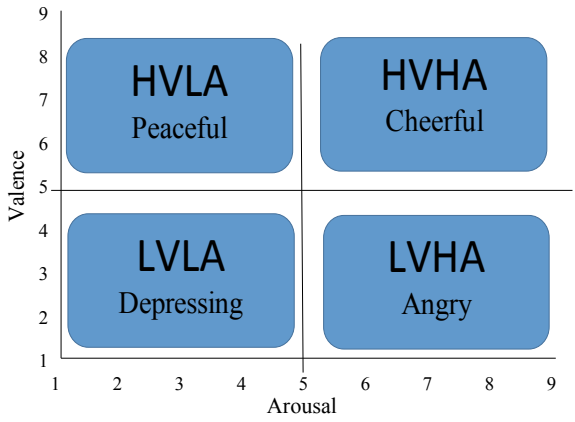

Fig. 3 A 2D emotion model

Table 1 The four cluster centers obtained by the *k*-means algorithm ($k = 4$)

Emotion class	Cluster center		Size of class (# of data in each class)
	Arousal	Valence	
Peaceful	3.21	6.61	340
Cheerful	7.48	6.76	354
Upset	6.35	4.05	309
Depressed	3.69	2.55	277

ground truth or golden yardstick) are unknown, we use the Calinski-Harabasz index to quantify the data clustering performance. The larger the Calinski-Harabasz index is, the higher the clustering quality turns. The Calinski-Harabasz index (Calinski and

Harabasz, 1974) is defined by:

$$s_K = \frac{N-K}{K-1} \cdot \frac{\mathrm{Tr}(B_k)}{\mathrm{Tr}(W_k)} \tag{1}$$

$$W_K = \sum_{q=1}^{K} \sum_{x \in \mathbf{c}_q} (\mathbf{x} - \mathbf{c}_q)(\mathbf{x} - \mathbf{c}_q)^{\mathrm{T}} \tag{2}$$

$$B_K = \sum_{q} N_q (\mathbf{c}_q - \mathbf{c})(\mathbf{c}_q - \mathbf{c})^{\mathrm{T}} \tag{3}$$

where B_k denotes the covariance matrix of clusters, W_k the covariance matrix of a single cluster, N is the sample size, K is the number of clusters, $\mathbf{c}_q$ represents the center of the q-th cluster, and N_q the size of the q-th cluster.

Figure 4 shows the Calinski-Harabasz index and the corresponding Sum of Squared Errors (SSE) when k is increased from 2 to 8. It can be seen that the Calinski-Harabasz index is largest (1180.69) when $k = 4$. On the other hand, the 2D emotion plane can be divided into four types of emotions by the threshold method. Therefore, the number of clusters is set to four.

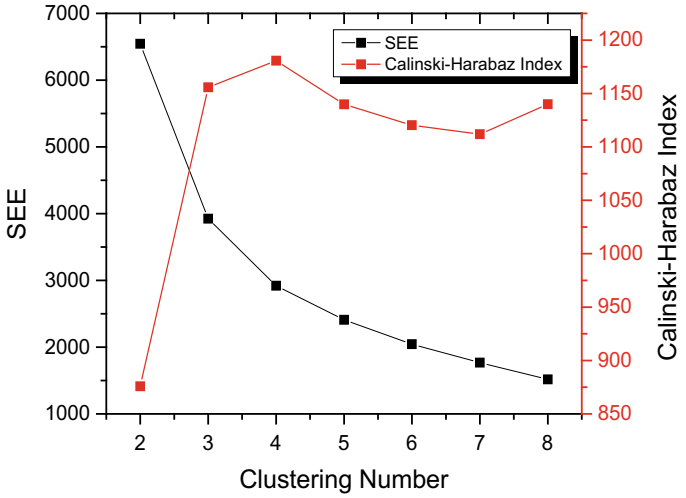

Fig. 4 The change of the Calinski-Harabasz index and SSE vs. the number of clusters

2.2 EEG Feature Extraction

Due to the inherent complexity of EEG signals, it is rather difficult to extract the complete set of salient emotion features/attributes from them. In recent years, nonlinear dynamics methods have been used to analyze EEG signals (Zhang et al., 2014; Vijith et al., 2016; Guido, 2018). Among them, approximate entropy (Pincus, 1991) and sample entropy (Richman & Moorman, 2000) are two important measures to quantify the complexity of a time series. In this work, we perform nonlinear dynamics analysis of EEG signals to extract approximate entropy and sample entropy features.

2.3 EEG Feature Reduction/Selection

EEG feature reduction/selection is crucial for emotion recognition due to the high-dimensionality of the EEG features extracted. In addition, they are usually needed for: (1) data visualization; (2) acceleration of the ML classifier training; or (3) alleviation of the notorious problem of curse of dimensionality to enhance prediction or generalization accuracy of the trained classifier.

If ApEn and SampEn are used jointly as the emotion features, the feature dimensionality is $32*2 = 64$. This paper compares the performance of three-dimensionality reduction algorithms (KSR, LPP, and PCA) and two feature selection algorithms (mRMR and Relieff). Here PCA is used as a reference for comparison of other algorithms and the kernel spectral regression (KSR) *discriminant analysis* algorithm (Cai et al., 2011) is very effective to deal with big data.

2.4 Classifiers

The constructions of the ML emotion classifier includes such steps as data preprocessing, EEG feature extraction, feature reduction, and optimal classifier design under predefined performance criteria (Kim et al., 2004). In order to obtain accurate recognition, we will focus on random forest (RF). The basic idea of RF, an ensemble learning method, is bagging, i.e., the RF classifier is constructed by combining a set of decision trees. We can decide the classifier output through voting among those decision trees (Breiman, 2001).

3 Results and Discussion

3.1 Comparison of Feature Extraction/Reduction Algorithms

In order to obtain more reliable recognition accuracy, for each subject the samples were divided into a training set and a test set by 5-fold cross-validation. Therefore, for each subject, the size of training set is 480 and the size of test set is 120. The feature dimensionality of approximate entropy and sample entropy is 32 and 32, respectively. Here, we use the RF classifier. By comparison of different classifiers, we found that the recognition rate of the RF classifier is higher than that of KNN and NB and the training speed of RF is higher than that of SVM. Here we compared five EEG feature reduction algorithms: KSR, LPP, mRMR, Relieff, and PCA. For the purpose of comparison, the emotion recognition accuracy when using all the original features, i.e., the case of No Dimensionality Reduction (NDR), is used as the baseline value.

The parameter setting for each dimensionality reduction algorithm is as follows: for the KSR and LPP, we select the Gaussian kernel function; for the KSR we select the L2 norm as the regularization type and set the regularization parameter as 0.01; for the LPP we set the number of nearest neighbors as 5 and use the Euclidean distance function; for mRMR and Relieff we set the number of features selected as 20; and for PCA we set the variance contribution to 0.98. There are four classes of emotions and approximate entropy and sample entropy are extracted as features of emotion.

The emotion recognition accuracy is shown in Table 2, in which Total means that both the approximate entropy and the sample entropy are used in the feature set. From Fig. 5, we can find that when we use KSR algorithm for feature dimensionality reduction, the joint use of approximate entropy and sample entropy as features led to a high classification accuracy of $92.8 \pm 2.8\%$ and that the classification accuracy of using different dimensionality reduction algorithms is significantly different. The KSR and LPP dimensionality reduction algorithms significantly outperform feature selection algorithms (mRMR and Relieff).

Table 2 The 4-class emotion classification accuracy (%) under different feature reduction/selection algorithms

Features	KSR	LPP	mRMR	Relieff	PCA	NDR
ApEn	89.9 ± 3.7	82.8 ± 4.1	75.7 ± 4.9	76.2 ± 5.1	82.9 ± 4.2	78.7 ± 5.6
SampEn	87.5 ± 6.3	81.7 ± 6.8	74.7 ± 6.3	75.7 ± 6.2	81.1 ± 7.0	77.4 ± 6.7
Total	$\mathbf{92.8 \pm 2.8}$	86.3 ± 6.6	75.2 ± 5.9	76.1 ± 5.7	83.8 ± 6.1	77.4 ± 5.9

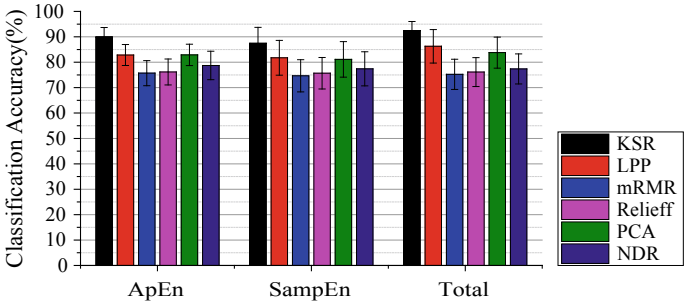

Fig. 5 The comparison of 4-class emotion classification results

3.2 Comparison of ML Classifiers

The classifiers under comparison include KNN, NB, SVM, and RF. The number of nearest neighbors in KNN is set as 6 by trial-and-error; in the SVM the radial basis kernel function is used and grid search is performed to find the optimal penalty factor C and parameter γ in interval $C \in \{2^{-8}, 2^{-7}, \cdots 2^{7}, 2^{8}\}$ and $\gamma \in \{2^{-8}, 2^{-7}, \cdots 2^{7}, 2^{8}\}$; for the RF, we empirically set the number of decision trees as 500 and the number of features selected for further splitting each time as $\sqrt{m}$, where m denotes the feature dimensionality.

Figure 6 shows the comparative results. It can be found that the subject-average classification accuracy of RF and SVM and KSR is 92.7% and 92.8%, respectively, much higher than that of KNN and NB. However, the tuning of SVM hyper-parameters is more tedious and time-consuming, while simple use of the empirical hyper-parameters of RF can obtain comparable classification accuracy.

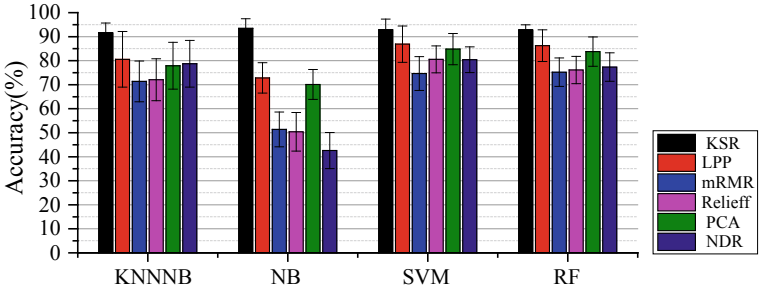

Fig. 6 The comparison of 4-class emotion classification accuracy of a combination of five feature reduction/selection algorithms and four ML classifiers

4 Conclusion and Future Outlook

In this paper, we study the EEG-based emotion recognition problem using the DEAP dataset. We consider and compare different feature extraction, feature reduction/selection, and ML classification methods and finally draw the following conclusions :

(1) When using the relative change of entropies as the features, rather than the absolute entropy of the EEG signals under emotional stimuli, the correct classification rate can be significantly improved.
(2) The classification rate can be increased if the approximate entropy and sample entropy features are used in combination.
(3) KSR is the best feature reduction/selection algorithm by comparison.
(4) SVM and RF classifiers outperform KNN and NB for EEG-based recognition of emotions.

The future work is anticipated as follows:

(1) The 3D or even higher-dimensional emotion model can be considered to determine more classes of emotion.
(2) We need further research on the method of determining the target classes. It may be also possible to better determine the target classes by taking into account the content of the emotional stimulus material.
(3) In order to further improve the accuracy of emotion recognition, we need to combine heterogeneous (multi-modal) physiological signals by certain data/information fusion methods to realize multi-modal emotion recognition.
(4) In real-world applied task environment, generic emotion classifiers would be preferred. We need to utilize transfer learning technique to design the subject-independent classifier so as to achieve a comparable/stable classification rate across different subjects with marked individual differences in terms of the recorded EEG signals.

Acknowledgements This research was funded in part by the OsloMet Faculty TKD Lighthouse Project 201369-100.

References

Anderson, K., & McOwan, P. W. (2006). A real-time automated system for the recognition of human facial expressions. *IEEE Transactions on Systems, Man, and Cybernetics, Pt B (Cybernetics), 36*(1), 96–105.

Brady, K., Gwon, Y., Khorrami, P., et al. (2016). Multi-modal audio, video and physiological sensor learning for continuous emotion prediction. In *Proceedings of the 6th International Workshop on Audio/Visual Emotion Challenge* (pp. 97–104). ACM.

Breiman, L. (2001). Random forests. *Machine Learning, 45,* 5–32.

Cai, D., He, X., & Han, J. (2011). Speed up kernel discriminant analysis. *The VLDB Journal, 20,* 21–33.

Caliński, T., & Harabasz, J. (1974). A dendrite method for cluster analysis. *Communications in Statistics, 3*(1), 1–27.

Chanel, G., Kronegg, J., Grandjean, D., et al. (2006). *Emotion assessment: Arousal evaluation using EEG's and peripheral physiological signals* (pp. 530–537). Berlin, Heidelberg: Springer.

Daimi, S. N., & Saha, G. (2014). Classification of emotions induced by music videos and correlation with participants' rating. *Expert Systems with Applications, 41*(13), 6057–6065.

Guido, R. C. (2018). A tutorial review on entropy-based handcrafted feature extraction for information fusion. *Information Fusion, 41,* 161–175.

Kim, K. H., Bang, S. W., & Kim, S. R. (2004). Emotion recognition system using short-term monitoring of physiological signals. *Medical & Biological Engineering & Computing, 42*(3), 419–427.

Koelstra, S., Mühl, C., Soleymani, M., et al. (2012). DEAP: A database for emotion analysis using physiological signals. *IEEE Transactions on Affective Computing, 3*(1), 18–31.

Li, X., Hu, B., Zhu, T., et al. (2009). Towards affective learning with an EEG feedback approach. In *Proceedings of the 1st ACM International Workshop on Multimedia Technologies for Distance Learning* (pp. 33–38). ACM.

Pantic, M., & Rothkrantz, L. J. M. (2000). Automatic analysis of facial expressions: The state of the art. *IEEE Transactions on Pattern Analysis and Machine Intelligence, 22*(12), 1424–1445.

Petrantonakis, P. C., & Hadjileontiadis, L. J. (2011). A novel emotion elicitation index using frontal brain asymmetry for enhanced EEG-based emotion recognition. *IEEE Transactions on Information Technology in Biomedicine, 15*(5), 737–746.

Petrushin, V. A. (1999). Emotion in speech: recognition and application to call centers. In *Proceedings of the 1999 Conference on Artificial Neural Networks in Engineering* (pp. 7–10).

Picard, R. W., Vyzas, E., & Healey, J. (2001). Toward machine emotional intelligence: Analysis of affective physiological state. *IEEE Transactions on Pattern Analysis & Machine Intelligence, 23*(10), 1175–1191.

Pincus, S. M. (1991). Approximate entropy as a measure of system complexity. *Proceedings of the National Academy of Sciences, 88*(6), 2297–2301.

Richman, J. S., & Moorman, J. R. (2000). Physiological time-series analysis using approximate entropy and sample entropy. *American Journal of Physiology-Heart and Circulatory Physiology, 278*(6), H2039–H2049.

Schmidt, L. A., & Trainor, L. J. (2001). Frontal brain electrical activity (EEG) distinguishes valence and intensity of musical emotions. *Cognition and Emotion, 15*(4), 487–500.

Vijith, V. S., Jacob, J. E., Iype, T. et al. (2016). Epileptic seizure detection using nonlinear analysis of EEG. In *Proceedings of International Conference on Inventive Computation Technologies* (pp. 1–6).

Wagner, J., Kim, J., & Andre, E. (2005) From physiological signals to emotions: implementing and comparing selected methods for feature extraction and classification. In *Proceedings of IEEE International Conference on Multimedia and Expo* (pp. 940–943).

Wang, X. W., Nie, D., & Lu, B. L. (2014). Emotional state classification from EEG data using machine learning approach. *Neurocomputing, 129*(4), 94–106.

Yin, Z., Zhao, M., Wang, Y., et al. (2017). Recognition of emotions using multimodal physiological signals and an ensemble deep learning model. *Computer Methods and Programs in Biomedicine, 140,* 93–110.

Yoon, H. J., & Chung, S. Y. (2013). EEG-based emotion estimation using Bayesian weighted-log-posterior function and perceptron convergence algorithm. *Computers in Biology and Medicine, 43*(12), 2230–2237.

Zhang, C., Wang, H., & Fu, R. (2014). Automated detection of driver fatigue based on entropy and complexity measures. *IEEE Transactions on Intelligent Transportation Systems, 15*(1), 168–177.
Zhong, Y., Zhao, M., Wang, Y., et al. (2017). Recognition of emotions using multimodal physiological signals and an ensemble deep learning model. *Computer Methods & Programs in Biomedicine., 140*(C), 93–110.

Optimized Correlation-Based Time Window Selection Algorithm for Motor Imagery Based BCIs

Zongmei Chen, Cili Zuo, Hak-Keung Lam, Yangyang Miao, Xingyu Wang, and Jing Jin

Abstract For motor imagery (MI)-based brain–computer interface (BCI) systems, the time latency and length of MI task vary between trials and subjects, due to the differences between subjects' reaction time and personal habits. Therefore, the starting and ending time point of each MI task can hardly be determined manually for different subjects. Fixed time window may contain task-irrelevant signals or does not contain sufficient task-related signals, which will lead to degraded the performance of MI-based BCI systems. To address this issue, an optimized correlation-based time window selection (OCTWS) algorithm is proposed for MI-based BCIs. The optimized starting point and length of MI task-relevant signals are determined simultaneously based on correlation analysis and performance evaluation. A public EEG dataset (BCI Competition IV Dataset I) is used to evaluate the proposed OCTWS method. Experimental results demonstrate that OCTWS helps improve the feature extraction and classification performance of MI.

1 Introduction

Brain–computer interface (BCI) systems can straightly transform brain signals such as electroencephalogram (EEG) to control external devices without the involvement of peripheral nerves or muscles (Makand and Wolpaw, 2009). BCIs provide a new communication/control channel for patients who have lost normal communication/control abilities due to severe motor impairments, which have gained interest in neuroscience and rehabilitation engineering (Birbaumerand Cohen, 2007). Motor imagery (MI) is a mental representation of motor behavior. The tasks associated with motor imagery can bring variations in the rhythmic activities of the brain elec-

Z. Chen · C. Zuo · Y. Miao · X. Wang · J. Jin (✉)
School of Information Science and Engineering, East China University of Science and Technology, Shanghai, China

H.-K. Lam
Department of Informatics, King's College London, London, UK

A. Lintas et al. (eds.), *Advances in Cognitive Neurodynamics (VII)*, Advances in Cognitive Neurodynamics,
https://doi.org/10.1007/978-981-16-0317-4_3

trophysiological signals which can be expressed as event-related desynchronization /synchronization (ERD/ERS) phenomenon (Pfurtscheller 1977, 1992), specifically in mu (8–12Hz) and beta rhythm (13–30Hz) (McFarland et al., 2000; Pfurtscheller et al., 2006). The corresponding differences in EEG signals can be transformed to control commands. Such MI-based BCIs are usually more convenient to use than stimuli-based BCIs since it can be operated without external stimuli (Qiu et al., 2016). It has shown promising application values in medical rehabilitation (post-stroke rehabilitation), auxiliary control (e.g., neuroprosthesis control (Müller-Putz et al., 2005), 2D cursor control (Long et al., 2012), wheelchair control (Tang et al., 2018), etc.), and social entertainment (Folgieri and Zampolin, 2014; van de Laar etal., 2013). However, it has reported that many MI-based BCIs users cannot obtain sufficient accuracy of control commands (Guger et al., 2003). One of the reasons is that it is hard to accurately extract the features about MI. Thus, an urgent problem in MI-based BCIs is how to further improve the feature extraction performance.

Various feature extraction methods have been proposed, such as adaptive autoregressive model (ARR) (Schlögl et al., 1997), wavelet transform (WT) (Hsu and Sun, 2009), wavelet packet transform (WPT) (Zhou and Wan, 2012), and common spatial pattern (CSP) (Yang and Wu, 2014). Particularly, CSP is always regarded as one of highly successful algorithms due to its good performance in extracting spatial domain features (Blankertz et al., 2008), which can extract task-related signal components from multi-channel EEG data and suppress uncorrelated signal components (Ramoser et al., 2000). Commonly, a fixed starting point and length of EEG signals have been used to extract the MI features in the majority of state-of-the-art MI-based BCIs (Qiu et al., 2016; Ang et al., 2012; Rodriguez-Bermudez et al., 2013). However, considering it is hard to determine certainly when participants begin to perform MI task and how long it lasts, and fixed time window method may lead to low classification accuracy because of deficient information or interference from invalid data. To address this issue, recently, a correlation-based time window selection (CTWS) algorithm has been proposed and achieved better classification accuracy than fixed time window method (Feng et al., 2018). In CTWS, the optimized starting point of MI task-relevant signals was determined based on correlation analysis. However, CTWS using a fixed window length did not consider the influence of window length to MI feature extraction.

In this paper, an optimized correlation-based time window selection (OCTWS) algorithm is proposed to select the starting point and length of MI task-relevant time windows simultaneously. In the proposed method, correlation analysis and performance evaluation are used to determine the starting point and length of time windows. The common spatial pattern (CSP) method is used to extract MI features, and a support vector machine (SVM) with linear kernel is then trained on the selected features to classify MI tasks. The proposed method is validated on a public EEG dataset (BCI Competition IV Dataset I) and compared with fixed time window length-based CSP and CTWS. Experimental results show that OCTWS achieves more superior classification performance.

The remainder of this paper is organized as follows: Sect. 2 describes the materials and methods in details; Sect. 3 shows the experimental results; Sect. 4 gives the discussion; and finally, Sect. 5 serves as conclusion.

2 Materials and Methods

2.1 Materials

The Dataset I from BCI Competition IV was used to evaluate the performance of proposed method. This dataset consists of EEG signals based on MI, obtained from seven subjects (numbered by S1–S7), recorded via 59 electrodes with 100 Hz sampling frequency. The timing scheme of single trial is shown in Fig. 1 where each trial lasts for 8 s, including three phases: in preparation phase (0–2 s), a fixation cross would show on the monitor to remind the subject focusing attention to the task, then in MI task phase (2–6 s), the subject was asked to perform corresponding MI task (Left hand/Right hand/Foot) according to the cue, finally, in rest period (6–8 s), a black screen would appear on the monitor. More details about the dataset can be found at Web site: https://www.bbci.de/competition/iv/. In this paper, only the calibration data in total of 200 trials for each subject were used to evaluate the algorithms.

2.2 Methods

CTWS is an effective method for selecting trial-specific time window for each subject that can facilitate effective feature extraction. The main principle of CTWS is to iteratively adjust the time window of the training data to find the optimized reference signals based on the maximum correlation between current reference signals and EEG signals with different starting points, as described in Eqs. (1) and (2).

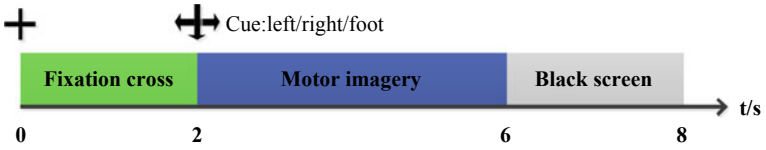

Fig. 1 Timing scheme of single MI trial

$$\mathrm{cov}(R_{ij}, C_{ij}) = \frac{1}{N_t}\sum_{t-1}^{N_t}(R_i(t) - \bar{R}_i(t))(C_i(t) - \bar{C}_i(t)), \quad i = 1, 2;\ j = C3, C4 \tag{1}$$

$$V = \underset{k}{\mathrm{argmax}}(\mathrm{cov}(R_{i3}, C_{i3}^k)) + \mathrm{cov}(R_{i4}, C_{i4}^k), k = 1, 2, \ldots, n \tag{2}$$

where $\boldsymbol{t}$ is the index of current point in the time window with the length of $\boldsymbol{Nt}$, $\boldsymbol{i}$ is the index of class, $\boldsymbol{j}$ is the index of channel (channel C3 and C4 were selected), $\boldsymbol{R}$ is the reference signal, $\boldsymbol{C}$ is the signal of current sample, $\overline{\boldsymbol{R}}$ and $\overline{\boldsymbol{C}}$ are the average value of $\boldsymbol{R}$ and $\boldsymbol{C}$ over $\boldsymbol{t}$; $\boldsymbol{V}$ represents the time window with maximum average correlation value, and $\boldsymbol{n}$ is the number of generated new time windows.

After obtaining the optimized reference signals, the starting points of the time windows for both training and test samples are adjusted using correlation analysis by Eqs. (1) and (2). Note that, in CTWS, only the starting point of the time window is adjusted, while the length of the time window is not considered.

As for the improvement of traditional CTWS, the proposed OCTWS aims to select optimal starting point and length of time window simultaneously. The CTWS is used to determine the starting point of the time window, and a wrapper-based feature selection method (Foitong et al. 2012) is used to select the best length of the time window. The CSP and SVM are used for feature extraction and classification, respectively. The procedure of OCTWS can be described as follows:

(1) Firstly, divide the preprocessed EEG samples ($\boldsymbol{X} \in \mathbb{R}^{\boldsymbol{M}} \times \boldsymbol{N} \times \boldsymbol{K}$, where $\boldsymbol{M}$, $\boldsymbol{N}$, and $\boldsymbol{K}$ denote the number of channels, sampling points, and trials, respectively) into two parts (training samples and test samples).

(2) Next, for the training samples, set the current window length to the minimum window length (1000 ms was selected in this paper), and perform the CTWS to obtain the optimized reference signals ($\boldsymbol{OR}_1$ and $\boldsymbol{OR}_2$) of each class; then, adjust the start time point for test samples with $\boldsymbol{OR}_1$ and $\boldsymbol{OR}_2$ based on Eqs. (1), and calculate the test classification accuracy.

(3) Then, update the length of the time window (increased by a window change step, 200 ms was used in this paper), and repeat (1) and (2) until the current window length reaches the maximum window length (3000 ms was selected in this paper). If the new classification accuracy is higher than the previous classification accuracy, replace $\boldsymbol{OR}_1$ and $\boldsymbol{OR}_1$ with the new reference signals ($\boldsymbol{NOR}_1$ and $\boldsymbol{NOR}_2$). The process above was repeated ten times with a tenfold cross-validation scheme to evaluate the average classification accuracies.

(4) Finally, select the $\boldsymbol{OR}_1$ and $\boldsymbol{OR}_2$ corresponding to the highest average classification accuracy as the optimized reference signals $\boldsymbol{NOR}_1$ and $\boldsymbol{NOR}_2$, which are then employed to select the optimal time windows for each raw sample using correlation analysis through Eqs. (1) and (2).

The pseudocode of OCTWS is given in Table 1.

Table 1 Pseudocode of OCTWS

Algorithm: Optimized Correlation-based Time Window Selection (OCTWS)
Inputs: Preprocessed EEG samples ($\boldsymbol{X}$), Minimum window length, Maximum window length, Window change step.
Outputs: Optimized time window for each sample.
Steps:
1 Initialize Current window length to Minimum window length;
2 **while** Current window length < Maximum window length
3 Generate reference signal $\boldsymbol{OR}_1$ and $\boldsymbol{OR}_2$ by CTWS with Current window length for training samples;
4 Adjust start time point for test samples with $\boldsymbol{OR}_1$ and $\boldsymbol{OR}_2$ based on Eqs.(1) and (2);
5 Calculate classification accuracy for test samples;
6 Current window length = Current window length + Window change step;
7 **end**
8 Set optimized reference signals $\boldsymbol{NOR}_1$ and $\boldsymbol{NOR}_2$ to $\boldsymbol{OR}_1$ and $\boldsymbol{OR}_2$ with the highest classification accuracy;
9 Obtain the optimized time window for each sample with $\boldsymbol{NOR}_1$ and $\boldsymbol{NOR}_2$ based on Eqs.(1) and (2).

3 Results

The proposed OCTWS was compared with traditional CSP and CTWS with fixed window length. For CSP and CTWS, window length is set to 2000 ms according to (Feng et al. 2018). For all three methods, all samples were filtered by a fifth order Butterworth filter (frequency band ranging from 8 to 30 Hz).

In order to test the performance of the proposed OCTWS, it was combined with CSP (OCTWS + CSP) to extract feature on BCI Competition IV Dataset I. The obtained feature distributions by CTWS + CSP and OCTWS + CSP are shown in Fig. 2, respectively, for seven subjects. The blue and red circles represent the two different feature classes. It can be clearly observed that compared to the traditional CTWS combined with CSP (CTWS+CSP) method, the OCTWS+CSP method improves the distinguishing degree of the two classes of EEG signals for each subject. Especially, subject 3 and subject 6 are of most obvious. Therefore, it qualitatively shows that the proposed OCTWS method provides a better effect on the extraction of EEG features than the CTWS method, which will promote the pattern classification of MI-based EEG signals.

The above results of feature distribution indicate that the optimization of time window length is also an important factor for MI-based BCIs. Figure 3 presents two examples to show the effects of varying time window length (from 1000 to 3000 ms)

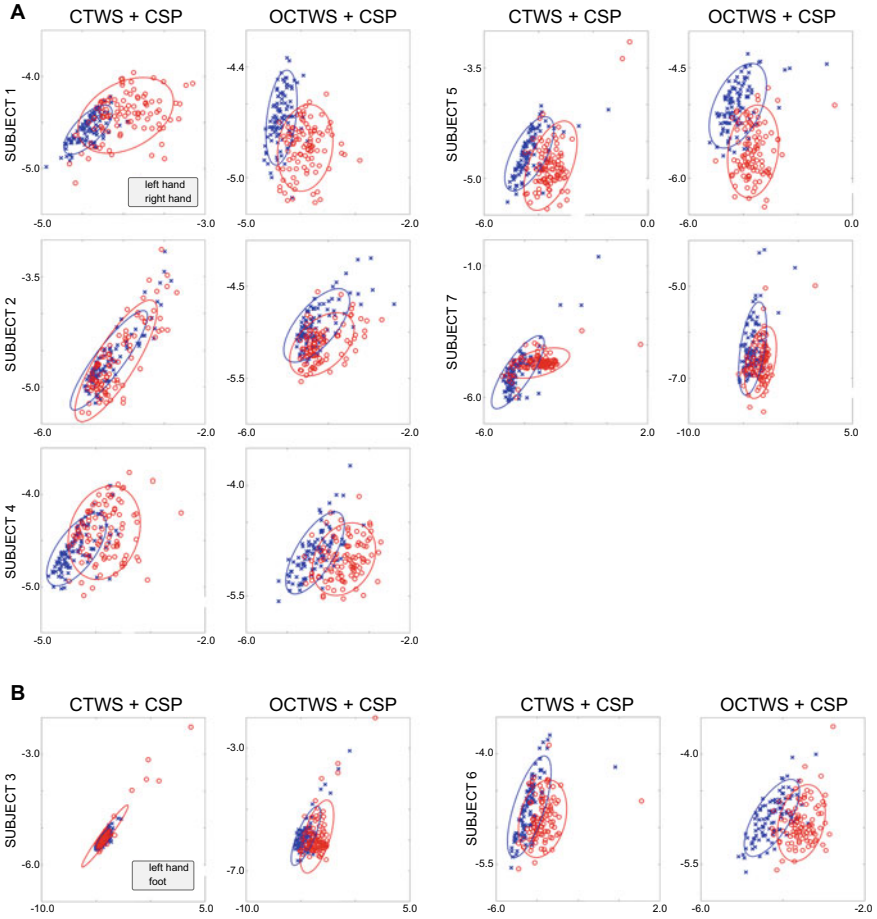

Fig. 2 Feature distribution of each class extracted by CTWS + CSP and OCTWS + CSP for seven subjects. **a** Five subjects tested on right and left hand. **b** Two subjects tested on right hand and foot

on the average classification accuracy in a tenfold cross-validation for subject 3 (S3) and 4 (S4). It can be seen that the average accuracy varies with the length of time, and the optimal time window length is subject specific, for S3 is 1600 ms and for S4 is 2600 ms.

To quantitatively evaluate the performance of the proposed OCTWS algorithm for time window length optimization, we compared the classification accuracy of OCTWS + CSP, CTWS + CSP, and CSP method using SVM with linear kernel as the classifier (Feng et al. 2018). A tenfold cross-validation is implemented to evaluate the classification performance. The experimental results of classification accuracy of OCTWS+CSP, CTWS+CSP, and CSP are given in Table 2, for seven subjects. The first obvious finding is that the classification accuracy of CTWS + CSP

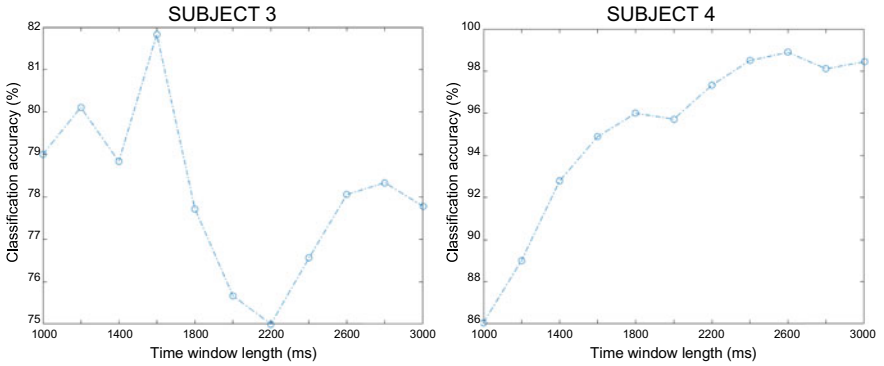

Fig. 3 Effects of varying time window length on the average classification accuracy for subject 3 (S3) and subject 4 (S4)

Table 2 Classification accuracy (%) of CSP, CTWS + CSP, and OCTWS + CSP, for seven subjects

Subjects	CSP	CTWS + CSP	OCTWS + CSP
S1	64.50	82.50	83.50
S2	51.50	76.00	78.00
S3	53.00	66.00	86.50
S4	89.00	96.00	96.00
S5	93.50	98.00	96.00
S6	46.00	80.00	90.50
S7	66.00	82.00	87.00
Mean±std	66.21±18.56	82.93±11.12	88.21±6.55

(82.93% ± 11.12%) and OCTWS + CSP (88.21% ± 6.55%) significantly outperform CSP (66.21% ± 18.56%) with fixed window. Moreover, the average classification accuracy of OCTWS+CSP method has improved by 5.28% compared to CTWS + CSP method (82.93% versus 88.21%). The comparison of classification results further verifies the superior performance of OCTWS in obtaining the optimal starting point and length of time window in MI-based BCI system.

4 Discussion

For motor imagery (MI)-based BCI systems, extracting the features matching MI tasks is a key link to improve the recognition rate. CSP is an effective feature extraction algorithm, and some improved CSP algorithms have been proposed in recent studies. In particular, the time window selection of EEG signals has an important

influence on the feature extraction based on CSP ((Feng et al., 2018)). The study based on CTWS algorithm has indicated that the starting point time window varies from one trail to the next among any one individual during motor imagery. However, the length is also a major factor in determining the time window. As shown in Fig. 3, the classification accuracy changed as time window length varied for different subjects. Therefore, it is necessary to select the starting point and length of time window at the same time before feature extraction.

In this study, the proposed OCTWS algorithm further considers the length of time window based on traditional CTWS algorithm (only considering the starting point of time window). It has confirmed that CTWS is more superior in feature extraction than CSP in BCI Computation IV Datasets. But as shown in Fig. 2, we can find that the distribution of MI feature based on OCTWS algorithm has once again improved. So overall, the proposed OCTWS algorithm is more conducive to feature extraction than CSP and CTWS algorithms.

As given in Table 2, the proposed OCTW algorithm also brings about a higher classification accuracy compared to CSP and CTWS algorithm, which evaluate the effectiveness and practicality. Of course, in both OCTWS and CTWS algorithms, only the time window of MI is selected. So in future work, we can further consider the frequency band selection of EEG signals in order to boost the performance of OCTWS algorithm.

5 Conclusion

In this paper, we have proposed an optimized correlation-based time window selection (OCTWS) algorithm for further improving the classification performance of traditional CTWS which can select optimal starting point and length of time window simultaneously. We incorporated CSP and SVM into the structure of the OCTWS algorithm for feature extraction and classification on BCI Competition IV Dataset I. The experimental results demonstrated that the optimization of time window length was also an important factor for MI-based BCIs besides starting time point. The features extracted by proposed OCTWS algorithm were easier to classify and could also achieve better classification performance compared to the traditional CTWS.

Acknowledgements This work was supported by the National Key Research and Development Program 2017YFB13003002. This work was also supported in part by the Grant National Natural Science Foundation of China, under Grant Nos. 61573142, 61773164, and 91420302, the program of Introducing Talents of Discipline to Universities (the 111 Project) under Grant B17017.

References

Ang, K. K., Chin, Z. Y., Zhang, H., & Guan, C. (2012). Mutual information-based selection of optimal spatial-temporal patterns for single-trial EEG-based BCIs. *Pattern Recognition*, *45*(6), 2137–2144. Brain Decoding.

Birbaumer, N., & Cohen, L. G. (2007). Brain-computer interfaces: communication and restoration of movement in paralysis. *Journal Physiology*, *579*(Pt 3), 621–36.

Blankertz, B., Blankertz, B., Tomioka, R., Lemm, S., Kawanabe, M., & Müller, K.-R. (2008). Optimizing spatial filters for robust EEG single-trial analysis. *IEEE Signal Processing Magazine*, *25*, 581–607.

Feng, J., Yin, E., Jin, J., Saab, R., Daly, I., Wang, X., et al. (2018). Towards correlation-based time window selection method for motor imagery BCIs. *Neural Networks*, *102*, 87–95.

Foitong, S., Pinngern, O., & Attachoo, B. (2012). Feature subset selection wrapper based on mutual information and rough sets. *Expert System Applications*, *39*(1), 574–584.

Folgieri, R., & Zampolini, R. (2014). BCI promises in emotional involvement in music and games. *Computers in Entertainment*, *12*(1), 4:1–4:10.

Guger, C., Edlinger, G., Harkam, W., Niedermayer, I., & Pfurtscheller, G. (2003). How many people are able to operate an EEG-based brain-computer interface (BCI)? *IEEE Transactions on Neural Systems and Rehabilitation Engineering*, *11*(2), 145–7.

Hsu, W.-Y., & Sun, Y.-N. (2009). EEG-based motor imagery analysis using weighted wavelet transform features. *Journal of Neuroscience Methods*, *176*(2), 310–8.

Long, J., Li, Y., Yu, T., & Gu, Z. (2012). Target selection with hybrid feature for BCI-based 2-D cursor control. *IEEE Transactions on Biomedical Engineering*, *59*(1), 132–140.

Mak, J., & Wolpaw, J. (2009). Clinical applications of brain-computer interfaces: Current state and future prospects. *IEEE Reviews in Biomedical Engineering*, *2*, 187–199.

McFarland, D. J., Miner, L. A., Vaughan, T. M., & Wolpaw, J. R. (2000). Mu and beta rhythm topographies during motor imagery and actual movements. *Brain Topography*, *12*(3), 177–86.

Müller-Putz, G. R., Scherer, R., Pfurtscheller, G., & Rupp, R. (2005). EEG-based neuroprosthesis control: A step towards clinical practice. *Neurosci Letters*, *382*(1–2), 169–74.

Pfurtscheller, G. (1977). Graphical display and statistical evaluation of event-related desynchronization (ERD). *Electroencephalography and Clinical Neurophysiology*, *43*(5), 757–60.

Pfurtscheller, G. (1992). Event-related synchronization (ERS): An electrophysiological correlate of cortical areas at rest. *Electroencephalography and Clinical Neurophysiology*, *83*(1), 62–9.

Pfurtscheller, G., Brunner, C., Schlögl, A., & Lopes da Silva, F. H. (2006). Mu rhythm (de)synchronization and EEG single-trial classification of different motor imagery tasks. *Neuroimage*, *31*(1), 153–9.

Qiu, Z., Jin, J., Lam, H., Zhang, Y., Wang, X., & Cichocki, A. (2016). Improved SFFS method for channel selection in motor imagery based BCI. *Neurocomputing*, *207*, 519–527.

Ramoser, H., Ramoser, H., Müller-gerking, J., & Pfurtscheller, G. (2000). Optimal spatial filtering of single trial EEG during imagined hand movement. *IEEE Transactions on Rehabilitation Engineering*, *8*, 441–446.

Rodriguez-Bermudez, G., Garcia-Laencina, P. J., & Roca-Dorda, J. (2013). Efficient automatic selection and combination of EEG features in least squares classifiers for motor imagery brain-computer interfaces. *International Journal Neural System*, *23*(04), 1350015.

Schlögl, A., Flotzinger, D., & Pfurtscheller, G. (1997). Adaptive autoregressive modeling used for single-trial EEG classification. *Biomedizinische Technik (Berlin)*, *42*(6), 162–7.

Tang, J., Liu, Y., Hu, D., & Zhou, Z. (2018). Towards BCI-actuated smart wheelchair system. *Biomedical Engineering Online*, *17*(1), 111.

van de Laar, B., Gürkök, H., Bos, D. P., Poel, M., & Nijholt, A. (2013). Experiencing BCI control in a popular computer game. *IEEE Transactions on Computational Intelligence and AI in Games*, *5*(2), 176–184.

Yang, H., & Wu, S. (2014). EEG classification for BCI based on CSP and SVM-GA. In *Applied Mechanics and Materials* (Vol. 459, pp. 228–231). Trans Tech Publ.

Zhou, Z., & Wan, B. (2012). Wavelet packet-based independent component analysis for feature extraction from motor imagery EEG of complex movements. *Clinical Neurophysiology*, *123*(9), 1779–88.

The Alpha Network Changes Elicited by Working Memory Training

Junling Ran, Huiling Zhang, Jayang Xu, Tianhao Li, Dong Wang, and Yin Tian

Abstract In the current study, we utilized EEG coherence and complex brain network to study the changes of working memory (WM) and constructed differential statistical networks under alpha rhythms before and after training. The results showed that the long-range frontoparietal and frontooccipital interactions during WM retention involved in the alpha frequency network. The findings revealed that the connections between neurons varied to complete the efficient transmission and processing of information, indicating the neural plasticity before and after WM training from the network level.

1 Introduction

Visual working memory (WM) involved neuronal activity in the various cortical regions including frontal, parietal, occipital, and temporal areas based on functional magnetic resonance imaging (fMRI). Brain oscillations at different frequencies are associated with cognitive processes such as emotion and memory (Jay & René, 2004). And the oscillation synchronization could be used to define interactions between different brain regions at relatively high temporal resolutions (Li et al., 2015). Moreover, the alpha synchronization prevents external input from interfering with ongoing working memory tasks (Ole & Tesche, 2010), implying neural synchronization activation of alpha oscillations could suppress information processing independent of WM (Li-Yu et al., 2013). The continuous activity of the brain is strong evidence, which reflected WM characterization during the delayed period of WM. Many brain areas of the cortex and subcortex also exhibited similar sustained activity and formed a brain networks for memory information interaction to support the processing and delivery of WM retention information (Curtis et al., 2005). EEG coherence

Junling Ran and Huiling Zhang—These authors contributed equally to this work.

J. Ran · H. Zhang · J. Xu · T. Li · D. Wang · Y. Tian (✉)
Bio-Information College, ChongQing University of Posts and Telecommunications, ChongQing 400065, China

A. Lintas et al. (eds.), *Advances in Cognitive Neurodynamics (VII)*, Advances in Cognitive Neurodynamics,
https://doi.org/10.1007/978-981-16-0317-4_4

was primarily a measure of phase consistency, reflecting the functional connection between paired brain regions (Nolte et al., 2004). Strong coherence reflected the simultaneous oscillation of neurons, while weak coherence indicated that the activity between these neural clusters was independent of each other. In brain science research, graphical theory analysis was widely used in brain network to provide a theoretical basis for understanding the brain network topology. Studies have shown that the human brain was a highly interconnected complex network (Langer et al., 2013). Therefore, we utilized the graph theory analysis method based on EEG coherence to construct a coherence network before and after WM training, and difference network relied on statistical analysis under different brain oscillations. We hope that the current study could reveal the plasticity of WM training from the brain network perspective based on EEG coherence.

2 Materials and Methods

Twenty right-handed normal male subjects (21 years old) participated in the experiment. All subjects did not have any cognitive impairment, history of mental and neurological diseases. The experiment was approved by the Ethics Committee of Chongqing University of Posts and Telecommunications. All subjects who participated in this experiment read the informed consent form in advance and signed it. After the experiment, subjects will receive corresponding compensation for their time and efforts. The experiment was similar to our previous design on working memory (Yin et al., 2017). Subjects were asked to remain relaxed throughout the experiment and to suppress as much as possible the wide range of motion. Subjects needed to perform three task difficulty levels (2, 4, and 8 items) delayed WM tasks consisting of two sessions. The experimental content of the two sessions was the same. The only difference was that the subject completed the first session tasks without training, and completed the task of the second session after receiving the short memory training. A 64-channel NeuroScan system was used to record subjects' EEG data during doing the WM experiment. The offline processing of EEG data mainly included: re-reference, data segmentation, artifact removal, filtering, and baseline correction. The coherence of EEG signals reflected the correlation of the time domain signals of the two brain regions in alpha frequency band. The coherence function between the two signals as shown in the previous literature (Curtis et al., 2005). The graph analysis method was used to construct the brain networks before and after WM training, and the network topological properties were measured by the optimal path length (Lp), clustering coefficient (CC), local efficiency (Eloc), global efficiency (Eg), degree (Deg) and small-world properties of the network (Palva et al., 2010).

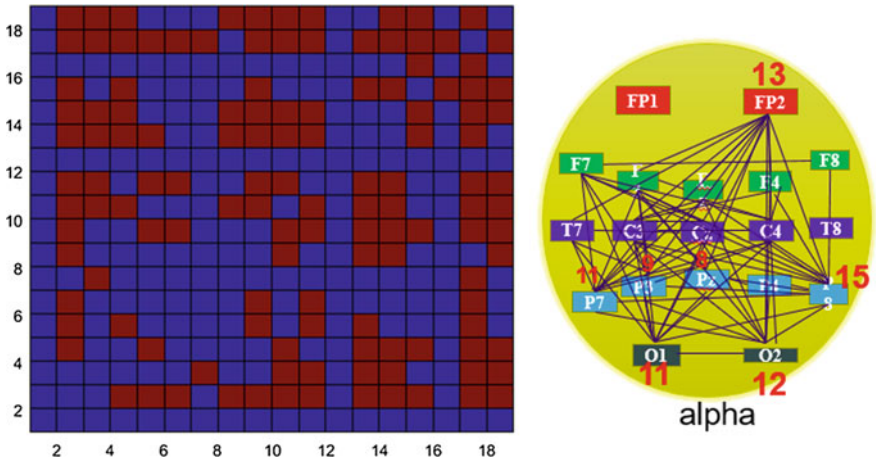

Fig. 1 Coherence statistical matrix and statistics network

3 Results and Discussion

For the coherence matrix in alpha brain oscillation, the paired t-test was utilized to statistically obtain the corresponding elements of the coherence statistical matrix before and after the training. That is, if there was a significant difference on the coherence values of WM network between the two nodes before and after WM training ($p < 0.05$, FDR correction), the corresponding elements of the statistical matrix was set to 1. Otherwise, the element of the statistical matrix was set to 0. Finally, statistical matrix before and after WM training (binary matrix) was obtained, and thus the difference statistical network of alpha rhythms was acquired. Figure 1 showed the statistical matrix and difference statistical networks of alpha rhythms before and after the WM training.

For the difference statistical network of alpha band, the node degrees at the FP2, P7, P3, Pz, P8, O1, and O2 electrode positions was significantly different before and after memory training, indicating that the increased coherence between paired nodes in fronto-occipital network under alpha rhythm after WM training. Moreover, it involved the long-range integration of the "top-down" information processing between the frontoparietal, fronto-occipital brain regions, similar to previous study (Palva et al., 2010).

Conflict of Interest There is no conflict of interest.

References

Curtis, C. E., Sun, F. T., Miller, L. M., & D'Esposito, M. (2005). Coherence between fMRI time-series distinguishes two spatial working memory networks. *Neuroimage, 26*(1), 177–183.

Huang, L.Y ., She, H. C., Chou, W. C., Chuang, M. H., Duann, J. R., & Jung, T. P. (2013). Brain oscillation and connectivity during a chemistry visual working memory task. *International Journal of Psychophysiology Official Journal of the International Organization of Psychophysiology, 90*(2), 172–179.

Jay, T. J., & René, M. (2004). Capacity limit of visual short-term memory in human posterior parietal cortex. *Nature, 428*(6984), 751–754.

Langer, N., Bastian, C. C. V., Wirz, H., Oberauer, K., & Jäncke, L. (2013). The effects of working memory training on functional brain network efficiency. *Cortex, 49*(9), 2424–2438.

Li, X., Hu, B., Xu, T., Shen, J., & Ratcliffe, M. (2015). A study on EEG-based brain electrical source of mild depressed subjects. *Computer Methods and Programs in Biomedicine, 120*(3), 135–141.

Nolte, G., Bai, O., Wheaton, L., Mari, Z., Vorbach, S., & Hallett, M. (2004). Identifying true brain interaction from EEG data using the imaginary part of coherency. *Clinical Neurophysiology, 115*(10), 2292–2307.

Ole, J., & Tesche, C. D. (2010). Frontal theta activity in humans increases with memory load in a working memory task. *European Journal of Neuroscience, 15*(8), 1395–1399.

Palva, J. M., Monto, S., Kulashekhar, S., & Palva, S. (2010). Neuronal synchrony reveals working memory networks and predicts individual memory capacity. *Proceedings of the National Academy of Sciences of the United States of America, 107*(16), 7580–7585.

Yin, T., Huiling, Z., Wei, X., Haiyong, Z., Li, Y., Shuxing, Z., et al. (2017). Spectral entropy can predict changes of working memory performance reduced by short-time training in the delayed-match-to-sample task. *Frontiers in Human Neuroscience, 11,* 437.

Symbolic Neural Dynamics Allow for Modeling Retrograde Amnesia as Well as False Memories

Pierre Bonzon

Abstract Symbolic neural dynamics abstracting the functionalities of synaptic plasticity has been proposed as a new approach to modeling brain cognitive capabilities and used to define the basic mechanisms of an associative memory. This formalism is extended here to reproduce optogenetic manipulations, thus defining a computational model of memory engrams. It is illustrated through simulations of reversible retrograde amnesia and false memories of contextual fear conditioning that reproduce the behavioral schedules of actual experiments. These results support the hypothesis that separate processes are involved in long-term memory, i.e., the retention of specific patterns of connectivity between engram cells required for the storage of information, on the one hand, and the synaptic strengthening needed for its consolidation and retrieval, on the other. Defined by a logic program, this simulation platform could be used to design and predict the results of experiments involving inhibitory/excitatory loops formed between various brain regions.

1 Introduction

The advent of optogenetic technology (Deisseroth et al., 2006) has opened new doors toward the investigation of the brain. It is now possible to trace down simple cognitive processes down to the activation of a group of neuronal cells. Following the seminal work of Tonegawa and colleagues (Liu et al., 2012; Ramirez et al., 2013; Ryan et al., 2015; Roy et al., 2017), new ideas about the formation and use of long-term memory are emerging (Tonegawa, 2015; Trettenbrein, 2016). Briefly, the hypothesis is that memory storage and retrieval involve two different circuits and mechanisms, i.e., the retention of specific patterns of connectivity between engram cells required for the storage of information, on the one hand, and the synaptic strengthening needed for its consolidation and retrieval, on the other. These hypotheses are supported by the observation that various expressions of memory can be obtained by leaving

P. Bonzon (✉)
Department of Information Systems, Faculty of HEC, University of Lausanne, Lausanne, Switzerland
e-mail: pierre.bonzon@unil.ch

A. Lintas et al. (eds.), *Advances in Cognitive Neurodynamics (VII)*, Advances in Cognitive Neurodynamics,
https://doi.org/10.1007/978-981-16-0317-4_5

connectivity patterns untouched and by acting on synaptic strengths only. These various expressions can be controlled, observed and measured through optogenetic manipulations, which in turn allow for the experimental induction of *retrospective amnesia*, the direct activation of *memory engrams* and the creation of false memories. Silent memory engrams (Roy et al., 2017), defined as memory traces whose access can be temporarily blocked and then restored at will, stand as the key concept of this new theory.

These findings are addressed here from a computational point of view, i.e., toward the goal of defining a model of such a dual memory that could lead to simulated experiments. Brain simulations using either artificial neural networks (Hopfield, 1982) or analytical methods (Izhikevich, 2006; Markram et al., 2015) (i.e., mainly differential equations modeling electrical currents (Hodgkin & Huxley, 1952)), as customarily performed today in computational neuroscience, have not been used so far to model such memories. Symbolic neural dynamic (Bonzon, 2017) abstracting the mechanisms of synaptic plasticity has been proposed as a new approach to modeling brain cognitive capabilities and used to define the basic mechanisms of an associative memory with dual store and retrieval processes. This formalism is extended here to reproduce optogenetic manipulations, thus defining a computational model of memory engrams.

2 Materials and Methods

This section introduces a formalism that has been previously published (Bonzon, 2017, 2019).

2.1 A New Approach to Modeling Brain Cognitive Functionalities

In this new formalism, brain processes representing synaptic plasticity are abstracted through asynchronous communication protocols and implemented as virtual *microcircuits*. The basic units of these microcircuits are constituted by *threads*, which correspond either to a single or to a cluster of connected neurons. Contrary to traditional neuron models in which incoming signals are summed in some integrated value, thread inputs can be processed individually, thus allowing for threads to maintain parallel asynchronous communications. Threads can be grouped into disjoint sets, or *fibers* to model neural assemblies, and discrete *weights* (e.g., integer numbers) can be attached to pairs of threads that communicate within the same fiber. A fiber containing at least one active thread constitutes a *stream.* Mesoscale *virtual circuits* linking perceptions and actions are built out of microcircuits. Circuits can be represented either graphically or by sets of *symbolic* expressions. These expressions can

```
…-P->=>-Q-…
```

Fig. 1 Circuit fragment implementing a synaptic transmission. Reproduced from Bonzon (2019)

be compiled into *virtual code implications* that are used just in time to deduce instructions to be finally interpreted by a *virtual machine* performing contextual deductions (Bonzon, 1997).

To introduce this formalism, let us consider a simple case of synaptic transmission between any two threads **P** and **Q** (NB throughout this text, identifiers starting with a capital letter stand for variable parameters). This can be represented by the circuit fragment (or wiring diagram) contained in the simple stream given in Fig. 1, where the symbol **->=>-** represents a synapse.

This circuit fragment can be represented by two symbolic expressions involving a pair of **send/receive** processes as shown in Fig. 2.

In Fig. 2, the thread **P** (e.g., a sensor thread **sense(us)** with **us** representing an external stimulus as in Fig. 4) will fire in reaction to the capture of an external stimulus, with the **send** process corresponding to the signal, or spike train, carried by a presynaptic neuron's axon. In the thread **Q** (e.g., an effector thread **motor(X)**, where the variable **X** becomes instantiated as the result of the stimulus), the **receive** process represents the possible reception of this signal by a postsynaptic neuron. The compilation of these expressions will give rise to the execution of virtual code instructions implementing the communication protocol given in Fig. 3.

This protocol corresponds to an *asynchronous* blocking communication subject to a threshold. It involves a predefined weight between the sender **P** and the receiver **Q** that can be either incremented or decremented. On one side, **t**hread **P** fires thread **Q** if necessary and sends it a signal. On the other side, thread **Q** waits for the reception of a signal from thread **P** and proceeds only if the weight between **P** and **Q** stands above a given threshold. The overall process amounts to opening a temporary *pathway*

```
thread(P,[…,send(Q)])
thread(Q,[receive(P),…])
```

Fig. 2 Thread patterns for a synaptic transmission. Reproduced from Bonzon (2019)

```
P:      …
        send(Q)          activate Q if Q is not active and post a signal for Q

Q:      receive(P)       wait for a signal from P and proceed if weight(P,Q)>0
        …
```

Fig. 3 Communication protocol for an asynchronous communication. Reproduced from Bonzon (2019)

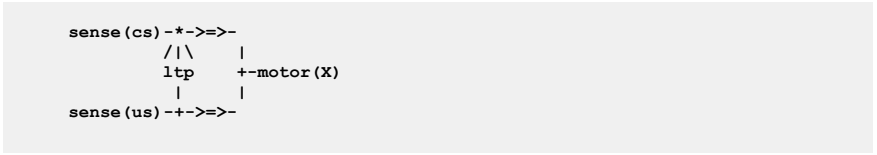

Fig. 4 A circuit implementing classical conditioning. Reproduced from Bonzon (2019)

between **P** and **Q** and allows for passing data by instantiating variable parameters (see example below).

Example

As a simple example, let us consider the classical conditioning of *Aplysia californica* (Kandel & Tauc, 1965). In this experiment, a light tactile conditioned stimulus **cs** elicits a weak defensive reflex, and a strong noxious unconditioned stimulus **us** produces a massive withdrawal reflex. After a few pairings of **cs** and **us**, where **cs** slightly precedes **us**, **cs** alone triggers a significantly enhanced withdrawal reflex. The corresponding circuit, adapted from a previous similar schema (Carew et al., 1981), is represented in Fig. 4. In this circuit, the symbol **/|** represents the modulation of a synaptic transmission, the sign * used in the upper branch indicates the conjunction of converging signals, and the sign + indicates either the splitting of a diverging signal, as used in the lower branch, or a choice between converging signals, as used in the right branch instantiating the thread **motor(X)**, where **X** is a variable parameter to be instantiated into either **cs** or **us**.

In Fig. 4, the thread **ltp** (standing for *long-term potentiation*) acts as a facilitatory interneuron reinforcing the pathway between **sense(cs)** and **motor(cs).** Classical conditioning then follows from the application of Hebbian learning (Hebb, 1949), i.e., "neurons that fire together wire together." Though it is admitted today that classical conditioning in *Aplysia* is mediated by multiple neuronal mechanisms including a postsynaptic retroaction on a presynaptic site (Antonov et al., 2003), the important issue is that this activity depends on the temporal pairing of the conditioned and unconditioned stimuli, which leads to implement the thread **ltp** as a *detector of coincidence* as done in the protocol given in Fig. 5.

The generic microcircuit abstracting the mechanism of long-term potentiation is reproduced in Fig. 5 with its communication protocol. In order to detect the coincidence of **P** and **Q**, thread **P** fires an **ltp** thread that in turn calls on process **join** to wait for a signal from thread **Q**. In parallel, thread **Q** calls on process **merge** to post a signal for **ltp** and then executes a **send(R)** command to establish a link with thread **R**. After its synchronization with thread **Q**, thread **ltp** increments the weight between **Q** and **R**.

The circuit in Fig. 4 can be represented by the fiber, or set of symbolic expressions, given in Fig. 6.

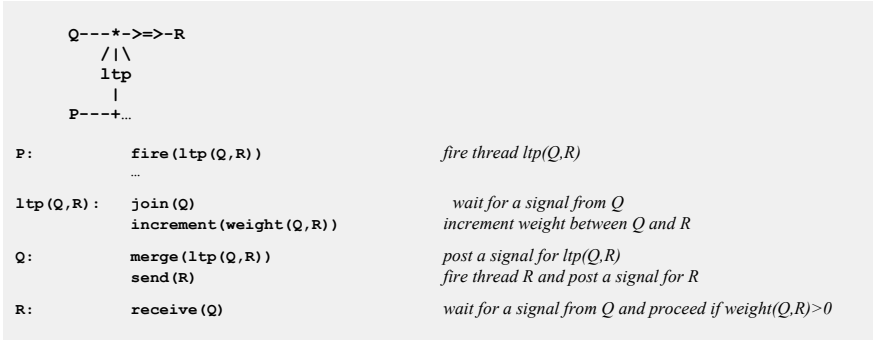

Fig. 5 Microcircuit and communication protocol for *ltp*. Reproduced from Bonzon (2019)

```
thread(sense(us),
 [fire(ltp(sense(cs),motor(cs))),
  send(motor(us))])
 thread(sense(cs),
 [merge(ltp(sense(cs),motor(cs))),
  send(motor(cs))])
thread(motor(X),
 [receive(sense(X)),
  effector(motor(X))])
thread(ltp(Q,R),
 [join(Q),
  increment(weight(Q,R))])
```

Fig. 6 Fiber corresponding to a circuit of classical conditioning

2.2 A Computational Model of an Associative Long-Term Memory

The concept of an associative memory has been studied from various perspectives (Palm, 1980). In our framework, an associative memory extends the mechanism of long-term potentiation by allowing for two threads **P** and **Q** attached to separate streams (and thus also possibly active at different times) to be associated in order to trigger a *recall* thread **R**. These two streams are linked together through a double communication protocol applied to a long-term memory **ltm(P)** thread, this construct being depicted by the symbol **-{P}-** meaning that **P** is both stored and retrievable through the thread **ltm(P)**. This new protocol involves two complementary *long-term storage/retrieval* (**lts/ltr**) threads that allow for the building of a storage trace and later retrieval of a previously active thread. This is in line with results by Rubin and Fusi (Rubin & Fusi, 2007) demonstrating that if the initial memory trace in neurons is below a certain threshold, then it cannot be retrieved immediately after the occurrence of the experience that created the memory. The corresponding microcircuit is given in Fig. 7 together with its communication protocol.

As a distinctive difference from an **ltp(Q,R)** thread (which gets fired by **P** and waits for a signal from **Q** in order to relate **Q** and **R**), an **ltr(P,Q,R)** thread is fired

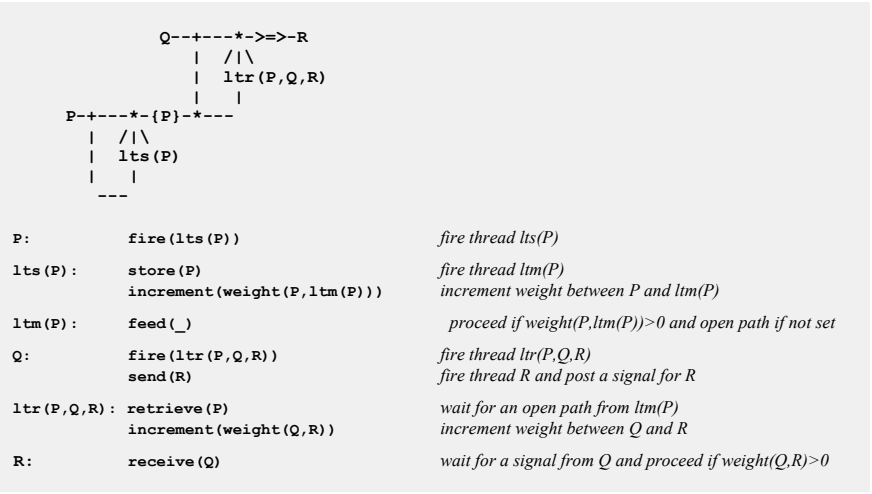

Fig. 7 Microcircuit and communication protocol for a long-term associative memory

by **Q** and waits for a path from **ltm(P)** in order to relate **Q** and **R,** thus defining the basic mechanisms of an associative memory.

2.3 Simulation Platform

A simulation platform has been designed to implement the formalism described above. Defined by a logic program of about 300 lines, this platform can be run on any PC equipped with a Prolog compiler, which thus allows for an easy reproduction of results. It does rely on three fundamental concepts, i.e., the formal notions of

- an *object in context* represented by symbolic expressions in a logical language
- *communicating processes* between *concurrent threads* that is used to model a network of interactive objects
- a *virtual machine* interpreting virtual code that differs from a processor's native code and thus constitutes the key mechanism allowing for interfacing high-level abstract objects, e.g., software, with their low-level physical support, e.g., hardware.

At its top level, this virtual machine executes a *"sense-act"* cycle of embodied cognition as defined in Fig. 8 (see the *Supplementary information* for its complete operational specifications).

As a key point, let us point out the *ist* predicate standing for "is true" and implementing *contextual deduction* (Bonzon, 1997). Clock register values T are used to deduce, for each active thread, a possible next instruction. As postulated independently (Zeki, 2015), there is no central clock, leading thus to the modeling of the brain

Let *Model* represent the state of the virtual machine holding virtual code implications compiled from fibers.
A virtual machine *run* is constituted by a loop comprising a *sense-react* cycle:

```
run(Model)
  loop sense(Model)
       react(Model)
```

Sense corresponds to the capture and input of an *interrupt* triggered by a spike train directed to a *stream:*

```
sense(Model)
  if interrupt(Stream(Input))
  then input(Model(Stream),Input)
```

React loops on each thread within each *stream* to deduce a virtual *instruction* at its clock time *T* and execute it:

```
react(Model)
  for each Stream(Thread),T:Instruction,
  such that ist(Model(Stream)(Thread),(clock(T), T:Instruction))
  do execute(Model(Stream)(Thread), T:Instruction)
```

Fig. 8 High-level definition of a virtual machine run. Reproduced from Bonzon (2019)

as a massively asynchronous, parallel organ. Whenever an instruction is executed successfully, the thread clock is advanced and the next instruction is deduced and executed, and whenever it fails, the current instruction is attempted again until it eventually succeeds. Before being executed, virtual machine instructions are deduced "just in time" from *circuits* which have been compiled into virtual code implications. The execution of virtual instructions leads to a wiring/unwiring process that produces model configurations that are akin to plastic brain states. This procedure matches a fundamental principle in circuit neuroscience according to which *inhibition* in neuronal networks during baseline conditions allows in turn for *disinhibition*, which then stands as a key mechanism for circuit plasticity, learning and memory retrieval (Letzkus et al., 2015). This framework thus represents a computing device that greatly departs from a traditional von Neumann computer architecture, and could prove to be close to that of a real brain.

3 Results

3.1 A Mesoscale Circuit Representing a Memory Engram of Contextual Fear Conditioning

Contextual fear conditioning can be viewed as a case of classical conditioning and modeled in our framework as represented in Fig. 9 with two parameters, i.e., a first parameter designating a context (e.g., **a** or **b**) that recruits cells for a second parameter designating a percept such as **fear**, where _ stands for the absence of a perception.

Memory engrams have been defined as connected neuronal ensembles that allow for the recall of information through various types of activations (Roy et al., 2017).

Fig. 9 Microcircuit implementing contextual fear conditioning

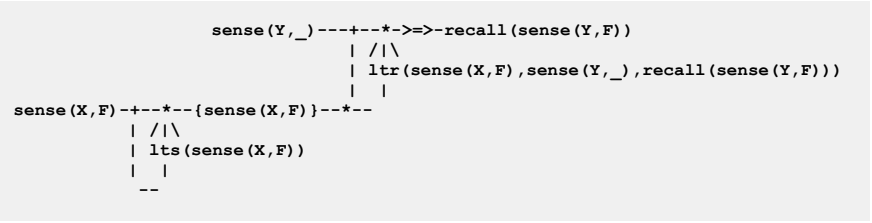

Fig. 10 Microcircuit representing a memory engram of contextual fear conditioning

In our framework, this can be achieved by extending the circuit of Fig. 9 into an associative memory as represented in Fig. 7. Replacing threads **P**, **Q** and **R** in Fig. 7 with, respectively, **sense(X,F)**, **sense(Y,_)** and **recall(sense(Y,F)** gives rise to the circuit given in Fig. 10. Depending on the application, **X** and **Y** can represent either the same (e.g., in the case of retrograde amnesia) or different (e.g., in the case of conditioning false memories) contexts. As for the possible projection of this circuit into actual brain regions, it is suggested that the left part of the circuit, i.e., the formation of **{sense(X,F)}** via **lts**, be identified with the upstream connections between the medial entorhinal cortex (MEC) and the dentate gyrus (DG) engram cells, on one side, and the right part, i.e., the possible **recall** via **ltr**, with the downstream connections of the DG with the hippocampal CA3 and basolateral amygdala (BLA) engram cells, on the other side.

3.2 Experimental Schedule Implementation

Using optogenetic technology (Liu et al., 2012; Ramirez et al., 2013; Ryan et al., 2015; Roy et al., 2017), memory engram cells can be first *tagged* by injection and *labeled* during a training session. At will, they can be then *blocked*, *unblocked* and *lighted* through various injections according to specific experimental schedules. Simulations performed with the circuit of Fig. 10 have reproduced some of the original behavioral schedules of actual experiments (Liu et al., 2012; Ramirez et al., 2013; Ryan et al., 2015; Roy et al., 2017). These schedules have been assembled from the set of fibers given in Fig. 11 (for the interpretation of instructions such as **tag**, **label**, **block**, **unblock**, **light**, **fire**, **send**, **receive**, see the Supplementary information section).

Targeting fiber

```
thread(inject(tag,X,F),      [tag(sense(X,Y),recall(sense(X,F)))]).
```

Training fiber

```
thread(sense(X,F),           [fire(lts(sense(X,F))),
                              label(sense(X,F),recall(sense(X,F))),
                              effector(sense(X,F))]).
```

Testing fiber

```
thread(sense(X,F),           [fire(ltr(sense(X,F),sense(X,_),recall(sense(X,F)))),
                              send(recall(sense(X,F)))].
thread(recall(sense(X,F)),   [receive(sense(X,F)),
                              effector(sense(X,F))]).
```

Closing fiber

```
thread(inject(block,X,F),    [block(sense(X,F),recall(sense(X,F)))]).
```

Opening fiber

```
thread(inject(unblock,X,F),  [unblock(sense(X,F),recall(sense(X,F)))]).
```

Activating fiber

```
thread(inject(light,X,F),    [light(sense(X,F),recall(sense(X,F))),
                              effector(sense(X,F))]).
```

Fig. 11 Fibers for the implementation of behavioral schedules

Each schedule starts with a ***targeting*** phase in which the dentate gyrus of transgenic mice is *tagged* with the injection of viruses and implanted with optic fibers. Active cells are then *labeled* through a contextual fear conditioning ***training*** session that results in the retention of a specific pattern of connectivity between engram cells required for the storage of information. A ***testing*** phase allows for its retrieval through natural cues. Memory consolidation can be *blocked* by an injection that inhibits protein synthesis and thus closes the pathway to memory consolidation, and subsequently *unblocked*. Finally, ***activating*** *lighted* cells demonstrate *silent engrams* (Ramirez et al. 2013) and the creation of *false memories* (Roy et al., 2017).

3.3 Simulation Results

Simulations based on the circuit of Fig. 10 and assembled from the fibers of Fig. 11 have reproduced the results of actual experiments (Liu et al., 2012; Ramirez et al., 2013; Ryan et al., 2015; Roy et al., 2017). Inputs to sensors and injectors are preceded by a prompt `|:` and outputs from effectors by ≫. Additional outputs report about the successive states of the engram.

Contextual fear conditioning control experiment

In the run of Fig. 12, cells involved in fear conditioning are tagged for any context, labeled for context `b` though a training session ending with an upstream synaptic strength and opened pathway (meaning that protein synthesis for memory consolidation is active). The consolidated memory with increased downstream synaptic strength then allows for a memory recall though natural cues.

```
|:targeting([injector(tag,_,_)]).                    ChR2 injection
tagged(sense(_,_),recall(sense(_,_)))                tagged cells

|:training([sensor(b,fear)]).                        shock exposure in context b
labeled(sense(b,fear),recall(sense(b,fear)))         labeled active cells
path(opened(sense(b,fear)|_))                        active protein synthesis
weight(sense(b,fear),ltm(sense(b,fear)))(1)          upstream synaptic strength
>>sense(b,fear)                                     freezing reaction in context b

|:testing([sensor(b,_)]).                           no shock exposure in context b
weight(sense(b,fear),recall(sense(b,fear)))(1)       downstream synaptic strength
>>sense(b,fear)                                     freezing reaction in context b
```

Fig. 12 Execution log of a control simulation run

Reversible retrograde amnesia

Under amnesia, impaired synaptic strengthening prevents the activation of engram cells by natural recall cues. Toward this end, the training session is directly followed by a blocking injection that causes a protein synthesis inhibition resulting in a retrograde amnesia without memory consolidation, which can be then reversed to allow for the reactivation of protein synthesis, the consolidation of memory and a freezing reaction due to memory recall though natural cues (Fig. 13).

Silent engram direct activation

Following retrograde amnesia in context **b**, the resulting silent engram for context **a** gets directly activated with *light* stimulation leading to a freezing behavior without memory recall (Fig. 14).

Creation of a false memory

In this experiment (Ramirez et al., 2013), the cells labeled in context **a** without shock exposure serve as a conditioned stimulus. They get then artificially stimulated

```
|:targeting([injector(tag,_,_)]).                    ChR2 injection
tagged(sense(_,_),recall(sense(_,_)))                tagged cells

|:training([sensor(b,fear)]).                        shock exposure in context b
labeled(sense(b,fear),recall(sense(b,fear)))         labeled active cells
path(opened(sense(b,fear)|_))                        active protein synthesis
weight(sense(b,fear),ltm(sense(b,fear)))(1)          upstream synaptic strength
>>sense(b,fear)                                     freezing reaction in context b

|:closing([injector(block,b,fear)]).                anisomycin injection
path(closed(sense(b,_)))                             protein synthesis inhibited

|:testing([sensor(b,_)]).                           no shock exposure
weight(sense(b,_),recall(sense(b,_)))(0)             no downstream synaptic strength

|:opening([injector(unblock,b,fear)]).              PAK1 injection
path(opened(sense(b,fear),recall(sense(b,fear))))    active protein synthesis

|:testing([sensor(b,_)]).                           no shock exposure in context b
weight(sense(b,fear),recall(sense(b,fear)))(1)       downstream synaptic strength
>>sense(b,fear)                                     freezing reaction in context b
```

Fig. 13 Simulation run of a reversible retrograde amnesia

Fig. 14 Simulation run of a light-induced direct silent engram activation

by *light* during the delivery of an unconditioned fear stimulus in context **b** and subsequently express a false fear memory by freezing in context **a**, but not in a novel context **c** (see the Supplementary information for a definition of the `light` virtual instruction that allows for a displaced memory consolidation) (Fig. 15).

Artificial association of independent memories

In this last example, we reproduce an experiment (Ohkawa et al., 2015) in which coincident firing of distinct neural assemblies generates an artificial link between

Fig. 15 Simulation run of a false memory

```
|:targeting([injector(tag,_,_)]).                    ChR2 injection
tagged(sense(_,_),recall(sense(_,_)))                tagged cells

|:training([sensor(a,_)]).                           no shock exposure for labeling a
labeled(sense(a,_),recall(sense(a,_)))               labeled active cells
path(opened(sense(a,_))                              active protein synthesis
weight(sense(a,_),ltm(sense(a,_)))(1)                upstream synaptic strength
>>sense(a,_)                                         no significant freezing reaction

|:training([sensor(b,fear)]).                        shock exposure for labeling b
labeled(sense(b,fear),recall(sense(b,fear)))         labeled active cells
path(opened(sense(b,fear)                            active protein synthesis
weight(sense(b,fear),ltm(sense(b,fear)))(1)          upstream synaptic strength
>>sense(b,fear)                                      freezing reaction

|:activating([injector(light,c,_)]).                 light injection in context c
>>sense(c,_)                                         no freezing reaction in c

|:testing([sensor(a,_)]).                            no shock exposure in context a
weight(sense(a,fear),recall(sense(a,fear)))(1)       downstream synaptic strength
>>sense(a,fear)                                      freezing reaction in a
```

Fig. 16 Simulation run of the artificial association of independent memories

distinct memory episodes. This looks similar to the creation of a false memory modeled above, except that in this case the conditioning occurs through the exposure to light stimulation, i.e., **`activating([injector(light,c,_)])`** in a third context **`c`** (Fig. 16).

4 Discussion

The simulations that have been presented provide an illustration of how impaired synaptic strengthening caused by the injection of a protein synthesis inhibitor immediately after contextual fear conditioning prevents the effective activation of engram cells by natural recall cues, thus leading to retrograde amnesia. The information stored in engram cell ensemble connectivity can nevertheless be retrieved by light-induced direct activation of labeled nodes. Altogether, these results support the hypothesis that separate processes are involved in long-term memory, i.e., the retention of specific patterns of connectivity between engram cells required for the storage of information, on the one hand, and the synaptic strengthening needed for its consolidation on the other (Tonegawa, 2015; Trettenbrein, 2016). In other words, synaptic connectivity could provide a substrate for memory storage whereas the potentiation of synapses would be required for its retrieval.

It is acknowledged today that individual fear memories require engram cells from multiple brain regions (Tonegawa, 2015). In our simulations, non-instantiated `tagged(sense(_,_),recall(sense(_,_)))` expressions are attached to cell populations whose elements can be indifferently recruited for labeling various contexts such as **`a`** and **`b`**. As our framework readily accommodates instantiated tags that could be used for recruiting specific cells for different contexts or tasks, it can be used to design and predict the results of finer grain experiments involving multiple brain regions (Abdou et al., 2018; Oishi et al., 2019).

Competing Interests The author declares no competing interests.

References

Abdou, K., et al. (2018). Synapse-specific representation of the identity of overlapping of memory engrams. *Science, 360*(6394), 1227–1231.

Antonov, I., Antonova, I., Kandel, E. R., & Hawkins, R. D. (2003). Activity-dependent presynaptic facilitation and hebbian LTP are both required and interact during classical conditioning in Aplysia. *Neuron, 37*(1), 135–147.

Bonzon, P. (1997). A reflective proof system for reasoning in contexts. In *14th National Conference on American Association Artificial Intelligence.* www.aaai.org/Papers/AAAI/1997/AAAI97-061.pdf (1997),

Bonzon, P. (2017). Towards neuro-inspired symbolic models of cognition: linking neural dynamics to behaviors through asynchronous communications. *Cognitive Neurodynamics, 11*(4), 327–353.

Bonzon, P. (2019). Symbolic modeling of asynchronous neural dynamics reveals potential synchronous roots for the emergence of awareness. *Frontiers in Computer Neuroscience.* https://doi.org/10.3389/fncom.2019.00001.

Carew, T., Walters, E., & Kandel, E. (1981). Classical conditioning in a simple withdrawal reflex in Aplysia californica. *The Journal of neuroscience, 1*(12), 1426–1437.

Deisseroth, K., et al. (2006). Next-generation optical technologies for illuminating genetically targeted brain circuits. *Journal of Neuroscience, 26*(41), 10380–10386.

Hebb, D. O. (1949). *The organization of behavior. A neuropsychological theory*. J. Wiley (1949).

Hodgkin, A., & Huxley, A. (1952). A quantitative description of membrane current & its application to conduction & excitation in nerve. *Journal of Physiology, 17*(4), 500–544.

Hopfield, J. J. (1982). Neural networks and physical systems with emergent collective computational abilities. *Proceedings of the National Academy of Sciences of the USA, 79*(8), 2554–2558.

Izhikevich, E. (2006). Polychronization: Computation with spikes. *Neural Computation, 18,* 245–282.

Kandel, E. R., & Tauc, L. (1965). Heterosynaptic facilitation in neurones of the abdominal ganglion of Aplysia depilans. *The Journal of Physiology., 181*(1), 1–27.

Letzkus, J., Wolff, S., & Lüthi, A. (2015). Disinhibition, a circuit mechanism for associative learning & memory. *Neuron, 8*(2), 264–276.

Liu, X., et al. (2012). Optogenetic stimulation of a hippocampal engram activates fear memory recall. *Nature, 484*(7394), 381–385.

Markram, H., et al. (2015). Reconstruction & simulation of neocortical microcircuitry. *Cell, 163,* 456–492.

Ohkawa, N., et al. (2015). Artificial association of pre-stored information to generate a qualitatively new memory. *Cell Reports, 11,* 261–269.

Oishi, N., et al. (2019). Artificial association of memory events by optogenetic stimulation of hippocampal CA3 cell ensemble. *Molecular Brain, 12,* 2.

Palm, G. (1980). On associative memories. *Biological Cybernetics, 36,* 19–31.

Ramirez, S., et al. (2013). Creating a false memory in the hippocampus. *Science, 341,* 387–391.

Roy DS, Muralidhar S, Smith LM, Tonegawa S. Silent memory engrams as the basis for retrograde amnesia. *Proc Natl Acad Sci U S A.*;114,46, (2017).

Rubin, D., & Fusi, S. (2007). Long memory lifetimes require complex synapses & limited sparseness. *Frontiers in Computer Neuroscience, 1,* 7.

Ryan, T. J., et al. (2015). Engram cells retain memory under retrograde amnesia. *Science, 348,* 1007–1013.

Tonegawa, S. (2015). Memory engram storage and retrieval. *Current Opinion in Neurobiology, 35,* 109–111.

Trettenbrein, P. (2016). The demise of the synapse as the locus of memory: A looming paradigm shift? *Frontiers in Systems Neuroscience, 10,* 88.
Zeki, S. (2015). A massively asynchronous, parallel brain. *Philosophical Transactions of the Royal Society B, 370,* 20140174.

A New Deep Neural Network Inspired by Directional Mutual Information Between Slow and Fast Neural Information Flow

Tao Zhang, Sitong Wang, and Zhuo Yang

Abstract Artificial neural networks are initially inspired by neuronal structures and connections, given that the neural connection is changed during a learning process. Yet, it is hard to directly validate that an adaptive structure truly works within complicated animal brains. Sufficient evidences have been given in the level of cells about the adaptive structure of synaptic plasticity. In the present study, it was found that the connective pattern of neurons was significantly altered for the period of a learning process in the level of neuronal groups. By inferring the coupling direction between slow neural information flow and fast one, a novel artificial neural network structure with a multi-layer architecture has been proposed, accordingly. The structure is constructed on the basis of the experimental electrophysiological data and accordant with the principle of maximum entropy. The potential efficiency may lead to an inspiration for the future architecture of artificial neural network.

1 Introduction

The artificial neural network (ANN) is a bio-inspired algorithm of machine learning, taking advantage of simulating a real biological neural network. Through adjusting the weight of the connection between computational units according to the training data, the output of ANNs can be optimized accordingly (Palus & Stefanovska, 2003). In intelligent animals, the connective pattern of neurons is also changed for producing new memories. Synaptic plasticity is one of its manifestations at the cellular level. However, it is difficult to directly observe changes in the pattern of neuronal connections in the complicated animal brain. It is necessary to establish a simple and concise model for investigating the connective pattern changes during learning, where a learning process can be controlled and connective patterns of neurons can be well represented. One of the strategies is that we can govern how much "learning material" a mouse could take via establishing two different kinds of the housing

T. Zhang (✉) · S. Wang · Z. Yang
College of Life Sciences, Nankai University, Tianjin 300071, China
e-mail: zhangtao@nankai.cedu.cn

A. Lintas et al. (eds.), *Advances in Cognitive Neurodynamics (VII)*, Advances in Cognitive Neurodynamics,
https://doi.org/10.1007/978-981-16-0317-4_6

conditions named enriched environment (EE) and social isolation (SI), respectively. Each model also corresponds to a specific size of "training data" in an artificial neural network.

In the present study, the enriched environment (EE) and the social isolation (SI) were introduced as two types of housing conditions, manipulating animal's learning process via setting how much "learning materials" a mouse could reach. The local field potentials (LFPs) in the hippocampal dentate gyrus (DG) were recorded two months after modeling. The original LFPs were decomposed into two parts, in which one retained only the low-frequency components and another consisted of high-frequency components. Conditional mutual information (CMI) measurements showed that the direction of information flows in the hippocampus DG area was from the fast oscillations to the slow oscillations. Accordingly, a hypothesis was raised that the directionality is due to a specific novel structure of neural network, in which neurons belong to either primary layer or advanced layer. When the information was transmitted from the primary layer to the advanced layer, the neurons in the primary layer were activated more frequently, thereby producing the fast oscillations. The neurons in the advanced layer, on the contrary, may be less frequently employed and therefore would generate the slow-frequency components of neural oscillations.

2 Materials and Methods

Total twelve male C57 mice at the age of weaning (21 days) were randomly divided into two groups. Mice in the EE group were raised in large ($60 \times 40 \times 35$ cm) and multi-layer space and various toys such as houses, running wheels, hammocks, scales, small bells, ladders and tunnels. Mice in the SI group were raised in standard cages ($36 \times 18 \times 14$ cm) with one mouse/cage without objects. The housing conditions, all but cages, were strictly identical between two groups. Temperature was constant at 22 ± 2 °C. Animals had free access to food and water during the experiment.

After being housed in different cage until 12 weeks of age, each mouse was anesthetized with 30% urethane. The animals were fixed on a stereotaxic frame (Narishige, Japan). A recording stainless steel electrode was lowered into the hippocampal dentate gyrus (DG) (0.5 mm posterior to the bregma, 3.2 mm lateral to midline, 1.5–2.0 mm ventral below the dura). The ground and reference electrodes were symmetrically placed over the skull and two hemispheres. The spontaneous local field potentials (LFPs) were recorded at 1 kHz sampling frequency and continued at least 20 min.

Conditional mutual information (CMI) is a measurement for detecting information flow's direction, by using the phase information derived from interacting neural rhythms recorded in related cerebral regions (Palus and Stefanovska, 2003). In the past cases, the neural oscillations that we adopted for calculating CMI were mainly recorded at specific pathway like perforant path and CA3-CA1 pathway. In this study, to find out the hierarchical structure of granule cells, slow and fast oscillations were extracted from the LFP signals recorded just at dentate gyrus. The phase information

of both slow and fast oscillations was obtained by Hilbert transformation. The ϕ_{fast} represented the phase of the envelope of the filtered high-frequency signal's amplitude and ϕ_{slow} denoted the phase of the filtered low-frequency signal. The conditional mutual information could be yielded from

$$I(\phi_{\text{slow}}; \Delta\phi_{\text{fast}}|\phi_{\text{fast}}) = H(\phi_{\text{slow}}|\phi_{\text{fast}}) + H(\Delta\phi_{\text{fast}}|\phi_{\text{fast}}) - H(\phi_{\text{slow}}, \Delta\phi_{\text{fast}}|\phi_{\text{fast}}) \quad (1)$$

$$I(\phi_{\text{fast}}; \Delta\phi_{\text{slow}}|\phi_{\text{slow}}) = H(\phi_{\text{fast}}|\phi_{\text{slow}}) + H(\Delta\phi_{\text{slow}}|\phi_{\text{slow}}) - H(\phi_{\text{fast}}, \Delta\phi_{\text{slow}}|\phi_{\text{slow}}) \quad (2)$$

The $\Delta\phi$ was yielded from $\Delta\phi = \phi(t + \tau) - \phi(t)$. We set sliding windows (length = 24 s) with 50% overlap and let phase increment $\tau = 100$ ms. The normalized directionality was defined as follows:

$$D_{1\to 2} = \frac{I(\phi_1; \Delta\phi_2|\phi_2) - I(\phi_2; \Delta\phi_1|\phi_1)}{I(\phi_1; \Delta\phi_2|\phi_2) + I(\phi_2; \Delta\phi_1|\phi_1)} \quad (3)$$

3 Results

We obtained local field potentials (LFPs) from the hippocampal DG area in both the EE group and the SI group. HE staining was performed to verify the location of the LFPs recording sites (Fig. 1a). A representative example of the power spectrum density was shown in Fig. 1b. It can be seen that the ~4 Hz theta rhythm (marked as O.1) is the dominant neural oscillations in the hippocampal DG region. Besides the theta rhythm, both slow oscillations (marked as O.2) and fast oscillations (marked as O.3) have also been observed in the power spectrum (Fig. 1b).

A representative example of modulation index (MI) was shown in Fig. 1c. There were two bright areas in the MI maps. The bright areas on the left side of both panels showed the coupling between the O.1 and O.2, also known as theta–gamma coupling. The bright areas on the right side of both panels showed phase-amplitude couplings between O.2 and O.3. Statistics showed that the strength of O.2–O.3 coupling was much higher in the EE group than that in the SI group (see Fig. 1d, $p < 0.05$), suggesting that the enriched environment significantly enhanced the coupling strength between O.2 and O.3.

We further applied the CMI to infer the direction of the information between O.2 and O.3. Figure 2a showed that the directionality $D_{2\to 3}$ was shifted from positive to negative when increasing the frequency of O.3 (fast oscillations), suggesting that the direction of information flows was from O.3 (fast oscillations) to O.2 (slow oscillations). In addition, the average value of $D_{3\to 2}$, when O.3 ranged from 50 to 100 Hz, was much higher in the EE group than that in the SI group ($p < 0.05$, Fig. 2b).

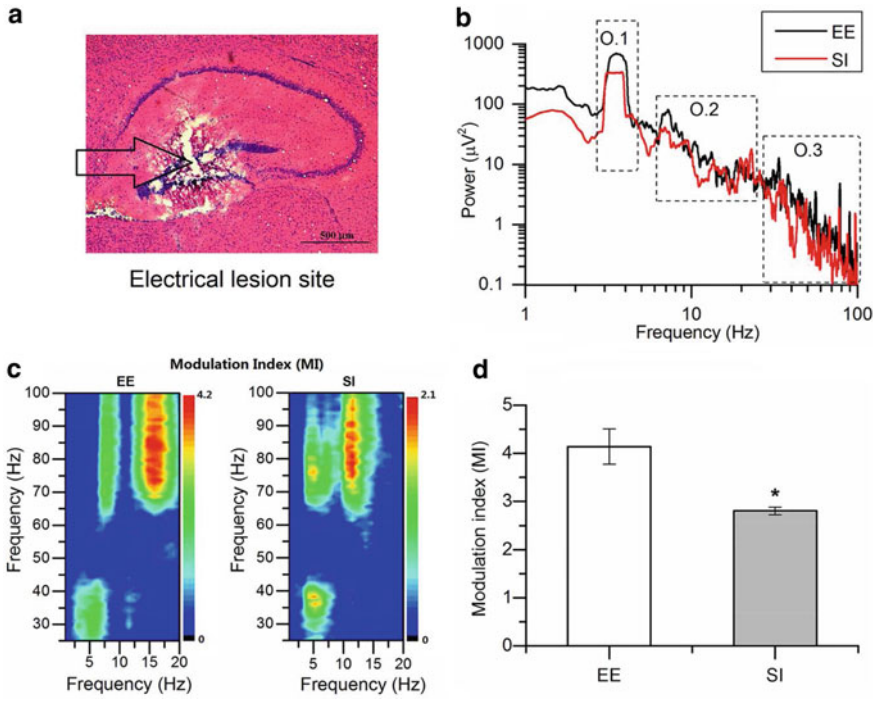

Fig. 1 **a** Location of LFP recording sites. **b** Examples of the power distribution in DG areas in the EE and SI groups. **c** A representative cross-frequency coupling indicated by modulation indexes (MI). **d** Average MI between O.2 and O.3. $*p < 0.05$ and $**p < 0.01$, when compared with the EE group

As shown in Fig. 2c, the high-frequency components of neural oscillations can be understood as a consequence of high-frequency firings in a group of neurons comprising a primary layer, in which neural information is preliminarily processed and integrated. Meanwhile, the low-frequency components of neural oscillations can be regarded as a result of the low-frequency firings in another group of neurons, defined as an advanced layer, in which the neurons receive the integrated inputs from the primary layer. With regard to the distribution of power spectrum (Fig. 1b), it can be seen that there is only a small proportion of power in the high-frequency components. In other words, despite of a higher firing rate, the total consumption of power in the primary layer is very limited, that is, because a majority of the functional tasks in the primary layer are simple and preliminary. On the contrary, due to the complexity of functional tasks performed in the advanced layer, a large amount of energy has been consumed even if the firing rate is relatively low in the advanced layer. Compared with the nervous system of mice, our novel structure of artificial neural network can be supposed to be practical and realistic to some extent. It is well known that there are numerous granule cells in the hippocampus DG region, in which they receive neural information from the entorhinal cortex (EC). After

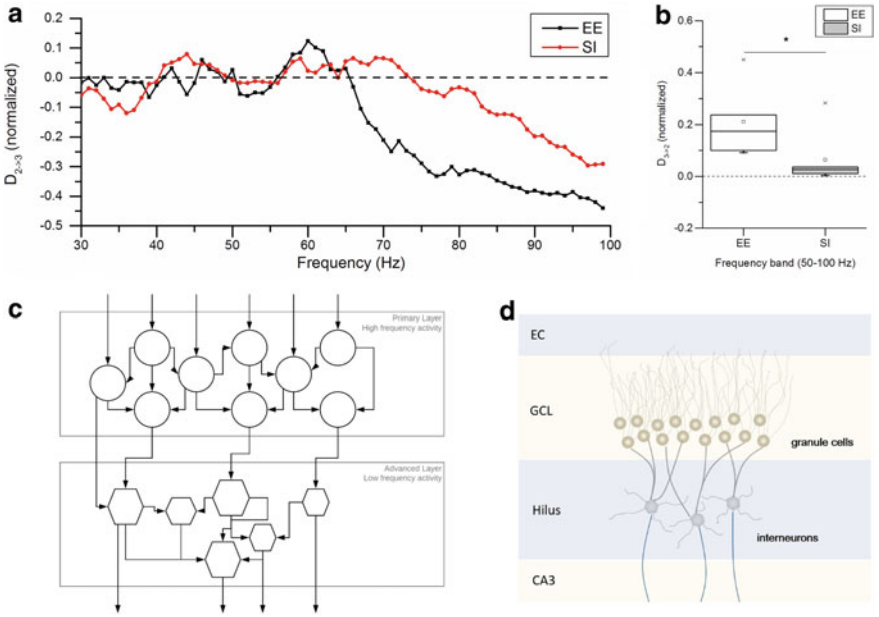

Fig. 2 Directionality of cross-frequency couplings between O.2 and O.3. **a** The representative directionality $D_{2\to3}$ varying with the frequency range of fast oscillations. Negative values show that information could be transmitted from O.3 to O.2. **b** The average $D_{2\to3}$ when O.3 ranges from 50 to 100 Hz. $*p < 0.05$, when compared with the EE group. **c** Two layers structures that can produce slow and fast oscillations. **d** Illustration of real DG anatomy

processing them, the integrated information is transmitted to the hippocampus CA3 region (Fig. 2d). However, the number of interneurons in the hippocampal dentate hilus is much fewer than that of granule cells in the GC layer. The axons from the GC layer to hilus are also relatively fewer than the plentiful paralleled dendrites from EC to GC layer. Accordingly, it is reasonable to speculate that the neural information is integrated by a special hierarchical structure of intercommunicating granule cells in the GC layer. Our observation may be exact one of the manifestations for an undiscovered hierarchical neuron structure in the granule cell layer.

4 Discussion

In recent years, more and more studies have been focused on combining deep learning with brain neural networks, aiming for the intelligence closer to humanity (Geminiani et al., 2018). In the study, a bio-inspired neural network has been proposed, in which the structure of the model has been constructed on the basis of the experimental electrophysiological signals. It reports that neurogenesis can sometimes occur in the adult vertebrate brain (Rakic, 2009). For instance, the granule cells predominate

in the hippocampus DG region, by which a lifelong neurogenesis ability is maintained. A previous study showed that the number of granule cells in the dentate gyrus significantly increased in the enriched environment (EE) (Kempermann et al., 1997). Moreover, the enriched environment could also promote the modulations of synapses with respect of axon sprouting, dendritic arbor growth and formation of dendritic spine (West & Greenough, 1972. Accordingly, it is safe to say that the granule cells in the hippocampus DG area form an adaptive neural network, through increasing the number of neurons and/or modifying the connection patterns. For instance, the measurement of MI suggests that the correlation between the slow oscillations and the fast oscillations was strengthened in the EE condition. In addition, the conditional mutual information (CMI) has been applied in measuring the directionality of neural information flow between the fast-frequency components and the slow-frequency counterpart in neuronal populations. The data showed that the information was transmitted from the fast-frequency components to the slow-frequency ones in the hippocampal DG area. Therefore, we speculate that it is ascribed to a certain multi-layer structure of neurons in the hippocampus DG region. In the structure of neural network, the fast-frequency neural activities are associated with the firing of a primary layer of neurons, while the slow-frequency neural activities are feasibly related to the firings of an advanced layer of neurons. Consequently, the primary neuronal populations merely process and integrate the information and then transmit it to the advanced neuronal populations. Due to the prominent repeatability of signal processing task, the primary layer of neuronal populations exhibits much more activities at the higher-frequency components. In contrast, a signal processing task in the advanced layer may be more complex but less frequently employed. Accordingly, the advanced layer of neuronal populations shows less frequent activities. Since it is a very preliminary study, we will test if the structure is suitable for deep neural network performance in future.

Acknowledgements This work was supported by grants from the National Natural Science Foundation of China (31771148).

References

Geminiani, A., Casellato, C., Antonietti, A., D'Angelo, E., & Pedrocchi, A. (2018). A multiple-plasticity spiking neural network embedded in a closed-loop control system to model cerebellar pathologies. *International Journal of Neural Systems*, *28*(5), 1750017.

Kempermann, G., Kuhn, H. G., & Gage, F. H. (1997). More hippocampal neurons in adult mice living in an enriched environment. *Nature*, *386*(6624), 493–5.

Palus, M., & Stefanovska, A. (2003). Direction of coupling from phases of interacting oscillators: an information-theoretic approach. *Physical Review E Statistical Nonlinear Soft Matter Physics*, *67*(5 Pt 2), 055201.

Rakic, P. (2009). Evolution of the neocortex: A perspective from developmental biology. *Nature Review Neuroscience*, *10*(10), 724–35.

West, R. W., & Greenough, W. T. (1972). Effect of environmental complexity on cortical synapses of rats: Preliminary results. *Behavioral Biology*, *7*(2), 279–84.

Nonlinear Fokker–Planck Approach to the Cohen–Grossberg Model

Roseli S. Wedemann and Angel R. Plastino

Abstract Distributions maximizing the S_q power-law entropies are observed in the behavior of complex systems arising in a remarkably wide range of disciplines, including neuroscience. One known effective description of processes leading to these maximum entropy distributions is provided by nonlinear, power-law Fokker–Planck equations. In this work, we explore an evolution equation of this type, associated with the celebrated Cohen–Grossberg model of neural network dynamics. We prove that the stationary distributions of this evolution equation have the S_q maximum entropy form. These distributions are q-exponentials with an argument proportional to the energy function (also known as Liapunov function) corresponding to the Cohen–Grossberg dynamics. The nonlinear Fokker–Planck equation investigated here also obeys an H-theorem in terms of a free energy-like quantity that is a linear combination of the energy function and of an S_q entropy. These findings may help to understand the origin of the S_q maximum entropy distributions observed in brain dynamics.

1 Introduction

The McCulloch–Pitts (MP) neuron model was historically the basic element of the first mathematical description of a neural network and still constitutes a fundamental paradigm of a computational system. It is at the basis of the Hopfield model for associative memory (Hopfield, 1984; Hertz et al., 1991) and, consequently, is an essential tool for the theoretical analysis of the manyfold mental processes associated

R. S. Wedemann (✉)
Instituto de Matemática e Estatística, Universidade do Estado do Rio de Janeiro, Rua São Francisco Xavier 524, 20550-900 Rio de Janeiro, RJ, Brazil
e-mail: roseli@ime.uerj.br

A. R. Plastino
CeBio y Departamento de Ciencias Básicas, Universidad Nacional del Noroeste de la Provincia de Buenos Aires, UNNOBA, Conicet, Roque Saenz Peña 456, Junin, Argentina
e-mail: arplastino@unnoba.edu.ar

A. Lintas et al. (eds.), *Advances in Cognitive Neurodynamics (VII)*, Advances in Cognitive Neurodynamics,
https://doi.org/10.1007/978-981-16-0317-4_7

with memory that are studied by psychology and neuroscience, in both the normal and the pathological regimes (Kandel, 2005; Cleeremans et al., 2007; Taylor, 2011). These applications of Hopfield's version of the MP model rest on neuroscience's standard working hypothesis stating that (associative) memory is physically codified in the architectural structure of the brain's neural network. Within this theoretical frame, in recent years, we have developed associative memory neuronal network models, for the theoretical analysis of various mind-related phenomena, including neurosis, creativity, and the interaction between consciousness and unconsciousness (Wedemann et al., 2009, 2011; Carvalho et al., 2003; Wedemann & Carvalho, 2012; Siddiqui et al., 2018). In these works, in order to simulate memory retrieval, we used the standard version of the Boltzmann machine (BM) (Hertz et al., 1991), as well as the generalized simulated annealing (GSA) algorithm proposed by Tsallis and Stariolo (1996).

The Tsallis–Stariolo GSA algorithm (Tsallis & Stariolo, 1996) is based on the S_q-thermostatistical formalism (Tsallis, 2009), and is considered to be a q-statistical generalization of the BM (Hertz et al., 1991). These two schemes share the same basic features of a simulated annealing (SA) process: in both of them, the probabilities of transitions between different states of the net are parameterized by a temperature Θ, that decreases gradually according to an appropriate annealing schedule. The transition probabilities $\mathcal{T}_{\mathrm{GSA}}$ governing the GSA dynamics are different from those governing the dynamics of the BM. The GSA transition probabilities are (Tsallis and Stariolo 1996)

$$\mathcal{T}_{\mathrm{GSA}}(S_i \to -S_i) = \left[1 - (1-q)\,\frac{(\mathcal{E}(\{-S_i\}) - \mathcal{E}(\{S_i\})}{\Theta}\right]^{\frac{1}{1-q}}, \qquad (1)$$

where q is the Tsallis parameter characterizing the S_q-thermostatistics. In the above equation, $\mathcal{E}(\{S_i\})$ stands for the the energy of the network state $\{S_i\} = \{S_1, \ldots, S_N\}$, where the $S_i \in \{-1, 1\}$, $i = 1, \ldots, N$, represent the individual states of each of the N neurons that the network comprises. In the discrete Hopfield network, the energy function is $\mathcal{E}(\{S_i\}) = -(1/2)\sum_{ij} \omega_{ij} S_i S_j$, where the weights ω_{ij} describing the interactions between the neurons are assumed to be symmetric, $\omega_{ij} = \omega_{ji}$ (without this symmetry assumption there is no energy function). When $q \to 1$, the GSA transition probabilities (1) reduce to the standard BM ones. The gist of the SA algorithm is that, when the system jumps from one state to next, according to the transition probabilities given by either the BM or the GSA prescriptions, the system's energy tends to decrease. Occasional increases of energy may occur, however, allowing the system to escape from local minima of the energy landscape. As the temperature is gradually lowered, the probability of these increases in energy become smaller, and the system tends to end up in a relatively deep energy minimum. Depending on how the annealing schedule is tuned, it is possible to reach shallower local minima, so as to simulate more loose (creative) associations in the network.

The S_q-thermostatistics (or nonextensive thermostatistics) is a theoretical framework based on the S_q, power-law entropic measures that has in recent years been

successfully applied to the study of several types of complex systems (Tsallis, 2009). The GSA scheme is of relevance because it is a natural dynamics generating the S_q-maximum entropy distributions, within the context of neural networks with discrete states (Wedemann et al., 2009; Siddiqui et al., 2018). For example, the avalanches occurring during the GSA memory retrieval process obey S_q-maximum entropy (q-MaxEnt), power-law distributions (Siddiqui et al., 2018). These distributions, the hallmark of the S_q-thermostatistics, have features that are in agreement with those exhibited by power-law distributions recently observed both in numerical simulations of theoretical models (Papa & da Silva, 1997) and in empirical data from experiments in neuroscience (see, for instance, (Siddiqui et al., 2018) and references therein). In particular, the q-MaxEnt distributions are consistent with the results of recently reported experimental studies (based on fMRI techniques) on the statistics of the time duration and the spatial reach of signal propagation during brain stimulation. Power-law and q-MaxEnt behavior is observed also in relation with other features of the neural models investigated in (Wedemann et al. 2009, 2011). These findings constitute our motivation to explore further the application of concepts and methods from the S_q thermostatistical theory to the study of the dynamics of neural network models.

The neurons in the MP model are regarded as systems admitting a discrete and finite number of possible states. But real biological neurons in animals (including humans) are more complex than that. It is more realistic to consider neurons having a continuous range of possible states and therefore characterized by continuous state variables (Hopfield, 1984; Cohen & Grossberg, 1983). The dynamics of networks consisting of neurons with continuous states is described by appropriate sets of coupled ordinary differential equations. An alternative treatment of the network's dynamics, that allows for the inclusion of the effects of noise, is given by the Fokker–Planck formalism. In this regard, we have recently explored various aspects of the Fokker–Planck approach in the study of Hopfield neural networks with continuous variables (Wedemann & Plastino, 2017), and also used the nonlinear Fokker–Planck formalism to discuss the problem of asymmetric synapses in biological networks (Wedemann & Plastino, 2016; Wedemann et al., 2016; de Luca et al., 2018). Our main purpose here is to introduce a Fokker–Planck dynamics appropriate for the Cohen–Grossberg continuous network model and to explore some of its basic features.

The Cohen–Grossberg model of neural networks (Cohen & Grossberg, 1983) describes a wide family of dynamical systems, consisting of co-evolving, interacting elements (neurons). In this model of continuous-time evolution of neural networks, the state of each neuron is described by a continuous variable. Particular instances of the Cohen–Grossberg model include the Hopfield model. The relevance of the Cohen–Grossberg model transcends the fields of computational neural networks and neuroscience because it also comprises, as particular instances, important dynamical systems central to other areas, such as the celebrated Lotka–Volterra systems in population dynamics and ecology (Lotka, 1956).

As the main contribution of the present work, we propose and investigate in Sects. 4 and 5 a nonlinear Fokker–Planck equation associated specifically with the equations of motion of the Cohen–Grossberg, neural network model. The nonlinear Fokker–

Planck equation (NLFPE) that we investigate here admits stationary densities having the q-MaxEnt shape. The Fokker–Planck dynamics has an associated free energy-like functional that, for general time-dependent solutions, decreases monotonously as the system evolves.

The Fokker–Planck dynamics explored here provides plausible mechanisms leading to the S_q maximum entropy, power-law densities observed in physical or biological complex systems that, as occurs with brain networks, are endowed with spatial disorder and/or non-local interactions (Tsallis, 2009). The dynamics advanced here, based on a nonlinear Fokker–Planck treatment, can be regarded as a generalization of the one recently studied by other authors (Yan et al., 2013), which was based on linear Fokker–Planck equations. This generalization incorporates the thermostatistical contexts associated with the power-law, S_q entropic measures. It also comprises, as a special limit situation, the Boltzmann–Gibbs scenario (equivalent to the Tsallis q parameter equal to one) corresponding to the standard, linear Fokker–Planck equations.

2 Nonextensive S_q Thermostatistics

The S_q-thermostatistics is the focus of intense and increasing attention, and is nowadays being applied to the study of a wide range of complex systems in diverse fields (Tsallis, 2009; Brito et al., 2016; Pluchino et al., 2013). This theoretical, thermostatistical framework is based on the power-law, entropy functional (Tsallis, 2009)

$$S_q[P] \,=\, \frac{1}{q-1}\int P(\mathrm{x})\left[1-\left(\frac{P(\mathrm{x})}{P_c}\right)^{q-1}\right] d^N\mathrm{x}\,, \tag{2}$$

where $P(\mathrm{x}, t)$ is a probability density defined on an appropriate N-dimensional configuration or phase space, whose points are represented by the vector $\mathrm{x} \in \Re^N$. The functional (2) is characterized by the dimensionless parameter q, and by the constant P_c whose dimensions are the same as those of the density $P(\mathrm{x})$. For $q \to 1$, the Boltzmann–Gibbs (BG) logarithmic entropy, $S_1 = S_{BG} = -\int P \ln\left(\frac{P}{P_c}\right) d^N\mathrm{x}$ is recovered. Central to the S_q thermostatistics is the $\exp_q(x)$ function (usually referred to as q-exponential function) defined as

$$\exp_q(x) = \begin{cases} [1+(1-q)x]^{1/(1-q)}\,, & \text{when } 1+(1-q)x > 0\,, \\ 0\,, & \text{when } 1+(1-q)x \le 0\,. \end{cases} \tag{3}$$

This function is ubiquitous in applications of the S_q-thermostatistics, because it describes the shape of densities optimizing the S_q entropy under constraints (Tsallis, 2009). We shall use also the alternative notation $\exp_q(x) = [1+(1-q)x]_+^{1/(1-q)}$.

The q-MaxEnt distributions themselves, and other mathematical aspects of models inspired on the S_q-statistics, have been applied to fit observational or experimental data coming from research on an astonishing variety of scientific themes, ranging from the mass distributions of of meteorites (Betzler & Borges, 2020) to the spread of the COVID-19 pandemic (Tirnakli & Tsallis, 2020). They have also been observed in numerical data generated by computer simulations of the behavior of diverse types of complex systems (Siddiqui et al., 2018; Tsallis, 2009). The theoretical framework of nonextensive thermostatistics has thus been applied to the study of problems in areas such as physics, astronomy, economics, biology, biomedicine, psychology, cognition, computer science and machine learning, among others. Physical systems which seem to be the best candidates for a description with the S_q-thermostatistics are those endowed with long-range interactions and characterized by long-live, quasi-equilibrium (or meta-equilibrium) states (Brito et al., 2016), those located at the edge of chaos (Pluchino et al., 2013), and systems exhibiting a behavior effectively governed by Fokker–Planck equations with power-law diffusion terms (Plastino & Plastino, 1995; Martinez et al.,1998; Franck, 2005; Malacarne et al., 2002; Schwämmle et al., 2007). The theoretical links between generalized thermostatistical formalisms and nonlinear Fokker–Planck dynamics have attracted considerable interest in recent years. These links are at the core of some of the applications of the S_q-thermostatistics that are best understood and rest on the firmest theoretical grounds (Schwämmle et al., 2007).

3 The Cohen–Grossberg Neural Network Model

The equations of motion of the neural network model proposed by Cohen and Grossberg (1983) are

$$\frac{\mathrm{d}x_i}{\mathrm{d}t} = a_i(x_i)\left[b_i(x_i) - \sum_{j=1}^{N} c_{ij} d_j(x_j)\right], \quad i = 1, \ldots, N\,, \tag{4}$$

where x_i is the state variable of the ith neuron, the c_{ij}'s are constant weights, and $a_i(x_i)$'s, $b_i(x_i)$'s, and $d_i(x_i)$'s are functions satisfying $a_i(x_i)d_i'(x_i) \geq 0$. Different choices for the functions $a_i(x_i)$'s, $b_i(x_i)$'s, and $d_i(x_i)$'s, correspond to different particular instances of the Cohen–Grossberg model. For symmetric weights $c_{ij} = c_{ji}$, the model admits an *energy function* (also referred to as the potential or Liapunov function), given by (Cohen & Grossberg 1983)

$$W = -\sum_{i=1}^{N} \int_0^{x_i} b_i(\epsilon_i) d_i'(\epsilon_i) d\epsilon_i + \frac{1}{2} \sum_{j,k=1}^{N} c_{jk} d_j(x_j) d_k(x_k). \tag{5}$$

The equations of motion (4) can be recast in terms of the partial derivative of W, as

$$\frac{\mathrm{d}x_i}{\mathrm{d}t} = -\left[\frac{a_i(x_i)}{d_i'(x_i)}\right]\frac{\partial W}{\partial x_i} = K_i(x_1, x_2, \ldots, x_N). \tag{6}$$

These equations determine the evolution of the dynamical state of the network, which at each instant in time is described by the set of N phase-space variables $\{x_1, x_2, \ldots, x_N\}$. Sometimes, it is convenient to express (6) more compactly as $\frac{\mathrm{dx}}{\mathrm{dt}} = \mathrm{K(x)}$, with $\mathrm{x}, \mathrm{K} \in \Re^N$. The system's state is then represented by a vector x evolving deterministically according to the phase-space flux field K.

Setting $a_i(x_i) = -1/\tau_i$, $b_i(x_i) = x_i$, $c_{ij} = \omega_{ij}$, and $d_i(x_i) = g(x_i)$, with the τ_i's all constants, in the equations (4), these are reduced to those governing the continuous Hopfield neural network,

$$\tau_i \frac{\mathrm{d}x_i}{\mathrm{d}t} = -x_i + \sum_{j=1}^{N} \omega_{ij} g(x_j). \tag{7}$$

That is, the well-known Hopfield model constitutes a particular case of the Cohen–Grossberg model.

4 Fokker–Planck Approach to Cohen–Grossberg Neural Networks

We shall first review basic notions concerning the linear Fokker–Planck equations, in order to introduce some relevant ideas and fix notation. One individual realization of the dynamical system, our neural network, when it evolves from one given set of initial conditions, is governed by the equations of motion (4) and (6). However, when dealing with complex dynamical systems of high dimensionality, instead of focussing on the evolution of a single instance of the system, it is frequently more instructive and often only feasible to consider the time evolution of a statistical ensemble of identical systems. For an interesting example of the ensemble approach to neural network dynamics, see Yan et al. (2013).

The aforementioned ensemble is described by a time-dependent probability density in phase space $P(x_1, \cdots, x_N, t)$, evolving according to Liouville's phase-space continuity equation $(\partial P/\partial t) + \boldsymbol{\nabla} \cdot (P\boldsymbol{K}) = 0$. Here, $\boldsymbol{\nabla} = (\partial/\partial x_1, \ldots, \partial/\partial x_N)$ is the N-dimensional gradient $\boldsymbol{\nabla}$-operator. To incorporate the effects of noise, which is often necessary when modeling biological neural networks, one adds a diffusion-like term to the continuity equation, resulting in the linear Fokker–Planck equation (FPE)

$$\frac{\partial P}{\partial t} - D\nabla^2 P + \boldsymbol{\nabla} \cdot (P\boldsymbol{K}) = 0\,, \tag{8}$$

where D is a diffusion constant. The term in (8) involving the flux K is usually called the *drift* term, and we thus refer to K as the *drift* field, or equivalently, the phase-space flux. If $\mathrm{K} = -\nabla W$, for some potential $W(\mathrm{x})$, then K corresponds to a phase-space flow that always points "downhill" in the potential landscape given by W. If one chooses an appropriate energy $W(\mathrm{x})$, the drift fields of the continuous neural networks considered here have this downhill behavior. Although the flow is not strictly in the direction of $-\nabla W$, it always has a positive projection along this direction. This can be seen by observing that the components of the vector flow K are not $\left(\frac{\partial W}{\partial x_1}, \ldots, \frac{\partial W}{\partial x_N}\right)$ but, instead,

$$\left(\frac{a_1(x_1)}{d_1'(x_1)}\frac{\partial W}{\partial x_1}, \ldots, \frac{a_N(x_N)}{d_N'(x_N)}\frac{\partial W}{\partial x_N}\right). \tag{9}$$

The fact that the drift field (phase-space flux) associated with the Cohen–Grossberg dynamics departs from the gradient will be important in our present developments. We have already explored in (Wedemann & Plastino 2016, Wedemann et al. 2016; de Luca et al. 2018) some scenarios involving drift fields not arising exclusively from a potential. However, in those previous works we focused on non-gradient situations different from the ones described by Eq. (9). The non-gradient flows appearing in (Wedemann & Plastino 2016; Wedemann et al. 2016; de Luca et al. 2018) originated from asymmetric synaptic interactions, which we shall not study here.

When the drift field corresponds to a gradient $K = -\nabla \mathrm{W}$, the FPE (8) admits stationary solutions of the BG type,

$$P_{\mathrm{BG}}(\mathrm{x}) \;=\; \frac{1}{Z}\exp\left[-\frac{1}{D}W(\mathrm{x})\right], \tag{10}$$

where the normalization constant Z (also known as partition function) is given by $Z = \int \exp\left[-W(\mathrm{x})/D\right] d^N\mathrm{x}$. As usual, we assume that the potential $W(x)$ is such that the integral defining Z converges. The probability density P_{BG} maximizes the entropic functional S_{BG} under the constraints given by the norm of P_{BG} and by the average value $\langle W\rangle = \int W(\mathrm{x})\, P(\mathrm{x})\, d^N\mathrm{x}$.

4.1 Nonlinear Fokker-Planck Dynamics and q-Statistics for Cohen–Grossberg Models

The nonlinear Fokker–Planck equation (Franck, 2005) is a versatile tool for the analysis of various phenomena in complex systems. As already mentioned, it represents possible dynamical processes giving rise to q-exponential densities. Here, we shall implement this kind of evolution equation within the context of the Cohen–Grossberg neural network models. In previous contributions, we have already considered the nonlinear Fokker–Planck approach to neural network dynamics (Wedemann & Plas-

tino, 2016, 2017; de Luca et al., 2018). However, those works were restricted to the particular case of Hopfield neural networks, or to linear networks devised to analytically explore conceptual problems related to the asymmetry of synaptic connections. A generalization of the linear Fokker–Planck equation (8), introducing a nonlinear diffusion term is given by

$$\frac{\partial P}{\partial t} = D\nabla^2[P^{2-q}] - \nabla \cdot [P\mathrm{K}]\,. \tag{11}$$

We now introduce a NLFPE specifically associated with the Cohen–Grossberg neural network models. Let us consider the Fokker–Planck equation

$$\begin{aligned}\frac{\partial P}{\partial t} = D\sum_i \frac{\partial}{\partial x_i}\left\{\left(\frac{q-2}{q-1}\right)\left(\frac{a_i(x_i)}{d_i'(x_i)}\right)P\frac{\partial}{\partial x_i}\left[\left(\frac{P}{P_c}\right)^{1-q}\right]\right\} \\ +\sum_i \frac{\partial}{\partial x_i}\left[\left(\frac{a_i(x_i)}{d_i'(x_i)}\right)P\frac{\partial W}{\partial x_i}\right]\,.\end{aligned} \tag{12}$$

The quantities

$$\mathcal{D}_i = D\left(\frac{q-2}{q-1}\right)\frac{a_i(x_i)}{d_i'(x_i)}\,, \tag{13}$$

appearing in (12), are akin to non-constant diffusion coefficients depending on the state-variables x_i. They can be construed as effective descriptions of the diffusion of substances generated by processes in localized neurons.

The stationary states of the complex network dynamics are of special interest, because they may represent stored memories. Understanding properties of these stationary states, and of the dynamics leading to them, are therefore essential ingredients for the description of mental processes in the brain (Wedemann et al., 2009, 2011; Carvalho et al., 2003; Wedemann & Carvalho, 2012; Siddiqui et al., 2018). We shall prove that the evolution equation (12) admits stationary solutions having the q-exponential shape

$$P_q(\mathrm{x}) = P_c A[1-(1-q)\beta W(\mathrm{x})]_+^{\frac{1}{1-q}}\,, \tag{14}$$

with A, β and P_c defined as appropriate constants, such that P_c has the same dimensions as P, as explained in Sect. 2. For a two-neuron circuit, we have shown figures illustrating the stationary solutions given by probability density (14), where the pair of neurons tends to have simultaneous firing or non-firing states as the strength of the connection becomes stronger, which is consistent with biological considerations.

For stationary densities, the nonlinear Fokker–Planck equation (12), associated with the Cohen–Grossberg model, reduces to

$$\sum_{i=1}^{N}\frac{\partial}{\partial x_i}\left\{\left(\frac{a_i(x_i)}{d_i'(x_i)}\right)P\left[D\left(\frac{2-q}{1-q}\right)\frac{\partial}{\partial x_i}\left[\left(\frac{P}{P_c}\right)^{1-q}\right]+\frac{\partial W}{\partial x_i}\right]\right\} = 0\,, \tag{15}$$

which corresponds to setting $\partial P/\partial t = 0$ in (12). It can be shown that, when the constants A, β and D comply with

$$(2-q)D\beta A^{1-q} = 1\,, \tag{16}$$

the ansatz (14) satisfies

$$\left(\frac{a_i(x_i)}{d_i'(x_i)}\right) P\left[D\left(\frac{2-q}{1-q}\right)\frac{\partial}{\partial x_i}\left[\left(\frac{P}{P_c}\right)^{1-q}\right] + \frac{\partial W}{\partial x_i}\right] = 0\,, \tag{17}$$

and consequently is a solution of (15). In summary, our Cohen–Grossberg-related Fokker–Planck equation (12) has q-exponential, stationary solutions.

5 H-Theorem

We shall now derive an H-theorem for the nonlinear Fokker–Planck equation associated with the Cohen–Grossberg dynamics. We shall prove that there exists a functional F, akin to a free energy, that is monotonously decreasing under the time evolution given by the Fokker–Planck equation (12). Let us consider the quantity

$$\begin{aligned} F &= \langle W\rangle - DS_{\tilde{q}}[P] \\ &= \int W(\mathrm{x})P(\mathrm{x})d^N\mathrm{x} + \frac{D}{1-\tilde{q}}\int P(\mathrm{x})\left[1-\left(\frac{P(\mathrm{x})}{P_c}\right)^{\tilde{q}-1}\right]d^N\mathrm{x}\,, \end{aligned} \tag{18}$$

where $\tilde{q}+q=2$. The rate of change of F is given by

$$\begin{aligned} \frac{\mathrm{d}F}{\mathrm{d}t} &= \int\left\{W + \frac{D}{1-\tilde{q}}\left[1-\tilde{q}\left(\frac{P}{P_c}\right)^{\tilde{q}-1}\right]\right\}\frac{\partial P}{\partial t}d^N\mathrm{x} \\ &= \int\left\{W + \frac{D}{q-1}\left[1+(q-2)\left(\frac{P}{P_c}\right)^{1-q}\right]\right\}\frac{\partial P}{\partial t}d^N\mathrm{x}\,. \end{aligned} \tag{19}$$

Taking advantage of the constancy in time of the norm $\int P d^N\mathrm{x}$, it is possible to rewrite $\mathrm{d}F/\mathrm{d}t$ in the fashion

$$\frac{\mathrm{d}F}{\mathrm{d}t} = \int\left[W + D\left(\frac{q-2}{q-1}\right)\left(\frac{P}{P_c}\right)^{1-q}\right]\frac{\partial P}{\partial t}d^N\mathrm{x}\,, \tag{20}$$

which, in turn, can be expressed as

$$\frac{\mathrm{d}F}{\mathrm{d}t} = -\int P \sum_{i=1}^{N} \frac{a_i(x_i)}{d_i'(x_i)} \left\{ \frac{\partial W}{\partial x_i} + D\left(\frac{q-2}{q-1}\right) \frac{\partial}{\partial x_i} \left[\left(\frac{P}{P_c}\right)^{1-q} \right] \right\}^2 d^N \mathrm{x} \leq 0 \,. \tag{21}$$

The steps followed to derive the above result include an integration by parts where, assuming that $P \to 0$ fast enough when $|\mathrm{x}| \to \infty$, one gets vanishing surface terms. To obtain the last inequality in (21) one has to bear in mind that the quantities $a_i(x_i)/d_i'(x_i)$ and $P(\mathrm{x})$ are always non-negative. In summary, our power-law NLFPE admits the H-theorem,

$$\frac{\mathrm{d}}{\mathrm{d}t} \left(\langle W \rangle - D S_{\tilde{q}}[P] \right) \leq 0 \,, \tag{22}$$

where equality holds for the stationary density. Consequently, the density that minimizes F under the normalization constraint has to be the stationary solution. Equivalently, the density that maximizes $S_{\tilde{q}}$ under the constraints given by normalization and by the average of $W(\mathrm{x})$ is the stationary one.

6 Conclusions

We have proposed and explored a nonlinear Fokker–Planck approach to the neural network model presented by Cohen and Grossberg in (1983). The dynamics investigated here is governed by a nonlinear Fokker–Planck equation comprising two terms: a drift term based on the Cohen–Grossberg network's phase-space flow and a power-law diffusion (Laplacian) term. The drift term in the Fokker–Planck equation advanced here inherits the nonlinearities present in the Cohen–Grossberg equations of motion. It also takes into consideration the non-gradient character of the Cohen–Grossberg dynamics. More precisely, the structure of the drift term is consistent with the fact that the Cohen–Grossberg flow is not equal, nor is it proportional, to $-\nabla W$, in spite of always having a positive projection into $-\nabla W$ and, consequently, always pointing downhill in the $W(\mathrm{x})$ landscape.

We proved that there is a functional F, akin to a free energy, that complies with an H-theorem under the dynamical evolution generated by our model. That is to say, F decreases as the system evolves. The functional F is expressible as a linear combination of the non-additive entropic functional $S_{\tilde{q}}$ and the average value of the Cohen–Grossberg potential energy function W. The stationary solutions of the Fokker–Planck equation, for which the time derivative of F vanishes, are given by maximum Tsallis entropy probability densities. These densities maximize $S_{\tilde{q}}$ under the constraints imposed by normalization and the average $\langle W \rangle$ of the potential W.

We hope that these findings may help to consolidate the theoretical foundations for the application of S_q-thermostatistics (and, in particular, for the application of q-exponential densities) in neurosciences.

Acknowledgements Partial financial support from the Brazilian Agencies CNPq, CAPES, and FAPERJ, is acknowledged with sincere gratitude.

References

Betzler, A. S., & Borges, E. P. (2020). Mass distributions of meteorites. *Monthly Notices of the Royal Astronomical Society*, *493*, 4058–4064.

Brito, S., Silva, L. R. da, & Tsallis, C. (2016). Role of dimensionality in complex networks. *Nature Scientific Reports, 6*, 27992.1–8.

Carvalho, L. A. V., Mendes, D. Q., & Wedemann, R. S. (2003). Creativity and delusions: The dopaminergic modulation of cortical maps. In P. M. A. Sloot, D. Abramson, A. V. Bogdanov, J. J. Dongarra, A. Y. Zomaya, & Y. E. Gorbachev (Eds.), *ICCS 2003* (Vol. 2657, pp. 511–520). LNCS Berlin, Heidelberg: Springer.

Cleeremans, A., Timmermans, B., & Pasquali, A. (2007). Consciousness and metarepresentation: A computational sketch. *Neural Networks*, *20*, 1032–1039.

Cohen, M. A., & Grossberg, S. (1983). Absolute stability of global pattern formation and parallel memory storage by competitive neural networks. *IEEE Transactions on Systems, Man, and Cybernetics*, *13*, 815–826.

Luca, V. T. F. de., Wedemann, R. S., & Plastino, A. R. (2018). Neuronal asymmetries and Fokker-Planck dynamics. In V. Kůrková, Y. Manolopoulos, B. Hammer, L. Iliadis, & I. Maglogiannis (Eds.), *ICANN 2018* (Vol. 11141, pp. 703–713). LNCS Cham: Springer.

Franck, T. D. (2005). *Nonlinear Fokker-Planck equations: Fundamentals and applications*. Berlin-Heidelberg: Springer.

Hertz, J. A., Krogh, A., & Palmer, R. G. (Eds.) (1991). *Introduction to the Theory of Neural Computation. Lecture Notes* (Vol. I). Cambridge, MA: Perseus Books.

Hopfield, J. J. (1984). Neurons with graded responses have collective computational properties like those of two-state neurons. *Proceedings of the National Academy of Sciences USA*, *81*, 3088–3092.

Kandel, E. (2005). *Psychiatry, psychoanalysis, and the new biology of mind*. Washington D.C., London: American Psychiatric Publishing Inc.

Lotka, A. J. (1956). *Elements of mathematical biology*. New York: Dover.

Malacarne, L. C., Mendes, R. S., Pedron, I. T., & Lenzi, E. K. (2002). N-dimensional nonlinear Fokker-Planck equation with time-dependent coefficients. *Physical Review E, 65*, 052101.1–10.

Martinez, S., Plastino, A. R., & Plastino, A. (1998). Nonlinear Fokker-Planck equations and generalized entropies. *Physica A*, *259*(1–2), 183–192.

Papa, A. R. R., & da Silva, L. (1997). Earthquakes in the brain. *Theory in Biosciences*, *116*, 321–327.

Plastino, A. R., & Plastino, A. (1995). Non-extensive statistical mechanics and generalized Fokker-Planck equation. *Physica A*, *222*, 347–354.

Pluchino, A., Rapisarda, A., & Tsallis, C. (2013). Noise, synchrony, and correlations at the edge of chaos. *Physical Review E*, *87*, 022910.1–5.

Schwämmle, V., Nobre, F. D., & Curado, E. M. F. (2007). Consequences of the H theorem from nonlinear Fokker-Planck equations. *Physical Review E, 76*, 041123.1–8

Siddiqui, M., Wedemann, R. S., & Jensen, H. J. (2018). Avalanches and generalized memory associativity in a network model for conscious and unconscious mental functioning. *Physica A*, *490*, 127–138.

Taylor, J. G. (2011). A neural model of the loss of self in schizophrenia. *Schizophrenia Bulletin*, *37*(6), 1229–1247.

Tirnakli, U., & Tsallis, C. (2020). Epidemiological model with anomalous kinetics: Early stages of the COVID-19 pandemic. *Frontiers of Physics*, *8*, 613168.1–10.

Tsallis, C. (2009). *Introduction to nonextensive statistical mechanics, approaching a complex world*. New York: Springer.

Tsallis, C., & Stariolo, D. A. (1996). Generalized simulated annealing. *Physica A*, *233*, 395–406.

Wedemann, R. S., & Carvalho, L. A. V. (2012). Some things psychopathologies can tell us about consciousness. In A. E. P. Villa, W. Duch, P. Érdi, F. Masulli, & G. Palm (Eds.), *ICANN 2012* (Vol. 7552, pp. 379–386). LNCS Berlin, Heidelberg: Springer.

Wedemann, R. S., & Plastino, A. R. (2016). Asymmetries in synaptic connections and the nonlinear Fokker-Planck formalism. In: A. E. P. Villa, P. Masulli, & A. J. Pons Rivero (Eds.) *ICANN 2016. LNCS* (Vol. 9886, pp. 19–27). Cham: Springer

Wedemann, R. S., & Plastino, A. R. (2017). q-maximum entropy distributions and memory neural networks. In A. Lintas, S. Rovetta, P. Verschure, & A. E. P. Villa (Eds.), *ICANN 2017* (Vol. 10613, pp. 300–308). LNCS Cham: Springer.

Wedemann, R. S., de Carvalho, L. A. V., & Donangelo, R. (2011). Access to symbolization and associativity mechanisms in a model of conscious and unconscious processes. In A. V. Samsonovich & K. R. Jóhannsdóttir (Eds.), *Biologically inspired cognitive architectures, frontiers in artificial intelligence and applications* (Vol. 233, pp. 444–449). USA: IOS Press.

Wedemann, R. S., Donangelo, R., & Carvalho, L. A. V. (2009). Generalized memory associativity in a network model for the neuroses. *Chaos*, *19*, 015116-1–11.

Wedemann, R. S., Plastino, A. R., & Tsallis, C. (2016). Curl forces and the nonlinear Fokker-Planck equation. *Physical Review E*, *94*(6), 062105.

Yan, H., Zhao, L., Hu, L., Wang, X., Wang, E., & Wang, J. (2013). Nonequilibrium landscape theory of neural networks. *PNAS*, *110*(45), E4185–E4194.

Functional Interactions in Neural Networks

Equalization Effect in Interpopulation Spike-Timing-Dependent Plasticity in Two Inhibitory and Excitatory Populations

Sang-Yoon Kim and Woochang Lim

Abstract We consider two inhibitory (I) and excitatory (E) populations with I to E and E to I interpopulation spike-timing-dependent plasticity (STDP). By changing the noise intensity D, we study the effect of interpopulation STDPs on fast sparsely synchronized rhythms that appear in the two I- and E-populations. Long-term potentiation (LTP) and long-term depression (LTD) for population-averaged values of saturated interpopulation synaptic strengths are thus found to take place. Then, the degree of fast sparse synchronization changes due to the effects of LTP and LTD. In a broad region of intermediate D, the degree of good synchronization (with larger synchronization degree) gets decreased. On the other hand, in a region of large D, the degree of bad synchronization (with smaller synchronization degree) becomes increased. As a result, an "equalization effect" in interpopulation synaptic plasticity occurs in each I- or E-population, where the synchronization degree gets nearly the same in a wide range of D.

1 Introduction

We are interested in fast sparsely synchronized rhythms, related to various cognitive functions (Wang, 2010). This kind of fast sparse synchronization has been much studied in diverse aspects (Wang, 2010; Fisahn et al., 1998; Brunel & Wang, 2003; Geisler et al., 2005; Brunel & Hakim, 2008). In such previous works, synaptic coupling strengths were static. However, in real brains, synaptic strengths may be potentiated (LTP) or depressed (LTD) to adapt to the environment. This kind of adjustment of synaptic strength is called the synaptic plasticity which gives the basis for learning, memory, and development (Abbott & Nelson, 2000).

S.-Y. Kim (✉) · W. Lim
Institute for Computational Neuroscience and Department of Science Education, Daegu National University of Education, Daegu 42411, South Korea
e-mail: sykim@icn.re.kr

W. Lim
e-mail: wclim@icn.re.kr

A. Lintas et al. (eds.), *Advances in Cognitive Neurodynamics (VII)*, Advances in Cognitive Neurodynamics,
https://doi.org/10.1007/978-981-16-0317-4_8

Here, we take into consideration, spike-timing-dependent plasticity (STDP) (Song et al., 2000). For the STDP, the synaptic strengths change depending on the relative time difference between the post- and the pre-synaptic spike times. In our recent works (Kim & Lim, 2018), the effects of inhibitory STDP (at I to I synapses) on fast sparse synchronization have been studied in networks of inhibitory fast spiking interneurons.

In contrast to the previous work on the I to I intrapopulation STDP, we consider interpopulation (I to E and E to I) STDPs between the I- and the E-populations. By changing the noise intensity D, we study the effects of interpopulation STDPs on fast sparse synchronization. In Sect. 2, the two I- and E-populations with interpopulation STDPs are described. Then, in Sect. 3, we investigate the effects of interpopulation STDPs on fast sparse synchronization. Finally, summary and discussion are given in Sect. 4.

2 Two I- and E-Populations with Interpopulation Synaptic Plasticity

As in the Ref. (Kim & Lim, 2020), we consider clustered small-world networks (SWNs) consisting of the I- and E-populations. Each I(E)-population is modeled as a directed Watts–Strogatz SWN (Watts & Strogatz, 1998), composed of N_I (N_E) ($N_E : N_I = 4 : 1$) interneurons (pyramidal cells). Connections between the I and the E SWNs are done in random and uniform way. The Izhikevich inhibitory fast spiking interneuron (excitatory regular spiking pyramidal cell) model (which is not only biologically plausible, but also computationally efficient (Izhikevich, 2007)) is chosen as elements in the I SWN (E SWN). Particularly, external noise (i.e., background noise) in our model denotes stochastic fluctuations of random external inputs from other brain regions (not included in the network). It is modeled in terms of a Gaussian white noise in the governing equations for our system, and its intensity is controlled by the parameter D. For the whole parameters used in our computations, refer to Table 1 in Kim and Lim (2020).

The coupling strength of the synapse from the pre-synaptic neuron j in the source Y-population to the post-synaptic neuron i in the target X-population is $J_{ij}^{(XY)}$. Initial synaptic strengths are normally distributed with the mean $J_0^{(XY)}$ and the standard deviation σ_0 ($= 5$); $J_0^{(II)} = 1300$, $J_0^{(EE)} = 300$, $J_0^{(EI)} = 800$, and $J_0^{(IE)} = 487.5$. The I to I synaptic strength ($J_0^{(II)} = 1300$) is so strong that fast sparse synchronization may appear in the I-population via balance between strong inhibition and strong external noise (Wang, 2010; Brunel & Wang, 2003; Geisler et al., 2005; Brunel & Hakim, 2008). This I-population is a dominant one, since $J_0^{(II)}$ is much stronger than the E to E synaptic strength ($J_0^{(EE)} = 300$). Moreover, the I to E synaptic strength ($J_0^{(EI)} = 800$) is so strong, and hence fast sparse synchronization may also occur in the E-population when the noise intensity D passes a threshold. In contrast, the E to I synaptic strength ($J_0^{(IE)} = 487.5$) is small in comparison with $J_0^{(EI)}$, and hence the

effects of the E-population to the I-population are small. In this way, we consider an inhibition-dominated case.

Here, we consider only the I to E and E to I interpopulation synaptic plasticity; in this case, intrapopulation synaptic strengths are static. For the interpopulation synaptic strengths $\{J_{ij}^{(XY)}\}$, we take into consideration a multiplicative STDP (dependent on states) (Kim & Lim, 2018). As the time t is increased, synaptic strength for each interpopulation synapse is updated with a nearest spike pair-based STDP rule:

$$J_{ij}^{(XY)} \to J_{ij}^{(XY)} + \delta(J^* - J_{ij}^{(XY)}) \, |\Delta J_{ij}^{(XY)}(\Delta t_{ij}^{(XY)})|, \tag{1}$$

where $J^* = J_h$ (J_l) for the LTP (LTD) and $\Delta J_{ij}^{(XY)}(\Delta t_{ij}^{(XY)})$ is the synaptic modification depending on the relative time difference $\Delta t_{ij}^{(XY)}$ ($= t_i^{(\text{post},X)} - t_j^{(\text{pre},Y)}$) between the nearest spike times of the post-synaptic neuron i in the target X-population and the pre-synaptic neuron j in the source Y-population. For the values of the lower and the upper bounds (J_l and J_h) and the update rate δ, refer to Table 1 in Kim and Lim (2020).

For the I to E STDP, we use a time-delayed Hebbian time window for the synaptic modification $\Delta J_{ij}^{(EI)}(\Delta t_{ij}^{(EI)})$ (Haas et al., 2006); refer to Eqs. (13) and (14) for $\Delta J_{ij}^{(EI)}(\Delta t_{ij}^{(EI)})$ in Kim and Lim (2020). As in the E to E Hebbian time window, LTP occurs for $\Delta t_{ij}^{(EI)} > 0$, while LTD takes place for $\Delta t_{ij}^{(EI)} < 0$. However, the time-delayed Hebbian time window has delayed maximum and minimum for $\Delta J_{ij}^{(EI)}$ [see Fig. 6a in Kim and Lim (2020)], in contrast to the E to E Hebbian time window.

For the E to I STDP, we employ an anti-Hebbian time window for the synaptic modification $\Delta J_{ij}^{(IE)}(\Delta t_{ij}^{(IE)})$ (Bell et al., 1997); refer to Eq. (15) for $\Delta J_{ij}^{(EI)}(\Delta t_{ij}^{(EI)})$ in Kim and Lim (2020). For $\Delta t_{ij}^{(IE)} > 0$, LTD occurs, while LTP takes place for $\Delta t_{ij}^{(IE)} < 0$ [see Fig. 6c in Kim and Lim (2020], in contrast to the Hebbian time window for the E to E STDP (Song et al., 2000).

3 Effects of Interpopulation STDPs on Fast Sparse Synchronization

We first consider the case without STDP. In this case, fast sparse synchronization has been found to occur in an wide range (D_1^*, D_2^*) of noise intensity D through balance between strong external noise and strong inhibition (Wang, 2010; Brunel & Wang, 2003; Geisler et al., 2005;Brunel & Hakim, 2008). In our model, when passing the first threshold D_1^* ($\simeq 91$), fast sparse synchronization is found to appear in both the I- and the E-populations. Such population synchronization may be well visualized in the raster plot of neural spikes which is a collection of spike trains of individual neurons. As a collective quantity showing population behaviors, we use an instantaneous population spike rate which may be obtained from the raster plots of spikes (Wang, 2010; Brunel & Wang, 2003; Geisler et al., 2005; Brunel & Hakim, 2008).

In the case of fast sparse synchronization, raster plots of spikes in the I- and the E-populations and the corresponding instantaneous population spike rates $R_I(t)$ and $R_E(t)$ are shown for various values of D as shown in Fig. 3b3–b7, c3–c7, and d3–d7 in Ref. (Kim & Lim, 2020). In the I-population, each raster plot is composed of spikes (upper black dots) of N_I (= 600) fast spiking interneurons, while in the E-population, each raster plot consists of spikes (lower gray dots) of N_E (= 2400) regular spiking pyramidal cells. Sparse spiking stripes (consisting of spikes and representing population sparse synchronization) appear successively in the raster plots of spikes in both the I- and the E-populations, and the corresponding instantaneous population spike rates $R_I(t)$ and $R_E(t)$ also show fast in-phase oscillations.

For quantitative analysis, we characterize the degree of fast sparse synchronization in each X-population (X = E or I) in terms of synchronization degree $S_d^{(X)}$, defined by the time-averaged amplitudes of the instantaneous population spike rate $R_X(t)$. As D is increased, the amplitude of $R_I(t)$ decreases monotonically, which results in monotonic decrease in $S_d^{(I)}$ of the I-population. On the other hand, with increasing D, the amplitude of $R_E(t)$ first increases to its peak at $D \sim 250$, and then it becomes decreased. Thus, $S_d^{(E)}$ for a bell-shaped curve. Due to a destructive role of noise to spoil fast sparse synchronization, a transition to desynchronization takes place in both I- and E-populations when passing the second threshold D_2^* ($\simeq$ 537). In a desynchronized case, spikes are completely scattered without forming any stripes [see Fig. 3b8 in Kim and Lim (2020)], and the corresponding instantaneous population spike rates $R_I(t)$ and $R_E(t)$ become nearly stationary, as shown in Fig. 3c8, d8 in Kim and Lim (2020). As a result, asynchronous irregular states emerge in the desynchronized region.

From now on, we take into interpopulation (both I to E and E to I) STDPs and investigate their effects on fast sparse synchronization by varying the noise intensity D. Time evolutions of population-averaged I to E synaptic strengths $\langle J_{ij}^{(EI)} \rangle$ and E to I synaptic strengths $\langle J_{ij}^{(IE)} \rangle$ for various values of D are shown in Fig. 7a1, a2, respectively. First, we take into consideration the case of I to E STDP. In each case of intermediate values of D = 110, 250, and 400 (shown in black color), $\langle J_{ij}^{(EI)} \rangle$ increases monotonically above its initial value $J_0^{(EI)}$ (=800), and eventually it converges to a saturated limit value $\langle J_{ij}^{(EI)^*} \rangle$ nearly at t = 1500 s. As a result, inhibitory LTP takes place for these values of D. In contrast, for small and large values of D = 95, 500, and 600 (shown in gray color), $\langle J_{ij}^{(EI)} \rangle$ decreases monotonically below $J_0^{(EI)}$ and converges to a saturated limit value $\langle J_{ij}^{(EI)^*} \rangle$. Consequently, inhibitory LTD occurs in the cases of D = 95, 500, and 600.

We next consider the case of E to I STDP. Due to the effect of anti-Hebbian time window, time evolutions of $\langle J_{ij}^{(IE)} \rangle$ are in contrast to those of $\langle J_{ij}^{(EI)} \rangle$ in the case of time-delayed Hebbian time window. For intermediate values of D = 110, 250, and 400 (shown in black color), $\langle J_{ij}^{(IE)} \rangle$ decreases monotonically below its initial value $J_0^{(IE)}$ (=487.5), and eventually, it approaches a saturated limit value $\langle J_{ij}^{(IE)^*} \rangle$ nearly at t = 1500 s. Consequently, excitatory LTD occurs for these intermediate values of D. On the other hand, for small and large values of D = 95, 500, and 600 (shown in

gray color), $\langle J_{ij}^{(IE)} \rangle$ increases monotonically above $J_0^{(IE)}$ and approaches a saturated limit value $\langle J_{ij}^{(IE)^*} \rangle$. Accordingly, excitatory LTP occurs for $D = 95$, 500, and 600.

Such saturated limit values in the cases of I to E and E to I STDPs are shown in Figs. 7b1 and b2 in Kim and Lim (2020), respectively. In the case of I to E STDP, plot of saturated limit values $\langle\langle J_{ij}^{(EI)^*} \rangle\rangle_r$ for a bell-shaped curve. Here, the horizontal dotted line represents the initial average value $J_0^{(EI)}$ ($= 800$) of I to E synaptic strengths. On the other hand, in the case of E to I STDP, the plot of saturated limit values $\langle\langle J_{ij}^{(IE)^*} \rangle\rangle_r$ (open circles) forms a well-shaped graph, where the horizontal dotted line denotes the initial average value of E to I synaptic strengths $J_0^{(IE)}$ ($= 487.5$). The lower and the higher thresholds, $\widetilde{D}_l$ ($\simeq 99$) and $\widetilde{D}_h$ ($\simeq 408$), for LTP/LTD (where $\langle\langle J_{ij}^{(EI)^*} \rangle\rangle_r$ and $\langle\langle J_{ij}^{(IE)^*} \rangle\rangle_r$ lie on their horizontal lines) are denoted by solid circles.

In the case of a bell-shaped graph for $\langle\langle J_{ij}^{(EI)^*} \rangle\rangle_r$, inhibitory LTP occurs in a broad region of intermediate D ($\widetilde{D}_l < D < \widetilde{D}_h$), while inhibitory LTD takes place in the other two (separate) regions of small and large D [$D_1^* < D < \widetilde{D}_l$ and $\widetilde{D}_h < D < D_{2,\text{inter}}^*$ ($\simeq 672$)]. We note that inhibitory LTP (inhibitory LTD) disfavors (favors) fast sparse synchronization [i.e., inhibitory LTP (inhibitory LTD) tends to decrease (increase) the degree of fast sparse synchronization] because of increase (decrease) in the mean value of I to E synaptic inhibition.

In contrast, in the case of a well-shaped graph for $\langle\langle J_{ij}^{(IE)^*} \rangle\rangle_r$, excitatory LTD takes place in a broad region of intermediate D ($\widetilde{D}_l < D < \widetilde{D}_h$), while excitatory LTP occurs in the other two (separate) regions of small and large D ($D_1^* < D < \widetilde{D}_l$ and $\widetilde{D}_h < D < D_{2,\text{inter}}^*$). We also note that the roles of LTP and LTD are reversed in the case of E to I STDP. Excitatory LTP (excitatory LTD) favors (disfavors) fast sparse synchronization [i.e., excitatory LTP (excitatory LTD) tends to increase (decrease) the degree of fast sparse synchronization] due to increase (decrease) in the mean value of E to I synaptic excitation.

The effects of LTP and LTD at inhibitory and excitatory synapses on population states after the saturation time ($t^* = 1500$ s) may be well seen in the raster plot of spikes in the I- and the E-populations and the corresponding instantaneous population spike rates $R_I(t)$ and $R_E(t)$. Raster plots of spikes in the I- and the E-populations and the corresponding instantaneous population spike rates $R_I(t)$ and $R_E(t)$ are shown for various values of D in Figs. 8b1–b6, c1–c6, and d1–d6, respectively. In comparison with the case without STDP, the degrees of fast sparse synchronization for intermediate values of D ($D = 110$, 250, and 400) are decreased (i.e., the amplitudes of $R_I(t)$ and $R_E(t)$ are decreased) due to increased I to E synaptic inhibition (i.e., increase in inhibitory LTP) and decreased E to I synaptic excitation (decrease in excitatory LTD). On the other hand, for small and large values of D ($D = 95$ and 500), the degrees of fast sparse synchronization are increased (i.e., the amplitudes of $R_I(t)$ and $R_E(t)$ are increased) due to decreased I to E synaptic inhibition (i.e., decrease in inhibitory LTD) and increased E to I synaptic excitation (increase in excitatory LTP).

We note that a desynchronized state for $D = 600$ in the absence of STDP is transformed into fast sparse synchronization through inhibitory LTD and excitatory LTP. In fact, desynchronized states for $D_2^* (\simeq 537) < D < D_{2,\text{inter}}^* (\simeq 672)$ in the absence of STDP become fast sparsely synchronized ones in the presence of inter-population STDPs, and thus the region of fast sparse synchronization becomes so much extended. Moreover, we also note that the degree of fast sparse synchronization in the I-(E-)population (i.e., the amplitude of $R_I(t)$ [$R_E(t)$]) tends to be nearly the same in an "extended" wide range of $\widetilde{D}_l < D < D_{2,\text{inter}}^*$, except for the narrow small-D region ($D_1^* < D < \widetilde{D}_l$). Hence, an equalization effect in the interpopulation synaptic plasticity occurs in such an extended wide range of D.

Finally, we make quantitative characterization of the degree of fast sparse synchronization in each X-population ($X =$ E or I) in terms of synchronization degree $S_d^{(X)}$ (defined by the time-averaged amplitudes of the instantaneous population spike rate $R_X(t)$). In each realization, $S_d^{(X)}$ is obtained through time average over 3000 global cycles of $R_X(t)$.

We first consider the case of I-population. Figure 1a shows plots of $\langle S_d^{(I)} \rangle_r$ versus D. In the gray region of intermediate D [$\widetilde{D}_l (\simeq 99) < D < \widetilde{D}_h (\simeq 408)$], the degrees of good synchronization (solid circles) in the absence of STDP get decreased to lower ones (open circles) via (E to I) excitatory LTD, while in the region of large D [$\widetilde{D}_h < D < D_{2,\text{inter}}^* (\simeq 672)$], the degrees of bad synchronization (solid circles) in the absence of STDP become increased to higher values (open circles) through (E to I) excitatory LTP. Consequently, in a wide region of $\widetilde{D}_l < D < D_{2,\text{inter}}^*$ (including both the intermediate and the large D regions), the values of $S_d^{(I)}$ become nearly the same. This kind of equalization effect may also be well seen in the histograms for

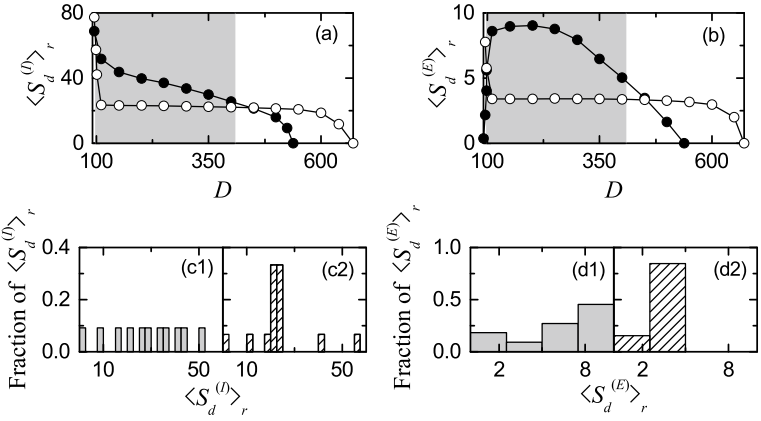

Fig. 1 Characterization of spiking degrees for fast sparse synchronization. Plots of **a** [(**b**)] the synchronization degree $\langle S_d^{(I)} \rangle_r$ ($\langle S_d^{(E)} \rangle_r$) (open circles) versus D in the I(E)-population. For comparison, those in the absence of STDP are also denoted by solid circles. Histograms for distribution of synchronization degrees $\langle S_d^{(I)} \rangle_r$ ($\langle S_d^{(E)} \rangle_r$) in the I(E)-population in the **c**1 [(**d**1)] absence and the **c**2 [(**d**2)] presence of interpopulation STDP

the distribution of $\langle S_d^{(I)} \rangle_r$ in the region of $\widetilde{D}_l < D < D^*_{2,\text{inter}}$. The gray histogram in the absence of STDP is shown in Fig. 1c1 and the hatched histogram in the presence of interpopulation STDP is given in Fig. 1c2. The standard deviation ($\simeq$12.4) in the hatched histogram is much smaller than that ($\simeq$ 20.4) in the gray histogram, and hence equalization effect emerges. Moreover, a dumbing-down effect also occurs because the mean value ($\simeq$ 23.7) in the hatched histogram is smaller than that ($\simeq$ 27.9) in the gray histogram.

Next, we consider the case of E-population. Figure 1b shows plots of $\langle S_d^{(E)} \rangle_r$ versus D. In the gray region of intermediate D ($\widetilde{D}_l < D < \widetilde{D}_h$), the degrees of good synchronization (solid circles) in the absence of STDP become decreased to lower ones (open circles) through (I to E) inhibitory LTP, while in the region of large D ($\widetilde{D}_h < D < D^*_{2,inter}$), the degrees of bad synchronization (solid circles) in the absence of STDP get increased to higher values (open circles) via (I to E) inhibitory LTD. As a result, in a broad region of $\widetilde{D}_l < D < D^*_{2,inter}$ (including both the intermediate and the large D regions), the values of $S_d^{(E)}$ get nearly the same, as in the case of $S_d^{(I)}$. This type of equalization effect may also be well seen in the histograms for the distribution of $\langle S_d^{(E)} \rangle_r$ in the region of $\widetilde{D}_l < D < D^*_{2,\text{inter}}$. The gray histogram in the absence of STDP and the hatched histogram in the presence of interpopulation STDP are shown in Fig. 1d1, d2, respectively. The standard deviation ($\simeq$0.9) in the hatched histogram is much smaller than that ($\simeq$3.1) in the gray histogram, and hence equalization effect appears. Furthermore, a dumbing-down effect also takes place because the mean value ($\simeq$ 3.0) in the hatched histogram is smaller than that ($\simeq$ 6.0) in the gray histogram.

4 Summary and Discussion

We considered clustered small-world networks consisting of I- and E-populations with interpopulation STDPs. A time-delayed Hebbian time window has been employed for the I to E STDP update rule. On the other hand, an anti-Hebbian time window has been used for the E to I STDP update rule. By changing the noise intensity D, we have studied the effects of interpopulation STDPs on fast sparsely synchronized rhythms. Thus, LTP and LTD have been found to occur, depending on D. These LTP and LTD affect the degree of fast sparse synchronization. In a broad region of intermediate D, the degree of good synchronization (with larger synchronization degree) has been found to get decreased. On the other hand, in the region of large D, the degree of bad synchronization has been found to become increased. Accordingly, the degree of fast sparse synchronization becomes nearly the same (i.e., a kind of "equalization effect" occurs) in a wide range of D. We note that this kind of equalization effect is distinctly in contrast to the Matthew effect in intrapopulation (I to I and E to E) synaptic plasticity where good (bad) synchronization becomes better (worse) (Kim & Lim, 2018).

Acknowledgements Supported by the Basic Science Research Program through the National Research Foundation of Korea (NRF) funded by the Ministry of Education (Grant No. 20162007688).

References

Abbott, L. F., & Nelson, S. B. (2000). Synaptic plasticity: Taming the beast. *Nature Neuroscience*, *3*(Suppl), 1178–83.

Bell, C. C., Han, V. Z., Sugawara, Y., & Grant, K. (1997). Synaptic plasticity in a cerebellum-like structure depends on temporal order. *Nature*, *387*(6630), 278–281.

Brunel, N., & Hakim, V. (2008). Sparsely synchronized neuronal oscillations. *Chaos*, *18*(1), 015113.

Brunel, N., & Wang, X.-J. (2003). What determines the frequency of fast network oscillations with irregular neural discharges? I. Synaptic dynamics and excitation-inhibition balance. *Journal Neurophysiology*, *90*(1), 415–30.

Fisahn, A., Pike, F. G., Buhl, E. H., & Paulsen, O. (1998). Cholinergic induction of network oscillations at 40 hz in the hippocampus in vitro. *Nature*, *394*(6689), 186–9.

Geisler, C., Brunel, N., & Wang, X.-J. (2005). Contributions of intrinsic membrane dynamics to fast network oscillations with irregular neuronal discharges. *Journal Neurophysiology*, *94*(6), 4344–61.

Haas, J. S., Nowotny, T., & Abarbanel, H. D. I. (2006). Spike-timing-dependent plasticity of inhibitory synapses in the entorhinal cortex. *Journal Neurophysiology*, *96*(6), 3305–13.

Izhikevich, E. (2007). *Dynamical systems in neuroscience*. Cambridge: MIT Press.

Kim, S.-Y., & Lim, W. (2018). Effect of inhibitory spike-timing-dependent plasticity on fast sparsely synchronized rhythms in a small-world neuronal network. *Neural Networks*, *106*, 50–66.

Kim, S.-Y., & Lim, W. (2020). Effect of interpopulation spike-timing-dependent plasticity on synchronized rhythms in neuronal networks with inhibitory and excitatory populations. *Cognitive Neurodynamics*, *14*(4), 535–567.

Song, S., Miller, K. D., & Abbott, L. F. (2000). Competitive hebbian learning through spike-timing-dependent synaptic plasticity. *Nature Neuroscience*, *3*(9), 919–26.

Wang, X.-J. (2010). Neurophysiological and computational principles of cortical rhythms in cognition. *Physiological Reviews*, *90*(3), 1195–268.

Watts, D. J., & Strogatz, S. H. (1998). Collective dynamics of 'small-world' networks. *Nature*, *393*(6684), 440–2.

Acetylcholine Effects on STDP Induced on Spatial and Non-spatial Information in Dentate Gyrus

Eriko Sugisaki, Yasuhiro Fukushima, and Takeshi Aihara

Abstract Spatial and non-spatial information, coming from medial perforant path (MPP) and lateral perforant path (LPP), respectively, is considered to be integrated on granule cell in dentate gyrus (DG) to play an important role in learning and memory. At both connected sites on dendrite, the phenomenon of learning and memory of spike timing-dependent plasticity (STDP) is known to be induced. Meanwhile, acetylcholine (ACh) is released from cholinergic terminals in DG when attentional processes are paid. And there are reports that ACh enhanced STDP in CA1 area. In order to investigate the ACh effects on STDP and its mechanism in DG, STDP-inducing protocol was applied to measure STDP on MPP or LPP in the presence of eserine, furthermore, the changes in baseline amplitude during the STDP protocol were investigated. As the results, STDPs at both sites were enhanced if ACh receptors were activated and then clarified that the baseline amplitude was one of the factors for the enhancement on MPP. These findings suggest that spatial and non-spatial information is strengthened in learning and memory if attentional processes are paid, but the underlain mechanisms are different.

1 Introduction

Dentate gyrus (DG) granule cells (GC) integrate spatial and non-spatial information. Spatial information is projecting from medial entorhinal cortex to medial dendrite of GC via medial perforant path (MPP) (Fyhn et al., 2004), while non-spatial information such as smell is projecting from lateral entorhinal cortex to distal dendrite via lateral perforant path (LPP) (Hargreaves et al., 2005). Meanwhile, it is known that acetylcholine (ACh) is released in the DG from the cholinergic terminals coming from the medial septum (Amaral et al., 2007) when attentional processes are paid,

E. Sugisaki (✉) · T. Aihara
Tamagawa University Brain Science Institute, Tokyo, Japan
e-mail: e-sugisaki@eng.tamagawa.ac.jp

Y. Fukushima
Kawasaki University of Medical Welfare, Okayama, Japan

A. Lintas et al. (eds.), *Advances in Cognitive Neurodynamics (VII)*, Advances in Cognitive Neurodynamics,
https://doi.org/10.1007/978-981-16-0317-4_9

and ACh enhances spike timing-dependent plasticity (STDP) induced in the CA1 (Sugisaki et al., 2016). However, how ACh influences on STDP in DG, furthermore, what mechanisms are functioning on that cholinergically induced STDP are still not clear. In this study, we clarified the effect of ACh on STDP induced at dendrite sites on MPP or LPP, respectively, and then found baseline amplitude was an important factor for deciding an STDP magnitude on MPP. These results can be useful for clarifying information integration in the DG during attentional processes in the future.

2 Method

All procedures were approved by the Tamagawa University Animal Care and Used Committee. Hippocampal slices (400 μm in thickness) were prepared from Wistar rats (20–25 days old), and whole cell patch clamp recordings were made from the soma of GC. Stimulating electrode was set on MPP or LPP to inject STDP-inducing protocol consisted of paired pulses (Fig. 1). The magnitude of STDP was defined as averaged EPSP slopes obtained from 20 to 30 min after STDP-inducing stimulus/averaged baseline EPSP slopes, while the lowest values of each membrane response induced by the paired pulses at the last 2 s of the STDP protocol were averaged as a baseline amplitude. Depending on the experiments, 2 μM eserine, 1 μM atropine and 10 μM mecamylamine were added to ACSF 5 min. before the application of the stimuli until it was finished. 25 μM Picrotoxin was added throughout the experiments. Analysis of variance (ANOVA) followed by Fisher's PLSD test was used for statistical analysis ($p < 0.05$).

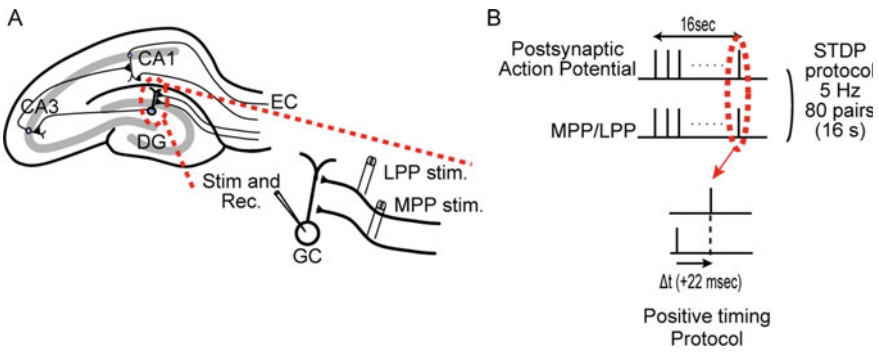

Fig. 1 Stimulus pattern

3 Results

3.1 ACh Effects on STDP Enhancement

Before performing STDP experiments, MPP was clarified by observing a paired pulse depression (Petersen et al., 2013). First, STDP was measured and LTP was induced in the control condition (145.8 ± 10.5%, n=5, $p < 0.05$; Fig. 2), while larger LTP was observed if eserine was applied to influence ACh (176.8 ± 6.3%, n=5, $p < 0.01$, $p < 0.05$ vs. control), although no STDP was seen when blocking nicotinic ACh receptor (nAChR) and muscarinic ACh receptor (mAChR) activation by mecamylamine and atropine application, respectively, named non-ACh condition (118.9 ± 7.0%, n=5, N.S., N.S. vs. control, $p < 0.01$ vs. eserine).

These results show STDP with MPP stimulation was increased depending on ACh concentration. Then, similar experiments were performed replacing stimulating electrode on LPP. The position was confirmed by paired pulse facilitation (Petersen et al., 2013). As the results, LTD was induced in control condition (75.1 ± 8.6%, n=6, $p < 0.01$), although STDPs were not observed despite of ACh existence (103.0 ± 1.6%, n=5, N.S., N.S. vs. control) or not existence (128.3 ± 1.9%, n=3, N.S., $p < 0.01$ vs. control, N.S. vs. eserine) conditions. Interestingly, small amount of ACh influenced STDP induction.

3.2 ACh Effects on Baseline Amplitude

As ACh effected on STDP enhancement at MPP stimulation, next baseline amplitude during the STDP stimulation was evaluated if some changes were occurred due to AChR activation. Then it was clarified that the baseline amplitude in the presence of

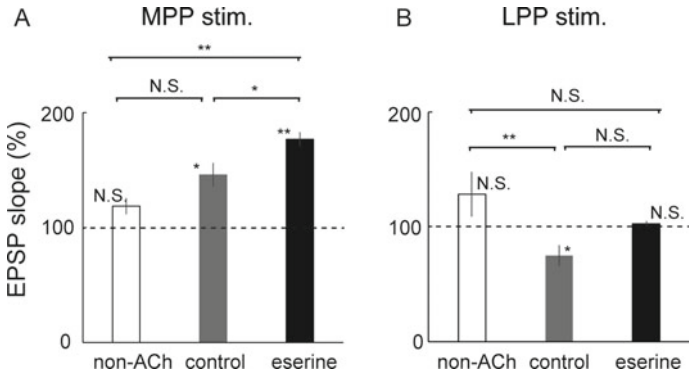

Fig. 2 ACh effects on STDP

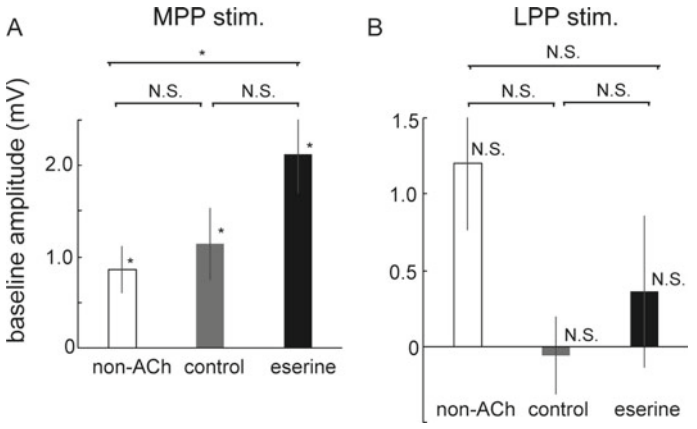

Fig. 3 ACh effects on baseline amplitude

eserine was higher (2.1 ± 0.4mV, n=5, $p < 0.05$; Fig. 3) than the one in non-ACh condition (0.9 ± 0.3 mV, n=5, $p < 0.05$, $p < 0.05$ vs. eserine).

These results suggest that the activation of AChRs effected on baseline amplitude. However, this tendency was not observed if replacing stimulating electrode on LPP that baseline amplitudes were similar in each condition (non-ACh: 1.2 ± 0.4 mV, n=3, N.S.; control: −0.06 ± 0.3 mV, n=5, N.S., N.S. vs. non-ACh; eserine: 0.4 ± 0.5 mV, n=5, N.S., N.S. vs. non-ACh, N.S. vs. control). These results suggest that the baseline amplitudes on LPP stimulation barely cooperated with STDP.

3.3 Contribution of mAChRs and nAChRs

As it was clarified that the ACh contributed to a larger STDP induction on MPP stimulation, next, the type of highly associated AChRs, mAChR or nAChR, was specified. Consequently, LTD was induced when only mAChRs were activated by mecamylamine application (56.5 ± 10.5%, n=4, $p < 0.01$, $p < 0.01$ vs. non-ACh; Fig. 4), though no STDP was observed if nAChRs were activated instead by atropine application (112.2 ± 5.9%, n=6, N.S., N.S. vs. non-ACh). Surprisingly, none of mAChRs nor nAChRs seemed to be cooperated with the larger STDP induction as it was observed in eserine condition (Fig. 2).

4 Conclusion

The direction and the magnitude of STDP in CA1 region are known to be decided by the postsynaptic $Ca2^+$ level (Nishiyama et al. 2000; Aihara et al., 2007) according to BCM rule (Bienenstock et al., 1982). Therefore, it is likely that postsynaptic $Ca2^+$

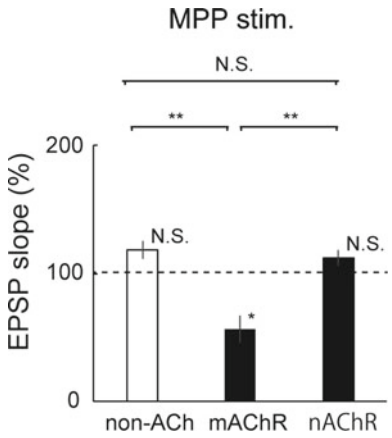

Fig. 4 Types of AChRs

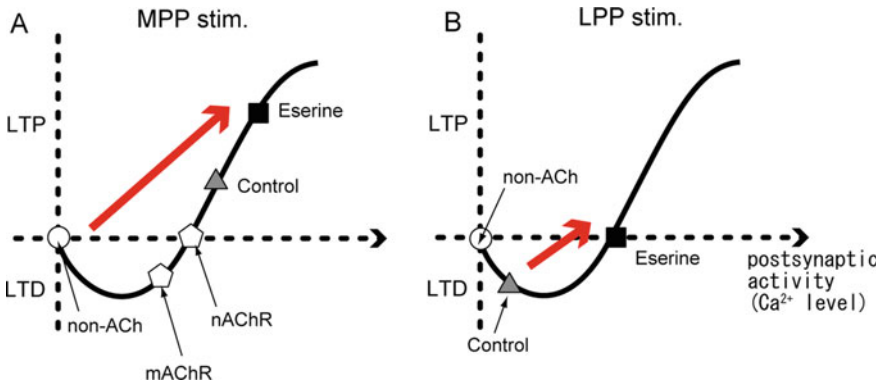

Fig. 5 BCM rule

level in our results with ACh on MPP stimulation might have been higher than the one without ACh treatment as shown in Fig. 5. Also, similar fits were observed on LPP. Taken together, the activation of AChRs facilitated postsynaptic $Ca2^{+}$ level according to BCM rule, especially, nAChRs were more responsible for STDP than mAChRs on MPP. However, the mechanism of STDP enhancement was not clear, so that we focused on baseline amplitude during the stimulation. Then it was clarified that the baseline amplitude on MPP was elevated by the activation of AChRs resulting in postsynaptic $Ca2^{+}$ level elevation along with BCM rule. On the other hand, some other mechanisms besides the baseline amplitude may have drove on LPP.

In this study, as a first step for simplification, experiments were performed under interneuron-blocked network. However, if it is excited, nAChRs and mAChRs on interneurons may be contributed to suppress the magnitude of STDP (Sil'kis, 2003) to LTD direction due to the excitation of those modulated interneurons. Furthermore,

it is known that different types of AChRs have different affinity that the concentration of ACh possibly influences on the magnitude of STDP through the relative strength of excitation and inhibition. Overall, this study is very important for clarifying the mechanisms of spatial and non-spatial information integration in accordance with attentional processes in the DG.

Acknowledgements This work was supported by JSPS KAKENHI Grant Number JP16K00405.

References

Aihara, T., Abiru, Y., Yamazaki, Y., Watanabe, H., Fukushima, Y., & Tsukada, M. (2007). The relation between spike-timing dependent plasticity and $Ca2^{+}$ dynamics in the hippocampal CA1 network. *Neuroscience*, *145*(1), 80–7.

Amaral, D. G., Scharfman, H. E., & Lavenex, P. (2007). The dentate gyrus: fundamental neuroanatomical organization (dentate gyrus for dummies). *Progress in Brain Research*, *163*, 3–22.

Bienenstock, E. L., Cooper, L. N., & Munro, P. W. (1982). Theory for the development of neuron selectivity: orientation specificity and binocular interaction in visual cortex. *Journal Neuroscience*, *2*(1), 32–48.

Fyhn, M., Molden, S., Witter, M. P., Moser, E. I., & Moser, M.-B. (2004). Spatial representation in the entorhinal cortex. *Science*, *305*(5688), 1258–64.

Hargreaves, E. L., Rao, G., Lee, I., & Knierim, J. J. (2005). Major dissociation between medial and lateral entorhinal input to dorsal hippocampus. *Science*, *308*(5729), 1792–4.

Nishiyama, M., Hong, K., Mikoshiba, K., Poo, M. M., & Kato, K. (2000). Calcium stores regulate the polarity and input specificity of synaptic modification. *Nature*, *408*(6812), 584–8.

Petersen, R. P., Moradpour, F., Eadie, B. D., Shin, J. D., Kannangara, T. S., Delaney, K. R., et al. (2013). Electrophysiological identification of medial and lateral perforant path inputs to the dentate gyrus. *Neuroscience*, *252*, 154–68.

Sil'kis, I. G. (2003). A possible mechanism for the effect of neuromodulators and modifiable inhibition on long-term potentiation and depression of the excitatory inputs to hippocampal principal cells. *Neuroscience and Behavioral Physiology*, *33*(6), 529–41.

Sugisaki, E., Fukushima, Y., Fujii, S., Yamazaki, Y., & Aihara, T. (2016). The effect of coactivation of muscarinic and nicotinic acetylcholine receptors on ltd in the hippocampal ca1 network. *Brain Research*, *1649*(Pt A), 44–52.

Context-Dependent Learning and Memory Based on Spatio-Temporal Learning Rule

Hiromichi Tsukada and Minoru Tsukada

Abstract Hebbian learning rule (HEB) with recurrent connections has the ability to stabilize memory patterns, while spatio-temporal learning rule (STLR) has high ability to discriminate temporal difference of spatial input patterns in spatio-temporal context. These learning rules are confirmed to coexist in the brain by experimental study; however, how these learning rules interact each other in memory processing is still unclear. Here, we constructed a recurrent neural network with two biological plausible learning rules (HEB and STLR), and evaluated how spatio-temporal context information is embedded in the memory by simulation. We found that spatio-temporal context patterns are embedded stably in the memory space as attractors with approximate balance of two learning rates and clustered with temporal history. These findings contribute to the understanding of the fundamental neural mechanisms of spatio-temporal context learning in the brain.

1 Introduction

From the viewpoint of spatio-temporal contexts in episodic memory, a spatio-temporal attractor structure is an important one in the neural network. Experimentally, Tsukada et al. (1994, 1996) showed that various spatio-temporal pattern stimuli can induce long-term potentiation (LTP) in the hippocampal neurons, and based on these results, they proposed the spatio-temporal learning rule (STLR) consisted of two factors; cooperative plasticity (coincidence) among presynaptic inputs without a postsynaptic spike (the destination neuron) and its temporal summation. Tsukada

H. Tsukada (✉)
College of Engineering, Chubu University, 1200 Matsumoto, Kasugai, Aichi 487-8501, Japan
e-mail: tsukada@isc.chubu.ac.jp

M. Tsukada
Brain Science Institute, Tamagawa University, 6-1-1 Tamagawa-gakuen,
Machida, Tokyo 194-8610, Japan
e-mail: tsukada@eng.tamagawa.ac.jp

A. Lintas et al. (eds.), *Advances in Cognitive Neurodynamics (VII)*, Advances in Cognitive Neurodynamics,
https://doi.org/10.1007/978-981-16-0317-4_10

et al. (2007) experimentally confirmed that STLR and Hebbian learning rule (HEB) coexist in hippocampal CA1 circuit. Tsukada and Pan (2005) systematically identified the functional difference between STLR and HEB in a simple one-layer neural network by computing their ability to differentiate spatio-temporal sequences. STLR has high ability in discriminating spatio-temporal pattern, while HEB in pattern completion.

In the modeling study of memory network, associative memory model (Amari, 1972; Nakano, 1972; Hopfield, 1982), memory model of successive retrieval, so-called "chaotic itinerancy" (Tsuda et al., 1987; Tsuda, 1992), and transitory memory retrieval model using biologically plausible neurons (Tsukada et al., 2013) have also been proposed so far. However, few memory network models have been studied in relation with the spatio-temporal context and attractors as memory.

Here, we propose a simple artificial memory network for storing spatio-temporal sequences using two types of unsupervised learning, HEB and STLR. We show that the interaction between these two learning rules plays an important role in constructing the context-dependent attractor on the memory network.

2 Models

The network is a single-layered network, which consists of N neurons (pyramidal cells), with feedforward excitatory connection and excitatory of feedback connections. Each neuron connects to all source (input) neurons $(x_1, x_2, \ldots, x_N)$ via an excitatory synapse. An input neuron i $(i = 1, 2, \ldots, N)$ connects an pyramidal (output) neuron j $(j = 1, 2, \ldots, N)$ through a synaptic weight w_{ij}, and the input pattern consists of the spatio-temporal pattern, whose spatial snap at one moment corresponds to a spatial frame of N-dimensional binary elements. We implemented two learning rules, which are Hebbian learning rule (HEB) and spatio-temporal learning rule (STLR) (Tsuda et al., 1994, 1996), in this network model (Fig. 1).

The internal state of the network model is defined as follows:

$$s_i(t) = \alpha \sum_{j=1}^{n} w_{ij}^S(t) x_j(t) + (1-\alpha) \sum_{j=1}^{n} w_{ij}^H(t) y_j(t), \tag{1}$$

$$y_i(t) = F(s_i(t) - \theta), \tag{2}$$

where $x_j(t)$ is an input and $w_{ij}(t)$ is a synaptic weight from neuron j to neuron i at time instant t, which is a discrete time. θ is the threshold, and α is a balance rate of potential between HEB and STLR.

The synaptic weight change Δw_{ij}^S of STLR depends on both spatial coincidence and its temporal summation factors of the input neuron-activity, without the firing of the output neurons Tsukada et al. (1996, 2007). This is under the subthreshold condition of membrane potentials $s_i(t)$ in each output neuron. The spatial coincidence

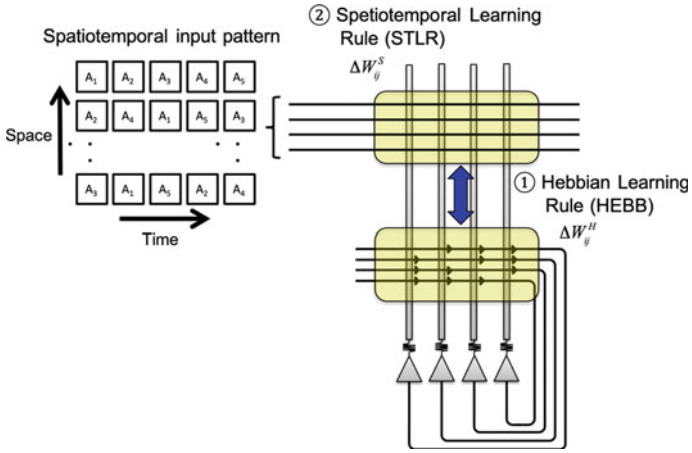

Fig. 1 Schematic diagram of the network architecture. The network consists of excitatory cells with feedforward and feedback connections. Five frames of spatial patterns are created and input them to the network. There are two weight matrices in the network, and each weight is updated by Hebbian learning rule and spatio-temporal learning rule, respectively

$I_{ij}(t)$ is a measure of cooperative activity of the input neurons when a spike of input neuron i arrived on an output neuron j at time t and defined as follows:

$$I_{ij}(t) = x_{ij}(t)w_{ij}\sum_{k\neq j}^{n} x_{kj}(t)w_{kj}(t). \tag{3}$$

The update rule of STLR is given by

$$\Delta w_{ij}^{S}(t+1) = \eta_{STLR}h(I_{ij}(t)), \tag{4}$$

$$h(x) = \begin{cases} 1 & (x \geq \theta_1) \\ 0 & (\theta_1 > x > \theta_2) \\ -1 & (x \leq \theta_2) \end{cases}, \tag{5}$$

where θ_1 and θ_2 are determined by Ca^{2+} influx density via NMDA channels, in which the high density induce LTP and the low, LTD. η_{STLR} is a learning rate coefficient.

The weight modification $\Delta w_{ij}^{H}(t+1)$ depends on the coincidence between previous output and current output and is given by

$$\Delta w_{ij}^{H}(t+1) = \eta_{HEB}y_i(t)y_j(t), \tag{6}$$

where η_{HEB} is a learning rate coefficient.

3 Results

The spatio-temporal pattern used in this simulation consists of five frames of spatial patterns, i.e., A_1, A_2, A_3, A_4, A_5 (A_i is a spatial frame). Every frame consists of N elements ($N = 120$), and each element is chosen as 1 or 0 randomly. We set the Hamming distance (HD) between each spatial frame to be 10 bits. In order to examine whether the network has context-dependent attractors or not, the spatio-temporal sequences are generated by permutations of A_1, A_2, A_3, A_4, A_5 in the initial five steps, and the follow-on steps are randomly selected.

Here, the 120 spatio-temporal context patterns of five frames are applied to the network as external input, and the differences between output vectors from the network are examined in order to investigate the existence of context dependent attractor. First, we focused on the influences of learning rate coefficients η_{STLR} and η_{HEB} for the context-dependent attractor. We calculated bit change rate of output vectors from the network during the last ten steps for 120 spatio-temporal context input patterns. The bit change rate with different parameter values of η_{STLR} and η_{HEB} is shown in Fig. 2a, and after given a threshold (<0.1) is shown in Fig. 2b. Number of different output vectors for 120 spatio-temporal context input patterns is shown in Fig. 2c, and after given a threshold (>96) is Fig. 2d. The common area of Fig. 2b, d is plotted in Fig. 2e. These results indicate that the context-dependent attractors are formed with the appropriate balance of two learning rate coefficients η_{STLR} and η_{HEB}, and appear mainly two separate regions.

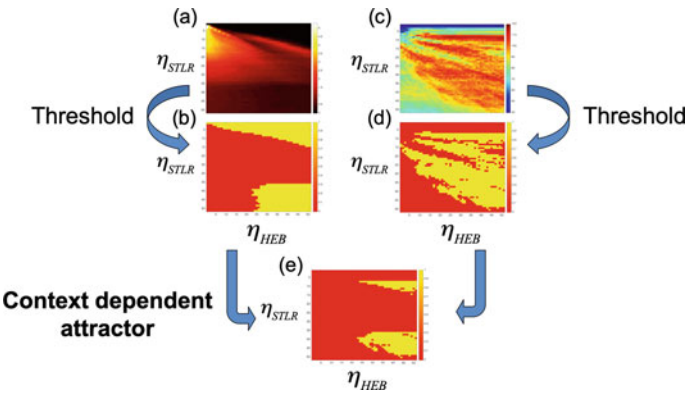

Fig. 2 Context-dependent attractor in the parameter space of η_{STLR} and η_{HEB}. (a) Stable regions of the network output vectors. Different color plots show bit change rate during the last ten steps. (b) Variety of the network output vectors. Different color plots show the number of different output vectors. (c), (d) These figures show binarized images given a threshold to the results of (a) and (b), respectively. (e) Regions of context-dependent attractor in the parameter space of η_{STLR} and η_{HEB}

4 Discussions

We proposed one-layer artificial neural network with feedforward and feedback connections using two types of learning rule. This network structure is based on a basic anatomical structure commonly existing in the brain memory system such as hippocampus (Klausberger and Somogyi, 2008) and cortex (Kubota, 2014) areas. In the process, learning rules play important roles to self-organize the dynamics in the memory neural network. Hebb learning with the recurrent network modifies synaptic weights depending on supra-threshold of destination neurons, which leads to pattern completion. On the other hand, STLR in feedforward connection modifies synaptic weights on sub-threshold of post-synaptic neurons, which leads to pattern separation.

We found that spatio-temporal context input patterns are embedded in the memory space stably as attractors with appropriate balance of two learning rates. Our results also showed that the context-dependent attractor emerges mainly two areas; however, how the memory dynamics are different between these two areas is currently under consideration and future study. These findings contribute to the understanding of the fundamental neural mechanisms of spatio-temporal context learning in the brain.

Acknowledgements This work was supported by JSPS KAKENHI Grant Numbers JP17K00322 and JP20H04246.

References

Amari, S. (1972). Characteristics of random nets of analog neuron-like elements. *IEEE Transactions on Systems, Man, and Cybernetics*, *2*, 643–657.

Hopfield, J. J. (1982). Neural networks and physical systems with emergent collective computational abilities. *Proceedings of the National Academy of Sciences*, *79*(8), 2554–2558.

Klausberger, T., & Somogyi, P. (2008). Neuronal diversity and temporal dynamics: The unity of hippocampal circuit operations. *Science*, *321*(5885), 53–57.

Kubota, Y. (2014). Untangling gabaergic wiring in the cortical microcircuit. *Current Opinion in Neurobiology*, *26*, 7–14.

Nakano, K. (1972). Associatron-a model of associative memory. *IEEE Transactions on Systems, Man, and Cybernetics*, *SMC–2*(3), 380–388.

Tsuda, I. (1992). Dynamic link of memory-chaotic memory map in nonequilibrium neural networks. *Neural Networks*, *5*(2), 313–326.

Tsuda, I., Koerner, E., & Shimizu, H. (1987). Memory dynamics in asynchronous neural networks. *Progress of Theoretical Physics*, *78*(1), 51–71.

Tsukada, H., Yamaguti, Y., & Tsuda, I. (2013). Transitory memory retrieval in a biologically plausible neural network model. *Cognitive Neurodynamics*, *7*(5), 409–416.

Tsukada, M., Aihara, T., Mizuno, M., Kato, H., & Ito, K. (1994). Temporal pattern sensitivity of long-term potentiation in hippocampal ca1 neurons. *Biological Cybernetics*, *70*(6), 495–503.

Tsukada, M., Aihara, T., Saito, H., & Kato, H. (1996). Hippocampal ltp depends on spatial and temporal correlation of inputs. *Neural Networks*, *9*(8), 1357–1365.

Tsukada, M., & Pan, X. (2005). The spatiotemporal learning rule and its efficiency in separating spatiotemporal patterns. *Biological Cybernetics*, *92*(2), 139–146.
Tsukada, M., Yamazaki, Y., & Kojima, H. (2007). Interaction between the spatiotemporal learning rule (STLR) and hebb type (HEBB) in single pyramidal cells in the hippocampal CA1 area. *Cognitive Neurodynamics*, *1*(2), 157–167.

Time Delayed Effect Can Bring Novel Hierarchical Complex Dynamics to Neural Network?

Shigetoshi Nara

Abstract A recurrent neural network model with including time delayed effect is investigated by means of theoretical consideration and computer experiments as well. The detailed contents were already published in Neural Computing and Applications, 11 (3 and 4), pp. 137–143 (2003) by Suemitsu, Y., & Nara, S., and this report was written only for an oral presentation of this work in ICCN2019.

Complex dynamics could play an important role in advanced information processing and control in biological systems, particularly in neural(brain)-systems since (Skarda & Freeman, 1987; Tsuda et al. 1987; Aihara et al. 1990; Nara & Davi, 1992). Along this viewpoint, a recurrent neural network model with including time delayed effect is investigated by means of theoretical consideration and computer experiments as well. The proposed model not only works as the conventional associative memory but also enables us to embed a new kind of memory attractors which are unable to realize in the model without time delayed effect, for example, chain ring like attractors or hierarchical structure of memory attractors as shown in Fig. 1. This is attributed to the fact that time delayed effect makes the available state space expand to larger dimensions than the given number of neurons and their states. Moreover, it is discovered that the basin volume for each embedded chain ring like attractor shrinks, and unstable itinerant orbits in the outer state space of the memory attractor basins emerge, where the itinerancy in outer space could be chaotic.

Now, let us indicate a model that time delayed effect explicitly introduced in updating rule of neuron activity with discrete time and binary state scheme, represented as

$$\mathbf{s}(t+1) = F_{\mu}(\mathbf{s}(t-\tau)) \quad 0 \leq \tau) \tag{1}$$

S. Nara (✉)
Department Electrical and Electronic Engineering, Graduate School of Natural Science and Technology, Okayama University, Okayama, Japan
e-mail: nara@ec.okayama-u.ac.jp

A. Lintas et al. (eds.), *Advances in Cognitive Neurodynamics (VII)*, Advances in Cognitive Neurodynamics,
https://doi.org/10.1007/978-981-16-0317-4_11

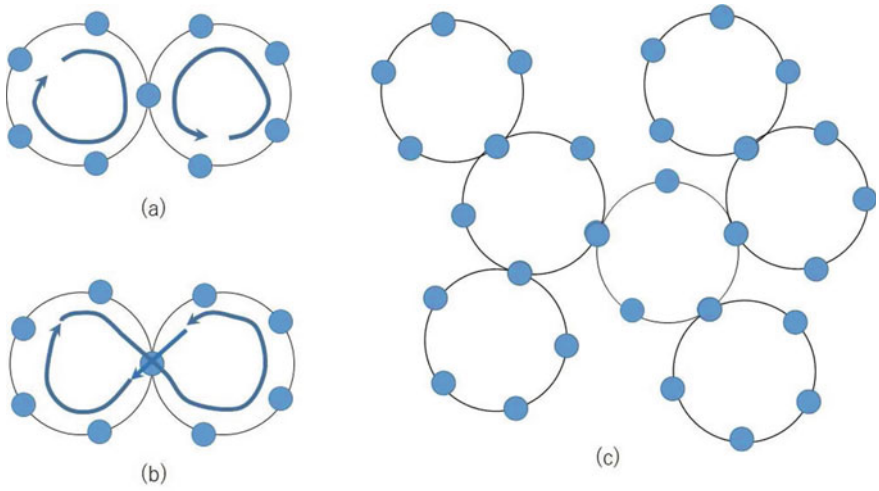

Fig. 1 A schematic description of new-kind attractors in high-dimensional state space, **a**, **b**: chain-ring and **c**: hierachical, which are able to be designed only with use of time-delayed effect [see Eq. (3])

where $\boldsymbol{s}$ is defined as a N-dimensional state vector consisting of binary (± 1) components, and F is certain sign function to describe updating of neuron activity and μ is a parameter set included in the model. $\tau = 0$ results in conventional model. Once this formulation of network activity is employed, then

$$\{s_i(t+q) \mid i = 1 \sim N,\ q = 0 \sim \tau\} \tag{2}$$

is an independent variable (element) set in given τ, so that the total number of independent state vectors is $\tau + 1$, and the number of independent variable is $(\tau + 1)N$ in this model. In contrast, the number of independent variable is infinite when continuous time and state scheme is employed because the cardinality of real number in $0 \leq t \leq \tau$ is infinitely dense, which is represented as $\aleph$. These remarkable extensions of state-space could generate emergent complex hierarchical dynamics in activity of neural system. In actual neural systems including brain, analogue property of real number is limited to finite resolution by biological restriction, so that infinite number of variables would be reduced considerably. Even if so, however, it may account for why human brain can show extraordinary memory-capacity comparing with speculated capacity from roughly estimated number of neurons concerning memorizing and recalling function. Moreover, advanced functional processing could be realized with use of such novel hierarchical complex dynamics with including chaos.

In this paper, based on the above mentioned idea, let us only show a case employed in the previous paper (Suemitsu and Nara, 2003). It is one of selectable varieties within this scheme, in which we take $\tau = 1$ and introduce a certain interaction between the two spaces of $\tau = 0$ and $\tau = 1$, as follows,

$$s_i(t+1) = \mathrm{sgn}\left(\sum_{j=1}^{N} w_{ij}^{(0)} s_j(t) + \sum_{j=1}^{N} w_{ij}^{(1)} s_j(t-1)\right) \tag{3}$$

Even in this simplified model with time delay, the novel properties stated in the initial paragraph are obtained.

More detailed considerations and computer experiments to develop our ideas will be given in future.

References

Skarda, C. A., & Freeman, W. J. (1987). *Behavioral and Brain Sciences*, *10*, 161–195.
Tsuda, I., Koerner, E., & Shimizu, H. (1987). *Progress Theoretical Physics*, *78*, 51–71.
Aihara, K., Takabe, T., & Toyoda, M. (1990). *Physics Letters A*, *114*(6/7), 333–340.
Nara, S., & Davis, P. (1992). *Progress of Theoretical Physics*, *88*, 845–855.
Suemitsu, Y., & Nara, S. (2003). A note on time delayed effect in a recurrent neural network model. *Neural Computing and Applications*, *11*(3 and 4), 137–143.

A Cortical Network Model for Visual Attention

Xiaochuan Pan, Tao Zhang, Xuying Xu, and Rubin Wang

Abstract It is known that visual attention can modulate firing patterns of neurons in visual cortexes and play important functional roles in visual information processes. Despite of several decades of studies, mechanisms of visual attention still remain unclear. Recent neurophysiological studies reported that attention could increase NMDA and AMPA synaptic strength. To understand how neuronal activity is modulated by attention at the synaptic level, we proposed a three-layer neural network in this study. Each neuron receives AMPA and NMDA currents and also GABA currents. In the synapse between every two neurons, neurotransmitters are stochastically bound with receptors in post-synaptic membranes. In the model, it is hypothesized that attention could make the binding process less stochastic, and more neurotransmitters are bound with postsynaptic receptors. Our simulation showed that attention resulted neurons in the model had stronger firing rates and less response variability. We also found that attention had stronger modulation of neuronal activity in higher layers than in lower layers. Inhibitory neurons had stronger attention effects than did excitatory neurons. Overall, our results demonstrated that attention may modulate neuronal activity by controlling the stochastic binding process.

1 Introduction

Visual attention has crucial roles in the process of visual information. It could selectively enhance neuronal responses to particular visual stimuli (Reynolds et al. 1999; Treue and Maunsell 1999). Some studies have reported that single neurons could increase its firing rate and reduce its response variability when attention is in work (Anton-Erxleben and Carrasco 2013). It was also found that neuronal activities in higher visual areas are modulated more strongly by attention than those in lower visual areas, and putative interneurons had stronger attention modulation than did putative pyramidal cells (Thiele et al. 2016). A recent experiment further reported

X. Pan (✉) · T. Zhang · X. Xu · R. Wang
Institute for Cognitive Neurodynamics, East China University of Science and Technology, 130 MeiLong Road, Shanghai 200237, China
e-mail: pxc@ecust.edu.cn

A. Lintas et al. (eds.), *Advances in Cognitive Neurodynamics (VII)*, Advances in Cognitive Neurodynamics,
https://doi.org/10.1007/978-981-16-0317-4_12

that attention increased the efficacy of neuronal communication between neurons, and a presynaptic input could more easily to drive a response of a postsynaptic neuron (Briggs et al. 2013). These experimental observations imply that attention may affect information transmission between neurons at the synaptic level, which thereby could change response patterns of neurons in various cortical regions. It is essential to investigate the underlying mechanism how attention modulates the efficiency of neural signal transmission.

There are lots of proposed computational models to reveal attentional modulation on neuronal activities (Lanyon and Denham 2009). The detail methods to model attentional effects are different in these models. Some models have neurons and their connected microcircuits with detailed biophysical information (Wagatsuma et al. 2013). Some models are constructed with abstract spiking neurons (Itti and Koch 2000) or dynamic rate coded populations (Beuth and Hamker 2015). Some models only have abstract mathematical descriptions (Reynolds and Heeger 2009). However, these models have some limitations to analyze synaptic information transmission modulated by attention. Therefore, the purpose of this study is to reveal how attention controls the binding processing of neurotransmitters to modulate information transmission between neurons.

To investigate this issue, a three-layer network model was proposed to study attentional modulations on neural activities. Each layer has excitatory and inhibitory neurons. Each neuron receives AMPA, NMDA, and GABA currents. Neurotransmitters are released, transmitted in the synaptic cleft, and finally are bound to receptors in the postsynaptic membrane. This binding process is considered as a random process (Dobrunz and Stevens 1997). It is hypothesized that the randomness in the binding process of neurotransmitters with receptors becomes smaller by attention. In effect, attention enables more neurotransmitters to be bound with receptors in the postsynaptic membrane.

The model could simulate attentional modulation on firing rates and response variability. The simulated results are consistent with observations found in experiments. Our model demonstrates that attention could control neurotransmitters transmission in the synapse, which further generates attention-modulated activity patterns.

2 Methods and Materials

As shown in Fig. 1, a three-layer network is prosed to simulate functions of visual attention. The first layer from the input is labeled as layer 1, the middle layer is labeled as layer 2, and the output layer is labeled as layer 3. There are 20 excitatory and 5 inhibitory neurons in each layer. The connections within a layer or between layers are described as following. Each excitatory neuron has inputs from five inhibitory neurons and inputs from five excitatory neurons selected randomly; one inhibitory neuron receives projections from one randomly selected excitatory neuron. An excitatory neuron in the current layer receives inputs from three randomly selected excitatory neurons in the previous layer. Excitatory neurons transmit information from

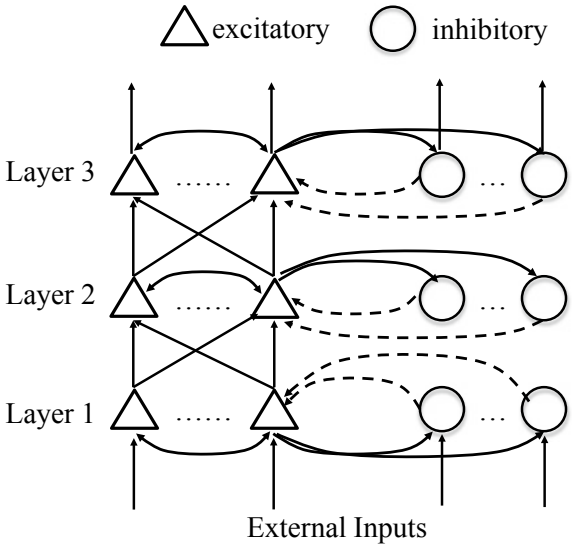

Fig. 1 Three-layered network model of visual attention. The black triangles indicate excitatory neurons. The black circles indicate inhibitory neurons. The solid arrows indicate excitatory connections, and the dashed arrows indicate inhibitory connections

one layer to next layer. Inhibitory neurons do not relay signals between layers. No signals are feedback from higher layers to lower layers. A sustained external current is inputted to all neurons in layer 1, and there are no external inputs to neurons in other layers.

The Hodgkin-Huxley model of single neurons is used in this study. This single-neuron model could describe in detail spike shapes and properties of excitatory and inhibitory neurons, respectively.

The membrane potential of an excitatory neuron (e) is the following:

$$C^e \frac{\mathrm{d}V^e}{\mathrm{d}t} = -I^e_{\mathrm{Na}}(V^e) - I^e_K(V^e) - I^e_L(V^e) - I^e_M(V^e) - I_{\mathrm{AMPA}}(V^e, r_{\mathrm{AMPA}}) - I_{\mathrm{NMDA}}(V^e, r_{\mathrm{NMDA}}) - I_{\mathrm{GABA_A}}(V^e, r_{\mathrm{GABA_A}}) \quad (1)$$

The membrane potential of an inhibitory neuron is the following:

$$C^i \frac{\mathrm{d}V^i}{\mathrm{d}t} = -I^i_{\mathrm{Na}}(V^i) - I^i_K(V^i) - I^i_L(V^i) - I_{\mathrm{AMPA}}(V^i, r_{\mathrm{AMPA}}) - I_{\mathrm{NMDA}}(V^i, r_{\mathrm{NMDA}}) \quad (2)$$

In the above equations, I_{AMPA} indicates the AMPA current. It is then described by the following equation:

$$I_{\mathrm{AMPA}} = g_{\mathrm{AMPA}} r_{\mathrm{AMPA}} (V - E_{\mathrm{AMPA}}) \quad (3)$$

I_{NMDA} is the NMDA current. Its dynamic properties is described by the following equation:

$$I_{\mathrm{NMDA}} = g_{\mathrm{NMDA}} f_{\mathrm{NMDA}}(V) r_{\mathrm{NMDA}}(V - E_{\mathrm{NMDA}}) \tag{4}$$

$$F_{\mathrm{NMDA}}(V) = \left(1 + \mathrm{e}^{\frac{-V+T_f}{\sigma_f}}\right)^{-1}$$

The $\mathrm{GABA_A}$ current is given by the following equation:

$$I_{\mathrm{GABA_A}} = g_{\mathrm{GABA_A}} r_{\mathrm{GABA_A}} \left(V - E_{\mathrm{GABA_A}}\right) \tag{5}$$

The kinetics of the ratio of bound receptors r is characterized by the following equation:

$$\frac{\mathrm{d}r_i}{\mathrm{d}t} = \alpha[T](1 - r_i) - \beta r_i, i = \mathrm{AMPA,NMDA,GABA_A} \tag{6}$$

where $[T]$ is the concentration of neurotransmitters.

The binding process of neurotransmitter with receptors is stochastic, which was simulated by one stochastic variable shown in the following equation:

$$\frac{\mathrm{d}r^i_{\mathrm{noise}}(t)}{\mathrm{d}t} = -\frac{1}{\tau}\left[r^i_{\mathrm{noise}}(t) - r^i_{\mathrm{noise}_0}\right] + \sqrt{\frac{2\sigma_i^2}{\tau}}\chi_i(t) \tag{7}$$

$$i = AMPA, NMDA, GABA_A$$

where χ_i(t) is the Gaussian white noise of zero mean and unit standard deviation, and $r^i_{\mathrm{noise}_0}$, σ_i are the average and standard deviation of the random sequence (i = AMPA, NMDA, $\mathrm{GABA_A}$), respectively. τ is the time constant.

In Eq. (7), the parameter σ_i could control the standard deviation of the stochastic process. This stochastic variable in Eq. (7) is then added to r_i to mimic randomness in the neurotransmitter binding process. Because we hypothesize that randomness in this bind process could be reduced by attention, the parameters of σ_{AMPA} and σ_{NMDA} are set lager values when attention is unattended (more randomness). And their values become smaller when attention is attended (less randomness). In this study, we do not take the attentional effect on $\mathrm{GABA_A}$ receptors into account, so the parameter of $\sigma_{\mathrm{GABA_A}}$ is set a constant regardless of attention conditions.

3 Results

During simulation, because the binding process was stochastic, the activity pattern of each neuron varied trial by trial even though the external current to the neurons in layer 1 was constant. We calculated neuronal activity in 48 trials for each condition. In each condition, all parameters were set as the same values for each trial, but the variable in Eq. (7) varies trial by trial. We then averaged firing rates and computed response variability for each neuron in the model across these 48 trials.

It was found that the mean firing rate of all neurons decreased when the σ_{AMPA} increased. σ_{AMPA} was set different values to indicate different attention conditions. For example, in AMPA channels connecting two excitatory neurons, $\sigma_{\mathrm{AMPA}} = 0.075$ in the attention-attended condition and $\sigma_{\mathrm{AMPA}} = 0.08$ in the attention-unattended condition. In AMPA channels projecting from excitatory cells to inhibitory cells, $\sigma_{\mathrm{AMPA}} = 0.075$ in the attended condition and $\sigma_{\mathrm{AMPA}} = 0.09$ in the unattended condition. These specific values were chosen for the two attention conditions. The model with these values could simulate results that were similar to experimental observations.

We did not find that attention significantly alters firing rates of neurons in layer 1 due to the large external current to each neuron (excitatory cells: $p = 0.107$; inhibitory cells: $p = 0.111$, Mann-Whitney U-test between the two attentional conditions for each type of cells). But firing rates of both excitatory and inhibitory cells in layer 2 and 3 showed significant differences between the two attentional conditions ($p < 0.01$, Mann-Whitney U-test).

The Fano factor in layer 1 was very small, indicating that these neurons had stable firing patterns. The Fano factor was not modulated by attention for either excitatory or inhibitory cells (excitatory cells: $p = 0.199$; inhibitory cells: $p = 0.548$, Mann-Whitney U-test). In layer 2, Fano factors of excitatory cells had significantly smaller values in the attention-attended condition than in the unattended condition ($p < 0.01$, Mann-Whitney U-test). Fano factors of inhibitory cells did not affect by attention ($p = 0.095$, Mann-Whitney U-test). Only five inhibitory cells in layer 2 may not have enough power to reach statistical significance. Fano factors of both excitatory and inhibitory cells in layer 3 were modulated by attention, showing smaller values in the attention-attended condition (excitatory cells: $p = 0.019$; inhibitory cells: $p < 0.01$; Mann-Whitney U-test between the two attention conditions for each type of cells).

The randomness in NMDA channels (controlled by σ_{NMDA}) also modulated firing patterns of neurons in layer 2 and layer 3. The firing rate became smaller when the value of σ_{NMDA} became larger. Different values were selected for σ_{NMDA} to indicate different attentional conditions. We chose $\sigma_{\mathrm{NMDA}} = 0.12$ in the attention-unattended condition and $\sigma_{\mathrm{NMDA}} = 0.04$ in the attended condition for NMDA channels connecting two excitatory cells. $\sigma_{\mathrm{NMDA}} = 0.16$ (unattended) and $\sigma_{\mathrm{NMDA}} = 0.04$ (attended) were selected for NMDA channels projecting from excitatory cells to inhibitory cells.

Neurons in layer 1 showed significantly stronger firing rates in the attention-attended condition (excitatory cells: $p < 0.01$; inhibitory cells: $p < 0.01$; Mann-Whitney U-test). This is the same case in layer 2; firing rates were increased by attention (excitatory cells: $p < 0.01$; inhibitory cells: $p < 0.01$; Mann-Whitney U-test). Similar results were found in layer 3, attention increased firing rates of both excitatory and inhibitory cells (excitatory cells: $p < 0.01$; inhibitory cells: $p < 0.01$; Mann-Whitney U-test).

We did not found that Fano factors in layer 1 were significantly modulated by attention (excitatory cells: $p = 0.561$; inhibitory cells: $p = 0.548$; Mann-Whitney U-test). Fano factors of both excitatory and inhibitory cells in layer 2 showed significant smaller in the attention-attended condition (excitatory cells: $p < 0.01$; inhibitory cells: $p < 0.01$; Mann-Whitney U-test to compare the two attentional conditions for each type of cells). Similar results were found in layer 3. Fano factors became significantly smaller in the attended condition (excitatory cells: $p < 0.01$; inhibitory cells: $p = 0.015$; Mann-Whitney U-test).

Attention-modulated effects on firing patterns were compared for different types of neurons in different layers. It was found that attention (controlled by σ_{AMPA} or σ_{NMDA}) had stronger modulation for inhibitory than excitatory cells in the same layer and stronger modulation for neurons in layer 3 than layer 2.

4 Discussion

We made the hypothesis that attention may reduce stochastic factors in the neurotransmitter binding process, which increase the number of bound receptors located in the post-membrane. The stochastic factors in AMPA and NMDA channels were controlled by the values of σ_{AMPA} and σ_{NMDA} in our model, respectively. On the basis of this assumption, the network model of visual attention simulated activity patterns of neurons modulated by attention, increasing their firing rates, reducing their response variability.

Some experiments have shown that the binding process of neurotransmitters with receptors is a stochastic process (Gibb 2001). It also reported that variation of firing rates of neurons was reduced by attention, which might enhance the reliability of information transmission between neurons (Briggs et al. 2013). This result suggested that attention may alter spike patterns of neurons by the method of controlling the stochastic process in neurotransmitter channels. The parameters of σ_{AMPA} and σ_{NMDA} in the network model constrain the ratio of bound AMPA or NMDA receptors, respectively. The ratio of bound receptors would increase with decreasing the values of σ_{AMPA} and σ_{NMDA}. This means that more neurotransmitters were bound with receptors. Therefore, the post-synaptic neuron receives larger synaptic currents and has higher probability to evoke a spike. Meanwhile, when the values of σ_{AMPA} and σ_{NMDA} became smaller in the attention-attended condition, stochastic factors in the AMPA or NMDA binding process reduced. This indicated that in the attention-attended condition, the post-synaptic neuron had more stable synaptic inputs to induce spikes

in repeated trials, and its response variation reduced. Visual attention may enhance efficiency and reliability of information communication among neurons by reducing stochastic factors in the neurotransmitter binding process.

How does attention control the randomness in the neurotransmitter binding process in the brain? It is an important question. Till now, we did not find experimental observations that directly support that attention controls the randomness in the stochastic binding process. Some reports demonstrated that attention enhanced efficient information transmission, and attention-induced activity modulation was impaired by block of AMPA or NMDA channels, indicating that attention is engaged in the synaptic information processing (Briggs et al. 2013; Herrero et al. 2013). In the literature, computational models of visual attention usually have sophisticated structure of neurons and consider the attentional signal as an external input to the network to generate attention-induced activity (Wagatsuma et al. 2013; Beuth and Hamker 2015). However, this external signal is not explained only as the attentional signal; it may be regarded as other types of signal (e.g., reward signal) but induce attention-like activity. The assumption in this study is that attention could be a process that controls stochastic factors in the synapse. The network model had not sophisticated connection patterns among neurons; the three-layered feed-forward network is enough to generate attention-modulated activity. Our network model proposes a new method to investigate how attention modulates spike activity underlying synaptic mechanisms. One experiment in vivo shows that the single-molecule imaging can measure the dynamic course of bound receptors located in postsynaptic membranes (Ueda and Shibata 2007). It is possible to use this new technology to measure the dynamical course of bound AMPA or NMDA receptors when an animal is performing an attentional task. Statistical properties of bound receptors during the dynamical course are compared between the attention-attended and unattended conditions to verify our hypothesis.

Acknowledgements This work was supported National Natural Science Foundation of China (No. 11972159).

References

Anton-Erxleben, K., & Carrasco, M. (2013). Attentional enhancement of spatial resolution: linking behavioural and neurophysiological evidence. *Nature Reviews Neuroscience, 14*(3), 188–200.

Beuth, F., & Hamker, F. H. (2015). A mechanistic cortical microcircuit of attention for amplification, normalization and suppression. *Vision Research, 116*(Pt B), 241–257.

Briggs, F., Mangun, G. R., & Usrey, W. M. (2013). Attention enhances synaptic efficacy and the signal-to-noise ratio in neural circuits. *Nature, 499*(7459), 476–480.

Dobrunz, L. E., & Stevens, C. F. (1997). Heterogeneity of release probability, facilitation, and depletion at central synapses. *Neuron, 18*(6), 995–1008.

Gibb, A. J. (2001). Neurotransmitter receptors. In Webster, R. (Ed.) *Neurotransmitters, drugs and brain function* (pp. 57–79). John Wiley & Sons Ltd.

Herrero, J. L., Gieselmann, M. A., Sanayei, M., & Thiele, A. (2013). Attention induced variance and noise correlation reduction in macaque V1 is mediated by NMDA receptors. *Neuron, 78*(4), 729–739.

Itti, L., & Koch, C. (2000). A saliency-based search mechanism for overt and covert shifts of visual attention. *Vision Research, 40*(10–12), 1489–1506.

Lanyon, L. J., & Denham, S. L. (2009). Modelling attention in individual cells leads to a system with realistic saccade behaviours. *Cognitive Neurodynamics, 3*(3), 223–242.

Reynolds, J. H., Chelazzi, L., & Desimone, R. (1999). Competitive mechanisms subserve attention in macaque areas V2 and V4. *Journal of Neuroscience, 19*(5), 1736–1753.

Reynolds, J. H., & Heeger, D. J. (2009). The normalization model of attention. *Neuron, 61*(2), 168–185.

Thiele, A., Brandt, C., Dasilva, M., Gotthardt, S., Chicharro, D., Panzeri, S., et al. (2016). Attention induced gain stabilization in broad and narrow-spiking cells in the frontal eye-field of macaque monkeys. *Journal of Neuroscience, 36*(29), 7601–7612.

Treue, S., & Maunsell, J. H. (1999). Effects of attention on the processing of motion in macaque middle temporal and medial superior temporal visual cortical areas. *Journal of Neuroscience, 19*(17), 7591–7602.

Ueda, M., & Shibata, T. (2007). Stochastic signal processing and transduction in chemotactic response of eukaryotic cells. *Biophysical Journal, 93*(1), 11–20.

Wagatsuma, N., Potjans, T. C., Diesmann, M., Sakai, K., & Fukai, T. (2013). Spatial and feature-based attention in a layered cortical microcircuit model. *PLoS ONE, 8*(12), e80788.

Fractal Structure in Hokusai's "Great Wave" and the Memory Neural Network

Minoru Tsukada and Hiromichi Tsukada

Abstract Google used 10 million natural images as input information and performed self-organized learning with a huge neural network with 10 billion synapses, and neurons with a receptive field resembling a cat's image appeared in the upper layer. Hokusai drew "Great Wave" by using his memory with a fractal structure. Which do you think is "beautiful": "Google's cat picture" and Hokusai's "Great Wave"? I think Hokusai's one is beautiful. Because it is based on stunning information compression. The proposed network in this paper is composed of a one-layer artificial neural network with feedforward and feedback connections. In the feedforward connections, the spatiotemporal learning rule (STLR) Tsukada et al. (1994, 1996) has high ability in pattern separation and in the recurrent connections, Hebbian learning rule (HEB) in pattern completion. The interaction between the two rules plays an important role to self-organize the context-dependent attractor in the memory network. The context-dependent attractors depend on the balance between STLR and HEB. The structure is an important factor of memory networks to hierarchically embed a sequence of events.

1 Introduction

A cat drawn by Google's artificial intelligence is shown in Fig. 1a, and a Great Wave drawn by Hokusai is in Fig. 1b. Google used 10 million natural images as input information and performed self-organized learning with a huge neural network with 10 billion synapses, and neurons with a receptive field resembling a cat's image appeared in the upper layer. It is said that artificial intelligence can recognize cats

M. Tsukada (✉)
Brain Science Institute, Tamagawa University, 6-1-1 Tamagawa-gakuen, Machida, Tokyo 194-8610, Japan
e-mail: tsukada@eng.tamagawa.ac.jp

H. Tsukada
College of Engineering, Chubu University, 1200 Matsumoto, Kasugai, Aichi 487-8501, Japan
e-mail: tsukada@isc.chubu.ac.jp

A. Lintas et al. (eds.), *Advances in Cognitive Neurodynamics (VII)*, Advances in Cognitive Neurodynamics,
https://doi.org/10.1007/978-981-16-0317-4_13

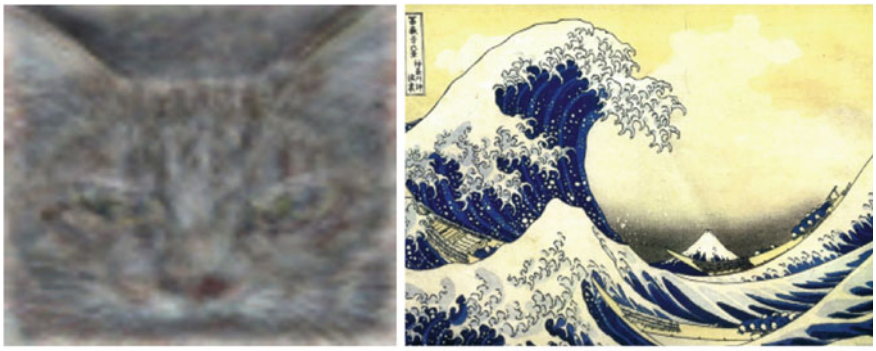

(a) (b)

Fig. 1 **a** Cat drawn by Google's artificial intelligence. **b** Great wave drawn by Hokusai

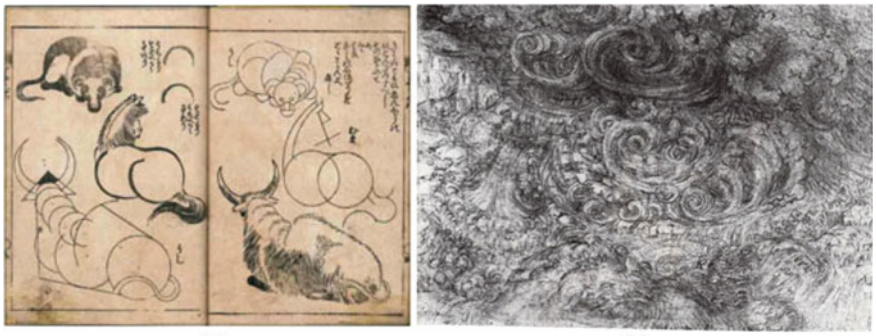

(a) (b)

Fig. 2 **a** Hokusai's "Pictorial Example". **b** "Big Flood" of da Vinci

without teaching the concept of cats. In contrast, for many years, Hokusai had repeatedly studied as a painter how to express the natural world, and drew "Great Wave".

Hokusai's "Great Wave" shows the shape of the wave drawn by Hokusai as it would appear when you capture the actual wave with a 1/5000 high-speed camera. At a speed lower than that, you cannot catch it. Of course, it cannot be seen with the naked human eye.

So, Hokusai was not able to see the world of 1/5000. How did he draw it? I am amazed by the clairvoyance of Hokusai. Did Hokusai have the ability to perceive the natural world intuitively? In case, Hokusai's "Pictorial Example" (Fig. 2a) was published. Furthermore, there was a drawing called "Big Flood" by da Vinci (Fig. 2b). Indeed, it turns out that these are a fractal. These painters had drawn knowing that the natural world is made of fractal structure! The word ""fractal" is a recent name coined by Mandelbrot attached, but already the artists had realized the rules of the formation of the natural world.

We convert the topic here to the memory experiment and theory that I have been working on for many years. It is a study of the fractal structure of memory. Experimentally, Tsukada et al. (1994, 1996) showed that various spatiotemporal pattern stimuli can induce long-term potentiation (LTP) in the hippocampal neurons, and based on these results, proposed the spatiotemporal learning rule (STLR) consisted by two factors; cooperative plasticity (coincidence) among presynaptic inputs without a postsynaptic spike and its temporal summation. Tsukada and Pan (2005) systematically identified the functional difference between STLR and HEB in a simple one-layer neural network by computing their ability to differentiate spatiotemporal sequences. STLR has high ability in discriminating spatiotemporal pattern, while HEB in pattern completion.

Theoretically, Tsuda (2001), and Tsuda and Kuroda (2001, 2004) showed the possibility that output pattern of CA1 neurons was hierarchically clustered in a self-similarity manner. In experimental relation, with Fukushima et al. (2007), this property was significant, observed at two and three time series in the post-synaptic membrane potential of single CA1 neurons measured by the patch-clamp method. Furthermore, Yamaguti et al. (2011) showed fractal-like clustering with a hierarchical structure which reflects the similarity of the input time series by using the two-compartment model with two types of conductance via AMPA and NMDA receptors. Tsukada et al. (2016, 2018) proposed a simple artificial memory network for storing spatiotemporal sequences by unsupervised learning. The network structure composed of a one-layer artificial neural network with feedforward and feedback connections. In the feedforward connections, the spatiotemporal learning rule (STLR) Tsukada et al. (1994, 1996) has high ability in pattern separation and in the recurrent connections, HEB in pattern completion. The interaction between the two rules plays an important role to self-organize the context-dependent attractor in the memory network.

2 Simulation Results

The two learning rules, HEB and STLR, play important roles to self-organize the dynamics in the memory neural network. HEB in recurrent networks produce increasingly similar output changes by its successive iterations until eventually the outputs become constant, that is called "pattern completion". This is closely related to the dynamic supra-threshold-behavior of output neurons. In contrast, STLR in feedforward connections dynamically modify the sub-threshold membrane potential as internal states, so that the input spatial pattern and its history are reflected in the membrane potential. The modification creates the pattern sensitivity on the output space along the time axis from next to next; that is called "pattern separation". The context-dependent attractors depend on the balance between STLR and HEB; that of learning coefficient η_{STLR} and η_{HEB}. The simulation results are shown in Fig. 3. From the results, context-dependent attractors were identified in two areas; A area (high, high) and B area (high, low) in (η_{HEB}, η_{STLR}). The time series and PCA results in

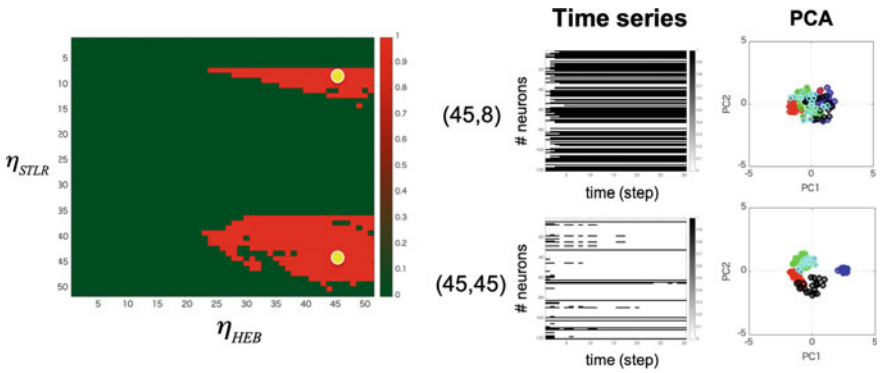

Fig. 3 Areas of context-dependent attractors and PCA results of the typical two attractors

Fig. 3 imply the different characteristics in organized structure of context-dependent attractors. The A attractor (45, 45) has some structure in PCA, while the B attractor (45, 8) has no structure. Such a structure of A is important as a memory to hierarchically embed a sequence of events.

3 Discussions

We see the flow of visual information. Vision has central (foveal) vision and peripheral vision. Central vision sends information to the temporal lobe as an object vision with high spatial resolution and relatively slow propagation speed. The information is associated with the frontal lobe left brain and partly analyzes the shape and meaning of the object. In contrast, peripheral vision propagates to the parietal lobe as a space vision with low spatial resolution but high temporal resolution and high propagation speed. The information cooperates with the frontal lobe on the right side and the amygdala and captures intuitive and overall outline image and mental information. Both pieces of information come in time series to the hippocampus, and information on the whole and parts is memorized in fractal structure. In short, when you view pictures, you first grab the overall impression, and then see what is drawn in the part of interest. In other words, the plane of the painting is spatially divided, and the information of the whole and the part is integrated with a dynamic line of sight to appreciate it. It is exactly like drawing a picture by spatial division and dynamics of the neural network. Figure 4 shows the process of drawing pictures of Google's cats, and Fig. 5 shows how Hokusai drew Great Wave by using his memory with a fractal structure. Which do you think is "beautiful": "Google's cat picture" and Hokusai's "Great Wave"?. I think the picture of Hokusai is beautiful. Because it is based on stunning information compression.

Finally, there are still many things to learn from the brain. The brain has made creative evolution over time. The neural network of human memory has acquired a

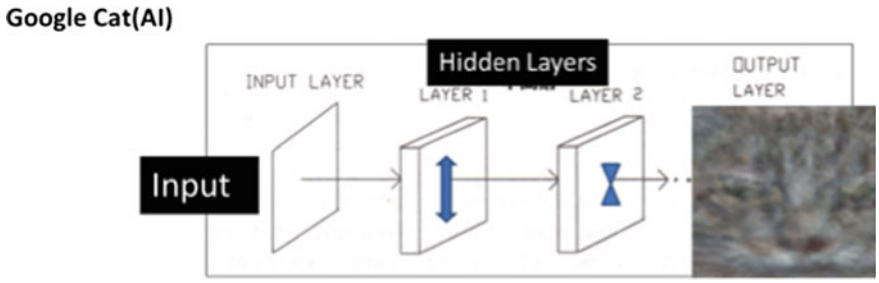

Fig. 4 Process of drawing pictures of Google's cats

Fig. 5 Process of drawing pictures using fractal structures

beautiful brain wear which processes past, present, and future memories by using space division and dynamics in memory neural networks. Artificial intelligence has not yet fully utilized the dynamics of the memory of the brain.

Acknowledgements This work was supported by JSPS KAKENHI Grant Numbers JP17K00322 and JP20H04246.

References

Fukushima, Y., Tsukada, M., Tsuda, I., Yamaguti, Y., & Kuroda, S. (2007). Spatial clustering property and its self-similarity in membrane potentials of hippocampal ca1 pyramidal neurons for a spatio-temporal input sequence. *Cognitive Neurodynamics*, *1*, 305–316.

Tsuda, I. (2001). Toward an interpretation of dynamic neural activity in terms of chaotic dynamical systems. *Behavioral and Brain Sciences*, *24*(5), 793–810.

Tsuda, I., & Kuroda, S. (2001). Cantor coding in the hippocampus. *Japan Journal of Industrial and Applied Mathematics*, *18*(2), 249–258.

Tsuda, I., & Kuroda, S. (2004). A complex systems approach to an interpretation of dynamic brain activity ii: Does cantor coding provide a dynamic model for the formation of episodic memory? In P. Érdi, A. Esposito, M. Marinaro, & S. Scarpetta (Eds.), *Computational Neuroscience: Cortical Dynamics* (pp. 129–139). Berlin Heidelberg, Berlin, Heidelberg: Springer.

Tsukada, H., Tsukada, M., & Isomura, Y. (2018). A structure and function of hippocampal memory networks in consolidating spatiotemporal contexts. In J. M. Delgado-García, X. Pan, R. Sánchez-Campusano, & R. Wang (Eds.), *Advances in Cognitive Neurodynamics (VI)* (pp. 103–108). Singapore: Springer Singapore.

Tsukada, H., Tsukada, M., & Tsuda, I. (2016). A concept of spatiotemporal attractors. In R. Wang & X. Pan (Eds.), *Advances in Cognitive Neurodynamics (V)* (pp. 749–753). Singapore: Springer Singapore.

Tsukada, M., Aihara, T., Mizuno, M., Kato, H., & Ito, K. (1994). Temporal pattern sensitivity of long-term potentiation in hippocampal ca1 neurons. *Biological Cybernetics*, *70*(6), 495–503.

Tsukada, M., Aihara, T., Saito, H., & Kato, H. (1996). Hippocampal ltp depends on spatial and temporal correlation of inputs. *Neural Networks*, *9*(8), 1357–1365.

Tsukada, M., & Pan, X. (2005). The spatiotemporal learning rule and its efficiency in separating spatiotemporal patterns. *Biological Cybernetics*, *92*(2), 139–146.

Yamaguti, Y., Kuroda, S., Fukushima, Y., Tsukada, M., & Tsuda, I. (2011). A mathematical model for cantor coding in the hippocampus. *Neural Networks*, *24*(1), 43–53.

Auditory and Multisensory Processing

Viewer's Attention Flow When Watching Audiovisual Cuts

Miguel Ángel Martín-Pascual, Celia Andreu-Sánchez, José María Delgado-García, and Agnès Gruart

Abstract Audiovisual works have plenty of cuts, but viewers hardly notice them. Movie edition creates a discontinuity in audiovisual works. We analyze the effects of cuts on 36 subjects, using electroencephalography (EEG) techniques. Cuts result in an increase of attention in viewers by decreasing their eyeblink rate. They also cause a spread of potentials from the occipital area to the frontal area at around 200 ms after the cut, as the perception of the media content progresses to more-complex areas of process. Our results are coherent with previous studies on early discrimination of visual stimuli. The mentioned flow of potential happens differently depending on the style of edition in which cuts are inserted. Cuts in continuous narrative have a lower impact on the visual zone than do cuts in chaotic and fragmented narrative. However, the opposite is found in the prefrontal area, with a higher activity when continuous and lifelike narrative is being watched. These results can be applied for the management of attention when creating media content.

1 Audiovisual Cuts

Cinema appeared in the last years of the 19th century (Gubern, 1973). After some years of experimentation, in the 1910s, the analysis of edition started to become a topic of great interest in communication studies (Gunning, 1994; Münsterberg,

M. Á. Martín-Pascual (✉)
Instituto RTVE, Sant Cugat del Vallès, Barcelona, Spain
e-mail: miguelangel.martin@rtve.es

C. Andreu-Sánchez
Serra Húter Fellow, Neuro-Com Research Group, Universitat Autònoma de Barcelona, Barcelona, Spain
e-mail: celia.andreu@uab.cat

J. M. Delgado-García · A. Gruart
Neuroscience Division, Pablo de Olavide University, Sevilla, Spain
e-mail: jmdelgar@upo.es

A. Gruart
e-mail: agrumas@upo.es

A. Lintas et al. (eds.), *Advances in Cognitive Neurodynamics (VII)*, Advances in Cognitive Neurodynamics,
https://doi.org/10.1007/978-981-16-0317-4_14

1916). Some experiments, such as (Kuleshov, 1974) and Pudovkin (2013), and some written works, such as (Eisenstein, 1988), showed that cuts and style of edition were key to the creation of films. Cuts are the most common transition between shots (Cutting, 2016; Cutting et al., 2011). Many researchers have investigated the impact that cuts have on the perception of media content (Francuz & Zabielska-Mendyk, 2013; Germeys & d'Ydewalle, 2007; Magliano & Zacks, 2011), proving that the use of cuts affects the understanding of the meaning of the story (Carroll & Bever, 1976; Eisenstein, 1977).

The level of attention required to understand narrative content in audiovisual works can be studied by analyzing viewers' eyeblink rate (Nakano et al., 2009; Shultz et al., 2011). Eyeblinks are fast movements that close and open the palpebral fissure and have the physiological function of wetting and protecting our cornea and the psychological one of managing attention (Cruz et al., 2011). Blinking is something that we constantly do without being aware of. A decrease of attention produces an increase of spontaneous eyeblink rate (SBR), while an increase of attention decreases the SBR (Wiseman & Nakano, 2016; Zheng et al., 2012). In this investigation, we analyzed how cuts and the style of edition containing them have an impact on viewers' SBR.

Cuts have also been studied from an electrophysiological viewpoint. In the 1950s, Gastaut and Bert proposed the study of cinema through electroencephalography (EEG). They found that any audiovisual content, regardless of how banal it may be, had an impact able to modify the EEG of a normal adult (Cohen-Séat et al., 1954; Gastaut and Bert, 1954). Despite those interesting studies not being followed up as a topic in communication research, there are some concrete studies in neuroscience developed during the last few decades. Reeves and colleagues showed the presence of alpha waves in central and occipital areas connected to edits (Reeves et al., 1985). More recent studies have proven that the relation between the shots that cuts connect is crucial for the brain activity of viewers (Francuz and Zabielska-Mendyk, 2013; Geiger and Reeves, 1993; Lang et al., 1993). Here, we also analyze the brain activity linked to cuts in different styles of edition.

2 Methods

2.1 Stimuli

We presented two stimuli having the same narrative content and the same duration (198 s), but with different style of edition. Both were movies: one followed a continuous style of edition with smooth transitions and clear presentation of the visual content, based on the Hollywood style of edition rules; the other stimulus was chaotic, discontinuous, with a faster style of edition, inspired by musical video clips and their style of edition—we called this stimulus MTV-style movie. The Hollywood-style movie had 33 shots with an average shot length (ASL) of 5.9 s, and the MTV-style movie had 79 shots with an ASL of 2.4 s.

2.2 Experimental Setup

The stimuli were presented on a 42-inch HD LED display (Panasonic TH42PZ70EA, Panasonic Corporation), at 150 cm from the participants, with Paradigm Stimulus Presentation (Perception Research System Incorporated). Continuous EEG was recorded using the wireless Enobio® system (Neuroelectrics) (Martín-Pascual et al., 2018). Twenty electrodes placed according to the International 10–20 System were used, one of which was for electrooculogram (EOG). Electrodes were referenced to mastoid electrodes. We also recorded participants's faces with an HD (1920 width $\times$ 1080 height pixels) video camera at 25 frames per second (Sony HDR-GW55VE, Sony Corporation).

2.3 Participants

Thirty-six participants (six women), aged 28–56 (43.97 ± 8.07), with normal or corrected-to-normal visual acuity, were recruited for this experiment. Written informed consent was obtained from all participants prior to participating in the study. All procedures were performed in accordance with relevant guidelines and regulations for human research. The study had the approval of the Ethics Commission for Research with Animals and Humans (CEEAH) of the University Autònoma de Barcelona, Spain.

2.4 Analysis

We used EEGLAB (Swartz Center for Computational Neuroscience, UC San Diego) (Delorme and Makeig, 2004) open-source software (version 15.3) running on MATLAB R2013a (The Mathworks Inc.) under MacOS version 10.9.5 (Apple Inc.), for the EEG analysis. For rejecting bad channels, artifacts, and wrong recordings with continued data with visible movement artifacts, we visually inspected our recorded data and also used the ADJUST plug-in for EEGLAB (Mognon et al., 2011). We used the DIPFIT plug-in for EEGLAB to locate dipoles. We analyzed viewers' eyeblinks using Brainstorm (Neuroimage, USC) (Tadel et al., 2011) also running on MATLAB R2013a. We applied Brainstorm's filers for detecting eyeblinks to the EOG signal, following Tadel and colleagues (Tadel et al., 2015). The results were contrasted manually with the blinks of the recordings.

3 Results

3.1 Decrease of Eyeblinks After the Cuts

We compared the eyeblink rate (blinks per minute) of participants ($N = 36$) from the cut to 1 s after it with their eyeblink rate, while they were watching the rest of the movie. Each participant was exposed to 112 cuts, so we analyzed responses to 4032 cuts. We found significant differences between the eyeblink rate 1 s after the cut ($11.074\,\text{min}^{-1} \pm 7.659$) and the rate during the rest of the stimulus ($12.328\,\text{min}^{-1} \pm 7.609$), $t(35) = -2.719$, $p = 0.01$, Student's paired t-test. According to our results, cuts decrease viewers' eyeblink rate during the 1 s after them. We also found significant statistical differences between those conditions when viewers watched the Hollywood-style movie with inserted cuts ($t(35) = -2.513$, $p = 0.017$, student's paired t-test). However, no significant differences were found when watching the MTV-style movie with inserted cuts ($t(35) = -1.482$, $p = 0.147$, student's paired t-test).

3.2 Spread of Potential from the Occipital to the Frontal Area

We computed ERPs associated to cuts within a time window of 500 ms before the cut and 1000 ms after the cut. We found that as the time after the cut progresses, there is a spread of potential from the occipital area to the frontal area, see Fig. 1. According to our results, this process is engaged after each cut is perceived in a media content. It is coherent with previous studies about visual perception (Hegdé, 2008; Milner and Goodale, 1995); thus, cuts can be understood as tools for resetting visual perception in viewers watching media content.

3.3 Styles of Edition Affect the Perception of the Cuts

We found that the style of edition in which cuts are inserted affects the viewers' processing. The cuts in a Hollywood-style movie result in a higher activation of the medial and (mostly) frontal areas, while cuts in an MTV-style movie produce a higher potential in occipital areas. Those differences appear after the cut and are maintained during the whole second after it, see Fig. 2. We can connect those results with previous studies studying the speed of processing conscious and unconscious stimuli in the human visual system (Thorpe et al., 1996). Cuts in a continuous narrative present a lower impact on the visual cortex, while there is a higher conscious processing. However, cuts in a chaotic and fragmented narrative cause a higher level of potential in the visual area, with a lower impact on conscious processing.

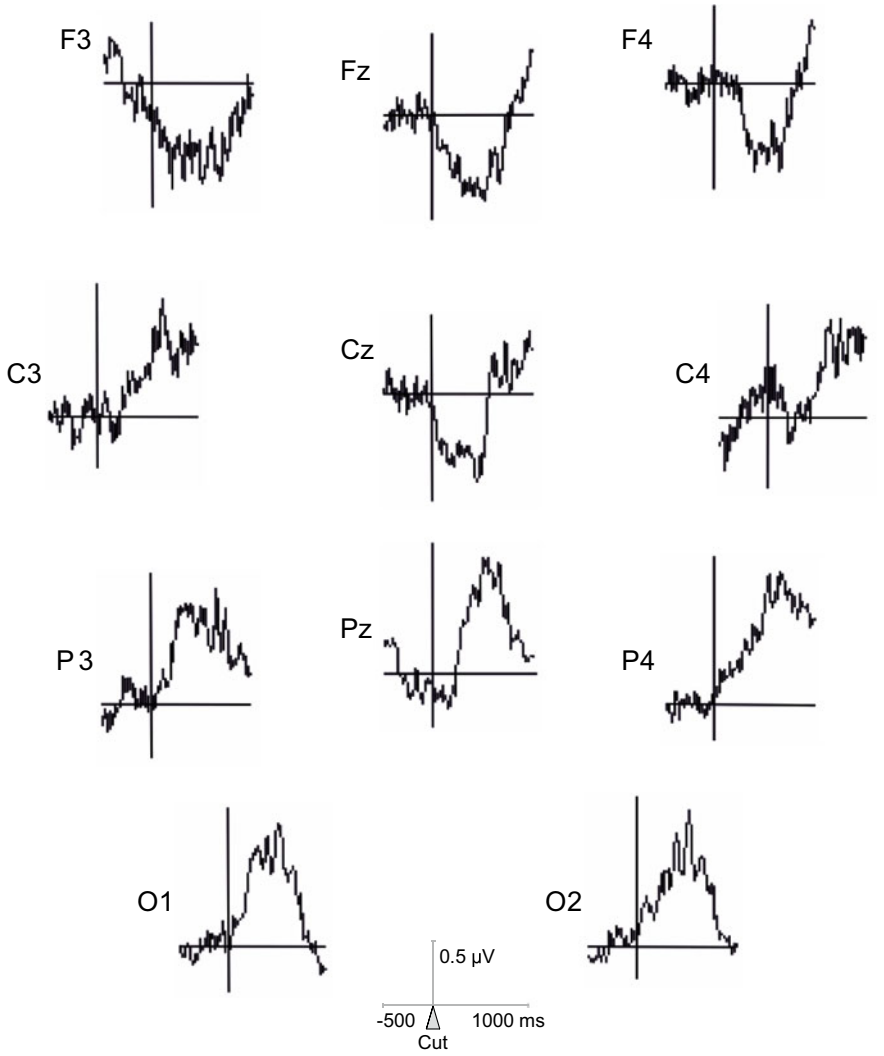

Fig. 1 Average ERPs for occipital, medial, and frontal electrodes after the cut

4 Conclusions

Media creators use cuts to present visual content with specific intentions. Sometimes, they want to clearly show what is happening in the scene; at other times, they want to be deliberately chaotic due to a stylistic or narrative strategy. During the last few decades, this has evolved, with an increase in stylistic fragmentation (Bordwell, 2002). Approaching the same narratives in different formats affects viewers' perception (Andreu-Sánchez et al., 2017b; Nakano and Kitazawa, 2010). We know

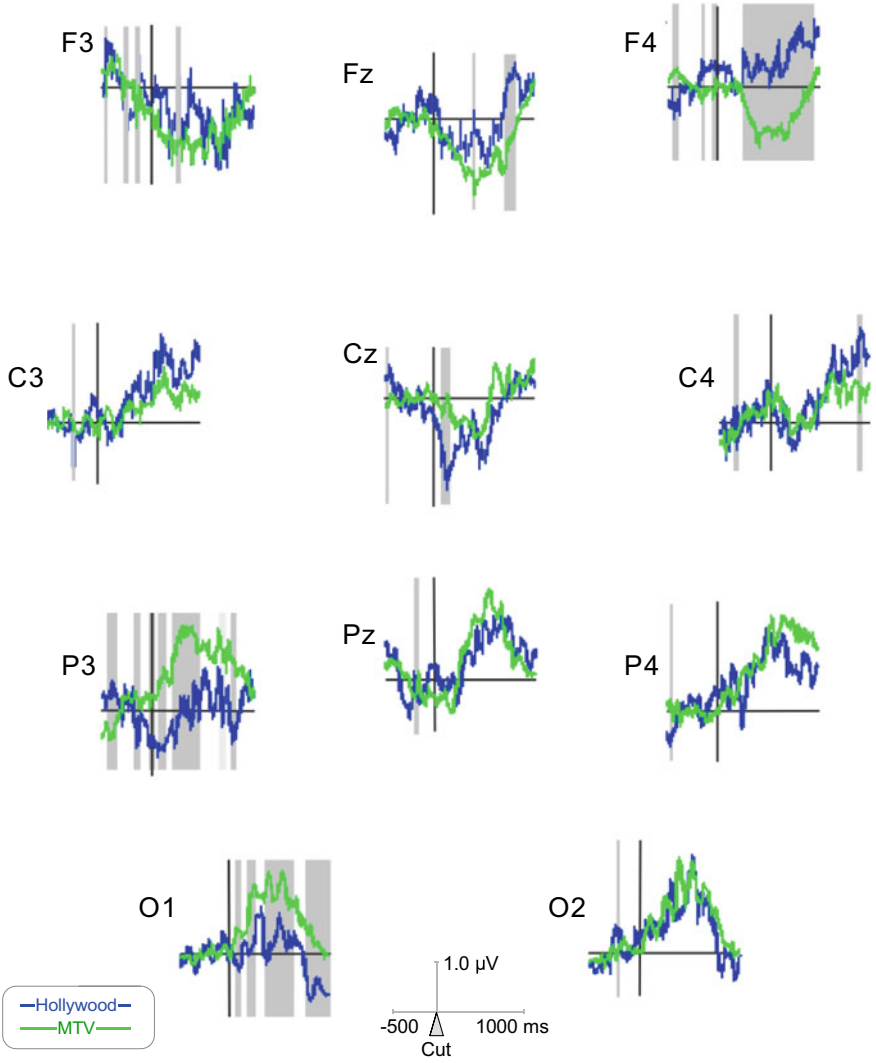

Fig. 2 ERPs for Hollywood-style (classic editing rules) and MTV-style movies (such as video clips), for occipital, medial, and frontal electrodes. Gray shadows indicate statistical differences found between them ($p < 0.05$, t-test)

that narratives in media content affect viewers' attention (Nakano et al., 2009). We also know that the different styles of edition used for presenting narratives affect viewers' eyeblinks (Andreu-Sánchez et al., 2017a). One of the most important elements for creating differences in the styles of edition is the cut. We found that cuts trigger a decrease of eyeblinks in viewers 1 s after them (Andreu-Sánchez et al., 2018). According to our results, this inhibition of the eyeblinks is clear when cuts are inserted in Hollywood-style movies, but is not so clear for cuts in an MTV-style movie. The reason could be related to the average shot length (ASL) in each case. In the Hollywood-style movie, we used an ASL of 5.9 s (a total amount of 33 shots presented in a movie of 198 s), while in the MTV-style stimulus, the ASL was 2.4 s (79 shots presented in a movie of 198 s). So, since the cuts in the MTV-style movie do not clearly decrease viewers' eyeblinks during the following second after them, we suggest that this is because there are so many cuts that viewers tend to avoid blinking while watching the whole movie (Andreu-Sánchez et al., 2017a).

Cuts are not always perceived by viewers (Smith and Henderson, 2008), and yet, we found that they produce a specific spread of brain activity from the occipital area throughout the visual cortex, to the prefrontal and frontal area, where higher processes are managed. Our results are coherent with previous studies on early discrimination of visual stimuli (Thorpe et al., 1996). The most interesting part of this is that whenever media creators present a different shot in their audiovisual works, they are triggering the reset of this well-known process of visual perception for any visual stimulus change. However, this process is different depending on the style of edition in which cuts are being perceived. We found that cuts in continuous, classical style editing have a higher impact in prefrontal and frontal areas, while cuts in chaotic-style editing have more impact in the occipital area. These results would be coherent with the previous comparison of related with unrelated cuts (Francuz and Zabielska-Mendyk, 2013). According to that, related cuts have a higher impact in the prefrontal area, while unrelated cuts have theirs in the occipital area. We suggest that the clear presentation of related content activates areas of higher processing. The unclear presentation of unrelated content has a high impact on the visual cortex, but for some unknown reason, that impact does not flow to higher-processing areas. In future research, it would be very interesting to contrast the discontinuity caused by the cuts with the perceptive segmentation of discrete real events and selective attention (Zacks et al., 2007).

Since the spontaneous eyeblink rate is a predictor of dopamine-related cognitive function (Iwaki et al., 2019; Jongkees and Colzato, 2016), it would be of interest for future investigations to understand how dopamine concentration can be different in viewers based on the style of edition, and how that can have an impact in visual processing (Silkis, 2007).

The results from this investigation can also be applied in the communication area to teach media workers how they can manage viewers' attention by using cuts and style of edition. We understand that this knowledge is highly valuable for media professionals and can have a great impact on future audiovisual creation.

References

Andreu-Sánchez, C., Martín-Pascual, M. Á., Gruart, A., & Delgado-García, J. M. (2017a). Eyeblink rate watching classical Hollywood and post-classical MTV editing styles, in media and non-media professionals. *Science Reports*, *7*, 43267.

Andreu-Sánchez, C., Martín-Pascual, M. Á., Gruart, A., & Delgado-García, J. M. (2017b). Looking at reality versus watching screens: Media professionalization effects on the spontaneous eyeblink rate. *PLoS One*, *12*(5), e0176030.

Andreu-Sánchez, C., Martín-Pascual, M. Á., Gruart, A., & Delgado-García, J. M. (2018). Chaotic and fast audiovisuals increase attentional scope but decrease conscious processing. *Neuroscience*, *394*, 83–97.

Bordwell, D. (2002). Intensified continuity visual style in contemporary American film. *Film Quarterly*, *55*(3), 16–28.

Carroll, J. M., & Bever, T. G. (1976). Segmentation in cinema perception. *Science*, *191*(4231), 1053–1055.

Cohen-Séat, G., Gastaut, H., & Bert, J. (1954). Modification de l'EEG pendant la projection cinématographique. *Revue Internationale de Filmologie*, *5*(16), 20.

Cruz, A. A. V., Garcia, D. M., Pinto, C. T., & Cechetti, S. P. (2011). Spontaneous eyeblink activity. *The Ocular Surface*, *9*(1), 29–41.

Cutting, J. E. (2016). Narrative theory and the dynamics of popular movies. *Psychonomic Bulletin & Review*, *23*(6), 1713–1743.

Cutting, J. E., Brunick, K. L., & Delong, J. E. (2011). The changing poetics of the dissolve in Hollywood film. *Empirical Studies of the Arts*, *29*(2), 149–169.

Delorme, A., & Makeig, S. (2004). EEGLAB: An open source toolbox for analysis of single-trial EEG dynamics including independent component analysis. *Journal of Neuroscience Methods*, *134*(1), 9–21.

Eisenstein, S. (1977). *Film form: Essays in film theory*. Harcourt Inc.

Eisenstein, S. (1988). *Selected works, Vol. 2: Towards a theory of montage*. British Film Institute.

Francuz, P., & Zabielska-Mendyk, E. (2013). Does the brain differentiate between related and unrelated cuts when processing audiovisual messages? An ERP study. *Media Psychology*, *16*(4), 461–475.

Gastaut, H. J., & Bert, J. (1954). EEG changes during cinematographic presentation: Moving picture activation of the EEG. *Electroencephalography and Clinical Neurophysiology*, *6*(3), 433–444.

Geiger, S., & Reeves, B. (1993). The effects of scene changes and semantic relatedness on attention to television. *Communication Research*, *20*(2), 155–175.

Germeys, F., & d'Ydewalle, G. (2007). The psychology of film: Perceiving beyond the cut. *Psychological Research*, *71*(4), 458–466.

Gubern, R. (1973). *Historia del cine* (Vol. 1). Ediciones Danae.

Gunning, T. (1994). *DW Griffith and the origins of American narrative film: The early years at Biograph*. University of Illinois Press.

Hegdé, J. (2008). Time course of visual perception: Coarse-to-fine processing and beyond. *Progress in Neurobiology*, *84*(4), 405–439.

Iwaki, H., Sogo, H., Morita, H., Nishikawa, N., Ando, R., Miyaue, N., et al. (2019). Using spontaneous eye-blink rates to predict the motor status of patients with Parkinson's disease. *Internal Medicine*, *58*(10), 1417–1421.

Jongkees, B. J., & Colzato, L. S. (2016). Spontaneous eye blink rate as predictor of dopamine-related cognitive function—A review. *Neuroscience & Biobehavioral Reviews*, *71*, 58–82.

Kuleshov, L. V. (1974). *Kuleshov on film: Writings by Lev Kuleshov*. University of California Press.

Lang, A., Geiger, S., Strickwerda, M., & Sumner, J. (1993). The effects of related and unrelated cuts on television viewers' attention, processing capacity, and memory. *Communication Research*, *20*(1), 4–29.

Magliano, J. P., & Zacks, J. M. (2011). The impact of continuity editing in narrative film on event segmentation. *Cognitive Science*, *35*(8), 1489–1517.

Martín-Pascual, M. Á., Andreu-Sánchez, C., Delgado-García, J. M., & Gruart, A. (2018). Using electroencephalography measurements and high-quality video recording for analyzing visual perception of media content. *Journal of Visualized Experiments* (135).

Milner, A., & Goodale, M. (1995). *The visual brain in action*. Oxford University Press.

Mognon, A., Jovicich, J., Bruzzone, L., & Buiatti, M. (2011). ADJUST: An automatic EEG artifact detector based on the joint use of spatial and temporal features. *Psychophysiology*, *48*(2), 229–240.

Münsterberg, H. (1916). *The photoplay: A psychological study*. D. Appleton and Co.

Nakano, T., & Kitazawa, S. (2010). Eyeblink entrainment at breakpoints of speech. *Experimental Brain Research*, *205*(4), 577–581.

Nakano, T., Yamamoto, Y., Kitajo, K., Takahashi, T., & Kitazawa, S. (2009). Synchronization of spontaneous eyeblinks while viewing video stories. *Proceedings of the Royal Society B: Biological Sciences*, *276*(1673), 3635–3644.

Pudovkin, V. I. (2013). *Film technique and film acting. The cinema writings of V.I. Pudovkin*. Read Books Ltd.

Reeves, B., Thorson, E., Rothschild, M. L., McDonald, D., Hirsch, J., & Goldstein, R. (1985). Attention to television: Intrastimulus effects of movement and scene changes on alpha variation over time. *International Journal of Neuroscience*, *27*(3–4), 241–255.

Shultz, S., Klin, A., & Jones, W. (2011). Inhibition of eye blinking reveals subjective perceptions of stimulus salience. *Proceedings of the National Academy of Sciences of the United States of America*, *108*(52), 21270–21275.

Silkis, I. (2007). A hypothetical role of cortico-basal ganglia-thalamocortical loops in visual processing. *Biosystems*, *89*(1–3), 227–235.

Smith, T. J., & Henderson, J. M. (2008). Edit blindness: The relationship between attention and global change blindness in dynamic scenes. *Journal of Eye Movement Research*, *2*(2), 1–17.

Tadel, A., Bock, E., Mosher, J., & Baillet, S. (2015). Detect and remove artifacts.

Tadel, F., Baillet, S., Mosher, J. C., Pantazis, D., & Leahy, R. M. (2011). Brainstorm: A user-friendly application for MEG/EEG analysis. *Computational Intelligence and Neuroscience*, *2011*, 879716.

Thorpe, S., Fize, D., & Marlot, C. (1996). Speed of processing in the human visual system. *Nature*, *381*(6582), 520–522.

Wiseman, R. J., & Nakano, T. (2016). Blink and you'll miss it: The role of blinking in the perception of magic tricks. *PeerJ*, *4*, e1873.

Zacks, J. M., Speer, N. K., Swallow, K. M., Braver, T. S., & Reynolds, J. R. (2007). Event perception: A mind–brain perspective. *Psychological Bulletin*, *133*(2), 273–293.

Zheng, B., Jiang, X., Tien, G., Meneghetti, A., Panton, O. N. M., & Atkins, M. S. (2012). Workload assessment of surgeons: Correlation between NASA TLX and blinks. *Surgical Endoscopy*, *26*(10), 2746–2750.

A Possible Mechanism of Learning-Evoked Reorganization of Receptive Fields in the Primary Auditory Cortex: A Role of the Basal Ganglia, Prefrontal Cortex, Hippocampus, Acetylcholine and Dopamine

Isabella G. Silkis

Abstract A hypothetical mechanism is advanced that determines a role of acetylcholine and dopamine in the reorganization of receptive fields (RFs) in the primary auditory cortical area A1 evoked by learning with a pure tone with a frequency F. This mechanism is based on dopamine- and acetylcholine-dependent long-term changes in the efficacy of neural connections in the auditory and limbic cortico-basal ganglia-thalamocortical loops. Dopamine, released in response to the tone F and reinforcing signal acting at D1 receptors on striatonigral cells of the dorsal striatum promotes the induction of LTP in the efficacy of inputs from A1 neurons with preferred tuning frequency (PTF) equal or close to F. As a result, basal ganglia (BG) output more strongly disinhibits neurons in the MGB with the PTF close to F, thus promoting a rise in the activity of tonotopically connected MGB and A1 neurons. Simultaneously, LTD is induced at other corticostriatal inputs, leading to inhibition of MGB and A1 neurons with PTF different from F. Voluntary attention promotes RFs narrowing due to a rise in the prefrontal cortex activity and its excitatory input to A1, as well as by dopamine-dependent disinhibition of MGB neurons by the limbic part of the BG that includes the nucleus accumbens. Hippocampus is involved in auditory processing due to its connections with the cortex and projections to the nucleus accumbens. Acetylcholine released by the basal forebrain and pedunculopontine nucleus (that is also under inhibitory control from the BG) modulates RFs due to activity reorganization in the whole network. The complex effect of acetylcholine is determined by location of muscarinic and nicotinic receptors at both pyramidal cell and GABAergic interneurons. Therefore, it depends on ACh concentration and strength of inhibition.

I. G. Silkis (✉)
Institute of Higher nervous Activity & Neurophysiology Russian Academy of Sciences, Moscow, Russia

A. Lintas et al. (eds.), *Advances in Cognitive Neurodynamics (VII)*, Advances in Cognitive Neurodynamics,
https://doi.org/10.1007/978-981-16-0317-4_15

1 Introduction

It is known that the receptive fields (RFs) of neurons in the primary auditory cortex A1 are modified during learning. Changes are highly specific, selective, quickly formed, and can be maintained during long time, i.e., possess the characteristics of associative memory (Weinberger, 2007). The cholinergic innervation from the basal forebrain has a significant effect on the learning-evoked plastic reorganization in the RFs of A1 neurons. These modifications are also highly specific and have characteristics of associative memory (Weinberger, 2007). The increase in acetylcholine (ACh) release in the neocortex has the same effect on the RF changes during learning as dopamine. Our previous analysis of possible mechanisms for processing of pure tones indicated that dopamine-dependent activity reorganization in the basal ganglia (BG) are involved in the creation of RFs of tonotopically connected neurons in the A1, the ventral part of the medial geniculate body (MGBv), and the central part of the inferior colliculus (ICc), since neurons of the BG output nuclei inhibit neurons of the MGBv and ICc (Silkis, 2015). Only a few models consider that the thalamus is under inhibitory control from the BG and that this inhibition is important for the information processing of ascending sensory information (Cabessa & Villa, 2018). In this paper, we introduce our hypothesis that during learning, a modulation of the cortico-striatal inputs by dopamine, which is released in response to reinforcement and a conditioning signal (CS), a pure tone with the frequency F, as well as modulation of neuronal activity in the neocortex, hippocampus and thalamus by Ach underlie changes in RFs of neurons in the A1 and MGBv.

2 A Hypothetical Mechanism for the Learning-Evoked Changes in the RFs of the A1 Neurons

2.1 Functional Organization of the Cortico-BG-thalamocortical Loops Involved in the Processing of Pure Tones

The information about pure tones entries into the A1 via the ICc and MGBv (bottom-up pathway), and there is a top-down pathway to A1 from the prefrontal cortex (PFC) (Fig. 1). Neurons from the A1 project back into the MGBv and also into the dorsal striatum, where they excite striatonigral (S-N) cells, giving rise to the direct disinhibitory pathway through the BG. S-N cells inhibit neurons of the ventral part of output BG nucleus, the substantia nigra pars reticulata (vSNr). Neurons of the ventral striatum, the nucleus accumbens (NAc) receive excitation from the PFC and contain both S-N cells and striatopallidal (S-P) cells. S-N cells inhibit the ventro-medial part

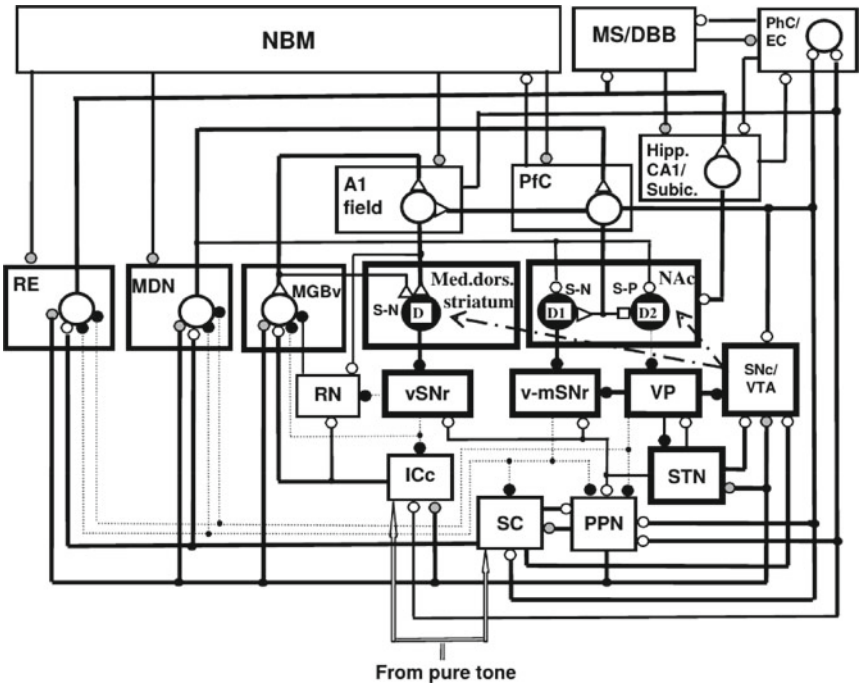

Fig. 1 The scheme of neuronal loops providing pure tone processing, shaping RFs, and their modulation by dopamine and acetylcholine. Cortical areas: A1, PFC, PhC, EC. Thalamic nuclei: MGBv, MDN, RE, reticular, RN. Basal ganglia nuclei: medio-dorsal striatum, NAc, vSNr, m-vSNr, VP, STN. Dopaminergic structures: SNc, VTA. Cholinergic structures: NBM, MS/DBB, PPN. Large light and dark circles, excitatory and inhibitory neurons, respectively; small light, dark and shaded circles, excitatory, inhibitory, and cholinergic inputs, respectively; small triangles and squares, potentiated and depressed excitatory inputs, respectively; arrows, dopaminergic inputs; thick and dashed lines, strong and weak inputs, respectively. Other abbreviations are in the text

of the SNr (v-mSNr), whereas S-P cells, giving rise to the indirect inhibitory pathway through the BG inhibit the ventral pallidum (VP). The output BG nuclei, SNr and VP tonically inhibit neurons in thalamic nuclei (Fig. 1). It is important to note that cortico-BG-thalamocortical (C-B-Th-C) loops are closed and topically organized.

2.2 A Possible Mechanism for the Participation of the BG and Dopamine in Learning-Evoked Plastic Reorganizations of the RFs of the A1 Neurons

Sound stimuli evoke the short-latency responses of dopaminergic cells in the substantia nigra pars compacta (SNc) and ventral tegmental area (VTA) since there are

inputs from the superior colliculus (SC), pedunculopontine nucleus (PPN), PFC, and subthalamic nucleus (STN) (Fig. 1). Dopamine, acting at D1 receptors on S-N cells, promotes induction of LTP of the efficacy of strong cortico-striatal inputs, and LTD of weak inputs (Silkis, 2001). The strong inputs are formed by those A1 neurons whose preferred tuning frequency (PTF) coincides or is close to F, so they are initially strongly activated by the stimulus, and their excitation of S-N cells allows opening postsynaptic NMDA channels. The inputs to other S-N cells from weakly responsive cortical neurons whose PTF is differed from F are weak, and therefore do not allow opening the NMDA channels (Silkis, 2015). Due to the topical organization of A1-BG-MGBv-A1 loops the dopamine-dependent reorganization of activity in the BG should lead to a disinhibitory action from the SNr on activity of MGBv neurons whose PTF is close to F. At the same time, the inhibition of the activity of MGBv neurons with PTF different from F will be enhanced. As a result, the RFs of tonotopically connected MGBv and A1 neurons will tend to be narrower. Since the neurons of the lateral part of the SN are projected into the ICc, the disinhibitory effect on some of ICc neurons from the BG can enhance the activity of neurons at the low level of auditory processing.

A class of long-range GABAergic cells (not shown in Fig. 1 to simplify) has recently been discovered in the auditory cortex and PFC. They send projections to spiny cells of the dorsal striatum and NAc, and are involved in learning (Lee et al., 2014; Rock et al., 2016). In the NAc, the inhibitory terminals were observed on both S-N and S-P cells. We assume that in the presence of such inhibition, the NMDA channels will be opened on a small number of spiny cells while LTD will be induced at cortical inputs to many other spiny cells. As a result, many thalamic cells will be inhibited, and therefore RFs will be narrower.

Since there are reciprocal connections between the MGBv and A1, the output signals from the BG can influence the efficacy of connections between all elements of talamo-cortical loops. We have earlier shown in in vivo experiments that microstimulation of a group of neurons with PTF F_1 leads to a shift towards to F the PTF of neurons in the adjacent locus of the A1 and in the tonotopically connected MGBv locus with initial PTF F_2. At the same time, we found long-term modification (LTP and LTD) of monosynaptic connections between elements of the thalamo-cortical loop (Sil'kis, 1996).

2.3 A Possible Mechanisms for the Participation of Attention in Plastic Reorganizations of RFs of the A1 Neurons

It is known that learning requires voluntary attention. We proposed that voluntary attention is a part of sensory processing and is triggered by activation of the PFC and dopamine release (Silkis, 2007). The effect of the PFC on the A1 neurons is sufficiently effective. Optogenetic stimulation of the PFC resulted in short-latency excitation of the A1 neurons, and combined stimulation of the PFC with a sound

led to an improvement of the representation of this sound in the A1 as well as sound discrimination (Winkowski et al., 2018). Since attention is normally directed to reinforced CS with the frequency F, we assume that additional PFC action at A1 neurons with the PTF F will cause an additional rise in activity of these neurons. It follows from proposed mechanism that this must be manifested in the better narrowed and intensive RFs of A1 neurons.

2.4 Possible Mechanisms for Participation of the Hippocampus in Plastic Reorganizations of RFs of the A1 Neurons

The hippocampus and adjacent parahippocampal cortex (PHC), that includes the entorhinal cortex (EC) and connects hippocampus with the sensory cortical areas are considered as a part of the brain involved in the perception. Memory of information about individual tones correlates with a rise in the interaction between the hippocampus and the inferior frontal gyrus (Kumar et al., 2016). Removing the medial temporal gyrus led to impaired auditory memory (Fritz et al., 2016). Activity in the hippocampus depends on both the parameters of sound and the source of its location. After prolonged tone presentation, the activity of the place cells in the hippocampus were changed (Goble et al., 2009). It is believed that long-range connections between the auditory cortex, hippocampus, and frontal cortex may underlie the maintenance of tone mapping in the working memory. Closing the loop connecting the hippocampus with the BG is carried out through the midline thalamic nucleus reuniens (RE) that innervates the hippocampal CA1 field (McKenna & Vertes, 2004). The BG influence hippocampal activity since RE is under inhibitory control from the SNr.

In turn, the hippocampus influencing the functioning of the limbic part of the BG since it facilitates the passage of signals from the PFC through the NAc. Normally the spiny cells of the NAc are in the low state of membrane polarization, and the excitation from the PFC is insufficient to spike generation by NAc cells (O'Donnell & Grace, 1995). However, simultaneous signal arriving from the hippocampus and the PFC brings the spiny cells to discharges. Subsequent disinhibition of the RE and mediodorsal nucleus (MDN) by the BG must lead to an increase in the activity of some hippocampal and PFC neurons.

3 The Effect of ACh on Changes in RFs of the A1 Neurons During Learning

The A1 and PFC neurons, as well as the midline thalamic nuclei receive cholinergic innervation from the nucleus basalis of Meynert (NBM). The hippocampal neurons are influenced by cholinergic cells of the medial septum and diagonal band of Broca

(MS/DBB). Sound stimuli statistically significant increased ACh release in both the hippocampus and neocortex (Inglis & Fibiger, 1995). Cholinergic terminals from the PPN innervate the ICc and MGB (Schofield, 2010). Latencies of the PPN neuron responses to sound stimuli is less than 80 ms (Vitale et al., 2019). Due to the direct projections from the PFC to NBM, there is a top-down effect on the Ach release (Sarter et al., 2005). The A1 neurons influence ACh release due to top-down projections to the PPN (Fig. 1).

ACh exerts a complex influence on the RFs of pyramidal neurons in the A1 via muscarinic and nicotinic receptors of various types that are placed on pyramidal cells and inhibitory interneurons in all structures involved in sound processing. According to the unified modulation rules that we formulated earlier (Sil'kis, 2003), the activation of postsynaptic nicotinic receptors and muscarinic M1/M5 receptors should promote the induction of LTP of efficacy of excitatory inputs to a neuron, whereas activation of M2–M4 receptors should promote the induction of LTD. The resulting effect must depend on the strength of the inhibitory input to a pyramidal target cell, as well as on the affinity of the cholinoreceptors, and therefore on the ACh concentration.

During associative Pavlovian learning with a pure tone as the CS, ACh concentration in the A1 consistently increases with the progress of learning. A conditioned stimulation of the NBM and a tone with a frequency F led to changes in RFs of the A1 neurons similar to those evoked by classical learning. In these experiments, RFs of the A1 neurons shifted towards the conditioned tone (Froemke et al., 2007), and the neural representation of this tone in the A1 was expanded (Weinberger, 2007). The PTF of neurons in the MGBv and ICc also shifted toward the frequency of the conditioned tone, the threshold of responses to this tone decreased, and the number of spikes in the response increased (Zhang et al., 2005; Zhang & Yan, 2008). Since these effects disappeared after inactivation of the cortex, it can be assumed that cortico-fugal influence makes a significant contribution to specific rearrangements of neuronal responses in the MGBv and ICc (Villa et al., 1991). The conditioned stimulation of the PPN and a tone with a frequency F also led to a significant shift of the PTF of neurons in the auditory cortex towards the frequency F (Luo & Yan, 2013). Application of muscarinic receptor antagonists has prevented all these effects. Systemic administration of nicotine also increased the responses of A1 neurons with determined PTF and narrowed their RFs, and this effect was obtained at the level of the IC and thalamus (Askew et al., 2017).

However, opposite effects were also observed. In some experiments, the application of ACh or activation of muscarinic receptors promoted a decrease in the responses to the tone matching PTF, and an increase in the responses to tones of different frequencies (Ashe et al., 1989; McKenna et al., 1989). From the point of view of the proposed mechanism, in mentioned experiments, the potentiating effect of ACh on the inhibitory cortical interneurons via M1 receptors prevailed and inhibition was so strong that it masked the potentiating effect of activation of M1 receptor on pyramidal cells. Presumably, the ACh concentration was sufficiently high to affect these receptors.

4 Conclusion

The proposed mechanism for the functioning of C-BG-Th-C loops differs from conventional models in which only strong inputs to the striatum are taken into account by default, and transmission via the direct and indirect pathways through the BG leads to opposite behavioral effects. However, it is inconsistent with the data that S-N and S-P cells are activated by the same cortical or thalamic neuron (Doig et al., 2010), and then the BG through the SNr and thalamus affect the same neocortical neuron. In known models of sensory processing, the RF shaping is explained by plastic reorganizations in the efficacy of connections between neurons in the thalamo-cortical loop, and by the presence of lateral inhibition in the neocortex. It is ignored that the thalamus is under inhibitory control from the BG, and it is unlikely that lateral inhibition can provide any input-specific effect due to the small number of inhibitory interneurons (a few percent) and the large convergence and divergence of their connections. In our model, signal transduction through both BG pathways synergistically lead to disinhibition of one group of connected thalamic and cortical cells, and simultaneous inhibition of other groups (Silkis, 2013). Shaping RFs is naturally performed due to the opposite sign of modification of the efficacy of strong and weak cortico-striatal inputs.

The proposed mechanism of learning-evoked reorganization of RFs in the primary auditory cortex determines the role of the BG, PFC, and hippocampus in pure tone processing. This is also in agreement with the role of C-BG-Th-C loops in controlling the complexity of processing ascending sensory information (Cabessa & Villa, 2014, 2018). Our new model also points out the significant role of CS-evoked dopamine release in shaping the RFs as well as modulatory effect of ACh on RFs of A1 neurons. The understanding mechanism of the effect of these neuromodulators on auditory processing can help in alleviating hearing impairment in some neurological diseases. For example, it was shown that nerve growth factor (NGF)-treatment increased following parameters: choline acetyltransferase activity in the septal area, functional cortico-cortical interactions in the short frequency range, the mean firing rate of MGB neurons, and interactions between pairs of distant MGB neurons (Villa et al., 1996, 2000). If taken into account that observed high MGB activity must promote firing of S-N cells and subsequent disinhibition of thalamic neurons via the BG, and that increased neuronal interactions may reflect LTP in the efficacy of cortico-cortical and thalamo-thalamic connections it is reasonable to assume that NGF has significant potential for the improvement of auditory processing and memory in patients with Alzheimer disease that is characterized by deficiency of ACh.

Acknowledgements This work is supported by the Russian Scientific Foundation, grant number 16-15-10403p.

References

Ashe, J. H., McKenna, T. M., & Weinberger, N. M. (1989). Cholinergic modulation of frequency receptive fields in auditory cortex: II. Frequency-specific effects of anticholinesterases provide evidence for a modulatory action of endogenous ACh. *Synapse*, *4*(1), 44–54.

Askew, C., Intskirveli, I., & Metherate, R. (2017). Systemic nicotine increases gain and narrows receptive fields in A1 via integrated cortical and subcortical actions. *eNeuro*, *4*(3), ENEURO.0192-17.2017.

Cabessa, J., & Villa, A. E. P. (2014). An attractor-based complexity measurement for Boolean recurrent neural networks. *PLoS One*, *9*(4), e94204.

Cabessa, J., & Villa, A. E. P. (2018). Attractor dynamics of a Boolean model of a brain circuit controlled by multiple parameters. *Chaos*, *28*(10), 106318.

Doig, N. M., Moss, J., & Bolam, J. P. (2010). Cortical and thalamic innervation of direct and indirect pathway medium-sized spiny neurons in mouse striatum. *Journal of Neuroscience*, *30*(44), 14610–14618.

Fritz, J. B., Malloy, M., Mishkin, M., & Saunders, R. C. (2016). Monkey's short-term auditory memory nearly abolished by combined removal of the rostral superior temporal gyrus and rhinal cortices. *Brain Research*, *1640*(Pt B), 289–298.

Froemke, R. C., Merzenich, M. M., & Schreiner, C. E. (2007). A synaptic memory trace for cortical receptive field plasticity. *Nature*, *450*(7168), 425–429.

Goble, T. J., Møller, A. R., & Thompson, L. T. (2009). Acute high-intensity sound exposure alters responses of place cells in hippocampus. *Hearing Research*, *253*(1–2), 52–59.

Inglis, F. M., & Fibiger, H. C. (1995). Increases in hippocampal and frontal cortical acetylcholine release associated with presentation of sensory stimuli. *Neuroscience*, *66*(1), 81–86.

Kumar, S., Joseph, S., Gander, P. E., Barascud, N., Halpern, A. R., & Griffiths, T. D. (2016). a brain system for auditory working memory. *Journal of Neuroscience*, *36*(16), 4492–4505.

Lee, A. T., Vogt, D., Rubenstein, J. L., & Sohal, V. S. (2014). A class of GABAergic neurons in the prefrontal cortex sends long-range projections to the nucleus accumbens and elicits acute avoidance behavior. *Journal of Neuroscience*, *34*(35), 11519–11525.

Luo, F., & Yan, J. (2013). Sound-specific plasticity in the primary auditory cortex as induced by the cholinergic pedunculopontine tegmental nucleus. *European Journal of Neuroscience*, *37*(3), 393–399.

McKenna, J. T., & Vertes, R. P. (2004). Afferent projections to nucleus reuniens of the thalamus. *Journal of Comparative Neurology*, *480*(2), 115–142.

McKenna, T. M., Ashe, J. H., & Weinberger, N. M. (1989). Cholinergic modulation of frequency receptive fields in auditory cortex: I. Frequency-specific effects of muscarinic agonists. *Synapse*, *4*(1), 30–43.

O'Donnell, P., & Grace, A. A. (1995). Synaptic interactions among excitatory afferents to nucleus accumbens neurons: Hippocampal gating of prefrontal cortical input. *Journal of Neuroscience*, *15*(5 Pt 1), 3622–3639.

Rock, C., Zurita, H., Wilson, C., & Apicella, A. J. (2016). An inhibitory corticostriatal pathway. *Elife*, *5*, e15890.

Sarter, M., Hasselmo, M. E., Bruno, J. P., & Givens, B. (2005). Unraveling the attentional functions of cortical cholinergic inputs: Interactions between signal-driven and cognitive modulation of signal detection. *Brain Research Reviews*, *48*(1), 98–111.

Schofield, B. R. (2010). Projections from auditory cortex to midbrain cholinergic neurons that project to the inferior colliculus. *Neuroscience*, *166*(1), 231–240.

Silkis, I. (2001). The cortico-basal ganglia-thalamocortical circuit with synaptic plasticity. II. Mechanism of synergistic modulation of thalamic activity via the direct and indirect pathways through the basal ganglia. *Biosystems*, 59(1), 7–14.

Silkis, I. (2007). A hypothetical role of cortico-basal ganglia-thalamocortical loops in visual processing. *Biosystems*, *89*(1–3), 227–235.

Silkis, I. (2015). The role of the basal ganglia in creating receptive fields in the primary auditory cortex and mechanisms of their plasticity. *Uspekhi fiziologicheskikh nauk*, *46*(3), 60–75.

Sil'kis, I. G. (1996). Long-term changes, induced by microstimulation of the neocortex, in the efficiency of excitatory postsynaptic transmission in the thalamocortical networks. *Neuroscience and Behavioral Physiology*, *26*(4), 301–312.

Sil'kis, I. G. (2003). A possible mechanism for the effect of neuromodulators and modifiable inhibition on long-term potentiation and depression of the excitatory inputs to hippocampal principal cells. *Neuroscience and Behavioral Physiology*, *33*(6), 529–541.

Silkis, I. G. (2013). Mechanisms of the influence of dopamine on the functioning of basal ganglia and movement choice (a comparison of models). *Neurochemical Journal*, *7*(4), 270–277.

Villa, A. E. P., Bajo Lorenzana, V. M., & Vantini, G. (1996). Nerve growth factor modulates information processing in the auditory thalamus. *Brain Research Bulletin*, *39*(3), 139–147.

Villa, A. E. P., Rouiller, E. M., Simm, G. M., Zurita, P., de Ribaupierre, Y., & de Ribaupierre, F. (1991). Corticofugal modulation of the information processing in the auditory thalamus of the cat. *Experimental Brain Research*, *86*(3), 506–517.

Villa, A. E. P., Tetko, I. V., Dutoit, P., & Vantini, G. (2000). Non-linear cortico-cortical interactions modulated by cholinergic afferences from the rat basal forebrain. *Biosystems*, *58*(1–3), 219–228.

Vitale, F., Capozzo, A., Mazzone, P., & Scarnati, E. (2019). Neurophysiology of the pedunculopontine tegmental nucleus. *Neurobiology of Disease*, *128*, 19–30.

Weinberger, N. M. (2007). Associative representational plasticity in the auditory cortex: A synthesis of two disciplines. *Learning & Memory*, *14*(1–2), 1–16.

Winkowski, D. E., Nagode, D. A., Donaldson, K. J., Yin, P., Shamma, S. A., Fritz, J. B., et al. (2018). Orbitofrontal cortex neurons respond to sound and activate primary auditory cortex neurons. *Cerebral Cortex*, *28*(3), 868–879.

Zhang, Y., Hakes, J. J., Bonfield, S. P., & Yan, J. (2005). Corticofugal feedback for auditory midbrain plasticity elicited by tones and electrical stimulation of basal forebrain in mice. *European Journal of Neuroscience*, *22*(4), 871–879.

Zhang, Y., & Yan, J. (2008). Corticothalamic feedback for sound-specific plasticity of auditory thalamic neurons elicited by tones paired with basal forebrain stimulation. *Cerebral Cortex*, *18*(7), 1521–1528.

Auditory Processing During Sleep: A Clinical Application in Tinnitus

Marisa Pedemonte

Abstract It is known that changes in neuronal activity occur during the sleep-wake cycle along the entire auditory pathway. Subjective tinnitus is an anomalous auditory perception resulting from dysfunction of neuronal plasticity. A therapeutic strategy using acoustic stimulation with sound mimicking tinnitus during sleep was developed, resulting in decrease in the reported intensity of tinnitus and improvement in the patients' quality of life. Since each stage of sleep has different roles in the memory consolidation process, the impact on the intensity of tinnitus with acoustic stimulation at different stages of sleep was analyzed separately. All patients stimulated at stage N2 (stage with spindles) showed significant decrement in the tinnitus intensity the day after stimulation, while nobody stimulated at the stage N3 (slow wave sleep) showed changes in tinnitus intensity. The results show that brain dynamics associated with N2 sleep stage is likely to be characterized by the possibility of establishing interactions with the auditory processing networks, thus resulting in a reduction of tinnitus intensity. These results are in agreement with other previous results showing more changes in power spectra and coherence in electroencephalographic waves in N2 sleep stage when there is sound stimulation.

1 Introduction

The processing of sensory information is constantly present, during the waking sleep cycle, although with profound modifications. All sensory systems—visual, auditory, vestibular, somesthetic and olfactory—show changes that depend on the functional state of the brain, sleep or waking (Velluti, 1997, 2018). There is agreement that during sleep the processing of new information and its consolidation as memory occurs, being the hippocampus an essential structure for them to be carried out correctly. The main evidence of the functional interactions among the auditory information, the wake-sleep cycle and the hippocampal theta rhythm will be shown.

M. Pedemonte (✉)
School of Medicine, Centro de Medicina del Sueño, CLAEH University, Punta del Este, Uruguay

A. Lintas et al. (eds.), *Advances in Cognitive Neurodynamics (VII)*, Advances in Cognitive Neurodynamics,
https://doi.org/10.1007/978-981-16-0317-4_16

1.1 Background

1.1.1 Auditory Processing During Sleep

Among sensory modalities, audition is particularly important as a telereceptor that remains open during sleep. The auditory input throughout the day is processed and consolidated as a memory during sleep. The Central Nervous System (CNS) continues processing information that enters from the environment, since the auditory system remains as a sentinel during sleep, capable of receiving information, analyzing it, and generating a response. Furthermore, auditory contents are reported in 65% of dreams (Hobson, 1990; McCarley & Hoffman, 1981) and sensory information can be incorporated into them (Bastuji & García-Larrea, 2005). Changes in neuronal activity linked to sleep-wake cycle have been reported along the entire auditory pathway in animals and humans (Issa & Wang, 2008; Pedemonte et al., 1994, 1996; Pedemonte & Velluti, 2005a; Peña et al., 1992, 1999).

Figure 1 shows the percentages of changes of unitary evoked activity at different levels of the auditory pathway on passing from wakefulness (W) to slow wave sleep (SWS) and from SWS to paradoxical sleep (PS). The subcortical nuclei—cochlear nucleus, inferior colliculus, and the lateral superior olive—exhibited a higher percentage of increasing-decreasing firing neurons. Around 50% of the cortical neurons

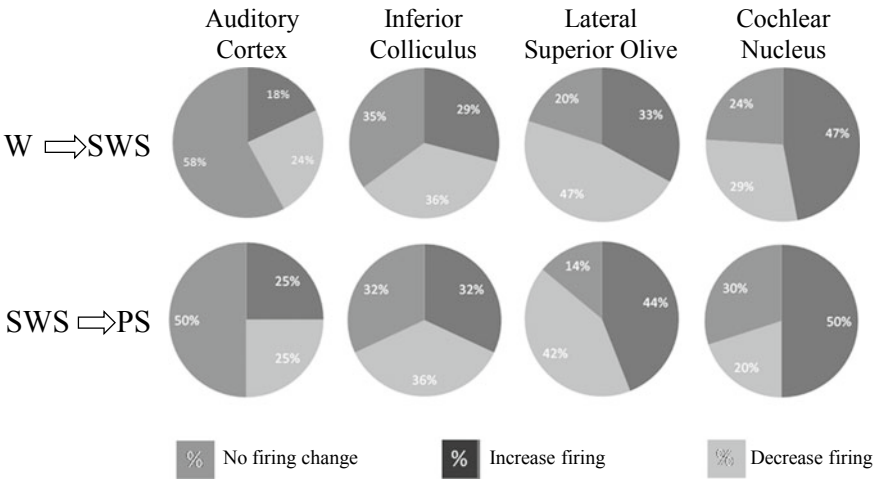

Fig. 1 Sound evoked neuronal activity changes depending on the moment in the sleep-waking cycle analyzed. Different levels of the auditory pathway were explored in guinea pigs, in more than 1500 neuronal discharges. W, wakefulness; SWS, slow wave sleep; PS, paradoxical sleep. Guinea pig percentages unitary evoked activity along the auditory pathway in the sleep-waking cycle. Pie charts show percentages (%) of neuronal firing shifts on passing from wakefulness to slow wave sleep and from slow wave sleep to paradoxical sleep. W, wakefulness; SWS, slow wave sleep; PS, paradoxical sleep. Data from: Peña et al. (1992, 1999), Pedemonte et al. (1994), and Morales-Cobas et al. (1995). Figure modified from Velluti (2005)

responded during wakefulness. No silent auditory neurons were detected on passing to sleep or during sleep in any pathway level.

Also, changes in the receptive field of cortical auditory neurons and in evoked responses were reported (Edeline et al., 2001; Erwin & Buchwald, 1986; Osterhammel et al., 1985). Additionally, hearing loss changes the sleep-wake cycle and the sleep architecture (Cutrera et al., 2000; Pedemonte et al., 1997). Also patients with intracochlear implants display differences in sleep architecture and electroencephalographic signals when the implant is switched on or off (Velluti et al., 2010).

1.1.2 Auditory Processing and Hippocampal Theta Rhythm

Many are the internal and external influences that modulate the auditory sensory input all along the waking-sleep cycle. Taking into account the great sensitivity of cochlear hair cells, it is not difficult to imagine that there are neurons in the auditory pathway that discharge in response to digestive or respiratory noises. We have demonstrated, for example, that 40% of the neurons of antero-ventral cochlear nucleus discharge synchronized with vascular flow (Velluti et al., 1994). However, these responses never end up being a conscious perception. A powerful efferent system constantly controls afferent input, minimizing the influence of disturbances and tuning into the input that requires our attention. Nevertheless, all these unconscious influences are surely at the service of other functions such as maintaining attention levels or collaborating with homeostatic systems.

The ultradian hippocampal theta rhythm, within the wakefulness-sleep circadian cycle, may modulate the sensory neuronal activity. It has been postulated as a temporal organizer for auditory sensory processing (Pedemonte et al., 1996; Pedemonte & Velluti, 2005a). Previously, recordings carried out in primary auditory cortex, showed evoked neuronal firing shifts evoked by electrical stimulation of the hippocampus, indicating that these brain regions are interconnected exhibiting a functional relationship (Pedemonte & Velluti, 1982). Furthermore, it was found hippocampal theta rhythm temporal correlations with motor activities, in spatio-temporal learning, associating distant, discontiguous events, and learning of temporal sequences. A role of the theta rhythm in learning and memory has been proposed from different viewpoints during all behavioral states (Pedemonte & Velluti, 2005b).

The temporal relationship between neuronal discharges and a certain phase of the theta rhythm (phase-locking) was demonstrated in the inferior colliculus and the auditory cortex. This functional correlation appeared and disappeared spontaneously, having been found in all stages of the sleep-wake cycle (Pedemonte et al., 1996; Pedemonte & Velluti, 2005a). Since the hippocampus theta rhythm was related to discontinuous events and sensory changes we began to study the temporal pattern of neuronal discharges when a change in sensory input was generated.

Figure 2 shows an example of auditory unit spontaneous discharge during SWS where the cross-correlograms did not exhibit phase-locking with the hippocampal theta rhythm, however, when the sound stimulation started, the neuron began to fire in close correlation with a particular theta rhythm phase (phase-locked).

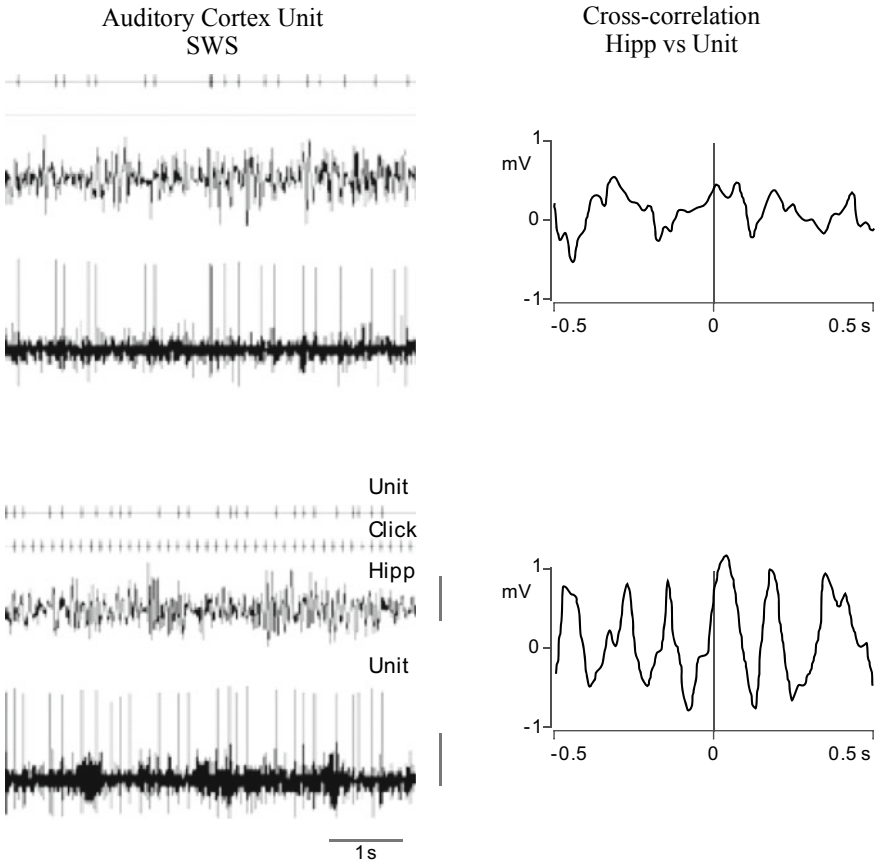

Fig. 2 Relationship between hippocampal theta rhythm and auditory cortical unit during slow wave sleep, in guinea pig. Left column: raw data showing—from top to bottom—digitized units, sound stimuli (clicks), hippocampal field electrogram (Hipp), and auditory cortical unitary discharges. The spontaneous activity is shown at the top and, at the bottom, the activity during sound stimulation (8/s). Right column, cross correlograms between unitary discharges and hippocampal electrogram. SWS, slow wave sleep; Cal: Hipp, 1 mV; unit, 50 μV; modified from Velluti et al. (2000)

This temporal relationship with the hippocampus theta rhythm that appears related to a change in the attention process, by a variation in the sensory input when the animal was habituated, was demonstrated both in wakefulness and during sleep (Liberman et al., 2009). This complex interaction, which would be at the service of the temporary coding of the sensory input, is another demonstration that the information is processed during the sleep.

1.2 Tinnitus, a Misperception

Taking into account everything seen above, we know that we face a sensory system that works with a precise dynamic balance between low threshold receivers with high processing precision and the CNS that generates the moment-by-moment sensory perception. When this subtle functional balance is broken, tinnitus occurs. It is accepted that interactions between altered cochlear inputs and distorted central auditory processing provoke tinnitus. It is now evident that most forms of subjective tinnitus are caused by changes in the function of the central auditory nervous system while these changes are not associated with any detectable anatomical lesion. The subjective tinnitus may be the result of the expression of neural plasticity and the anomalies may develop because of decreased or deprivation input from the ear of sound stimulation, over stimulation, or yet unknown factors. The functional imbalance created in some central neural networks generates the "phantom sensation", so-called because it is a perception created by the CNS without a sound source that causes it. The CNS cannot discern whether this perception is related to a real ambient sound or an internal creation (Jastreboff, 1990).

1.2.1 Tinnitus Treatment with Sound Stimulation During Sleep

Considering all the antecedents that demonstrate that the auditory system continues receiving information during sleep, and this is processed by organizing sensory inputs and consolidating memories, we decided to devise a protocol for the treatment of tinnitus based on sound stimulation applied during sleep. We proposed the sound stimulation with the same characteristics in frequencies and intensity as the tinnitus as a way of reinstalling the normal balance in the central level processing of information, hypothesizing that tinnitus emerges to replace an input deficit. Our results showed in two clinical trials have demonstrated the decrement in the tinnitus intensity and, as a consequence, the quality of life of patients improved (Drexler et al., 2016; Pedemonte et al., 2010).

The results shown in both trials were that the statistically significant decrease in the intensity of tinnitus appears in the first fourteen days, continuing a slow decrease in the following weeks (Fig. 3b). The spontaneous evolution of tinnitus in one week in these patients was to keep its intensity unchanged (Fig. 3a).

The sound stimulation treatment during sleep was performed all during 3 months and the result was an average decrease in the intensity of tinnitus of 14.1 dB SPL, this decrease is perceived by the patient as a reduction of 62% in intensity sound. In addition, the patients' sleep improved both in duration and quality (lower latency to start sleeping and fewer awakenings during the night). The visual analog scale (VAS) was used to evaluate and quantify the degree of general discomfort produced by tinnitus. An overall improvement of 61% of the pre-treatment scores was observed (Fig. 3c).

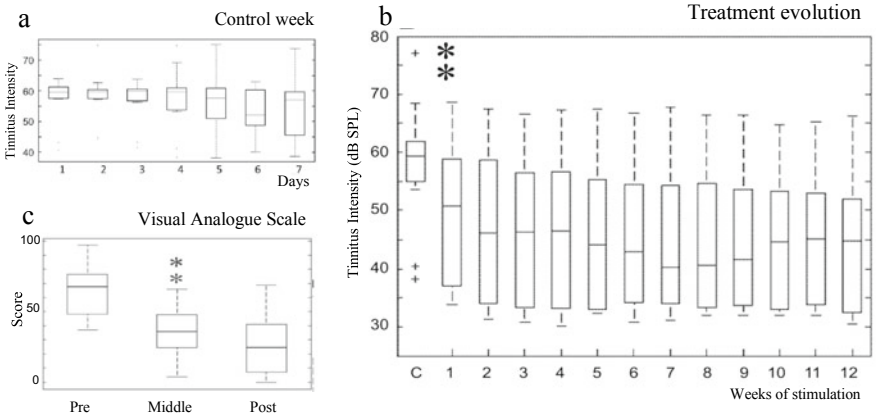

Fig. 3 Evolution of tinnitus intensity through 12 weeks. **a** The box plot shows the averages of tinnitus intensity, performed during 7 days of measurements without stimulation. Each box represents the daily average for 11 patients. No statistically significant changes were observed between any of the tinnitus intensity averages ($p = 0.09$, ANOVA). **b** The box plot shows the average weekly intensities for 11 patients during three months of stimulation during sleep. "C", is the "control", averaging the tinnitus intensity 7 days previous of stimulation. Tinnitus intensity decreased 14.1 dB SPL between "C" and week 12. These results are statistically significant ($p < 0.001$) comparing values between control versus the 1st week and 12th week (Wilcoxon test). **c** Visual analog scale for assessing tinnitus annoyance. This scale was done before starting treatment (pre), in the sixth week (middle), and twelfth week (post). Box plots show the data of all patients; results are statistically significant comparing between (pre) and (middle) values ($p < 0.001$, Wilcoxon test). Modified from Drexler et al. (2016).

Furthermore, the method is in many ways advantageous since sleep provides a long period of time for daily treatment without interfering with the patient daytime activity; and sound stimulation during sleep decreases tinnitus perception, thus improving sleep disorders and emotional disturbs caused by tinnitus (Pedemonte et al., 2010).

2 Mechanisms that Underlie the Decrease in Tinnitus Intensity

Once these beneficial results were obtained for the patients, we began to explore the changes that could appear in brain activity due to this sound stimulation, to begin to understand the mechanisms that could cause this improvement (Pedemonte et al., 2014).

2.1 Changes in the Electroencephalographic Waves During Sound Stimulation

2.1.1 Methods

Ten patients from the second clinical trial were studied with the Polysomnography (PSG) that was carried out with the usual clinical protocol recording ten electroencephalographic channels (EEG, frontals, F3, F4; centrals: C3, C4; parietals: P3, P4; temporal: T3, T4, T5, T6), following the internationally accepted standard denomination, electrocardiogram, electromyogram, eye movements, and oxygen saturation. All EEG recordings were monopolar, recorded from scalp electrodes and separate ear electrodes A1 and A2, with electrodes referenced to linked ear lobes. The sampling frequency was set 256 Hz. The EEG acquisition system is equipped with hardware high-pass filters with cut-off frequency at 0.5 Hz and hardware low-pass filters with cut-off frequency 100 Hz. Also, there is a selectable notch filter to suppress 50/60 Hz power line noise. No digital post-processing filters were applied. One researcher accompanied the patient all night, diagnosing the sleep stages online.

After beginning the night with the usual sound stimulation for tinnitus treatment, sound are stopped after a minimum of one pass through each of the sleep stages, N1, N2, N3, and REM sleep. The rest of the night the patients continue to sleep in silence. Twenty temporal windows (2 s duration each one) were selected in each sleep stage; ten of them during silence and the other ten during sound stimulation. Always data were compared in the same patient. The power spectra and the coherence in electroencephalographic waves recorded by electrodes F3, F4, T3, and T4 were analyzed. We compared the power spectra during noiseless (as a "Control") versus sound stimulation, exploring different electroencephalographic frequency bands (delta: 0.5–3.5 cps; theta: 4–7.5 cps; alpha: 8–12 cps) in the same sleep stage. A comparison between the left and right hemispheres (T3 vs. T4 and F3 vs. F4) was also carried out.

2.1.2 Results

Our studies showed that the sound applied during the night introduced changes both in the power spectra of the different EEG frequency bands and in the analysis of both intra- and interhemispheric coherence.

Analyzing the power spectra of the EEG waves, changes were observed during all stages of sleep, with the predominance of changes in stages N2 and N3 of slow wave sleep (36% in each), being lower in REM sleep (28%). The theta frequency band was the one that showed the most changes (48%), the delta band followed with 36%. The electrodes located in the temporal regions showed greater change than the electrodes located in the frontal regions (61% vs. 39%). All the mentioned changes were statistically significant.

The coherence study, comparing the results during silence with sound stimulation, showed statistically significant changes. These changes were observed in both intra-hemispheric coherence and inter-hemispheric coherence. Each stage of sleep as well as the different frequency bands was analyzed separately.

The inter-hemispheric and intra-hemispheric differences that arose as a consequence of sound stimulation and were absent while there was in silent were considered. However, patients showed differences in coherence in silence. These differences found did not depend on whether the tinnitus was unilateral or bilateral, that is, we must consider that there are many factors that are conditioning coherence, for example hemispheric dominance.

N2 was the sleep stage that presented the most coherence changes when stimulated with sound. Stage N3, with slow waves, presented fewer changes, and the impact of sound being even less in REM sleep (Pedemonte et al., 2014).

2.2 Which Is the Stage of Sleep Responsible for the Improvement of Tinnitus?

Currently, we still cannot say whether the different categories of memories (such as declarative and procedural) are consolidated in different sleep stages. There is research that would support the hypothesis that slow wave sleep would be involved in the generation of declarative memory, while working memory would be processed mainly during REM sleep. However, other authors have suggested that it is the appropriate succession of the different stages of sleep that generates the final product of a new memory and, therefore, learning and change (Cipolli, 2005).

Taking into account that with sound stimulation during sleep our aim was to act on neuronal plasticity, producing a decrease in the tinnitus intensity, the question was whether this auditory learning occurred in one or several stages of sleep.

2.2.1 Methods

Patients were selected with the same inclusion and exclusion criteria than in previous trials. Inclusion criteria were: (1) subjects with subjective idiopathic tinnitus (unilateral or bilateral), (2) with a score in the Tinnitus Handicap Inventory above 17, and (3) experiencing tinnitus for more than 6 months. The exclusion criteria were: (1) secondary tinnitus, (2) subjects wearing hearing aids or having hearing loss with indication of using them, (3) subjects undergoing other treatments for tinnitus, (4) use of hypnotic or other psychoactive drugs, (5) depression (Hamilton scale test above 13) and (6) sleep disorders other than those caused by tinnitus itself, for example, patients with apnea, restless legs syndrome, narcolepsy, and insomnia with other etiology than tinnitus.

Combinations of pure tones, harmonic tone, white noise, and/or bandpass noise were designed for matching each patient's perception by a highly customized sound. This sound was loaded on an iPod Touch and delivered through personalized headphones created for each patient. The stimulus intensity was adjusted to match the intensity of the tinnitus measured right before falling asleep. The device used was the same as in the clinical trials (Drexler et al., 2016).

The stage of sleep in which each patient was stimulated was selected at random; 4 patients were stimulated in the Stage N2, 4 in Stage N3, and 3 in REM sleep. The intensity of tinnitus was measured 10 times during the day prior to stimulation compared with the intensity of tinnitus measured 10 times the day after stimulation, and analyzed statistically (paired Student *t* test). The measurements had at least one hour of separation between them. The criterion for measuring tinnitus intensity was the lowest level of sound stimulation reported as indistinguishable from the tinnitus perception. This measurement was conducted using the stimulation application, which can be adjusted within safe ranges, by the patients themselves [according to the device described by Drexler et al. (2016)].

2.2.2 Results

Figure 4a show that all patients stimulated at stage N2 showed statistically significant decrease in tinnitus intensity the day after stimulation. No patient stimulated in stage N3 reported changes in the intensity of tinnitus (Fig. 4b). Only one patient out of three stimulated during REM sleep reported changes (Fig. 4c).

3 Conclusions

Our results suggest that N2 is the sleep stage in which the interaction between auditory processing and sleep generating networks leads to the strongest reduction in tinnitus intensity by external sound stimulation. These results are consistent with the previous ones that showed more changes in electroencephalographic wave's coherence in N2 sleep stage during sound stimulation. Moreover, sleep spindles, characteristic of N2 sleep stage, are those that change their intra and interhemispheric coherence.

Despite theta rhythm is the one that most increases its power spectrum with the stimulation of sound, with the greatest increases in stage N3, the exclusive stimulation at this stage does not act on the intensity of tinnitus (Pedemonte et al., 2014, 2019). These changes could be contributing to the relearning process by modulating the state of the brain, since this rhythm is involved in the detection of changes.

The hypothesis based on re-learning an auditory perception through a mechanism of nocturnal consolidation provides information on how interacts the auditory input with the CNS in the different stages of sleep. However, this is the beginning of a long way to understand how the interaction between the auditory input and the sleeping brain occurs to achieve change in a phantom perception.

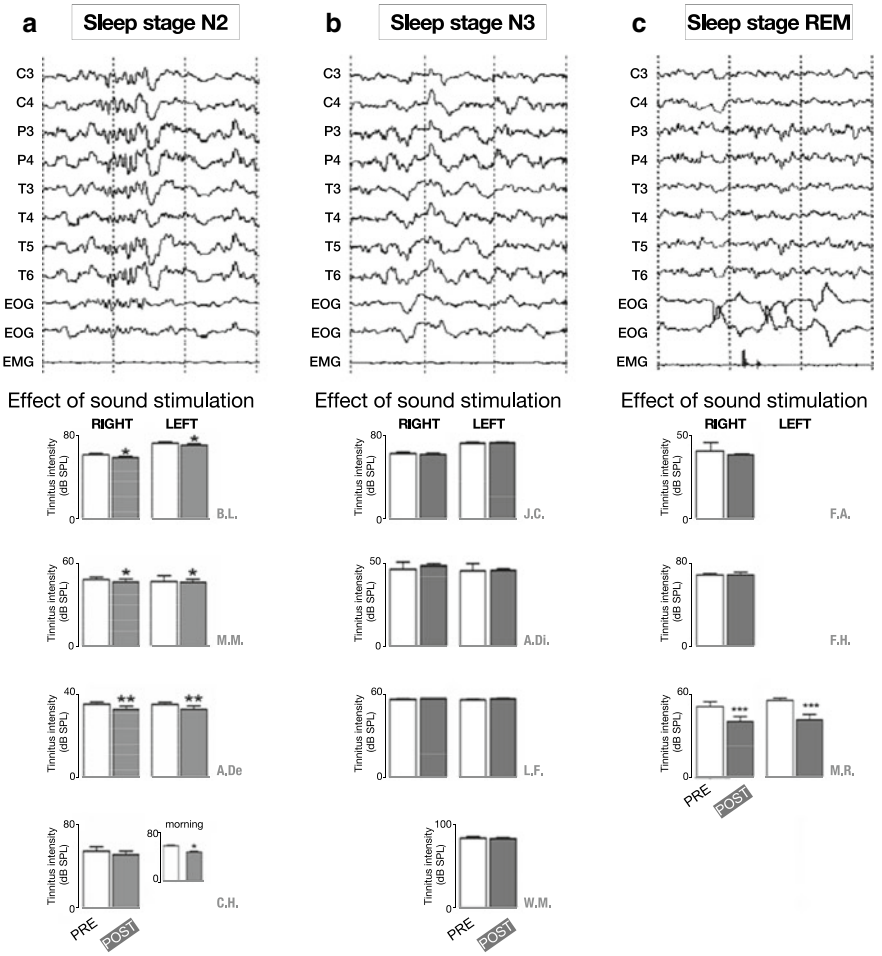

Fig. 4 Patients stimulated with sound mimicking tinnitus in different sleep stages: **a** stage N2; **b** stage N3; **c** stage REM. At the top of each panel, 3 s of polysomnographic raw recorded traces include 8 electroencephalographic channels (EEG centrals: C3, C4; parietal: P3, P4; temporal: T3, T4, T5, T6; eye movements, EOG; and electromyogram, EMG, masseter muscle). The EEG shows in panel **a** the characteristic spindles of stage N2; panel **b** shows slow waves of stage N3; panel **c** shows rapid eye movements (REM stage), muscle atonia with twitches, and electroencephalographic desynchronization. The histograms represent the average and standard deviation of 10 tinnitus intensities before (pre) and after (post) stimulation. Inset (in panel **a**, patient C.H.) represents intensity averages of 5 values in the morning, before and after sound stimulation. Student t test, * $p \leq 0.05$, ** $p \leq 0.01$. In panel **a**, all patients showed significant tinnitus intensity decrement after N2 sound stimulation. In panel **b**, no significant changes were found after N3 sound stimulation. In panel **c**, one out of three showed significant changes after REM sound stimulation. Modified from Pedemonte et al. (2019).

References

Bastuji, H., & García-Larrea, L. (2005). Human auditory information processing during sleep assessed with evoked potentials. In P. L. Parmeggiani & R. A. Velluti (Eds.), *The physiologic nature of sleep* (pp. 509–534). Imperial College Press.

Cipolli, C. (2005). Sleep and memory. In P. L. Parmeggiani & R. A. Velluti, (Eds.), *The physiologic nature of sleep* (pp. 601–629). Imperial College Press.

Cutrera, R., Pedemonte, M., Vanini, G., Goldstein, N., Savorini, D., Cardinali, D. P., et al. (2000). Auditory deprivation modifies biological rhythms in the golden hamster. *Archives Italiennes de Biologie*, *138*(4), 285–293.

Drexler, D., López-Paullier, M., Rodio, S., González, M., Geisinger, D., & Pedemonte, M. (2016). Impact of reduction of tinnitus intensity on patients' quality of life. *International Journal of Audiology*, *55*(1), 11–19.

Edeline, J. M., Dutrieux, G., Manunta, Y., & Hennevin, E. (2001). Diversity of receptive field changes in auditory cortex during natural sleep. *European Journal of Neuroscience*, *14*(11), 1865–1880.

Erwin, R., & Buchwald, J. S. (1986). Midlatency auditory evoked responses: Differential effects of sleep in the human. *Electroencephalography and Clinical Neurophysiology*, *65*(5), 383–392.

Hobson, J. A. (1990). Sleep and dreaming. *Journal of Neuroscience*, *10*(2), 371–382.

Issa, E. B., & Wang, X. (2008). Sensory responses during sleep in primate primary and secondary auditory cortex. *Journal of Neuroscience*, *28*(53), 14467–14480.

Jastreboff, P. J. (1990). Phantom auditory perception (tinnitus): Mechanisms of generation and perception. *Neuroscience Research*, *8*(4), 221–254.

Liberman, T., Velluti, R. A., & Pedemonte, M. (2009). Temporal correlation between auditory neurons and the hippocampal theta rhythm induced by novel stimulations in awake guinea pigs. *Brain Research*, *1298*, 70–77.

McCarley, R. W., & Hoffman, E. (1981). REM sleep dreams and the activation-synthesis hypothesis. *American Journal of Psychiatry*, *138*(7), 904–912.

Morales-Cobas, G., Ferreira, M. I., & Velluti, R. A. (1995). Firing of inferior colliculus neurons in response to low-frequency sound stimulation during sleep and waking. *Journal of Sleep Research*, *4*(4), 242–251.

Osterhammel, P. A., Shallop, J. K., & Terkildsen, K. (1985). The effect of sleep on the auditory brainstem response (ABR) and the middle latency response (MLR). *Scandinavian Audiology*, *14*(1), 47–50.

Parmeggiani, P. L., Lenzi, P., Azzaroni, A., & D'Alessandro, R. (1982). Hippocampal influence on unit responses elicited in the cat's auditory cortex by acoustic stimulation. *Experimental Neurology*, *78*(2), 259–274.

Pedemonte, M., Díaz, M., Medina-Ferret, E., & Testa, M. (2019). Impact of sound stimulation during different sleep stages in patients with tinnitus. *Loquens*, *5*(2),

Pedemonte, M., Drexler, D., Rodio, S., Geisinger, D., Bianco, A., Pol-Fernandes, D., et al. (2010). Tinnitus treatment with sound stimulation during sleep. *International Tinnitus Journal*, *16*(1), 37–43.

Pedemonte, M., Peña, J. L., Morales-Cobas, G., & Velluti, R. A. (1994). Effects of sleep on the responses of single cells in the lateral superior olive. *Archives Italiennes de Biologie*, *132*(3), 165–178.

Pedemonte, M., Peña, J. L., Torterolo, P., & Velluti, R. A. (1997). Auditory deprivation modifies sleep in the guinea-pig. *Neuroscience Letters*, *223*(1), 1–4.

Pedemonte, M., Peña, J. L., & Velluti, R. A. (1996). Firing of inferior colliculus auditory neurons is phase-locked to the hippocampus theta rhythm during paradoxical sleep and waking. *Experimental Brain Research*, *112*(1), 41–46.

Pedemonte, M., Testa, M., Díaz, M., & Suárez-Bagnasco, D. (2014). The impact of sound on electroencephalographic waves during sleep in patients suffering from tinnitus. *Sleep Science*, *7*(3), 143–151.

Pedemonte, M., & Velluti, R. A. (2005a). Sensory processing could be temporally organized by ultradian brain rhythms. *Revue Neurologique*, *40*(3), 166–172.

Pedemonte, M., & Velluti, R. A. (2005b). What individual neurons tell us about encoding and sensory processing in sleep. In P. L. Parmeggiani & R. A. Velluti (Eds.), *The physiologic nature of sleep* (pp. 489–508). Imperial College Press.

Peña, J. L., Pérez-Perera, L., Bouvier, M., & Velluti, R. A. (1999). Sleep and wakefulness modulation of the neuronal firing in the auditory cortex of the guinea pig. *Brain Research*, *816*(2), 463–470.

Peña, J. L, Jr., Pedemonte, M., Ribeiro, M. F., & Velluti, R. (1992). Single unit activity in the guinea-pig cochlear nucleus during sleep and wakefulness. *Archives Italiennes de Biologie*, *130*(3), 179–189.

Velluti, R. (2005). Remarks on sensory neurophysiological mechanisms participating in active sleep processes. In P. L. Parmeggiani & R. A. Velluti (Eds.), *The physiologic nature of sleep* (pp. 247–265). Imperial College Press.

Velluti, R. (2018). *The auditory system in sleep* (2nd ed.). Academic Press.

Velluti, R. A. (1997). Interactions between sleep and sensory physiology. *Journal of Sleep Research*, *6*(2), 61–77.

Velluti, R. A., Pedemonte, M., Suárez, H., Bentancor, C., & Rodríguez-Servetti, Z. (2010). Auditory input modulates sleep: An intra-cochlear-implanted human model. *Journal of Sleep Research*, *19*(4), 585–590.

Velluti, R. A., Peña, J. L., & Pedemonte, M. (2000). Reciprocal actions between sensory signals and sleep. *Biological Signals and Receptors*, *9*(6), 297–308.

Velluti, R. A., Peña, J. L., Pedemonte, M., & Narins, P. M. (1994). Internally-generated sound stimulates cochlear nucleus units. *Hearing Research*, *72*(1–2), 19–22.

Synchronization and Granger Causality Associated to Audiovisual Cuts

Celia Andreu-Sánchez, Miguel Ángel Martín-Pascual, José María Delgado-García, and Agnès Gruart

Abstract We are not aware of the vast majority of the cuts when watching media content. However, they affect our perception. This research analyzes the effects of cuts in synchronization (phase locking value, PLV) and Granger causality in 36 subjects, using electroencephalography (EEG) techniques. The PLV was studied as a phase synchronization index for the cut in theta, alpha, beta, and low gamma bands, before (from −500 to 0 ms) and after (from 0 to 500 ms) the cut. We found differences for the theta band in frontal, central, and occipital areas. We also evaluated the PLV depending on the style of edition in which cuts are inserted: The style of edition did not affect brain synchrony. Analyzing Granger causality differences for the 500 ms before the cut and 500 ms after the cut, we found Granger causality before the cut higher than after it. The style of edition seems not to affect causality either. This study proposes a new way to approach the study of media perception.

1 Audiovisual Cuts and Viewers' Connectivity

The development of how brain manages the perception of audiovisual content started in the 1950s (Cohen-Séat et al., 1954); however, it has recently got an impulse in neuroscience research (Cha et al., 2015; Kang et al., 2015; Nakano et al., 2009).

C. Andreu-Sánchez (✉)
Serra Húter Fellow, Neuro-Com Research Group, Universitat Autònoma de Barcelona, Barcelona, Spain
e-mail: celia.andreu@uab.cat

M. Á. Martín-Pascual
Instituto RTVE, Sant Cugat del Vallès, Barcelona, Spain
e-mail: miguelangel.martin@rtve.es

J. M. Delgado-García · A. Gruart
Neuroscience Division, Pablo de Olavide University, Sevilla, Spain
e-mail: jmdelgar@upo.es

A. Gruart
e-mail: agrumas@upo.es

A. Lintas et al. (eds.), *Advances in Cognitive Neurodynamics (VII)*, Advances in Cognitive Neurodynamics,
https://doi.org/10.1007/978-981-16-0317-4_17

Many investigations have been focused on finding what are the effects of the fragmentation and of the event boundaries of the media works in viewers' perception (Andreu-Sánchez et al., 2017a; Francuz & Zabielska-Mendyk, 2013; Germeys & d'Ydewalle, 2007; Zacks et al., 2010). Some other investigations have approached synchronization between subjects watching films (Hasson et al., 2004; Lahnakoski et al., 2014; Nakano et al., 2009). There are also investigations studying the dynamics of brain networks related to aesthetic appreciation (Cela-Conde et al., 2013).

Here, we propose to study viewers' connectivity related to watching media works containing cuts, paying attention to the main styles of edition in which those cuts tend to appear in our audiovisual works. The brain connectivity variable is addressed with functional and effective connectivity.

Functional connectivity refers to temporal correlation between two electro/neurophysiological measurements from different parts of the brain (Friston et al., 1993). It alludes to the dependence between signals and is defined in terms of correlations or covariance (Friston, 1994). A way to approach functional connectivity is with a phase synchronization index. In this investigation, we employed the phase locking value (PLV) for this purpose. PLV uses responses to a stimulus that is presented repeatedly and looks for latencies with a phase locking (the phase difference between the signals varies little across trials) (Lachaux et al., 1999).

Effective connectivity is understood as a time-dependent circuit that replicates the timing relationship between the recorded sources (Aertsen, 1991). Here, we employed the Granger causality for analyzing the effective connectivity of viewers when they were watching cuts in media content. This index is based on the idea that for two simultaneously measured signals, if one signal can be predicted better by incorporating the past information from the other signal than using only information from the former, then the latter signal can be called causal to the first (Granger, 1969; Niso et al., 2013; Wiener, 1956).

2 Methods

2.1 Participants

Thirty-six participants with normal or corrected-to-normal visual acuity participated in this study. Subjects were aged 28–56 (43.97 $\pm$ 8.07) years. The study had the approval of the Ethics Commission for Research with Animals and Humans (CEEAH) of the University Autònoma de Barcelona, Spain. All experiments were performed in accordance with relevant guidelines and regulations. Written informed consent was obtained from all participants.

2.2 Stimuli

We analyzed here brain activity associated with cuts. Movies are made up of shots, continuous short film sequences, spliced together with cuts. The term cut refers to the interruption of the shot with another shot with a change in space, time, or action, due to narrative or aesthetic edition requirements. We presented two video stimuli with the same narrative but different style of edition. Both stimuli had a duration of 198 s. Stimulus 1 had 33 shots, with an average shot length (ASL) of 5.9 s, and had been edited according to classical rules of edition, based on Hollywood films (smooth transitions, visual continuity, clear presentation of visual information, and among others) (Bordwell et al., 1996). Stimulus 2 had 79 shots, with an ASL of 2.4 s, and was edited breaking all the classical rules of edition; it was based on the so-called post-classic style with a more restless camera, greater number of shots, and framing jumps (Bordwell, 2002)—well represented in musical video clips that first appeared on the MTV channel, some decades ago.

2.3 Experimental Setup

The stimuli were presented on a 42-inch HD LED display (Panasonic TH42PZ70EA, Panasonic Corporation) and synchronized with EEG-recorded data using paradigm stimulus presentation (perception research system incorporated). Continuous EEG was recorded using the wireless Enobio® system (neuroelectrics). Twenty electrodes [(O1, O2, P7, P3, Pz, P4, P8, T7, C3, Cz, C4, T8, F7, F3, Fz, F4, F8, Fp1, Fp2, and an external electrode used for electrooculography (EOG)] were placed according to the international 10–20 System and referenced to electronically linked mastoid electrodes (Martín-Pascual et al., 2018).

2.4 Analysis

We used the open-source toolbox HERMES (Center for Biomedical Technology) (Niso et al., 2013) running on MATLAB R2013a (The Mathworks Inc.) under MacOS version 10.9.5 (Apple Inc.), for the functional and effective connectivity analysis. For cleaning the data, EEGLAB (Swartz Center for Computational Neuroscience, UC San Diego) was used (Delorme & Makeig, 2004). We band passed the EEG data with filter between 0.5 and 40 Hz. Then, we made epochs 500 ms before the cuts and 1000 ms after the cuts, removing the baseline. For rejecting artifacts, wrong data, and bad channels, we visually inspected the data and applied ADJUST plug-in (Mognon et al., 2011) for EEGLAB.

As mentioned, to determine functional connectivity, we chose analysis of the PLV, a phase synchronization index, while for the effective connectivity, Granger causality was studied. For the PLV analysis, we plotted the averaged connectivity of PLV in all the participants ($N = 36$) with 100 surrogates of the original data. We applied a Wilcoxon test with multiple comparisons with a false discovery rate of Type 1 ($q = 0.1$). For the Granger causality analysis, we also did a Wilcoxon test with 100 surrogates and a false discovery rate correction of type 1 ($q = 0.1$). More information about the implementation of these indices can be found in HERMES (Niso et al., 2013).

3 Results

3.1 Synchronization Associated with Cuts

To approach the PLV, we evaluated the instantaneous phase differences of the signals generated before and after the cut. The main idea was to evaluate whether those signals evolve together in time. We also analyzed differences between the styles of edition in which those cuts were inserted to detect if they affected functional connectivity. The PLV was analyzed in different bands: theta (4–8 Hz), alpha (8–12 Hz), beta 1 (12–20 Hz), beta 2 (20–28 Hz), and low gamma (28–40 Hz). We made those approaches for the activity before (from −500 to 0 ms) and after (from 0 to 500 ms) the cuts. We found statistically significant differences in synchronization between before and after the cut. More synchronization after the cuts was found in theta and beta 1 bands. A residual synchronization between electrodes P3 and Pz was also found in low gamma band, see Fig. 1.

We also approached synchronization associated with cuts by studying differences between the styles of edition in which cuts were inserted. Comparing the PLV after the

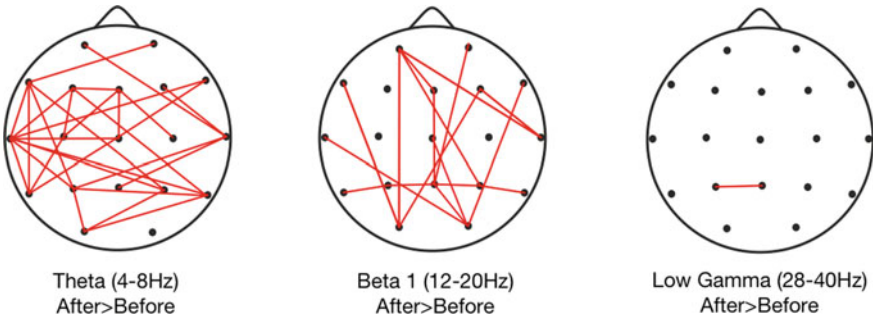

Fig. 1 Significant differences ($p < 0.05$, Wilcoxon test) in theta, beta 1, and low gamma bands found after (from 0 to 500 ms) the cut in comparison with before the cut (from −500 to 0 ms), in PLV analysis

cut (from 0 to 500 ms) in Hollywood-style movie with that in MTV-style movie, we did not find statistical differences between them. In a second approach, we compared the PLV in the whole epoch (from −500 to 1000 ms) in both styles of edition. In this case, we only found residual statistical differences in theta band between T7 and F7.

Overall, these results indicate that brain network activation after the cut in a movie is more intense than before the cut. However, the style of edition in which cuts are presented does not affect brain synchrony.

3.2 Granger Causality Associated to Cuts

Effective connectivity was approached by analyzing Granger causality. We compared that index between the before (from −500 to 0 ms) and after (from 0 to 500 ms) conditions. We found Granger causality before the cut was statistically significantly higher than after the cut, see Fig. 2. According to that result, causality in brain signal activity decreases as a consequence of the change of shots managed by cuts.

We also wanted to analyze whether the style of edition affected this index. For that, we first compared the before condition between the styles (Hollywood and MTV). We found only a very residual higher level of Granger causality in MTV-style movie than in Hollywood-style movie in left parietal and right frontal areas. Secondly, we compared the after condition between the styles. Again, we found only very residual significant connectivity with a higher level in the left parietal area in Hollywood style and a higher level in left parieto-frontal area in MTV style. As mentioned, these results were very residual and are not considered to be relevant for this investigation.

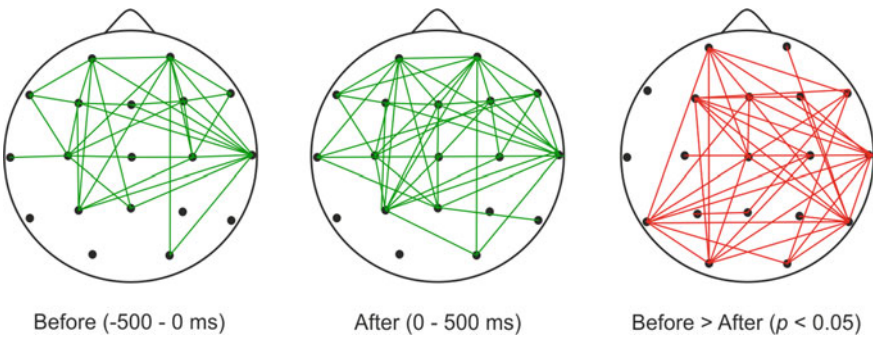

Fig. 2 Granger causality in the cut. Green lines indicate average causal connectivity, while red lines indicate significant differences found ($p < 0.05$, Wilcoxon test) when comparing connectivity before the cut (from −500 to 0 ms) with that after the cut (from 0 to 500 ms)

4 Conclusions

There are not many studies about connectivity and causality exploring parameters of the communication process through the cerebral cortex. Most join emotional processes or their effects in cortical structures of deep regions of the brain when subjects are watching media content (Cha et al., 2015; Raz et al., 2016) or making aesthetical appreciations (Cela-Conde et al., 2013).

In this investigation, we approached viewers' functional and effective connectivity related to a very specific variable: the cut. Previous studies have proven that despite viewers not always being aware of cuts (Smith & Henderson, 2008), these have an impact on their perception (Andreu-Sánchez et al., 2017a, b; Francuz & Zabielska-Mendyk, 2013). Our results suggest that the cut causes a synchronization effect. We approached this index through bands, since PLV seems to evaluate the synchronization better over a whole band (Bruña et al., 2018). We found a higher phase synchronization after the cut than before it in the theta and beta 1 bands. However, we found that Granger causality presents greater connectivity before than after the cuts. This result suggests that with regard to Granger causality, cuts interrupt connectivity in brain activity.

With the aim of studying differences in connectivity related to the styles of edition, we also analyzed the PLV and the Granger causality parameters between those styles. We found that the style of edition in which cuts are inserted seems not to affect connectivity in viewers' brain activity.

This investigation brings new insights to learning how media content editing styles and audiovisual cuts affect viewers' perception. It is also interesting to be aware that differences in editing of media contents could be used as attentional markers for creating new experimental approaches. This could be a line of research of interest for application in different areas in the near future.

References

Aertsen, A. H. M. J. (1991). Dynamics of activity and connectivity in physiological neuronal networks. In H. G. Schuster (Ed.), *Nonlinear dynamics and neuronal networks. Proceedings of the 63rd WE Heraeus Seminar, Friedrichsdorf, 1990* (pp. 281–302). VHC-Verlag.

Andreu-Sánchez, C., Martín-Pascual, M. Á., Gruart, A., & Delgado-García, J. M. (2017a). Eyeblink rate watching classical Hollywood and post-classical MTV editing styles, in media and non-media professionals. *Science Reports*, *7*, 43267.

Andreu-Sánchez, C., Martín-Pascual, M. Á., Gruart, A., & Delgado-García, J. M. (2017b). Looking at reality versus watching screens: Media professionalization effects on the spontaneous eyeblink rate. *PLoS One*, *12*(5), e0176030.

Bordwell, D. (2002). Intensified continuity visual style in contemporary American film. *Film Quarterly*, *55*(3), 16–28.

Bordwell, D., Staiger, J., & Thompson, K. (1985 [1996]). *The classical Hollywood cinema: Film style & mode of production to 1960*. Columbia University Press, [Repr.] edition.

Bruña, R., Maestú, F., & Pereda, E. (2018). Phase locking value revisited: Teaching new tricks to an old dog. *Journal of Neural Engineering*, *15*(5), 056011.

Cela-Conde, C. J., García-Prieto, J., Ramasco, J. J., Mirasso, C. R., Bajo, R., Munar, E., et al. (2013). Dynamics of brain networks in the aesthetic appreciation. *Proceedings of the National Academy of Sciences of the United States of America*, *110*(Suppl. 2), 10454–10461.

Cha, H.-S., Chang, W.-D., Shin, Y. S., Jang, D. P., & Im, C.-H. (2015). EEG-based neurocinematics: Challenges and prospects. *Brain-Computer Interfaces*, *2*(4), 186–192.

Cohen-Séat, G., Gastaut, H., & Bert, J. (1954). Modification de l'EEG pendant la projection cinématographique. *Revue Internationale de Filmologie*, *5*(16), 20.

Delorme, A., & Makeig, S. (2004). EEGLAB: An open source toolbox for analysis of single-trial EEG dynamics including independent component analysis. *Journal of Neuroscience Methods*, *134*(1), 9–21.

Francuz, P., & Zabielska-Mendyk, E. (2013). Does the brain differentiate between related and unrelated cuts when processing audiovisual messages? An ERP study. *Media Psychology*, *16*(4), 461–475.

Friston, K. J. (1994). Functional and effective connectivity in neuroimaging: A synthesis. *Human Brain Mapping*, *2*(1–2), 56–78.

Friston, K. J., Frith, C. D., Liddle, P. F., & Frackowiak, R. S. (1993). Functional connectivity: The principal-component analysis of large (PET) data sets. *Journal of Cerebral Blood Flow & Metabolism*, *13*(1), 5–14.

Germeys, F., & d'Ydewalle, G. (2007). The psychology of film: Perceiving beyond the cut. *Psychological Research*, *71*(4), 458–466.

Granger, C. W. J. (1969). Investigating causal relations by econometric models and cross-spectral methods. *Econometrica*, *37*(3), 424–438.

Hasson, U., Nir, Y., Levy, I., Fuhrmann, G., & Malach, R. (2004). Intersubject synchronization of cortical activity during natural vision. *Science*, *303*(5664), 1634–1640.

Kang, D., Kim, J., Jang, D.-P., Cho, Y. S., & Kim, S.-P. (2015). Investigation of engagement of viewers in movie trailers using electroencephalography. *Brain-Computer Interfaces*, *2*(4), 193–201.

Lachaux, J. P., Rodriguez, E., Martinerie, J., & Varela, F. J. (1999). Measuring phase synchrony in brain signals. *Human Brain Mapping*, *8*(4), 194–208.

Lahnakoski, J. M., Glerean, E., Jääskeläinen, I. P., Hyönä, J., Hari, R., Sams, M., et al. (2014). Synchronous brain activity across individuals underlies shared psychological perspectives. *Neuroimage*, *100*, 316–324.

Martín-Pascual, M. Á., Andreu-Sánchez, C., Delgado-García, J. M., & Gruart, A. (2018). Using Electroencephalography measurements and high-quality video recording for analyzing visual perception of media content. *Journal of Visualized Experiments* (135).

Mognon, A., Jovicich, J., Bruzzone, L., & Buiatti, M. (2011). ADJUST: An automatic EEG artifact detector based on the joint use of spatial and temporal features. *Psychophysiology*, *48*(2), 229–240.

Nakano, T., Yamamoto, Y., Kitajo, K., Takahashi, T., & Kitazawa, S. (2009). Synchronization of spontaneous eyeblinks while viewing video stories. *Proceedings of the Royal Society B: Biological Sciences*, *276*(1673), 3635–3644.

Niso, G., Bruña, R., Pereda, E., Gutiérrez, R., Bajo, R., Maestú, F., et al. (2013). HERMES: Towards an integrated toolbox to characterize functional and effective brain connectivity. *Neuroinformatics*, *11*(4), 405–434.

Raz, G., Touroutoglou, A., Wilson-Mendenhall, C., Gilam, G., Lin, T., Gonen, T., et al. (2016). Functional connectivity dynamics during film viewing reveal common networks for different emotional experiences. *Cognitive, Affective, & Behavioral Neuroscience*, *16*(4), 709–723.

Smith, T. J., & Henderson, J. M. (2008). Edit Blindness: The relationship between attention and global change blindness in dynamic scenes. *Journal of Eye Movement Research*, *2*(2), 1–17.

Wiener, N. (1956). The theory of prediction. In E. F. Beckenbach (Ed.), *Modern mathematics for the engineers* (Chap. 8, pp. 165–190). McGraw-Hill.

Zacks, J. M., Speer, N. K., Swallow, K. M., & Maley, C. J. (2010). The brain's cutting-room floor: Segmentation of narrative cinema. *Frontiers in Human Neuroscience*, *4*, e00168.

Event-Related Potentials and Fast Optical Imaging of Cortical Activity During an Auditory Oddball Task

Manon E. Jaquerod, Ramisha Knight, Alessandro E. P. Villa, and Alessandra Lintas

Abstract Event-related potentials (ERP) have been repeatedly used to study the spatiotemporal dynamics of the attentional response in the well-known oddball paradigm. We combined electroencephalography (EEG) with frequency-domain near-infrared spectroscopy (fNIRS) of the frontal cortex to measure neuronal activity with a high spatial and temporal resolution. The aim of this study was to determine the precise chronology of event-related optical signals (EROS) and their consistency with ERPs. In agreement with previous studies, the oddball condition produced larger waveforms for rare (1500 Hz pure tone) with respect to frequent stimuli (1000 Hz), with N1, P2, N2, P3a, and P3b components. At a latency corresponding to the mismatch negativity/N2 wave component, EROS showed the organization of a complex activity in a functional network of frontal areas, with rare tones activating the left premotor dorsal cortex and the left inferior frontal cortex and decreasing the activity of the right superior frontal gyrus. Rare tones elicited also a strong N500 (N400-like) wave component that EROS contributed to localize at the level of the right medial frontal gyrus by EROS. The simultaneous recording of fNIRS and EEG measure-

M. E. Jaquerod (✉) · A. E. P. Villa · A. Lintas
NeuroHeuristic Research Group, University of Lausanne, Internef 138, Quartier UNIL-Chamberonne, 1015 Lausanne, Switzerland
e-mail: manon.jaquerod@unil.ch
URL: http://www.neuroheuristic.org

A. E. P. Villa
e-mail: alessandro.villa@unil.ch

A. Lintas
e-mail: alessandra.lintas@unil.ch

A. E. P. Villa
LABEX, HEC Lausanne, Faculty of Law, Criminal Justice and Public Administration, University of Lausanne, Quartier UNIL-Chamberonne, 1015 Lausanne, Switzerland

R. Knight
University of Illinois, 2111 Beckman Institute, 405 North Mathews Avenue, Urbana, IL 61801, USA
e-mail: rsknight@illinois.edu

A. Lintas et al. (eds.), *Advances in Cognitive Neurodynamics (VII)*, Advances in Cognitive Neurodynamics,
https://doi.org/10.1007/978-981-16-0317-4_18

ments with high temporal accuracy over the human prefrontal cortex supports the potential for this approach to unravel the functional cortical network involved in cognitive processing.

1 Introduction

A fundamental property of animal behavior is habituation, i.e., the decrement of response with repeated stimulation, which is a necessary process to detect deviant or novel stimuli (Blumstein, 2016; Thompson, 2009). A classical paradigm, called "oddball" paradigm, used to study the responsiveness to a repeated auditory stimulus consists of a long sequence of repetitive identical stimuli (the frequent stimuli) that is replaced with a low probability, and at random, by a different stimulus (the rare stimulus). Brain activity elicited by frequent and rare stimuli has been recorded by electrophysiological means to study the brain processes underlying attention switches to, and involuntary discrimination of, rare among the frequent stimuli. Animal studies showed that responses at the level of the cerebral cortex are associated with attentional circuits that are strongly affected during anesthesia (Apelbaum et al., 1960; Eriksson & Villa, 2005; Ruusuvirta et al., 1996).

In humans, the oddball paradigm was implemented in active and passive conditions (Näätänen, 1990; Squires et al., 1975). The active condition is an attentional task, such that the participant must attend to all stimuli in order to detect the rare stimuli and generate a motor response, e.g., a key-press. In the passive condition, the participant is usually instructed to ignore all stimuli and to attend other stimuli, usually presented in another sensory modality. Maintaining a goal-directed behavior that requires selective attention, brain responses to the habituation of the frequent stimuli, and the salient perception of rare stimuli may bring insights about reorientation of attention. The oddball paradigm has been extensively studied by electroencephalography (EEG), i.e., by measuring variations in the electric field at the scalp induced by the summation of mass neuronal firing rates with a millisecond-level of resolution. The selective sensitivity of the technique for brain layers with correlated dipoles makes neural activity in sulci far less represented in the EEG signal than neural activity in gyri (Nunez, 1995). Furthermore, the spatial filtering of fields by the head volume conductor implies interdependencies of measurements between electrode sites and strongly restrain the capacity for EEG to depict the precise spatial distribution of patterns of activity (Nunez, 1995). The event-related potentials (ERPs) are obtained by averaging, over many trials, the EEG signal variations triggered by sensory or behavioral events. Endogenous ERPs are thought to reflect the neurophysiological correlates of cognitive processes.

In the oddball paradigm, the auditory stimuli elicited ERPs characterized by several components (N1, P2, N2, P3) whose latencies and amplitudes differentiated rare from frequent stimuli (Alexander et al., 1994; Michalewski et al., 1986; Näätänen, 1990). The N1 wave is generated by a stimulus-driven attention-trigger mechanism (Näätänen & Picton, 1987). A positive component P2 of the ERP is often preced-

ing the negative component N2 at approximately 250 ms after rare stimuli (Goodin et al., 1978). This wave may often be dissociated into an earlier fronto-central N2a component (also known as "mismatch negativity") and a later, more frontally distributed, N2b component associated with the allocation of attention to the eliciting stimulus in the active oddball condition (Näätänen, 1990; Squires et al., 1975). The mismatch negativity (MMN), characterized by its responsiveness to low probability stimuli even in the passive auditory oddball condition, may underlie the ability to discriminate acoustic differences, a fundamental aspect of sensory perception. The N2 is followed by the P3 (P300) component, with larger amplitude in active than in passive conditions, formed by a fronto-central wave complex N2-P3a that can be dissociated from a temporo-parietal P3b wave (Molnár, 1994; Näätänen, 1990; Polich, 2007; Squires et al., 1975; Verleger, 1988). In addition, at 400–500 ms from stimulus onset, the rare stimuli elicited a slow frontally maximal negativity, referred to as N500 (N400-like) (Gaillard, 1976).

Signals recorded by functional magnetic resonance imaging (fMRI) are associated with the blood-oxygen-level-dependent (BOLD) signal, an hemodynamic indirect measure of neural activity with severe limitations in temporal resolution and with challenging interpretation to make deductions about the nervous system. The activation of spatially limited neuronal populations may not be strong enough to produce significant hemodynamic changes, but still produce a significant ERP wave. Brain imaging with fMRI has been used to localize the brain areas activated during the P3 wave elicited by the oddball paradigm (Linden et al., 1999; McCarthy et al., 1997; Menon et al., 1997). In fMRI studies, the detection of rare stimuli in oddball tasks related to BOLD signal increased in the supramarginal (Horovitz et al., 2002; Mangalathu-Arumana et al., 2012; McCarthy et al., 1997; Menon et al., 1997) and superior temporal gyri (Mangalathu-Arumana et al., 2012; Opitz et al., 1999), in agreement with greater wave amplitude of P3b observed at the temporal/parietal electrode sites of EEG. A significant hemodynamic response was also reported in the frontal lobe, in particular at the level of the middle frontal gyrus (MFG) (Horovitz et al., 2002; McCarthy et al., 1997; Stevens et al., 2005), frontal midline areas (Menon et al., 1997) an the opercular area of the inferior frontal gyrus (IFG), corresponding to Brodmann area 44 (Linden et al., 1999). The ERP response to the oddball paradigm is complex and cannot be reduced to its P3 component. Besides the spatial dependency of its signal on the location of blood vessels, fMRI relies on an indirect correlate of neural activity which is intrinsically too slow to reveal the complexity of neurodynamics. Hence, it is likely that BOLD fMRI signal generation reflects the sustained activity of a large neuronal system triggered by the rare stimuli and that brief synaptic activity, evoked by those stimuli in dynamic neural circuits, might be detectable only with methods characterized by signal-to-response dynamics faster than neurovascular signals.

Transcranial near infrared spectroscopy (NIRS) allows the non invasive differentiation between tissues with different light attenuation or scattering properties and can provide spectroscopic information on the concentrations of chromophores, in particular oxy- and deoxy-haemoglobin, HbO2 and Hb (Chance et al., 1993; Delpy & Cope, 1997; Gratton et al., 1995; Scholkmann et al., 2014; Strait & Scheutz, 2014;

Torricelli et al., 2014). A slow hemodynamic signal, corresponding to cerebral blood oxygenation variations, is measured as a function of near-infrared light propagation through extra-cerebral and cerebral tissue. Both the optical path length and the cerebrospinal fluid layer affect the measurement, but the geometry of the sulci and the boundary between the gray and the white matter have little effect on the detected light distribution (Okada et al., 1997). The NIRS hemodynamic signal, which is similar to the BOLD signal measured by fMRI, is modified by neuronal activity through neurovascular coupling with latencies of several seconds. In addition to the measurement of changes in light intensity, fNIRS instruments with a frequency-domain technology of measurement allow the recording of a fast optical signal with a latency in the order of milliseconds (Gratton & Fabiani, 2010). This measurement, made possible by the modulation of light sources at a high radio-frequency (e.g., 110 MHz), is based on a complex function of the tissue absorption and scattering coefficients to include changes in light intensity with distance, phase, and modulation depth changes of intensity-modulated light and the temporal dispersion of light from an ultrashort input light pulse (Gratton et al., 1997; Gratton & Fabiani, 2001; Wolf et al., 2002). Neural activity can be directly detected by fast fNIRS signal through changes in the scattering coefficient of the brain tissue. A change in neuronal cell volume following an action potential discharge is meant to account for subtle, yet measurable, variation in the scattering properties of the tissue (Lee & Kim, 2010; Steinbrink et al., 2000; Villringer & Chance, 1997). Although optical imaging with fast fNIRS signals has the potential for a millimeter-level of spatial resolution, it is limited to brain regions located only few centimeters below the scalp (Gratton et al., 1997).

The two main cortical associative auditory pathways include a posterior dorsal stream processing spatial (“where”) information from the posterior superior temporal gyrus (STG) to the parietal cortex, and an anterior ventral stream processing an object (“what”) from the anterior part of STG to IFG (Ahveninen et al., 2006). Both pathways send projections to the prefrontal cortex with dorsal (DLPFC) and ventral (VLPFC) regions involved in different roles during the processing of auditory information with high cognitive load (Plakke & Romanski, 2016). Simultaneous recording of ERP and the corresponding NIRS response has recently raised considerable interest to complement the study of the spatial distribution of cortical and subcortical activation during oddball and go-nogo tasks. Source localization based on the NIRS slower hemoglobin response showed significant oddball activation in temporal/parietal areas (Kennan et al., 2002) with a gender effect suggesting females’ event-categorization process is more efficient than in males (Jausovec and Jausovec, 2009), and activation of MFG by tasks that require heavy cognitive processing (Jeong et al., 2018). Stronger hemodynamic responses were reported in the left prefrontal cortex when participants were performing an auditory oddball task under mental stress (Liu et al., 2011), but the response was stronger in the right VLPFC when attending to stimuli that required higher cognitive load and negatively correlated with the level of state anxiety (Tseng et al., 2018). The averaging of optical responses evoked by the repetition of the same stimulus allowed the analysis of event-related transient optical responses based on continuous wave measurements of light intensity (Kubota et al., 2008; Medvedev et al., 2008) and the development of event-related

optical signal (EROS) analysis by means of frequency-domain instruments, based on a measurement of phase-shifts of the fast optical signal as the photons migrate through the brain tissue, which is optically modified by neural activation (Gratton & Fabiani, 1998). In passive detection of deviant auditory stimuli, source localization by EROS reported early activity co-occurring with ERP waves localized in the auditory areas of STG (Rinne et al., 1999) followed by activation of VLPFC in pre-attentive auditory change detection (Tse et al., 2013). At a later latency, consistent with P3 and frontal negativity, EROS data have shown activation in the right MFG (DLPFC) by rare stimuli during an auditory oddball task (Low et al., 2006).

In this study, we analyzed ERPs and EROS in the frontal cortex elicited by a passive two-tone auditory oddball discrimination task. The task consisted of a random stream of frequent auditory tones (1000 Hz, $p = 92\%$) or an infrequent oddball auditory tone (1500 Hz, $p = 8\%$) being played at a constant interval of 1600 ms. In this paradigm, attention is directed away from the acoustic stimuli with an explicit instruction to fixate on a white cross centered on a screen. Our EROS analysis was mainly based on changes in the phase delay because it has the advantage of a greater sensitivity for deeper locations and a greater spatial resolution than light intensity measurements (Gratton & Fabiani, 2010). These results indicate that the passive auditory oddball task modulated the brain activity measured by EROS in the frontal cortex within the same time range as EEG measures. The simultaneous recording of fNIRS and EEG measurements with high temporal accuracy over the human prefrontal cortex supports the potential for this approach to unravel the functional network involved in cognitive processing.

2 Methods

2.1 Participants

Ten healthy volunteers participated in the study (mean age = 28.1 years; 6 women). All subjects were right-handed and reported normal hearing and normal or corrected-to-normal vision. Prior to participation, subjects were informed about the procedure and provided signed informed consent for their participation in line with the Declaration of Helsinki (World Medical Association, 2013) and the recommendations of ethical and data security guidelines of the University of Lausanne. Two subjects (1 male and 1 female) were treated as pilot data and were excluded from the analysis.

2.2 Procedure

The task consisted of 12 blocks with 120 trials each, following the passive auditory oddball paradigm. Frequent (1000 Hz at occurrence probability $p = 92\%$) and a

rare (1500 Hz, $p = 8\%$) computer generated tones, lasting 500 ms, were presented at approximately 60 dB SPL. Each block consisted of a randomized sequence of frequent and rare tones where stimuli onsets were separated by 1600 ms. Subjects were only instructed to watch a white fixation cross in the center of a computer screen placed horizontally at 65 cm in front of the middle of their eyes. In order to minimize the noise added by environmental light in the NIRS data, experiments were run with the lights off and the computer screen background was black.

2.3 *Electrophysiological Recording*

Continuous EEG was recorded using 64 scalp Ag/AgCl active electrodes (ActiveTwo MARK II Biosemi EEG System, BioSemi B.V., Amsterdam, The Netherlands), sampled 1024 Hz and referenced to the linked mastoids. Impedance was kept below 20 kΩ. Electrodes were mounted on a head-cap (10/20 layout, NeuroSpec Quick Cap) that was modified in order to allow the optical equipment to have direct contact with the scalp (Fig. 1a). Data were preprocessed and analyzed with the EEGLAB toolbox (MATLAB, The MathWorks, Inc.) (Delorme & Makeig, 2004). EEG data were then segmented into epochs using markers. Epochs of the continued data with visible large movement artifacts were removed from the analysis. A poor EEG signal from a selected electrode was reconstructed by combining signals from neighbor-

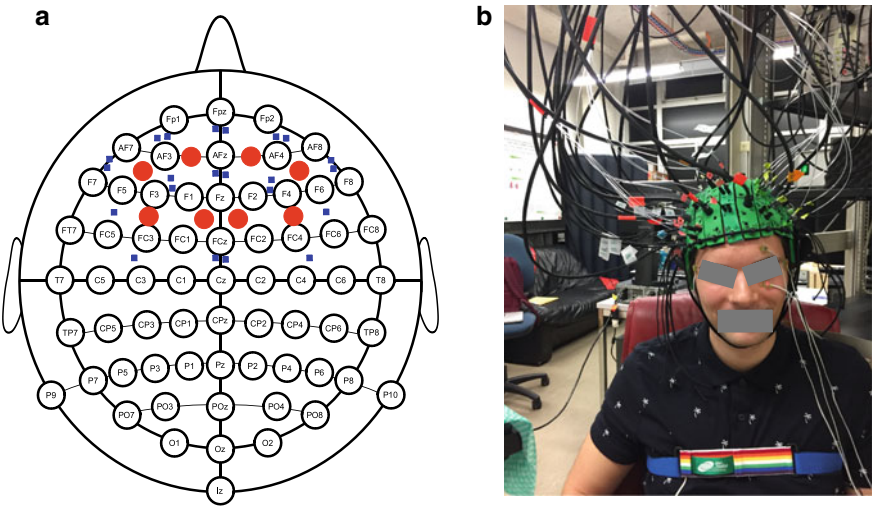

Fig. 1 **a** Schematic representation of the co-localization of the 8 light detectors (red circles) and 22 light sources (blue squares) over prefrontal and premotor areas of the cerebral cortex and the 64-channel electrophysiological setup with the standardized International 10/20 system. **b** The photo-multiplier tube detectors and fiber optic bundles placed over the participant's forehead using a custom-made mounting system

ing electrodes using interpolation. The EEG signal was decomposed using an Infomax Independent Component Analysis (ICA) in order to correct eye blink artifacts. Epochs containing visible artifacts after ICA preprocessing were rejected. All epochs kept for the analysis were bandpass filtered between 0.1 and 40 Hz before ERPs were computed.

A grand average of the ERP response to the oddball task was calculated by averaging individual participants' ERPs. In this study, we report data recorded at electrode sites Fz, Cz, and Pz, separately for frequent and rare tones. The amplitude was calculated as the voltage difference between a pre-stimulus baseline and the respective peak. The latency was defined by the lag for the ERP wave to reach its peak amplitude. We focused our topographic analysis on the time windows corresponding to the main ERP components. The N1/P2 was identified as negative deflection between 120 and 150 ms post-stimulus followed by a positive deflection between 170 and 230 ms post-stimulus. The MMN/N2 was identified as the largest peak occurring 230–260 ms after stimulus presentation, the P3a as the positive deflection between 280 and 300 ms and the P3b as the largest peak occurring 350–400 ms after stimulus presentation. A large negative wave between 460 and 650 ms post-stimulus characterized the N500 (N400-like) component of the ERP.

2.4 Optical Recording

Optical data were collected using a frequency-domain NIRS system ISS Imagent (Champaign, Illinois, USA) with 8 detectors and 22 frequency-modulated light (830 nm wavelength modulated at 110 MHz) sources. The sources and detectors were co-located with the EEG setup, as shown in Fig. 1a. In the present study, EROS was recorded with source-to-detector distances between 20 and 55 mm. The fiber optic bundles connected to the laser diodes emitting light sources and the fiber optic bundles connected to the detectors (photomultiplier tubes) were held in place using a custom-built head mounting system (Fig. 1b). Detectors amplifiers' were modulated at a frequency of 110.005 MHz. Hence, a heterodyning frequency (or cross-correlation frequency) was generated equal to the difference between the frequency modulation of the sources and detectors, i.e. 5000 Hz, thus implying a period of oscillation of 0.2 ms. The photomultiplier output current was Fast Fourier Transformed (FFT) on four oscillations (i.e., 0.8 ms). One oscillation was skipped in order to avoid cross-talk between sources, thereby yielding a data acquisition period of 1 ms for each source. Light sources were time multiplexed in a cycle of eight per sampling point, which corresponds to an effective time resolution of 8 ms (i.e., an effective sampling rate 125 Hz). Notice that for each data point, we measured the DC (average) intensity, AC (amplitude) intensity, and relative phase delay.

The locations of each source and detector were digitized with a 3D digitizer (FASTRAK 3Space, Polhemus Inc.). Phase delay measurements in the cross-correlation signal were corrected off-line for phase wrapping and their mean was adjusted to zero. The algorithm described in Gratton and Corballis (1995) was used to remove the pulse artifacts from the signal. Only channels with phase standard deviation smaller than 200 ps were included for further analysis (Gratton et al., 2006). Data were band-pass filtered between 0.1 and 10 Hz before statistical topographical surface projection maps of fast optical signals were computed using the Opt3D software (Gratton, 2000) available at the NeuroImaging Tools & Resources Collaboratory (https://www.nitrc.org/). EROS data were spatially filtered with an 8-mm Gaussian kernel and for each subject, contrast, and voxels, t-scores were computed and converted to Z-scores. This approach removes emphasis on larger effects in relation to the smaller effects and was chosen because of our small sample size ($N = 8$).

The regions of interests (ROIs, cf. Table 1 and Fig. 2) were selected on the basis of previous studies on auditory deviance detection. The Talairach space boundaries of our ROIs were kept consistent with anatomical structures and we assigned each ROI to a Brodmann area with the BioImage Suite software package (http://www.bioimagesuite.org, Lacadie et al., 2008).

Table 1 Coordinates (x, y, z) are in Talairach space (Talairach & Tournoux, 1988) of the areas studied here

Region	Left	Right	Broadmann area
Superior frontal gyrus (SFG)	$x \in [-35, -15]$	$x \in [30, 10]$	BA 9/BA 8
	$y \in [25, 55]$	$y \in [25, 55]$	
	$z \in [50, 35]$	$z \in [50, 35]$	
Middle frontal gyrus (MFG) dorsolateral prefrontal cortex (DLPFC)	$x \in [-50, -35]$	$x \in [45, 30]$	BA 46 (/BA 10), BA 8 / BA 9
	$y \in [25, 55]$	$y \in [25, 55]$	
	$z \in [30, 15]$	$z \in [20, 30]$	
Inferior frontal gyrus (IFG)	$x \in [-60, -45]$	$x \in [60, 45]$	BA 44 (/BA 45)
ventrolateral prefrontal cortex (VLPFC)	$y \in [15, 30]$	$y \in [15, 30]$	
	$z \in [15, 30]$	$z \in [15, 30]$	
Dorsal premotor (PMd) cortex	$x \in [-40, -15]$	$x \in [35, 10]$	BA 6
	$y \in [25, 55]$	$y \in [25, 55]$	
	$z \in [45, 60]$	$z \in [45, 60]$	

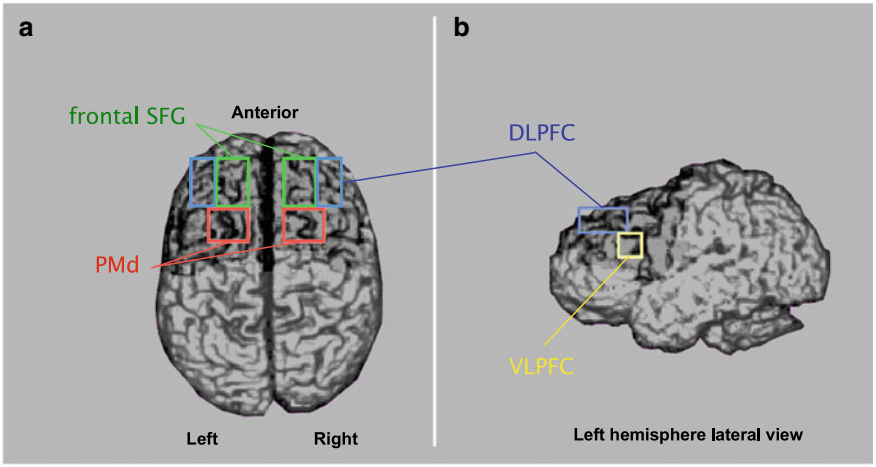

Fig. 2 Antero-posterior (**a**) and left hemisphere lateral (**b**) views of selected regions of interest (ROIs). The area in darker grey represents the brain region sampled by the recording montage. VLPFC: ventrolateral prefrontal cortex; DLPFC: dorsolateral prefrontal cortex; SFG: superior frontal gyrus; PMd: dorsal premotor cortex

3 Results

3.1 Grand Average ERPs

The sample size for the ERP analysis was $N = 7$ because one more subject (male) was excluded due to a technical problem that occurred during EEG data collection. The frequent and rare tones elicited similar negative ERP component between 120 and 150 ms (N1), followed by a small positive wave P2 (P180), along the midline sites, somewhat larger in the rare condition and towards frontal areas (Fig. 3a, B1). A second ERP peak negativity was mainly elicited in the rare tone condition at 230–260 ms post-stimulus (MMN/N2) at all three midline sites (Fig. 3a). We observed distinct topographic maps of electrical activity between the conditions during this time window (Fig. 3B2), but it was significantly different from the frequent tone ERP only on the frontal site ($p < 0.05$, Bonferroni-corrected for 64 electrodes). It is possible that such fronto-central N2 wave is a composite of N2a and N2b components, which overlap in time and scalp distribution.

Consistently with the literature, a significant difference between the two conditions ($p < 0.05$, Bonferroni-corrected for 64 electrodes) appeared for a large positive deflection elicited with a lag of approximately 300–400 ms (P300) after rare tones at all reported electrode sites. This positive wave included a fronto-central component P3a (Fig. 3B3) peaking between 280 and 330 ms and a second component P3b with

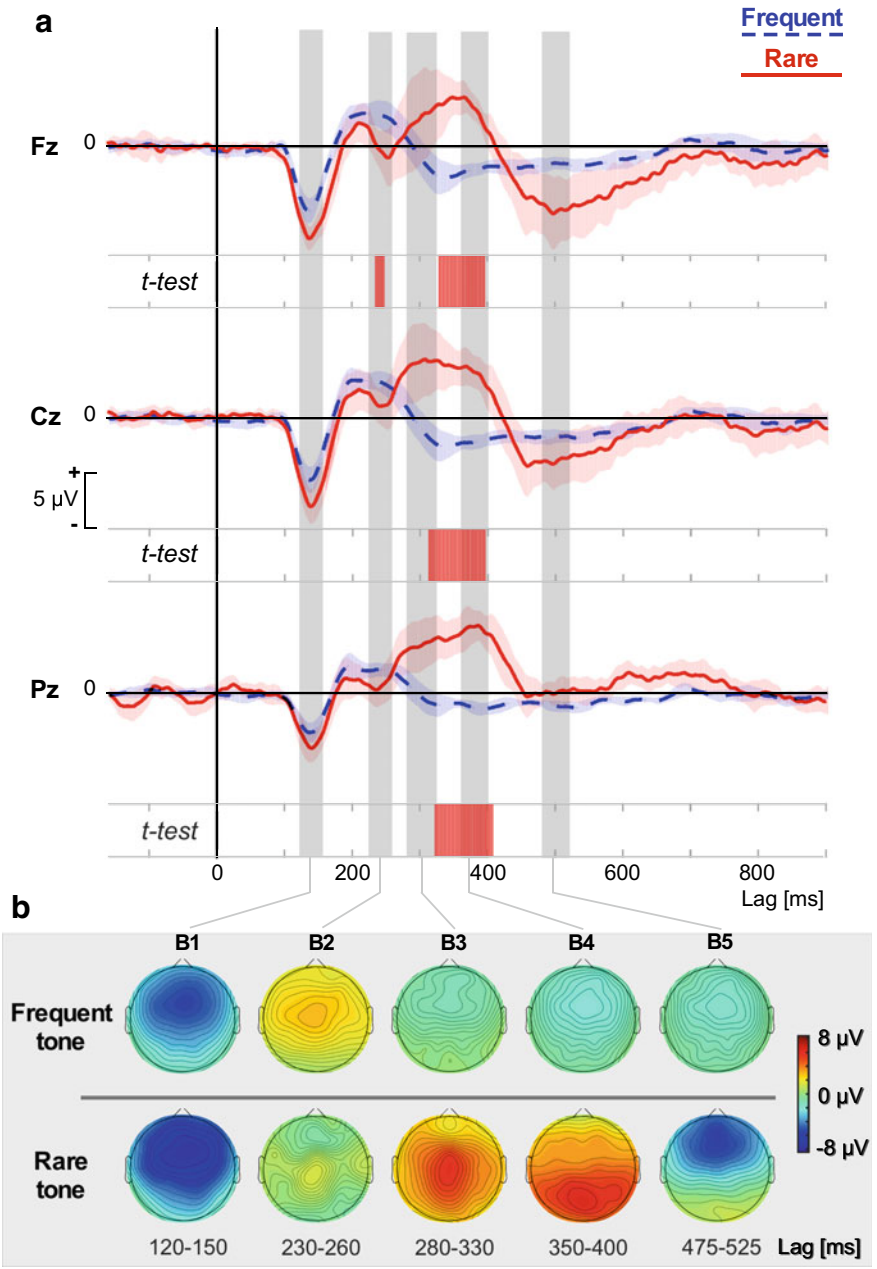

Fig. 3 **a** Grand average ERP waveforms (mean $\pm 2\times$ SEM) at electrode sites Fz, Cz and Pz ($N = 7$ participants). Each plot is followed by the result of a paired t-test between the frequent (dashed blue) and rare (red) tones (Bonferroni-corrected for 64 electrodes, in red when $p < 0.05$). **b** Topographic maps of scalp potential distribution at the main ERP components. **B1**: N1 at 120–150 ms post-stimulus; **B2**: MMN/N2 at 230–260 ms; **B3**: P3a at 280–330 ms; **B4**: P3b at 350–400 ms; **B5**: N500 (N400-like) at 475–525 ms

a posterior maximum (Fig. 3B4), peaking between 350 and 400 ms. A large frontal negativity observed between 450 and 600 ms (N400-like/N500) was characterized by maximal response over midline frontal electrodes (Fig. 3B5).

3.2 EROS

The data acquisition problem encountered during EEG recording of one participant did not affect fNIRS, therefore the sample size for the EROS analysis was $N = 8$. The spatiotemporal profile of the optical signal response corresponded to the topographical maps on group-level Z statistics of a 'differential EROS response', which resulted from the contrasts conducted within the ROIs for each condition separately relative to pre-stimulus baseline and for rare versus frequent tones, to the three time points of the peak contrasts, i.e. at 40, 256, and 480 ms (Fig. 4).

Rare tones elicited less bilateral activation compared to frequent tones between 32 and 40 ms following the stimulus onset (Fig. 4A). In the left hemisphere, the negative peak voxel activity was located in the Brodmann Area BA46 (DLPFC, ROI in blue in Fig. 2, Talairach coordinates $x = -43$, $y = 27$) and did not reach ($Z = -2.135$) the level of significance ($p = 0.05$) when averaging the voxels within the ROI ($Z_{\text{crit}(0.05)} = -2.60$). The right negative peak voxel activity belonged to the posterior part of BA8 ($x = 24$, $y = 27$) across superior frontal gyrus (ROI in green in Fig. 2) and did not reach the ROI significance criterion ($Z = -2.169 > Z_{\text{crit}(0.05)} = -2.85$).

At 256 ms post-stimulus, Fig. 4b shows the statistical maps resulting from differential EROS responses and Fig. 5 shows also the responses in the rare and frequent tone conditions, representing a complex pattern of activity co-occurring with N2 component of the ERP. Between 240 and 272 ms in the rare tone condition, we observed greater activation ($Z > 2$) in the ROI corresponding to the left PMd (ROI in red in Fig. 2, $x = -21$, $y = 12$, BA6) with a peak voxel activity at 256 ms ($Z = 2.263 < Z_{\text{crit}(0.05)} = 2.67$). Between 240 and 264 ms, we observed a reduced differential EROS response in the right SFG (BA8, $x = 24$, $y = 29$) with a peak voxel activity at 256 ms ($Z = -2.368 > Z_{\text{crit}(0.05)} = -2.89$). Those two effects were very close to their ROI criterion of significance at $p = 0.05$.

Broca's area (VLPFC, ROI in yellow in Fig. 2, $y = 22$, $z = 22$), corresponding to BA44 contained and limited by pars opercularis of the left inferior frontal gyrus, was characterized by a greater activation in the rare tone condition in the interval 248–264 ms with a significant peak voxel activity at 264 ms ($Z = 2.234 > Z_{\text{crit}(0.05)} = 2.20$). This ROI was activated almost exclusively during the rare tone condition, as emphasized by the significant contrast (maximum at 272 ms, $Z = 2.245 > Z_{\text{crit}(0.05)} = 2.19$) of this condition with the baseline between 248 and 280 ms (Fig. 5b, sagittal projection). In the left hemisphere, it is interesting to notice also an activation at the level of the auditory cortex in the postcentral gyrus (BA 43) only after frequent tones (Fig. 5c). This activation fell below a significant contrast ($Z < 2$) and was not visible in the differential EROS response (Fig. 5a).

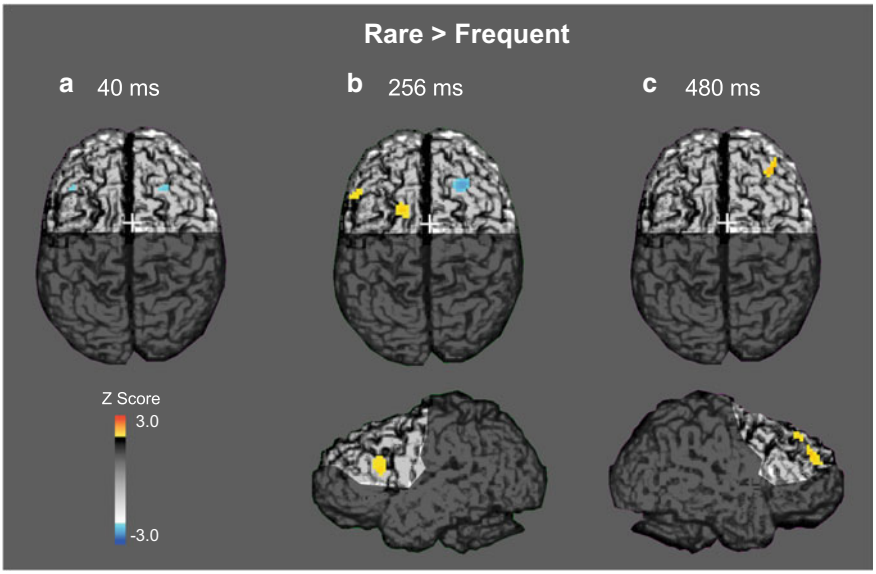

Fig. 4 Spatial maps based on group-level ($N = 8$) Z statistics for the EROS data contrasting rare versus frequent tones in the passive auditory oddball task relative to the pre-stimulus baseline. The area in light grey represents the brain region sampled by the recording montage. **a** Projection of EROS data to the axial surface at 40 ms after stimulus onset. The differential EROS response shows that superior frontal gyrus was activated after frequent tones by the dorsal spatial ("where") processing stream, BA46 in the left hemisphere and BA8 in the right hemisphere. **b** Spatial maps of the EROS data projected to the axial (top) and left sagittal (bottom) surfaces of significant ROIs at 256 ms after stimulus onset, co-occurring with N2b ERP wave. Notice the complex pattern of response, see Fig. 5 for more details. **c** Projection to the axial (top) and right sagittal (bottom) surfaces of significant ROIs at 480 ms after stimulus onset, co-occurring with N500 (N400-like) ERP wave. In the right hemisphere, notice the strong activation of DLPFC after rare tones at the level of BA9 (axial projection) and BA46 (sagittal projection)

In the right middle frontal gyrus (Fig. 4C), at the level of BA9 of DLPFC (Talairach coordinates $x = 32$, $y = 39$), a greater activation was observed between 464 and 520 ms in the rare tone condition with a peak voxel activity at 488 ms ($Z = 2.361 < Z_{\text{crit}(0.05)} = 2.97$). This activation co-occurred with the N500 (N400-like) ERP wave. A more anterior part of DLPFC, corresponding to BA46 (see the right hemisphere sagittal view of Fig. 4c), was also activated by the differential EROS response during this interval, but it was located outside the predefined ROIs.

4 Discussion

We report results on the neural dynamics of frontal cortex response to a passive auditory oddball task studied by simultaneous recording of fast optical signals with high temporal resolution (EROS) and ERPs. To the best of our knowledge, no other

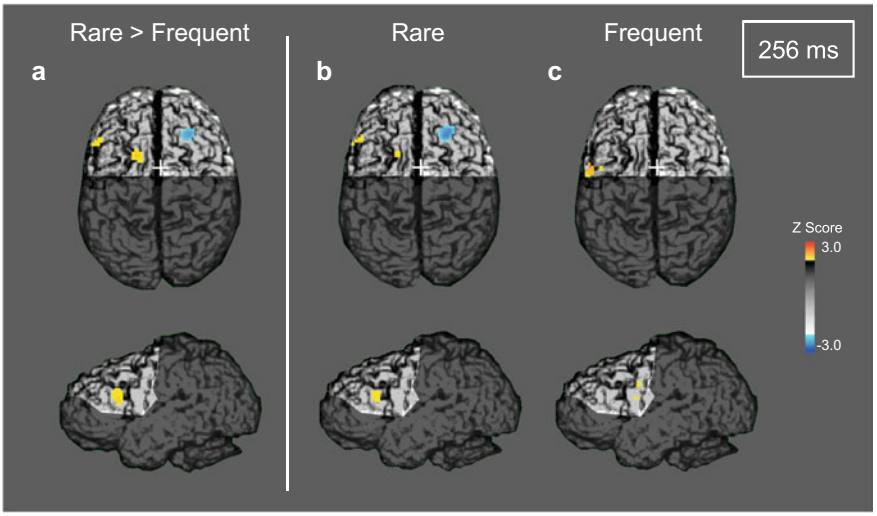

Fig. 5 Spatial maps based on group-level ($N = 8$) Z statistics for the EROS data at 256 ms after tone onset, co-occurring with N2b ERP wave, projected to the axial (top) and left sagittal (bottom) surfaces. **a** Response contrasting rare versus frequent tones compared to pre-stimulus baseline, same as Fig. 4b. **b** Response to rare tones separately contrasted with pre-stimulus baseline. Notice the same ROIs visible in panel (**a**), although with a different significant voxel density. **c** Response to frequent tones contrasted with pre-stimulus baseline. Notice a small activation in the postcentral gyrus, at the border of the area under investigation

study has yet combined EROS with a similar temporal resolution (i.e. 8 ms sampling time) with a 64-channel EEG system in an auditory oddball task. Electrophysiological recordings revealed all the ERP components (N1, P2, N2, P3) well described in the literature (Alexander et al., 1994; Michalewski et al., 1986; Näätänen, 1990). We observed also several commonalities and some differences regarding the brain areas and the response timing with the few previous studies reporting EROS analyses in auditory and visual oddball tasks (Low et al., 2006; Proulx et al., 2018; Tse & Penney, 2008; Tse et al., 2006, 2013). Despite controversial observation about the significance of fast optical signals measured by fNIRS (Steinbrink et al., 2005; Syré et al., 2003), the co-occurrence of optical signals and ERP waves found here confirms that such a methodological approach carries the potential for investigating neurodynamics of cognitive activity in a wide range of tasks (Gratton et al., 2018). However, there are several limitations that should be acknowledged in our results. First, this study may be considered somewhat preliminary because of the small sample size ($N = 7$ for ERP and $N = 8$ for EROS analyses), although the statistical analyses showed suitable effects. Additional data are being collected and a final report with a larger sample will be soon completed. Second, fast optical signals suffer from a low signal-to-noise ratio and the response signal is limited to a few centimeters below the scalp (Gratton & Fabiani, 2010). It is important to underline that complementary studies using different and independent measures of brain activity are necessary to gain

further insights of the spatiotemporal patterns of brain dynamics while performing behavioral tasks.

After the stimulus onset, the earliest response observed in this study is an optical signal in the differential EROS response, appeared as early as between 32 and 40 ms post-stimulus showing a bilateral activation that is larger for frequent than rare stimuli, thus suggesting a short latency input from the auditory system. The localization of the signal at the level of BA46 of DLPFC in the left hemisphere and at the level of BA8 of the superior frontal gyrus in the right hemisphere suggests that the input is not from the sensory ascending subcortical pathway. The DLPFC is the end point for the dorsal stream that transmits spatial ("where") information (Ahveninen et al., 2006; Plakke & Romanski, 2016).

The next evoked activity response was an ERP component with a negative peak observed along the midline, mainly fronto-central sites, between 120 and 150 ms post-stimulus followed by a smaller positive wave. The profile and the latency of this wave was similar after frequent and rare tones, although the amplitude after rare tones tended to be larger. The latency and localization of this peak is in agreement with the N1/P2 (N100-P200) complex reported for the auditory oddball task with strong generators in the auditory areas of the STG and with association with a stimulus-driven attention-trigger mechanism (Näätänen & Picton, 1987; Rinne et al., 1999). In previous imaging studies coupled with EEG, the N100 component during auditory tasks co-occurred also with a signal in the anterior cingulate cortex (ACC) (Esposito et al., 2009; Walz et al., 2013). At this latency, we could not observe any significant optical response in our ROIs of the prefrontal cortex. This is likely due to the fact that our fNIRS montage was not designed to record neither from the auditory cortex nor from ACC.

The typical event-related response to the stimulus presentation observed in the auditory oddball task is the N2/P3 (P300) wave complex (Alexander et al., 1994; Fabiani & Friedman, 1995; Näätänen & Picton, 1987; Squires et al., 1975). This wave is characterized by several components, which may overlap in time and scalp distribution. We observed a fronto-central N2b-P3a component (Fig. 3B2 and B3) between 230 and 330 ms post-stimulus, followed by a P3b component with a parietal maximum (Fig. 3B4), peaking between 350 and 400 ms. Source locations determined from fMRI showed that the ACC was the principal generator of N2b-P3a ERP wave following dipole modeling of ERPs (Crottaz-Herbette & Menon, 2006). We observed fast optical signals correlated with the timing of this wave, but their latency was different (up to approximately 100 ms later) than the lag reported from other oddball-related EROS analyses (Low et al., 2006, 2009; Proulx et al., 2018; Tse et al., 2006, 2013; Tse & Penney, 2008). Differences in the protocol of our passive oddball task with respect to previous studies might explain differences in the temporal profile of the response. The current occurrence probability of rare (i.e., deviant) stimuli was $p = 8\%$ compared to $p = 20\%$ (Low et al., 2006, 2009; Proulx et al., 2018), which could suggest that in our protocol rare tones were likely to be much more unattended. The duration of our tones was 500 ms, that was much longer than usual stimuli duration in oddball studies, i.e. 70–100 ms (Ruusuvirta et al., 2007; Tse & Penney, 2008; Tse et al., 2006, 2013), and longer than 400 ms used in similar EROS

settings (Baniqued et al., 2013; Low et al., 2006, 2009). Moreover, we 1500 Hz instead 500 Hz for the rare tone frequency pip and 60 dB SPL instead of 70 db SPL for the loudness (Low et al., 2006, 2009; Proulx et al., 2018). Hence, our protocol might have triggered a different dynamics or slightly different processes that we observed in our EROS analysis. Filtering parameters are very important for the detection of fast optical signals with a low signal-to-noise ratio (Maclin et al., 2003). In this study EROS was bandpass filtered in the range 0.1–10 Hz, compared to 0–5 Hz (Low et al., 2006, 2009), 0.5–10 Hz (Baniqued et al., 2013), 1–10/12 Hz (Tse & Penney, 2008; Tse et al., 2006, 2013), and 2–20 Hz (Proulx et al., 2018) of the other studies.

The differential EROS response occurring at the same time of the N2/P3 ERP showed an activation in the inferior frontal gyrus at the level of left PMd (BA6) for the rare tones. Both action control and action observation require premotor functions and left PMd participates to mapping external action parameters onto the appropriate motor repertoire (Moisa et al., 2012; Stadler et al., 2012). In addition to the premotor functions, our finding supports the hypothesis that the activation of the left PMd may reflect encoding of the semantic features of actions (i.e., cognitive aspects of the sensorimotor sequences associated with the detection of deviant stimuli) (Press et al., 2012). Around at the same time, a pattern of activation opposite to this one for PMd was observed for EROS in the superior frontal gyrus at the level of BA8, near the border of BA46 in the DLPFC. This area was slightly activated by frequent tones, but it was strongly deactivated by rare tones compared to baseline activity. This signal was not observed by Low et al. (2006), but in their study rare tones were less unattended (20% of the total number of stimuli vs. 8% in our protocol). BA46 is mostly related with the executive control of language production (Ardila et al., 2016) and we suggest that the source of the observed signal was rather BA8. This area of right DLPFC is involved in pitch and memory processing of the auditory stimulus (Kumar et al., 2015; Schaal et al., 2017). Hence, our results might suggest that in the passive oddball task this part of BA8 would be more active when a retrieval attempt of the frequent tone succeeded than when it failed.

We observed an optical signal in the left VLPFC (BA44, Broca's area) occurring with N2 ERP component, in agreement with previous studies (Linden et al., 1999; Medvedev et al., 2010; Tse et al., 2006). The activation in BA44 was strong after rare tones and occurred about at the same time of a lesser activated area in the left postcentral gyrus (BA43) after frequent tones. The anterior ventral stream that brings information about the stimuli's characteristics (i.e., processing an object "what" information) projects to VLPFC (Ahveninen et al., 2006; Plakke & Romanski, 2016). Broca's area (BA44 in the left VLPFC) is involved in semantic tasks, in the motor aspect of speech, and in music perception (Bezgin et al., 2014; Flinker et al., 2015; Levitin & Tirovolas, 2009). The activation of BA43 and surrounding areas in STG was reported for abstract auditory representations and mental imagery of speech (Chiang et al., 2013; Tian et al., 2016). The differential spatial pattern of response observed in our results, between BA44 and BA43, might suggest that the oddball task could engage inhibitory processes triggered by deviant stimuli, as suggested in the literature in association with theta band oscillations (Harper et al., 2014; Jonides

et al., 1998; Proulx et al., 2018). We did not analyze here these oscillations, but this is certainly an interesting analysis to be developed in our extended experiment and future studies.

Previous studies have shown ERP negative waves at a latency between 300 and 500 ms post-stimulus elicited in target detection and oddball tasks (Codispoti et al., 2006; Kiehl et al., 2006; Low et al., 2006; Stevens et al., 2005), which was observed in our results as a large N500 (N400-like) wave. Our ERP analysis showed that N500 was almost exclusively elicited by rare tones and its amplitude was much larger for Fz, in agreement with the frontal and right hemisphere topographical distribution reported in those previous studies. The N400-like component has been usually reported with a spatial distribution over centro-parietal or centro-posterior sites in lexical decision tasks and in relation to predictability of stimuli and in the inferior frontal regions, if the effect reflected integration difficulty (Kutas & Hillyard, 1984; Kutas & Federmeier, 2000; Lau et al., 2008; Rossi et al., 2013). Our EROS analysis showed an activation at the level of DLPFC, more specifically in the right hemisphere for two close regions across the Brodmann areas BA9 and BA46. Neuroimaging analysis by fMRI reported that the DLPFC corresponding to the areas BA9/BA46 in the right middle frontal gyrus was involved in maintaining integrated information (Collette et al., 2005; Prabhakaran et al., 2000), associated with the acquisition of abstract rules (Monte-Ordoño & Toro, 2017; Sun et al., 2012) and accompanying conscious experience of abstract auditory percepts (Brancucci et al., 2016).

5 Conclusion

The data of the current study demonstrate that cognitive neural dynamics or pre-frontal cortical activity during a passive auditory oddball task can be studied by a non-invasive fast optical imaging technique (EROS) with co-localized EEG measurements. We identified significant co-occurrences of EROS and ERP responses to rare tones. By combining high spatial and temporal resolution we observed that left and right pre-frontal structures were differentially affected. The left dorsal premotor cortex and Broca's area in the left VLPFC were activated by rare tones during the mismatch negativity and N2 ERP components, whereas frequent tones activated a small area in the right superior frontal gyrus involved in memory processing of the auditory stimulus. Moreover, our results showed a significant N500 (N400-like) wave associated with the activity of DLPFC after rare tones, likely related with the maintenance of integrated information.

Acknowledgements We acknowledge the support by the Swiss National Science Foundation, grant no. POLAP1_178329 for MEJ and grant no. IZSEZ0_183401 for RK.

References

Ahveninen, J., Jääskeläinen, I. P., Raij, T., Bonmassar, G., Devore, S., Hämäläinen, M., et al. (2006). Task-modulated "what" and "where" pathways in human auditory cortex. *Proc Natl Acad Sci U S A*, *103*(39), 14608–13.

Alexander, J. E., Polich, J., Bloom, F. E., Bauer, L. O., Kuperman, S., Rohrbaugh, J., et al. (1994). P300 from an auditory oddball task: inter-laboratory consistency. *Int J Psychophysiol*, *17*(1), 35–46.

Apelbaum, J., Silva, E. E., Frick, O., & Segundo, J. P. (1960). Specificity and biasing of arousal reaction habituation. *Electroencephalogr Clin Neurophysiol*, *12*, 829–840.

Ardila, A., Bernal, B., & Rosselli, M. (2016). How Localized are Language Brain Areas? A Review of Brodmann Areas Involvement in Oral Language. *Arch Clin Neuropsychol*, *31*(1), 112–22.

Baniqued, P. L., Low, K. A., Fabiani, M., & Gratton, G. (2013). Frontoparietal traffic signals: a fast optical imaging study of preparatory dynamics in response mode switching. *J Cogn Neurosci*, *25*(6), 887–902.

Bezgin, G., Rybacki, K., van Opstal, A. J., Bakker, R., Shen, K., Vakorin, V. A., et al. (2014). Auditory-prefrontal axonal connectivity in the macaque cortex: quantitative assessment of processing streams. *Brain Lang*, *135*, 73–84.

Blumstein, D. T. (2016). Habituation and sensitization: new thoughts about old ideas. *Anim Behav*, *120*, 255–262.

Brancucci, A., Lugli, V., Perrucci, M. G., Del Gratta, C., & Tommasi, L. (2016). A frontal but not parietal neural correlate of auditory consciousness. *Brain Struct Funct*, *221*(1), 463–72.

Chance, B., Zhuang, Z., UnAh, C., Alter, C., & Lipton, L. (1993). Cognition-activated low-frequency modulation of light absorption in human brain. *Proc Natl Acad Sci U S A*, *90*(8), 3770–3774.

Chiang, T.-C., Liang, K.-C., Chen, J.-H., Hsieh, C.-H., & Huang, Y.-A. (2013). Brain deactivation in the outperformance in bimodal tasks: an FMRI study. *PLoS One*, *8*(10), e77408.

Codispoti, M., Ferrari, V., Junghöfer, M., & Schupp, H. T. (2006). The categorization of natural scenes: brain attention networks revealed by dense sensor ERPs. *Neuroimage*, *32*(2), 583–91.

Collette, F., Olivier, L., Van der Linden, M., Laureys, S., Delfiore, G., Luxen, A., et al. (2005). Involvement of both prefrontal and inferior parietal cortex in dual-task performance. *Brain Res Cogn Brain Res*, *24*(2), 237–51.

Crottaz-Herbette, S., & Menon, V. (2006). Where and when the anterior cingulate cortex modulates attentional response: combined fMRI and ERP evidence. *J Cogn Neurosci*, *18*(5), 766–80.

Delorme, A., & Makeig, S. (2004). EEGLAB: an open source toolbox for analysis of single-trial EEG dynamics including independent component analysis. *J Neurosci Methods*, *134*(1), 9–21.

Delpy, D. T., & Cope, M. (1997). Quantification in tissue near-infrared spectroscopy. *Philos Trans R Soc Lond B Biol Sci*, *352*(1354), 649–659.

Eriksson, J. L., & Villa, A. E. P. (2005). Event-related potentials in an auditory oddball situation in the rat. *BioSystems*, *79*(1–3), 207–212.

Esposito, F., Mulert, C., & Goebel, R. (2009). Combined distributed source and single-trial EEG-fMRI modeling: application to effortful decision making processes. *Neuroimage*, *47*(1), 112–21.

Fabiani, M., & Friedman, D. (1995). Changes in brain activity patterns in aging: the novelty oddball. *Psychophysiology*, *32*(6), 579–94.

Flinker, A., Korzeniewska, A., Shestyuk, A. Y., Franaszczuk, P. J., Dronkers, N. F., Knight, R. T., et al. (2015). Redefining the role of Broca's area in speech. *Proc Natl Acad Sci U S A*, *112*(9), 2871–5.

Gaillard, A. W. (1976). Effects of warning-signal modality on the contingent negative variation (CNV). *Biol Psychol*, *4*(2), 139–54.

Goodin, D. S., Squires, K. C., Henderson, B. H., & Starr, A. (1978). An early event-related cortical potential. *Psychophysiology*, *15*(4), 360–365.

Gratton, E., Fantini, S., Franceschini, M. A., Gratton, G., & Fabiani, M. (1997). Measurements of scattering and absorption changes in muscle and brain. *Philos Trans R Soc Lond B Biol Sci*, *352*(1354), 727–35.

Gratton, G. (2000). "Opt-cont" and "Opt-3D": A software suite for the analysis and 3D reconstruction of the event-related optical signal (EROS). *Psychophysiology*, *37*, S44.

Gratton, G., Brumback, C. R., Gordon, B. A., Pearson, M. A., Low, K. A., & Fabiani, M. (2006). Effects of measurement method, wavelength, and source-detector distance on the fast optical signal. *NeuroImage*, *32*(4), 1576–1590.

Gratton, G., Cooper, P., Fabiani, M., Carter, C. S., & Karayanidis, F. (2018). Dynamics of cognitive control: Theoretical bases, paradigms, and a view for the future. *Psychophysiology*, *55*(3), e13016.

Gratton, G., & Corballis, P. M. (1995). Removing the heart from the brain: compensation for the pulse artifact in the photon migration signal. *Psychophysiology*, *32*(3), 292–299.

Gratton, G., Corballis, P. M., Cho, E., Fabiani, M., & Hood, D. C. (1995). Shades of gray matter: noninvasive optical images of human brain responses during visual stimulation. *Psychophysiology*, *32*(5), 505–509.

Gratton, G., & Fabiani, M. (1998). Dynamic brain imaging: Event-related optical signal (EROS) measures of the time course and localization of cognitive-related activity. *Psychon Bull Rev*, *5*(4), 535–563.

Gratton, G., & Fabiani, M. (2001). Shedding light on brain function: the event-related optical signal. *Trends Cogn Sci*, *5*(8), 357–363.

Gratton, G., & Fabiani, M. (2010). Fast optical imaging of human brain function. *Front Hum Neurosci*, *4*, e00052.

Harper, J., Malone, S. M., & Bernat, E. M. (2014). Theta and delta band activity explain N2 and P3 ERP component activity in a go/no-go task. *Clin Neurophysiol*, *125*(1), 124–132.

Horovitz, S. G., Skudlarski, P., & Gore, J. C. (2002). Correlations and dissociations between BOLD signal and P300 amplitude in an auditory oddball task: a parametric approach to combining fMRI and ERP. *Magn Reson Imaging*, *20*(4), 319–25.

Jausovec, N., & Jausovec, K. (2009). Do women see things differently than men do? *Neuroimage*, *45*(1), 198–207.

Jeong, E., Ryu, H., Jo, G., & Kim, J. (2018). Cognitive Load Changes during Music Listening and its Implication in Earcon Design in Public Environments: An fNIRS Study. *Int J Environ Res Public Health*, *15*(10), e2075.

Jonides, J., Smith, E. E., Marshuetz, C., Koeppe, R. A., & Reuter-Lorenz, P. A. (1998). Inhibition in verbal working memory revealed by brain activation. *Proc Natl Acad Sci U S A*, *95*(14), 8410–3.

Kennan, R. P., Horovitz, S. G., Maki, A., Yamashita, Y., Koizumi, H., & Gore, J. C. (2002). Simultaneous recording of event-related auditory oddball response using transcranial near infrared optical topography and surface EEG. *Neuroimage*, *16*(3), 587–592.

Kiehl, K. A., Bates, A. T., Laurens, K. R., Hare, R. D., & Liddle, P. F. (2006). Brain potentials implicate temporal lobe abnormalities in criminal psychopaths. *J Abnorm Psychol*, *115*(3), 443–53.

Kubota, M., Inouchi, M., Dan, I., Tsuzuki, D., Ishikawa, A., & Scovel, T. (2008). Fast (100–175 ms) components elicited bilaterally by language production as measured by three-wavelength optical imaging. *Brain Res*, *1226*, 124–33.

Kumar, U., Guleria, A., & Khetrapal, C. L. (2015). Neuro-cognitive aspects of "OM" sound/syllable perception: A functional neuroimaging study. *Cogn Emot*, *29*(3), 432–41.

Kutas, M., & Federmeier, K. D. (2000). Electrophysiology reveals semantic memory use in language comprehension. *Trends Cogn Sci*, *4*(12), 463–470.

Kutas, M., & Hillyard, S. A. (1984). Brain potentials during reading reflect word expectancy and semantic association. *Nature*, *307*(5947), 161–163.

Lacadie, C. M., Fulbright, R. K., Rajeevan, N., Constable, R. T., & Papademetris, X. (2008). More accurate Talairach coordinates for neuroimaging using non-linear registration. *Neuroimage*, *42*(2), 717–25.

Lau, E. F., Phillips, C., & Poeppel, D. (2008). A cortical network for semantics: (de)constructing the N400. *Nat Rev Neurosci*, *9*(12), 920–33.

Lee, J., & Kim, S. J. (2010). Spectrum measurement of fast optical signal of neural activity in brain tissue and its theoretical origin. *Neuroimage*, *51*(2), 713–22.

Levitin, D. J., & Tirovolas, A. K. (2009). Current Advances in the Cognitive Neuroscience of Music. *Ann N Y Acad Sci*, *1156*(1), 211–231.

Linden, D. E., Prvulovic, D., Formisano, E., Völlinger, M., Zanella, F. E., Goebel, R., et al. (1999). The functional neuroanatomy of target detection: an fMRI study of visual and auditory oddball tasks. *Cereb Cortex*, *9*(8), 815–23.

Liu, X., Iwanaga, K., & Koda, S. (2011). Circulatory and central nervous system responses to different types of mental stress. *Ind Health*, *49*(3), 265–73.

Low, K. A., Leaver, E., Kramer, A. F., Fabiani, M., & Gratton, G. (2006). Fast optical imaging of frontal cortex during active and passive oddball tasks. *Psychophysiology*, *43*(2), 127–36.

Low, K. A., Leaver, E. E., Kramer, A. F., Fabiani, M., & Gratton, G. (2009). Share or compete? Load-dependent recruitment of prefrontal cortex during dual-task performance. *Psychophysiology*, *46*(5), 1069–79.

Maclin, E. L., Gratton, G., & Fabiani, M. (2003). Optimum filtering for EROS measurements. *Psychophysiology*, *40*(4), 542–7.

Mangalathu-Arumana, J., Beardsley, S. A., & Liebenthal, E. (2012). Within-subject joint independent component analysis of simultaneous fMRI/ERP in an auditory oddball paradigm. *Neuroimage*, *60*(4), 2247–2257.

McCarthy, G., Luby, M., Gore, J., & Goldman-Rakic, P. (1997). Infrequent events transiently activate human prefrontal and parietal cortex as measured by functional mri. *J Neurophysiol*, *77*(3), 1630–1634.

Medvedev, A. V., Kainerstorfer, J., Borisov, S. V., Barbour, R. L., & VanMeter, J. (2008). Event-related fast optical signal in a rapid object recognition task: improving detection by the independent component analysis. *Brain Res*, *1236*, 145–58.

Medvedev, A. V., Kainerstorfer, J. M., Borisov, S. V., Gandjbakhche, A. H., & Vanmeter, J. (2010). "seeing" electroencephalogram through the skull: imaging prefrontal cortex with fast optical signal. *J Biomed Opt*, *15*(6), 061702.

Menon, V., Ford, J. M., Lim, K. O., Glover, G. H., & Pfefferbaum, A. (1997). Combined event-related fMRI and EEG evidence for temporal-parietal cortex activation during target detection. *Neuroreport*, *8*(14), 3029–3037.

Michalewski, H. J., Prasher, D. K., & Starr, A. (1986). Latency variability and temporal interrelationships of the auditory event-related potentials (N1, P2, N2, and P3) in normal subjects. *Electroencephalogr Clin Neurophysiol*, *65*(1), 59–71.

Moisa, M., Siebner, H. R., Pohmann, R., & Thielscher, A. (2012). Uncovering a context-specific connectional fingerprint of human dorsal premotor cortex. *J Neurosci*, *32*(21), 7244–52.

Molnár, M. (1994). On the origin of the P3 event-related potential component. *Int J Psychophysiol*, *17*(2), 129–44.

Monte-Ordoño, J., & Toro, J. M. (2017). Different ERP profiles for learning rules over consonants and vowels. *Neuropsychologia*, *97*, 104–111.

Näätänen, R. (1990). The role of attention in auditory information processing as revealed by event-related potentials and other brain measures of cognitive function. *Behav Brain Sci*, *13*, 201–288.

Näätänen, R., & Picton, T. (1987). The N1 wave of the human electric and magnetic response to sound: a review and an analysis of the component structure. *Psychophysiology*, *24*(4), 375–425.

Nunez, P. (1995). *Neocortical Dynamics and Human EEG Rhythms*. Oxford University Press, New York, NY., xii, 708 pages.

Okada, E., Firbank, M., Schweiger, M., Arridge, S. R., Cope, M., & Delpy, D. T. (1997). Theoretical and experimental investigation of near-infrared light propagation in a model of the adult head. *Appl Opt*, *36*(1), 21–31.

Opitz, B., Mecklinger, A., Von Cramon, D. Y., & Kruggel, F. (1999). Combining electrophysiological and hemodynamic measures of the auditory oddball. *Psychophysiology*, *36*(1), 142–7.

Plakke, B., & Romanski, L. M. (2016). Neural circuits in auditory and audiovisual memory. *Brain Res*, *1640*, 278–88.

Polich, J. (2007). Updating P300: an integrative theory of P3a and P3b. *Clin Neurophysiol*, *118*(10), 2128–2148.

Prabhakaran, V., Narayanan, K., Zhao, Z., & Gabrieli, J. D. (2000). Integration of diverse information in working memory within the frontal lobe. *Nat Neurosci*, *3*(1), 85–90.
Press, C., Weiskopf, N., & Kilner, J. M. (2012). Dissociable roles of human inferior frontal gyrus during action execution and observation. *Neuroimage*, *60*(3), 1671–7.
Proulx, N., Samadani, A.-A., & Chau, T. (2018). Quantifying fast optical signal and event-related potential relationships during a visual oddball task. *Neuroimage*, *178*, 119–128.
Rinne, T., Gratton, G., Fabiani, M., Cowan, N., Maclin, E., Stinard, A., et al. (1999). Scalp-recorded optical signals make sound processing in the auditory cortex visible? *Neuroimage*, *10*(5), 620–4.
Rossi, S., Hartmüller, T., Vignotto, M., & Obrig, H. (2013). Electrophysiological evidence for modulation of lexical processing after repetitive exposure to foreign phonotactic rules. *Brain Lang*, *127*(3), 404–14.
Ruusuvirta, T., Huotilainen, M., & Näätänen, R. (2007). Preperceptual human number sense for sequential sounds, as revealed by mismatch negativity brain response? *Cereb Cortex*, *17*(12), 2777–9.
Ruusuvirta, T., Korhonen, T., Arikoski, J., & Kivirikko, K. (1996). ERPs to pitch changes: a result of reduced responses to standard tones in rabbits. *Neuroreport*, *7*(2), 413–416.
Schaal, N. K., Kretschmer, M., Keitel, A., Krause, V., Pfeifer, J., & Pollok, B. (2017). The Significance of the Right Dorsolateral Prefrontal Cortex for Pitch Memory in Non-musicians Depends on Baseline Pitch Memory Abilities. *Front Neurosci*, *11*, e00677.
Scholkmann, F., Kleiser, S., Metz, A. J., Zimmermann, R., Mata Pavia, J., Wolf, U., et al. (2014). A review on continuous wave functional near-infrared spectroscopy and imaging instrumentation and methodology. *Neuroimage*, *85*, 6–27.
Squires, N. K., Squires, K. C., & Hillyard, S. A. (1975). Two varieties of long-latency positive waves evoked by unpredictable auditory stimuli in man. *Electroencephalogr Clin Neurophysiol*, *38*(4), 387–401.
Stadler, W., Ott, D. V. M., Springer, A., Schubotz, R. I., Schütz-Bosbach, S., & Prinz, W. (2012). Repetitive TMS suggests a role of the human dorsal premotor cortex in action prediction. *Front Hum Neurosci*, *6*, e00020.
Steinbrink, J., Kempf, F. C. D., Villringer, A., & Obrig, H. (2005). The fast optical signal-robust or elusive when non-invasively measured in the human adult? *Neuroimage*, *26*(4), 996–1008.
Steinbrink, J., Kohl, M., Obrig, H., Curio, G., Syré, F., Thomas, F., et al. (2000). Somatosensory evoked fast optical intensity changes detected non-invasively in the adult human head. *Neurosci Lett*, *291*(2), 105–8.
Stevens, M. C., Calhoun, V. D., & Kiehl, K. A. (2005). Hemispheric differences in hemodynamics elicited by auditory oddball stimuli. *Neuroimage*, *26*(3), 782–792.
Strait, M., & Scheutz, M. (2014). What we can and cannot (yet) do with functional near infrared spectroscopy. *Front Neurosci*, *8*, e00117.
Sun, F., Hoshi-Shiba, R., Abla, D., & Okanoya, K. (2012). Neural correlates of abstract rule learning: an event-related potential study. *Neuropsychologia*, *50*(11), 2617–24.
Syré, F., Obrig, H., Steinbrink, J., Kohl, M., Wenzel, R., & Villringer, A. (2003). Are VEP correlated fast optical signals detectable in the human adult by non-invasive nearinfrared spectroscopy (NIRS)? *Adv Exp Med Biol*, *530*, 421–31.
Talairach, J. and Tournoux, P. (1988). *Co-Planar Stereotaxic Atlas of the Human Brain. 3-Dimensional Proportional System: An Approach to Cerebral Imaging*. Georg Thieme Verlag.
Thompson, R. F. (2009). Habituation: a history. *Neurobiol Learn Mem*, *92*(2), 127–134.
Tian, X., Zarate, J. M., & Poeppel, D. (2016). Mental imagery of speech implicates two mechanisms of perceptual reactivation. *Cortex*, *77*, 1–12.
Torricelli, A., Contini, D., Pifferi, A., Caffini, M., Re, R., Zucchelli, L., et al. (2014). Time domain functional nirs imaging for human brain mapping. *Neuroimage*, *85*, 28–50.
Tse, C.-Y., & Penney, T. B. (2008). On the functional role of temporal and frontal cortex activation in passive detection of auditory deviance. *Neuroimage*, *41*(4), 1462–70.
Tse, C.-Y., Rinne, T., Ng, K. K., & Penney, T. B. (2013). The functional role of the frontal cortex in pre-attentive auditory change detection. *Neuroimage*, *83*, 870–879.

Tse, C.-Y., Tien, K.-R., & Penney, T. B. (2006). Event-related optical imaging reveals the temporal dynamics of right temporal and frontal cortex activation in pre-attentive change detection. *Neuroimage*, *29*(1), 314–20.

Tseng, Y.-L., Lu, C.-F., Wu, S.-M., Shimada, S., Huang, T., & Lu, G.-Y. (2018). A Functional Near-Infrared Spectroscopy Study of State Anxiety and Auditory Working Memory Load. *Front Hum Neurosci*, *12*, e00313.

Verleger, R. (1988). Event-related potentials and cognition: A critique of the context updating hypothesis and an alternative interpretation of P3. *Behav Brain Sci*, *11*(3), 343–356.

Villringer, A., & Chance, B. (1997). Non-invasive optical spectroscopy and imaging of human brain function. *Trends Neurosci*, *20*(10), 435–42.

Walz, J. M., Goldman, R. I., Carapezza, M., Muraskin, J., Brown, T. R., & Sajda, P. (2013). Simultaneous EEG-fMRI reveals temporal evolution of coupling between supramodal cortical attention networks and the brainstem. *J Neurosci*, *33*(49), 19212–22.

Wolf, M., Wolf, U., Choi, J. H., Gupta, R., Safonova, L. P., Paunescu, L. A., et al. (2002). Functional frequency-domain near-infrared spectroscopy detects fast neuronal signal in the motor cortex. *Neuroimage*, *17*(4), 1868–75.

World Medical Association. (2013). World Medical Association Declaration of Helsinki: ethical principles for medical research involving human subjects. *JAMA*, *310*(20), 2191–4.

Human Brain Dynamics and Motor Control

Synchronization and Beta Oscillations in Globus Pallidus: Role of the Striatum

Ying Yu, Kaijie Liang, and Qingyun Wang

Abstract Striatum, the main entrance of cortical afferents to the basal ganglia, plays an important role in the Parkinson's disease, and it is often overlooked in the study of Parkinson's disease. In this paper, we add globus pallidus externus (GPe), globus pallidus internus (GPi), and subthalamic nucleus (STN) nuclei on the basis of the striatum-inhibiting microcirculation and build a striatum-GP-STN model. Numerical analysis results show that increasing the synaptic connections of medium spiny neurons (MSNs) to GPe and GPi neurons results in a pathological synchronization of GPe and GPi neurons, and the power spectral density indicates a significant increase in beta-band energy. This is likely to be a potential source of beta-band in the Parkinson's disease. The expansion of the striatum-GP-STN model also provides new ideas for studying Parkinson's disease in the future.

1 Introduction

The effect of the striatum-inhibiting microcirculation in Parkinson's disease (PD) has been increasingly recognized. The striatum, as the main entrance of cortical afferents to the basal ganglia (BG), plays an important role in cognitive processes such as behavioral selection, motor planning, and decision making (Wu et al., 2017). In the current study, the model of the striatum microcirculation mainly includes medium spiny neurons (MSNs) expressing dopamine D1 receptors (D1 MSNs) and MSNs expressing dopamine D2 receptors (D2 MSNs), as well as fast-firing interneurons (FSIs). MSNs receive inhibitory effects from FSIs and other MSNs and receive excitatory projections from the cortex (Damodaran et al., 2015). FSIs receive convergent inputs from multiple cortical regions, and they are interconnected by gap junctions (GJ), which increases the synchronicity of FSI firing (Damodaran et al., 2015). However, the effect of the striatum microcirculation on the rest of the BG is unclear. In particular, the role of the striatum microcirculation in PD remains unknown.

Y. Yu · K. Liang · Q. Wang (✉)
Department of Dynamics and Control, Beihang University, Beijing 100191, China
e-mail: nmqingyun@163.com

A. Lintas et al. (eds.), *Advances in Cognitive Neurodynamics (VII)*, Advances in Cognitive Neurodynamics,
https://doi.org/10.1007/978-981-16-0317-4_19

Mathematical models provide useful tools for studying dynamic behaviors such as abnormal oscillations of neurons, especially the study of the cortical-thalamic-basal ganglia (BGTC) loop. van Albada et al. proposed a mean-field model of the BGTC based on physiology and anatomy to study the mechanism of PD (van Albada & Robinson, 2009). Humphries et al. constructed a new three-dimensional model of the striatal microcircuit's connectivity by using the Izhikevich model (Humphries et al., 2009). Recently, Cabessa and Villa studied the complexity of the attractor dynamics of the basal ganglia cortex network Boolean model, which is more suitable for studying brain models with complex connections (Cabessa & Villa, 2018). Here, we use the conductivity-based Hodgkin–Huxley (HH) model for modeling analysis (So et al., 2012). Based on the striatum-inhibiting microcirculation, we add the globus pallidus externus (GPe), globus pallidus internus (GPi), and subthalamic nucleus (STN) nuclei to build a striatum-GP-STN network model. It is known that the increased beta-band (14–30 Hz) oscillations and abnormal synchronous oscillations of neurons are the main features of PD (McCarthy et al., 2011). As shown in Fig. 1, we analyze the effects of three conditions on synchronization and beta oscillations energy of GPi and GPe neurons. Previous studies have shown that the desynchronization of

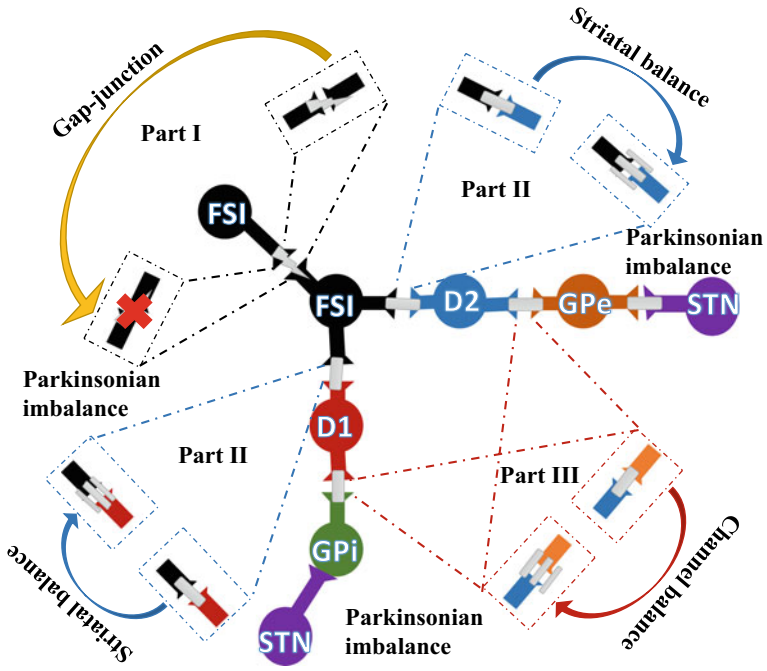

Fig. 1 Striatum-GP-STN network. FSI: fast-firing interneurons; D1:D1 MSNs; D2:D2 MSNs; GPe: globus pallidus externus; GPi: globus pallidus internus. STN: subthalamic nucleus. Part I means the effect of removing GJ connections on GPe and GPi neurons. Part II and Part III represent the effects of increasing synaptic connection of FSIs to D2 MSNs and increasing the synaptic connections of MSNs to GPi and GPe, respectively

FSIs firing is sufficient to alter balanced firing between D1 and D2 MSNs (Damodaran et al., 2014), so Part I means the impact of removing GJ connections on GPe and GPi neurons. In addition, Gittis et al. proposed that there is a selective increase in FSIs-D2 MSNs connectivity in the PD (Gittis et al., 2011), and the balance between direct and indirect channels is closely related to PD, so Part II and Part III represent the effects of increasing synaptic connections of FSIs to D2 MSNs and increasing the synaptic connections of MSNs to GPi and GPe, respectively. Simulation results show that when we change the output of D1/D2 MSNs to the GPi/GPe, the level of synchronization and the energy of the beta-band of globus pallidus (GP) neurons increase significantly. Increasing the connection strength of FSIs to D2 MSNs will enhance the synchronization level of D2 MSNs and also cause the beta oscillations in GP. Our results provide new insights into the role of striatal inhibitory microcircuits in Parkinson's disease.

2 Models and Methods

2.1 Models of Each Neuron

The model we used for GPe, STN, and GPi neurons is established by So et al. (2012), which is the conductance-based model HH neurons. It can be described by a set of ordinary differential equations as follow:

$$C_m \frac{\mathrm{d}V_{\mathrm{STN}}}{\mathrm{d}t} = -I_L - I_K - I_{\mathrm{Na}} - I_T - I_{\mathrm{Ca}} - I_{\mathrm{AHP}} - I_{\mathrm{syn}} + I_{\mathrm{app}} \tag{1}$$

$$C_m \frac{\mathrm{d}V_{\mathrm{GP}}}{\mathrm{d}t} = -I_L - I_K - I_{\mathrm{Na}} - I_T - I_{\mathrm{Ca}} - I_{\mathrm{AHP}} - I_{\mathrm{syn}} + I_{\mathrm{app}} \tag{2}$$

where I_K, I_L, I_{Na}, I_T, I_{Ca}, and I_{AHP} are the potassium current, the leak current, the sodium current, the low-threshold T-type calcium current, the high-threshold calcium current, and the after hyperpolarization potassium current, respectively. I_{app} is the applied constant current, which can adjust the neuron firing property. The specific formulas and parameters for these ion currents can be found in the previous works (Damodaran et al., 2014). I_{syn} is the synaptic current. For STN neurons, the synaptic currents is the inhibitory projections from GPe neurons. For GPi neurons, the synaptic currents include from GPe ($I_{\mathrm{GPe}\to\mathrm{GPi}}$), STN ($I_{\mathrm{STN}\to\mathrm{GPi}}$) and D1 MSNs ($I_{\mathrm{D1}\to\mathrm{GPi}}$), and the synaptic currents for GPe neurons include $I_{\mathrm{GPe}\to\mathrm{GPe}}$, $I_{\mathrm{STN}\to\mathrm{GPe}}$ and $I_{\mathrm{D2}\to\mathrm{GPe}}$. Similar to the previous studies, the modeling of synaptic currents also can be considered as a first-order dynamical differential equation (So et al., 2012).

For the HH model of MSNs, we consider the potassium current, the leak current, the sodium current, and M-current. The interaction between M-current and GABAa

current can produce a robust beta-band oscillation in the striatum (McCarthy et al., 2011). In the previous studies, loss of dopamine is simulated by varying the conductance of the M-current. So the voltage change of MSNs can be described as:

$$C_m \frac{\mathrm{d}V_{\mathrm{MSN}}}{\mathrm{d}t} = -I_L - I_K - I_{\mathrm{Na}} - I_M - I_{\mathrm{syn}} + I_{\mathrm{app}} \tag{3}$$

where the synaptic currents I_{syn} of D1/D2 MSNs include the effects from FSIs and D2/D1 MSNs. Here, we only consider the interaction between D1 and D2 MSNs. For D1 MSNs and D2 MSNs, the I_{syn} include $I_{\mathrm{D2}\to\mathrm{D1}}$, $I_{\mathrm{fs}\to\mathrm{D1}}$ and $I_{\mathrm{D1}\to\mathrm{D2}}$, $I_{\mathrm{fs}\to\mathrm{D2}}$, respectively. Here, $I_{\mathrm{app}} = 6$. Except the strength of the connection between neurons, the detail formulas of ionic currents and parameter values can be found in the works of McCarthy et al. (2011).

FSIs are modeled in the same ways of MSNs except the M-current. And we add the electrical connection between a FSI and its two nearest neighbors. So the formula of FSI can be considered as:

$$C_m \frac{\mathrm{d}V_{\mathrm{FSI}}}{\mathrm{d}t} = -I_L - I_K - I_{\mathrm{Na}} - I_{\mathrm{GJ}} - I_{\mathrm{syn}} + I_{\mathrm{app}} \tag{4}$$

where $I_{\mathrm{GJ}} = g_{\mathrm{GJ}}(V - V_{\mathrm{pre}})$ is the electrical connection, the g_{GJ} is the connection strength, and V_{pre} is the membrane potential of the last neuron. We consider the chemical synaptic connections and electrical connections of FSIs. Here $I_{\mathrm{app}} = 5$. For the parameters of FSI, we refer to the works of Nomura et al. (2003).

2.2 The Network.

Another important problem of modeling is the network connection. The establishment of the connection mode is similar to the work of So et al. (2012). This network is composed of six equally sized group of FSIs, D1 MSNs, D2 MSNs, STN, GPe, and GPi. Here, due to the robustness of MSNs connections (McCarthy et al., 2011), we consider a relatively sparse connection type. Each nucleus is represented by ten neurons, and there is a periodic structure, so the first neuron and the tenth neuron are adjacent. As shown in Fig. 2, each D1 MSN inhibits two immediate neighboring D2 MSNs, as well as sends inhibitions to the three immediate neighboring GPi neurons. Each D2 MSN can send inhibitions to the nearest three D1 MSNs and three GPe neurons. Each FSI projects inhibitions to two adjacent D1 and D2 MSNs simultaneously and has electrical and chemical synaptic connections to two the nearest FSIs. Each GPe neuron inhibits two the nearest GPi neurons, two STN neurons, and two GPe neurons. Each STN neuron sends excitations to two GPe neurons and two GPi neurons. The external input acts on each neuron.

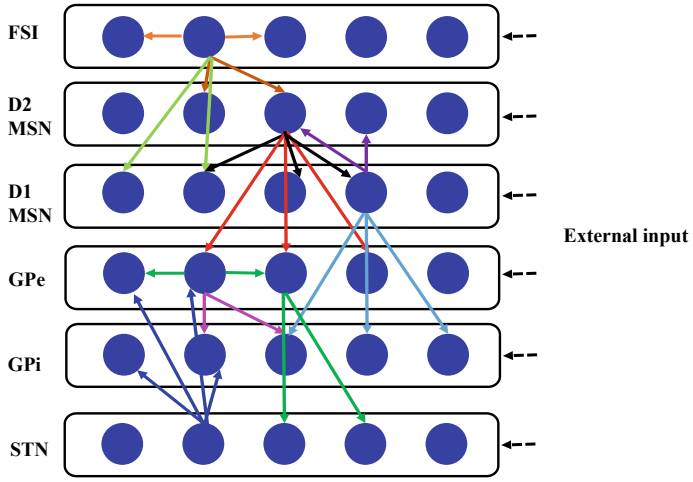

Fig. 2 Striatum-GP-STN network connection diagram. Different colors indicate different synaptic currents. For example, a red arrow indicating the inhibitory current output of D2 to GPe. Each nucleus is represented by ten neurons, and each neuron satisfies the connection shown in the figure. The external input is mainly from the cortex, which acts on each neuron

2.3 The Connection Parameters

Based on the connection data from the previous studies (Damodaran et al., 2015; Gittis et al., 2011; Wu et al., 2017), we define the synaptic strengths of the networks as given in Table 1. g_{ab} is the synaptic strength from b to a. $g_{fsfsgaba}$ means the chemical synaptic connection strength between FSIs, and $g_{fsfsgap}$ means the gap connection strength.

3 Results

Table 1 Synaptic strengths of the networks

Connection		Connection	
g_{d2d1}	0.01 mS/cm^2	$g_{fsfsgap}$	0.1 mS/cm^2
g_{d1d2}	0.03 mS/cm^2	$g_{fsfsgaba}$	0.1 mS/cm^2
g_{d1fs}	0.1 mS/cm^2	g_{ged2}	0.15 mS/cm^2
g_{d2fs}	0.06 mS/cm^2	g_{gid1}	0.15 mS/cm^2
g_{gesn}	0.15 mS/cm^2	g_{gisn}	0.15 mS/cm^2
g_{snge}	0.5 mS/cm^2		

Abnormal synchronization is a major characteristic of PD (Fan & Wang, 2015). To fully understand the effects of the striatum on downstream structures, we consider the changes in the synchrony of GPe, GPi, and STN neurons. Figure 3 represents the spike rasters for the four nuclei in the network. As shown in Fig. 3a, in the healthy state, these neurons exhibit a random discharge state. Figure 3b shows the case of removing GJ. We can see that GPe and GPi neurons seem to have a synchronous tendency, especially GPi neurons, but this trend is not obvious. Figure 3c represents that the connection strength of FSIs to D2 MSNs increases and the connection strength to D1 MSNs is unchanged, i.e., $g_{\mathrm{d1fs}} = 0.1$, $g_{\mathrm{d2fs}} = 0.12$. Due to the increased inhibition of FSIs, it can be seen that D2 MSNs synchronization level is increased significantly, which is consistent with previous experimental results (Gittis et al., 2011). The synchrony of GPe and GPi is also increased, and it is a state of out-of-phase synchronization. Figure 3D shows the increase in synaptic strength of the striatum to GPe and GPi neurons, and here, we define the $g_{\mathrm{gid1}} = g_{\mathrm{ged2}} = 0.3$. GPe and GPi neurons exhibit significant strong bursting synchrony, which is also a characteristic of the Parkinsonian state. It can be seen that the increase in the output of the striatum to GPe and GPi is also responsible for the synchronization of these neurons. However, the changes of STN neurons are not very obvious, and the dis-

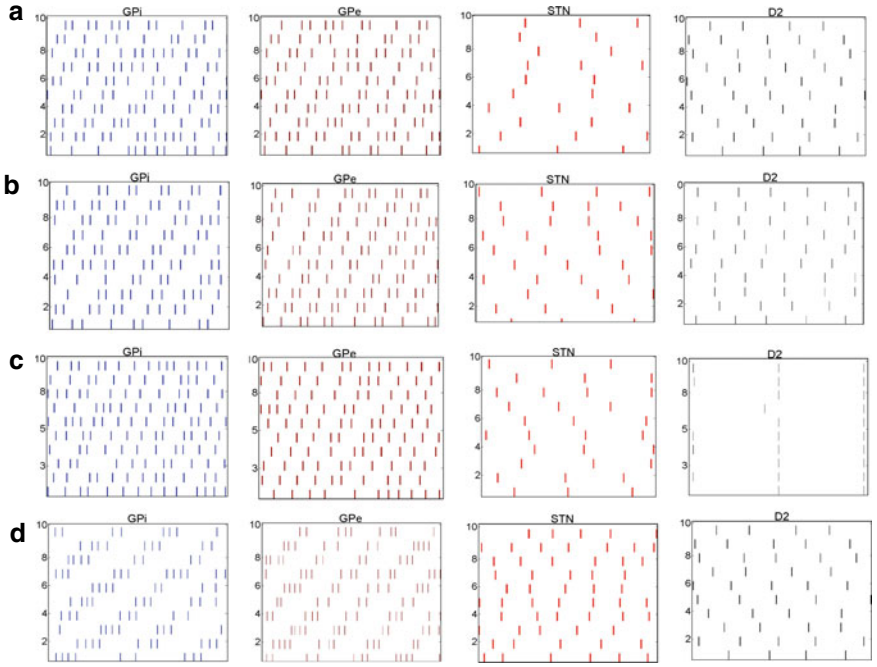

Fig. 3 Spike rasters of striatum-GP-STN network. **a** Normal state. **b** Remove GJ. **c** Increase the inhibitory synapses of FSIs to D2 MSNs, i.e., $g_{\mathrm{d2fs}} = 0.12$. **d** Increase in synaptic strength of the striatum to GPe and GPi, i.e., $g_{\mathrm{d1fs}} = 0.2$, $g_{\mathrm{d2fs}} = 0.1$

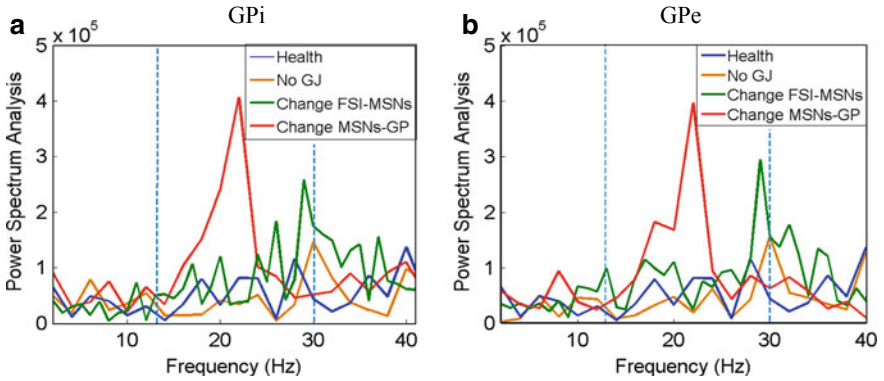

Fig. 4 Power spectral density of GPe and GPi neurons under the four conditions

charge rate is significantly increased only when the inhibitory effect of MSN on GP increased.

Another important feature of PD is the excessive abnormal oscillation of beta-band (McCarthy et al., 2011). So we consider the power of the beta-band in the three pathological conditions and compared them with the state of health. As shown in Fig. 4, the power spectral density of GPe and GPi neurons is displayed. In the healthy state, we can see that there are no distinct peaks in the beta-band. Removing the electrical synapse connection results in a small increase in beta-band power. Previous studies have mentioned that removing GJ will cause a beta oscillation in MSNs (Damodaran et al., 2015), so the beta-band in GPe and GPi neurons are likely to be derived from D1 and D2 MSNs. Increasing the connection strength of FSIs to D2 MSNs also leads to a distinct peak at 28 Hz in GP, which indicates that it is in the Parkinsonian state (Damodaran et al., 2015). It is worth noting that changing the synaptic connections of the striatum to the downstream structures leads to the power of beta-band increase dramatically. This excessive inhibition breaks the internal balance of the GPi and GPe neurons and causes the neurons fire in burst-like manner. Spectral analysis of the spike times of GPi and GPe neurons reveals that the output balance of the striatum to GP plays an important role in PD.

4 Conclusion

The striatum is an important nucleus in the BG. Changing the internal parameters will cause a pathological beta oscillation, which is closely related to Parkinson's disease. By increasing the output parameters of the striatum to the downstream nuclei, we find that the GPe and GPi neurons exhibit a pathological synchronization phenomenon, and the power spectral density indicates a significant increase in the energy of the

beta-band. At the same time, increasing the connection strength of FSIs to D2 MSNs also has an impact on GPe and GPi neurons.

The model can be further extended to a more complete BGTC loop model in the future. The first is the improvement of the interior of the striatum. In addition to MSNs and FSIs, there are cholinergic interneurons and low-threshold spiking neurons in the striatum. Cholinergic interneurons play an important role in the functioning of not only the MSNs via muscarinic receptors but also inhibitory interneurons via nicotinic receptors. In addition to dopamine, muscarinic receptor antagonists are commonly used to treat Parkinson's disease. It was also shown that altered striatal cholinergic tone differentially modulates distinct beta sub-bands (Pittman-Polletta et al., 2018). Secondly, the overall loop structure also can be improved in future studies. Previous studies have shown that pallido-striatal afferents innervate not only MSNs but also interneurons, thus providing inhibition and disinhibition, respectively (Saunders et al., 2015). Such reciprocal inhibition must strongly influence the frequency of oscillations in the network. Besides, neocortical cells also modulate striatal output neurons and motor activity (Melzer et al., 2017). Therefore, the striatum-GP-STN network provides a new idea for the future study of Parkinson's disease, and the development of a more complete model of the cortical-thalamic-basal ganglia will help us better understand the pathogenesis of Parkinson's disease.

Acknowledgements This research was supported by the National Science Foundation of China (Grants 11572015, 11772019).

References

Cabessa, J., & Villa, A. E. P. (2018). Attractor dynamics of a Boolean model of a brain circuit controlled by multiple parameters. *Chaos*, *28*, 106318.

Damodaran, S., Evans, R. C., & Blackwell, K. T. (2014). Synchronized firing of fast-spiking interneurons is critical to maintain balanced firing between direct and indirect pathway neurons of the striatum. *Journal of Neurophysiology*, *111*, 836–848.

Damodaran, S., Cressman, J. R., Jedrzejewski-Szmek, Z., & Blackwell, K. T. (2015). Desynchronization of fast-spiking interneurons reduces β-band oscillations and imbalance in firing in the dopamine-depleted striatum. *Journal of Neuroscience*, *35*, 1149–1159.

Fan, D., & Wang, Q. (2015). Improving desynchronization of parkinsonian neuronal network via triplet-structure coordinated reset stimulation. *Journal of Theoretical Biology*, *370*, 157–170.

Gittis, A. H., et al. (2011). Rapid target-specific remodeling of fast-spiking inhibitory circuits after loss of dopamine. *Neuron*, *71*, 858–868.

Humphries, M. D., Wood, R., & Gurney, K. (2009). Dopamine-modulated dynamic cell assemblies generated by the GABAergic striatal microcircuit. *Neural Networks*, *22*, 1174–1188.

McCarthy, M. M., et al. (2011). Striatal origin of the pathologic beta oscillations in Parkinson's disease. *Proceedings of the National Academy of Sciences*, *180*, 11620–11625.

Melzer, S., Gil, M., Koser, D. E., Michael, M., Huang, K. W., & Monyer, H. (2017). Distinct corticostriatal GABAergic neurons modulate striatal output neurons and motor activity. *Cell Reports*, *19*, 1045–1055.

Nomura, M., Fukai, T., & Aoyagi, T. (2003). Synchrony of fast-spiking interneurons interconnected by GABAergic and electrical synapses. In *International Conference on Neural Information Processing*. IEEE.

Pittman-Polletta, B. R., Quach, A., Mohammed, A. I., Romano, M., Kondabolu, K., Kopell, N. J., et al. (2018). Striatal cholinergic receptor activation causes a rapid, selective and state-dependent rise in cortico-striatal activity. *European Journal of Neuroscience*, *48*, 2857–2868.

Saunders, A., Oldenburg, I. A., Berezovskii, V. K., Johnson, C. A., Kingery, N. D., Elliott, H. L., et al. (2015). A direct GABAergic output from the basal ganglia to frontal cortex. *Nature*, *521*, 85–89.

So, R. Q., Kent, A. R., & Grill, W. M. (2012). Relative contributions of local cell and passing fiber activation and silencing to changes in thalamic fidelity during deep brain stimulation and lesioning: A computational modeling study. *Journal of Computational Neuroscience*, *32*, 499–519.

van Albada, S. J., & Robinson, P. A. (2009). Mean-field modeling of the basal ganglia-thalamocortical system. I. *Journal of Theoretical Biology*, *257*, 642–663.

Wu, Z., Guo, A., & Fu, X. (2017). Generation of low-gamma oscillations in a GABAergic network model of the striatum. *Neural Networks*, *95*, 72–90.

ERPs in Controls and ADHD Patients During Dual N-Back Task

Alessandra Lintas, Sarah K. Mesrobian, Michel Bader, and Alessandro E. P. Villa

Abstract Attention Deficit/Hyperactivity Disorder (ADHD) is a behavioral disorder of childhood and adolescence characterized by symptoms that include impulsiveness, inattention, hyperactivity, impaired decision making, and primary deficits of executive functions. In a vast proportion of the diagnosed adolescents, the clinical symptoms may persist into adulthood and ADHD patients are characterized by Working Memory (WM) impairment. In the present study, we analyze brain dynamics by EEG recordings during the dual *n*-back task in a population of young adults with ADHD and healthy controls. The WM capacity and attention span are tested by *n*-back task, and divided attention is tested by running the task in the visual and auditory modalities concurrently. We analyzed the event-related potentials (ERPs) triggered by the onset of the audio-visual stimuli. In ADHD the amplitude of N200 wave component was only slightly reduced and the peak latency was unaffected. The amplitude of P300 peak was reduced in ADHD with respect to controls at all sites along the midline. The latency of P300 peak in ADHD was reduced at Fz and Cz. In particular, at Fz the latency of ADHD was reduced after a response that required matching the visual cue 1 or 2 trials back in time. These results support the hypothesis that the P300 component, associated with a cognitive workload, peaked earlier in the ADHD than in controls and it may be used to follow the outcome of cognitive training.

A. Lintas (✉) · S. K. Mesrobian · A. E. P. Villa
NeuroHeuristic Research Group, University of Lausanne, Internef 138, Quartier UNIL-Chamberonne, 1015 Lausanne, Switzerland
e-mail: alessandra.lintas@unil.ch
URL: http://www.neuroheuristic.org

A. E. P. Villa
LABEX, HEC Lausanne, Faculty of Law, Criminal Justice and Public Administration, University of Lausanne, Quartier UNIL-Chamberonne, 1015 Lausanne, Switzerland

M. Bader
Research Unit of the University Department of Child and Adolescent Psychiatry (SUPEA), CHUV University Hospital and Faculty of Biology and Medicine, University of Lausanne, 1004 Lausanne, Switzerland

A. Lintas et al. (eds.), *Advances in Cognitive Neurodynamics (VII)*, Advances in Cognitive Neurodynamics,
https://doi.org/10.1007/978-981-16-0317-4_20

1 Introduction

Attention deficit/hyperactive disorder (ADHD) is a persistent neurobiological disorder reflecting a complex interplay between genetic, neurobiological, and environmental risk factors affecting brain networks, leading to emotional and behavioral disturbances, as well as functional impairments and academic failures (Faraone et al., 2015). Patients with ADHD are characterized by inattention, hyperactivity, impulsivity and a multiple range of associated disorders. Working memory (WM) dysfunction has been proposed as one exemplar process involved in ADHD with adverse functional consequences for learning and everyday life activities that might lead to academic failures (Kasper et al., 2012; Rogers et al., 2011). College students with ADHD traits showed deficiency in verbal WM, possibly due to difficulties in memory updating or attentional allocation (Kim & Kim, 2016).

The hypothesis that cognitive training might improve the symptoms in ADHD patients suggested that key brain networks dynamics impaired in ADHD can be recovered through controlled exposures to information processing tasks (Ansari, 2015; Keshavan et al., 2014; Sonuga-Barke et al., 2014; Vinogradov et al., 2012). The dual *n*-back task is a particular WM training aimed at increasing the demand for cognitive processes with the potential of leading to the expansion of resources, i.e. the stimulation of neural plasticity, associated with cognitive functioning (Lilienthal et al., 2013; Lövdén et al., 2010; Salminen et al., 2016). Dual *n*-back working memory training has demonstrated to improve performance gains in tasks such as digit span and reading span, but the transfer to measures of fluid intelligence is yet a controversial issue (Au et al., 2015; Blacker et al., 2017).

Electroencephalography studies are necessary for a deeper level of insight in the underlying cognitive and neural processes involved during cognitive training. An increase in mental workload has been reported to be correlated with a decrease in the EEG power spectrum in the alpha band, an increase at frontal sites in the power of the theta band and a decrease in the P300 amplitude (Brouwer et al., 2012; Gevins & Smith, 2000; Käthner et al., 2014; Roy et al., 2016). A study involving college students during WM training has reported that the ADHD group tended to be less accurate and showed lower posterior EEG power in the alpha band compared to healthy peers (Liu et al., 2016). Poor performance during a WM task in a group of adult subjects with ADHD was associated with inaccuracy in the discrimination of stimulus categories and specific ERPs (Stroux et al., 2016). Functional MRI studies showed decreased activation of the dorso-lateral prefrontal cortex in patients with ADHD for high-load visuospatial WM. These studies showed also greater reliance on posterior spatial attention circuits to store and update spatial position than healthy controls (Bédard et al., 2014).

Impaired decision making is another characteristic of subjects with ADHD which leads them to choose riskier options with unfavorable outcomes in economic and financial settings (Barkley & Fischer, 2010). We have recently tested risk-taking activity of young adult ADHD and we observed that frontal sites were most affected during a probabilistic gambling task, whereas global brain activity was likely to be

affected in controls (Mesrobian et al., 2018a). We have also provided evidence that WM training affects both performance and cortical activity during the gambling task (Mesrobian et al., 2018b). In the current study, for the first time, we present ERPs recorded in ADHD and controls during the dual n-back task. The working memory capacity and attention span are tested by *n*-back task. During this task, participants were required to store a series of letters in memory until they decided to whether or not press a key based on one of those letters during a later trial. We tested also the divided attention by running the *n*-back task in the dual modality, i.e. running visual and auditory modalities concurrently. The brain activity was analyzed by ERPs triggered by the onset of the sensory cues to be remembered for 1-back and 2-back trials. The spatiotemporal distribution of ERP amplitudes and latencies is different for ADHD and control participants. These results suggest that, beyond cognitive training, the dual n-back task can be used to assess the behavioral deficits characteristic of ADHD.

2 Experimental Protocol

2.1 Participant Recruitment

This study was carried out with written informed consent from all participants in accordance with the Declaration of Helsinki (World Medical Association, 2013) and the recommendations of ethical and data security guidelines of the University of Lausanne. The protocol was approved by the Cantonal Ethics Committee of the Canton Vaud (Switzerland). The sample of participants included in this study was formed by young adults, aged between 18 and 29 years. After an initial screening to ensure that they were fulfilling the DSM-IV-TR criteria for inattentive, hyperactive/impulsive or mixed subtypes (American Psychiatric Association (APA), 2000), ADHD patients (number of participants $N = 45$, 21.8 ± 0.5 years, mean $\pm$ SEM) were recruited among patients clinically referred either by the Psychiatric Department of the University Hospital of Lausanne or at a psychiatrist's practice in collaboration with the University Hospital. All participants of the ADHD sample were free of any drug prescription. The ADHD sample was tested against healthy age-matched controls ($N = 42$, 21.9 ± 0.5 years) recruited after a short structured diagnostic interview assessing any major potential psychiatric disorder.

The median (mean $\pm$ SEM) ADHD Index corresponding to the normalized T-score of the Conners' Adult ADHD Rating Scales-Self Report (Screening Version, CAARS-S:SV) (Conners et al., 1999; Fumeaux et al., 2016) was equal to 57.0 (57.3 ± 1.3) and 47.0 (47.8 ± 1.2) for ADHD and controls, respectively. The DSM-IV Inattentive Symptoms Subscale (CAARS-A), the DSM-IV Hyperactive-Impulsive Symptoms Subscale (CAARS-B) and the DSM-IV Total ADHD Symptoms Subscale (CAARS-C) in the ADHD and control groups were equal to 74.0 (71.0 ± 1.9) and 53.0 (52.8 ± 1.6), 61.0 (61.2 ± 1.7) and 46.5 (47.3 ± 1.5), 69.0 (68.8 ± 2.2), and 51.5 (50.6 ± 1.5), respectively.

2.2 Dual n-back task

The dual *n*-back task was adapted in French from the task proposed by Jaeggi et al. (2008). The task consisted of 20 blocks of 20+*n* trials. The participants had to press a key to start a block of trials. In order to test the divided attention, each trial was composed of an auditory and a visual stimuli presented simultaneously. Participants were asked to store a series of auditory and a visual stimuli in memory. They were instructed to maintain their gaze on a white fixation cross at the center of a 19-inch computer screen at a viewing distance of about 70 cm. The visual stimuli were represented by 3.8 × 3.8 cm blue squares, taking place at one of 8 possible locations on the center of the computer screen. Participants were required to press the keyboard key "A" whenever the currently presented square was at the same position as the one *n* stimuli back in the series, depending on level *n* of difficulty. The auditory stimuli were one of 8 letters (Q, D, H, G, K, M, R, and Z) pronounced by a female voice. In a way similar to the visual stimuli, participants were required to press the "L" key whenever the auditory stimulus matched the cue that was presented *n* stimuli back in the sequence.

The task consisted of congruent conditions, under which the current stimulus is the same as the cue presented *n* trials earlier, and incongruent conditions, under which the current stimulus is not the same as the cue presented *n* trials earlier. The participants were asked to store both series of stimuli in memory and to press the key corresponding to the modality of either congruent stimulus. No active responses were required for non-targets, i.e. if a stimulus was not matching the corresponding cue *n* trials back in the sequence. Figure 1 illustrates a dual *2*-Back task with the four possible conditions. If both stimuli matched the cues, the participant had to press keys "A" and "L" simultaneously and the response was termed AcVc, i.e. auditory and visually "congruent" stimuli (response R6 in Fig. 1). If only the auditory stimulus matched the cue to be remembered, the participant had to press only key "L" and the response was termed AcVi, i.e. auditory "congruent" and visually "incongruent" stimuli (response R4 in Fig. 1). Conversely, if the matched cue was only in the visual modality, the participant had to press the key "A" and the response termed AiVc, i.e. auditory "incongruent" and visually "congruent" stimuli (response R3 in Fig. 1). If both auditory and visuospatial stimuli were not matching the cues, the correct response was to refrain pressing any key and let the trial finish 3000 ms after its onset, which corresponds to AiVi response, i.e. auditory and visually "incongruent" stimuli (response R5 in Fig. 1). Notice that in our implementation of the dual *n*-back task, the value of *n* was always the same for visual and auditory stimuli. The task included the four possible conditions described above, irrespective of the level *n* of difficulty.

At the beginning of the session, the goal of the task was to compare the currently presented cues with the stimuli presented in the previous trial, i.e. 1 trial back in time that was a dual *1*-back task. If the response was correct, a green warning light switched on, otherwise a red light indicated a wrong response. The level of difficulty was adjusted as a function of the performance (adaptive difficulty). In one block of trials, a participant had to perform less than 3 mistakes in each modality to raise the level

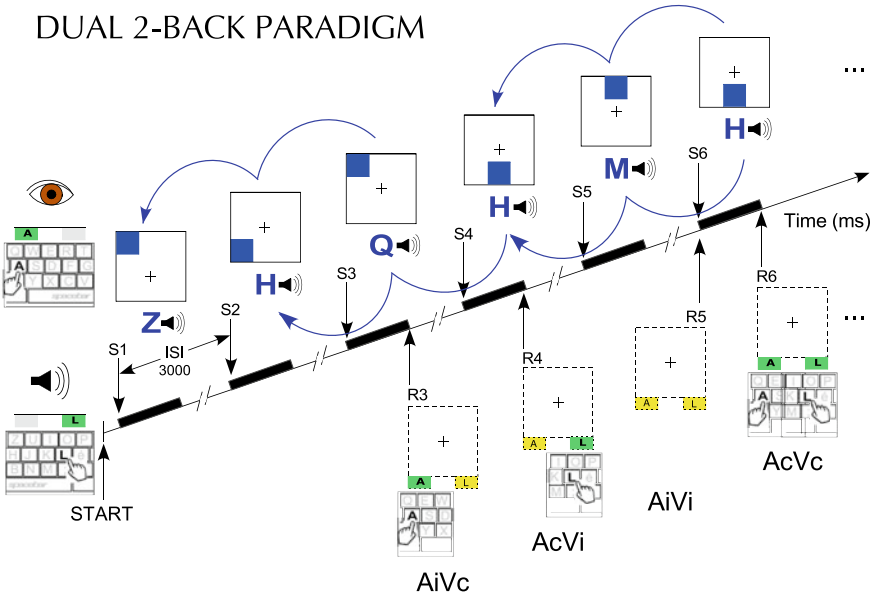

Fig. 1 Experimental design of the dual *2*-back Task. At each trial, the participants were asked to press the "A" key for the visual modality and/or the "L" key for the auditory modality if the stimulus in either modality is identical to the cue presented *2*-trials back in time. This example illustrates the four response conditions occurring in the task: R3: AiVc (auditory "incongruent" and visually "congruent" stimuli); R4: AcVi (auditory "congruent" and visually "incongruent" stimuli); R5: AiVi (auditory and visually "incongruent" stimuli); R6: AcVc (auditory and visually "congruent" stimuli)

of difficulty by 1 in the next block (e.g., from *1*-back to *2*-back). Conversely, 5 errors in any modality provoke a decrease by 1 in the level of difficulty of the next block. In any other case, the level of difficulty remained unchanged between two successive blocks of trials. Each trial lasted 3000 ms after the stimulus onset. The visual stimulus was presented for 500 ms together with the auditory stimulus. The participants had to give an answer during 2500 ms before the next trial, otherwise accounted as no response. The overall duration of the dual *n*-back task was approximately 30 min, depending on the level of difficulty of the blocks and on the pauses taken by the participants between the blocks.

2.3 Electrophysiological Recordings

During the entire duration of a session, electrophysiological signals were recorded using 64 scalp Ag/AgCl active electrodes (ActiveTwo MARK II Biosemi EEG System, BioSemi B.V., Amsterdam, The Netherlands), mounted on a headcap (extended

international 10/20 layout, NeuroSpec Quick Cap) and referenced to the linked earlobes. Electrode impedances were checked and kept always below 20 kΩ for all channels before starting the continuous recording of the EEG. Vertical and horizontal ocular movements were recorded using two pairs of bipolar electrodes and Independent Component Analysis (ICA) was used to remove ocular artifacts (Jung et al., 1997; Mesrobian, 2015). The data acquisition (DC amplifiers and software by Biosemi, USA) was set with a sampling rate 1024 Hz at 24 bits resolution and band-passed filtered with a lower cutoff at 0.05 Hz and an upper cut-off 200 Hz. The brain signals were preprocessed and analyzed with BrainVision Analyzer 2.0.4 (Brain Products, Gilching, Germany). Recorded epochs with incorrect behavioral responses were excluded from the analysis. During the *n*-back task performance, previous studies have shown that the signals recorded by the midline electrodes Fz, Cz, and Pz provided the most significant ERP wave components, more specifically the P300 (Mahncke et al., 2006; Watter et al., 2001). Hence, we decided in this study to analyze ERPs over these sites. The analyses presented here are limited to the N200 and P300 wave components on individual and grand-averaged ERPs. The N200 was defined as the most negative peak observed in the 125–250 ms time window after stimulus onset. The P300 was defined as the most positive peak observed in the 280–500 ms time window after stimulus-onset. For both wave components we measured the peak amplitudes, in μV, and the peak latencies, in ms.

2.4 Statistical Analysis

We used the R framework for statistical computing (R Core Team, 2013; Venables & Ripley, 2002) for all statistical analyses. The median and the mean ± SEM are reported for most variables. All statistical hypotheses were tested with a level of significance of $p = 0.05$, unless otherwise reported. For normally distributed variables we used Student's *t*-test to assess comparisons between groups. Nonparametric analysis (Mann-Whitney-Wilcoxon test) were performed in the other cases. The effect size was computed for all tests with Cohen's *d* for Student's *t*-test and the corresponding *r* for the Mann-Whitney-Wilcoxon test.

3 Results

3.1 Behavioral Performance

During the dual *n*-back task, all participants of both ADHD and control groups reached at least level 2 (i.e., a 2-back task). The index levels for ADHD and controls were equal to 1.80 (1.89 ± 0.07) and 2.00 (2.06 ± 0.08), respectively. These values were not normally distributed and we ran a Mann-Whitney's *U*-test to evaluate the

difference in the index levels. We found no significant difference between the index levels of the two groups ($U = 1137$, $Z = -1.63$, $p = 0.10$, $d = 0.18$). We merged blocks of levels *1*-back and *2*-back trials in a unique merged block of *(1, 2)*-back trials.

The reaction times (RTs) to the auditory and visuospatial stimuli were measured as the interval between the onset of the stimulus and the key-press for the corresponding modality. The distributions of the RTs were not Gaussian. For the auditory stimuli, the RTs for *(1, 2)*-back trials were 1168.0 ms (1167.6 $\pm$ 23.3) and 1062.8 ms (1122.3 $\pm$ 21.9) for ADHD and controls, respectively. For the visuospatial stimuli, the RTs for *(1, 2)*-back trials were 1195.5 ms (1201.1 $\pm$ 22.9) and 1156.8 ms (1200.3 $\pm$ 28.1) for ADHD and controls, respectively. We found no significant difference between the RTs of the two groups neither for the auditory ($U = 3303$, $Z = 1.44$, $p = 0.15$, $d = 0.11$) nor for the visuospatial stimuli ($U = 3597.5$, $Z = 0.55$, $p = 0.58$, $d = 0.04$).

3.1.1 Event-Related Potentials

Figure 2 shows the grand average ERPs triggered by either stimulus in correct trials during performance of the dual *(1, 2)*-back task. In the upper panels of this figure we show that the topographic maps of N200 and P300 are similar for controls (CNTL) and ADHD. The color scales in the topographic maps emphasize that the differences between the groups are mainly in the amplitudes of the signals, as shown in the lower panels by the ERP curves recorded at Fz, Cz and Pz.

Amplitudes and latencies of N200 and P300 reported in Table 1 show that at the frontal site Fz the amplitude of both wave components are significantly reduced in the ADHD group. The amplitude of P300 evoked by the dual *(1, 2)*-back task was reduced in ADHD patients along all the midline sites, but at the central location Cz the difference did not reach the criterion of significance. Table 1 shows also that the latency of N200 peak was not different between groups, but P300 peaked earlier in ADHD at frontal and central sites.

The presentation of two independent streams of stimuli challenged the participant to focus the working memory on a divided attention task. In order to assess the effect of each sensory modality and the combination of both modalities, we have analyzed further in detail the ERPs recorded after correct responses to the four possible combinations, i.e. AcVc (auditory "congruent" and visually "congruent"), AcVi (auditory "congruent" and visually "incongruent"), AiVc (auditory "incongruent" and visually "congruent") and AiVi (auditory "incongruent" and visually "incongruent"). Table 2 shows the values of the N200 and P300 peak amplitudes and peak latencies measured in the four response conditions at the Fz location. Figure 3 shows the ERPs for all *(1, 2)*-back trials recorded at the midline sites.

Notice that for the N200 wave component at site Fz (Table 2), the amplitude tended to be lower in ADHD than in controls for all the response conditions, in particular after a correct auditory and visual "congruent" response (AcVc), but the difference did not reach the level of significance $p < 0.05$. On the opposite, the latencies of

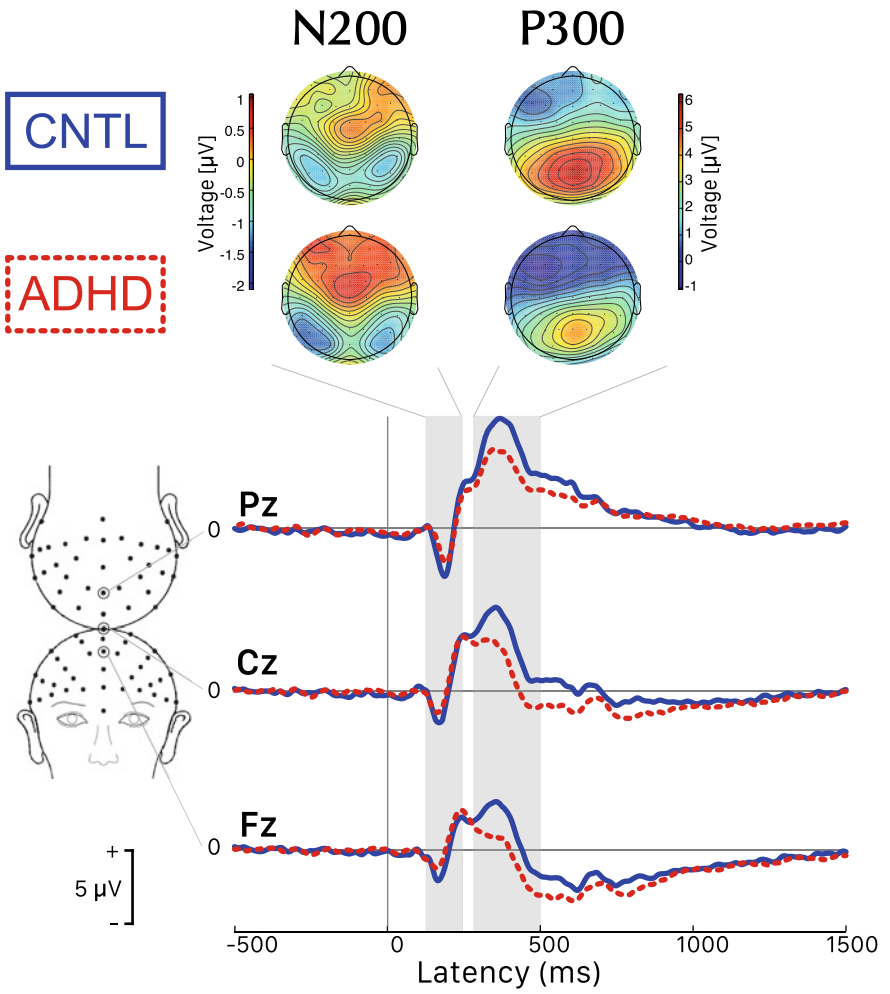

Fig. 2 Grand-averaged ERPs in control and ADHD participants triggered by the stimuli onset in the dual *(1, 2)*-back task. The upper panels show the topographic maps of N200 (time window 125–250 ms) and P300 (time window 280–500 ms). The lower panels show the ERPs recorded at Fz, Cz, and Pz sites for controls (blue curves) and ADHD (dashed red curves). The grey shaded areas correspond to N200 and P300 wave components

N200 peak at Fz tended to be approximately the same in both groups for all response conditions. At the frontal site Fz, the P300 peak amplitude was always significantly lower in ADHD than in controls for all response conditions (Table 2). The latencies of the P300 peak tended to be shorter in ADHD, in particular, if the response condition included a visual "congruent" component (AcVc and AiVc conditions). During these conditions, the latency of the P300 peak for ADHD was approximately 20 ms shorter than in controls.

Table 1 Peak amplitudes and latencies of N200 and P300 wave components

Mesurement	Electrodes	N200			P300		
		ADHD	CNTL	Stat	ADHD	CNTL	Stat
Amplitude (μV)	Fz	2.35	3.61	**0.05**	3.10	4.84	**.004**
		2.77 ± 0.37	3.58 ± 0.34	(0.21)	2.95 ± 0.46	5.07 ± 0.58	(0.30)
	Cz	2.46	3.26	.07	5.38	7.00	0.07
		2.91 ± 0.50	3.94 ± 0.40	(0.20)	5.33 ± 0.58	7.37 ± 0.73	(0.19)
	Pz	3.68	4.03	.08	6.89	9.39	**0.05**
		3.74 ± 0.54	4.48 ± 0.39	(0.19)	7.34 ± 0.60	9.30 ± 0.70	(0.21)
Latency (ms)	Fz	165.8	168.8	0.22	344.2	357.4	.07
		167.3 ± 2.9	172.0 ± 2.9	(0.13)	347.6 ± 5.0	359.5 ± 4.9	(0.19)
	Cz	168.2	169.8	.42	338.1	355.0	**0.05**
		168.5 ± 2.6	171.7 ± 2.8	(0.09)	347.2 ± 5.5	360.0 ± 5.1	(0.21)
	Pz	187.3	181.4	.29	367.7	373.1	.40
		186.7 ± 2.5	182.8 ± 2.2	(0.11)	370.2 ± 5.1	376.9 ± 4.4	(0.09)

At each electrode site, the reported values are median, mean ± SEM; the comparisons between groups are assessed by the Wilcoxon-Mann-Whitney test and the statistic reported here are the p value and the effect size (r), in parenthesis

Table 2 Peak amplitudes and latencies of N200 and P300 wave components at electrode site Fz for the correct trials corresponding to four conditions of the dual *(1, 2)*-back task[a]

Condition	Measurement	*N200*			*P300*		
		ADHD	CNTL	Stat	ADHD	CNTL	Stat
AcVc	Amplitude	2.40	4.05	.06	2.81	5.81	**.02**
	(μV)	2.84 ± 0.50	4.00 ± 0.52	(0.20)	3.66 ± 0.68	5.94 ± 0.72	(0.26)
	Latency	163.1	167.5	.62	342.8	368.2	**.05**
	(ms)	164.5 ± 3.9	167.8 ± 3.8	(0.05)	352.4 ± 7.9	369.3 ± 7.1	(0.21)
AcVi	Amplitude	2.78	4.25	.12	3.00	3.99	**.04**
	(μV)	3.33 ± 0.49	4.11 ± 0.43	(0.17)	2.84 ± 0.57	4.73 ± 0.57	(0.22)
	Latency	167.0	170.4	.26	339.8	348.1	.51
	(ms)	170.4 ± 3.6	175.2 ± 3.5	(0.12)	350.7 ± 7.9	354.9 ± 6.8	(0.07)
AiVc	Amplitude	2.27	2.54	.21	1.94	4.78	**.01**
	(μV)	2.42 ± 0.41	3.22 ± 0.42	(0.14)	2.72 ± 0.56	4.92 ± 0.59	(0.27)
	Latency	162.1	167.0	.10	331.1	355.0	**.04**
	(ms)	162.9 ± 3.6	171.8 ± 4.0	(0.17)	342.6 ± 7.5	363.7 ± 8.1	(0.22)
AiVi	Amplitude	2.08	2.98	.24	1.99	4.15	**.01**
	(μV)	2.48 ± 0.37	2.99 ± 0.36	(0.13)	2.58 ± 0.47	4.59 ± 0.58	(0.28)
	Latency	168.0	167.5	.62	336.9	347.2	.28
	(ms)	171.2 ± 3.9	173.3 ± 4.0	(0.05)	344.6 ± 6.9	350.0 ± 5.2	(0.12)

The reported values are median, mean ± SEM; the comparisons between groups are assessed by the Wilcoxon-Mann-Whitney test and the statistic reported here are the p value and the effect size (r), in parenthesis

[a] Response conditions. *AcVc* Auditory and visually *congruent* stimuli; *AcVi* Auditory *congruent* and visually *incongruent* stimuli; *AiVc* Auditory *incongruent* and visually *congruent* stimuli; *AiVi* Auditory and visually *incongruent* stimuli

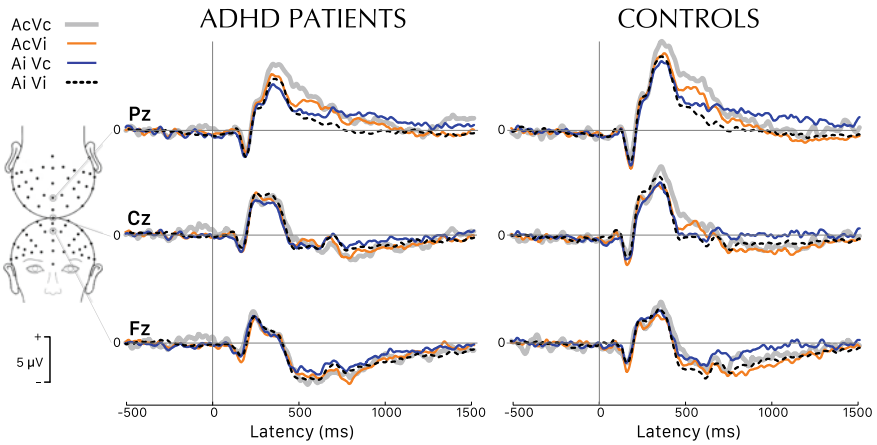

Fig. 3 Grand-averaged ERPs for channels Fz, Cz, and Pz elicited by audio-visual congruent (AcVp, thick grey curves), mixed (AcVi, orange curves; AiVc, blue curves) and incongruent (AiVi, dashed black curves) stimuli for ADHD(left panels) and healthy controls (right panels) triggered by the onset of the dual *(1, 2)*-back task

A factorial analysis of N200 and P300 peaks values was performed with factors group (2 levels: ADHD and controls), response condition (4 levels: AcVc, AcVi, AiVc, AiVi) and electrode sites (3 levels: Fz, Cz, Pz). We used a robust version of three-way ANOVA with default trimming level tr = 0.2 (Wilcox & Schönbrodt, 2016). For N200 we observed a significant main effect of the electrode site for the peak amplitude, $F(2) = 10.782$, $p < 0.01$, and for the peak latency, $F(2) = 150.228$, $p < 0.001$, but no main effect of the group of participants. However, for N200 peak latency we observed a main effect for the group $F(1) = 28.494$, $p < 0.001$ and a significant interaction between group × electrode, $F(1, 2) = 6.359$, $p < 0.05$. The factorial analysis of P300 peak latencies showed a main effect for group, $F(1) = 17.545$, $p < 0.001$, electrode site, $F(2) = 41.057$, $p < 0.001$, and for the response condition, $F(3) = 16.372$, $p < 0.01$, but no effect of interactions between factors. For P300 peak amplitudes we observed also significant main effects for group, $F(1) = 33.696$, $p < 0.001$, electrode site, $F(2) = 129.444$, $p < 0.001$, and for the response condition, $F(3) = 10.865$, $p < 0.05$, but no effect of interactions between factors.

4 Discussion

This study investigated, for the first time to our knowledge, the electrophysiological correlates of the activity evoked by complex auditory/visual stimuli during the dual *n*-back task in young adults with ADHD and age-matched healthy controls. In this study, we observed that performance declined as cognitive load was increased for

both groups. Controls tended to score slightly better than ADHD (a higher level *n* of difficulty in the task), but the difference was not statistically significant as shown by other studies (Bédard et al., 2014; Karatekin et al., 2009; Massat et al., 2012; Mies et al., 2018; Roberts et al., 2012).

During a visual verbal *n*-back task (i.e., the stimuli are letters displayed on a computer screen), Bayerl et al. (2010) observed that mean RTs were significantly higher in ADHD subjects. Other previous studies in a visual verbal *n*-back task emphasized that RT variability was higher in ADHD than controls (Epstein et al., 2011; Feige et al., 2013; Forns et al., 2014). No data of ADHD performance to pure auditory *n*-back task is reported in the literature, to our knowledge. In the dual *n*-back task of this study, we observed, in both groups, that RTs increased with the level *n* of difficulty and we observed that RTs to the congruent auditory stimulus tended to be faster than RTs to the congruent visual stimulus. However, the absence of group differences in RTs found in our results supports the hypothesis that in presence of divided attention the fluctuations of attention are not characteristic of ADHD. It is interesting that this is in line with a recent report that children with ADHD shows less impaired performance when performing the double task (Elosúa et al., 2017).

Abnormal cognitive event-related potentials (ERPs) components were reported in ADHD patients tested with visual and auditory cues other than those of the dual *n*-back task (Barry et al., 2003). Then, even in presence of a behavioral performance that was little impaired, if any, it is likely that early sensory processing is altered in ADHD patients. The N200 is a fronto-central wave component elicited during the dual *n*-back task known to be associated with retrieval of memory representations of a presented stimulus with conflict processing, but it was only slightly affected by cognitive training in healthy subjects (Oelhafen et al., 2013). In line with a visual verbal *n*-back task, we observed that the amplitude of N200 peak was reduced in ADHD, in particular at the frontal sites, without a significant effect on the latency of this peak (Stroux et al., 2016). The N200 is assumed to be an index of interference control when incorrect response preparation must be monitored (Folstein & Van Petten, 2008) and a reduction of its amplitude, although to a lesser extent than reported by Stroux et al. (2016), may suggest reduced interference control abilities in ADHD. However, this is still controversial and other findings do not support the hypothesis of WM and response inhibition representing one integral phenotype of ADHD mediated by the prefrontal cortex (Schecklmann et al., 2013).

The literature reports that under a congruent condition P3 amplitudes were larger and P3 latencies were shorter than under an incongruent condition McEvoy et al. (1998). Higher cognitive demands are associated with a decrease in P300 amplitude in several tasks that evaluate WM, including the *n*-back task, in particular at parieto-central sites (Barker & Bialystok, 2019; Chuang et al., 2019; Käthner et al., 2014; Kim & Kim, 2016; Mun et al., 2017). In both controls and ADHD, we found amplitudes at Pz larger than at Cz, and at Cz larger than at Fz. For all stimuli conditions we observed significantly smaller P300 amplitudes in ADHD, which is consistent with previous studies with ADHD patients (Kim & Kim, 2016). The P300 waveform is thought to reflect general processes of attentional control, stimulus categorization, and processing capacity (Watter et al., 2001). The P300 latency in a high-load task is

shorter than in a low-load task (Dong et al., 2015). In ADHD, the cognitive demand is larger and our results show, in agreement with Kim and Kim (2016), that even in the frontal region the latency of P300 is shorter for visuospatial congruent stimuli, and the difference was statistically significant. Thus, P300 showed that classification of congruent stimuli through the comparison of a current stimulus with the one presented *n* trials earlier is also reflected in the pre-frontal region.

In conclusion, our overall results do not contradict evidence that executive functioning deficits in ADHD underlies impaired emotion regulation, attentional problems, and cognitive deficits (Barkley & Fischer, 2010; Rogers et al., 2011), but the behavioral results alone, in the absence of cognitive training, did not provide evidence for mental effort problems in young adults with ADHD. The subtle electrophysiological effects, however, suggest that ADHD patients may allocate effort in a different way than controls.

Acknowledgements This study was supported by the Swiss National Science Foundation (grant CR 1311-138032). We thank Damiano Cereghetti for his technical contribution to the computer implementation of the *n*-back task.

References

American Psychiatric Association (APA). (2000). *Diagnostic and statistical manual of mental disorders* (4th, text rev. edition). American Psychiatric Association.

Ansari, S. (2015). The therapeutic potential of working memory training for treating mental disorders. *Frontiers in Human Neuroscience*, *9*, 481.

Au, J., Sheehan, E., Tsai, N., Duncan, G. J., Buschkuehl, M., & Jaeggi, S. M. (2015). Improving fluid intelligence with training on working memory: A meta-analysis. *Psychonomic Bulletin & Review*, *22*(2), 366–377.

Barker, R. M., & Bialystok, E. (2019). Processing differences between monolingual and bilingual young adults on an emotion n-back task. *Brain and Cognition*, *134*, 29–43.

Barkley, R. A., & Fischer, M. (2010). The unique contribution of emotional impulsiveness to impairment in major life activities in hyperactive children as adults. *Journal of the American Academy of Child and Adolescent Psychiatry*, *49*(5), 503–513.

Barry, R. J., Clarke, A. R., & Johnstone, S. J. (2003). A review of electrophysiology in Attention-Deficit/Hyperactivity Disorder: I. Qualitative and quantitative electroencephalography. *Clinical Neurophysiology*, *114*(2), 171–183.

Bayerl, M., Dielentheis, T. F., Vucurevic, G., Gesierich, T., Vogel, F., Fehr, C., et al. (2010). Disturbed brain activation during a working memory task in drug-Naive adult patients with ADHD. *Neuroreport*, *21*(6), 442–446.

Bédard, A.-C. V., Newcorn, J. H., Clerkin, S. M., Krone, B., Fan, J., Halperin, J. M., et al. (2014). Reduced prefrontal efficiency for visuospatial working memory in attention-deficit/hyperactivity disorder. *Journal of the American Academy of Child and Adolescent Psychiatry*, *53*(9), 1020–1030.e6.

Blacker, K. J., Negoita, S., Ewen, J. B., & Courtney, S. M. (2017). N-back versus complex span working memory training. *Journal of Cognitive Enhancement*, *1*(4), 434–454.

Brouwer, A.-M., Hogervorst, M. A., van Erp, J. B. F., Heffelaar, T., Zimmerman, P. H., & Oostenveld, R. (2012). Estimating workload using EEG spectral power and ERPs in the n-back task. *Journal of Neural Engineering*, *9*(4), 045008.

Chuang, K.-Y., Chen, Y.-H., Balachandran, P., Liang, W.-K., & Juan, C.-H. (2019). Revealing the electrophysiological correlates of working memory-load effects in symmetry span task with HHT method. *Frontiers in Psychology*, *10*, 855.

Conners, C. K., Erhardt, D., & Sparrow, E. (1999). *Conner's adult ADHD rating scales: Technical manual*. Multi-Health Systems Incorporated (MHS).

Dong, S., Reder, L. M., Yao, Y., Liu, Y., & Chen, F. (2015). Individual differences in working memory capacity are reflected in different ERP and EEG patterns to task difficulty. *Brain Research*, *1616*, 146–156.

Elosúa, M. R., Del Olmo, S., & Contreras, M. J. (2017). Differences in executive functioning in children with attention deficit and hyperactivity disorder (ADHD). *Frontiers in Psychology*, *8*, 976.

Epstein, J. N., Langberg, J. M., Rosen, P. J., Graham, A., Narad, M. E., Antonini, T. N., et al. (2011). Evidence for higher reaction time variability for children with ADHD on a range of cognitive tasks including reward and event rate manipulations. *Neuropsychology*, *25*(4), 427–441.

Faraone, S. V., Asherson, P., Banaschewski, T., Biederman, J., Buitelaar, J. K., Ramos-Quiroga, J. A., et al. (2015). Attention-deficit/hyperactivity disorder. *Nature Reviews Disease Primers*, *1*, 15020.

Feige, B., Biscaldi, M., Saville, C. W. N., Kluckert, C., Bender, S., Ebner-Priemer, U., et al. (2013). On the temporal characteristics of performance variability in attention deficit hyperactivity disorder (ADHD). *PLoS One*, *8*(10), e69674.

Folstein, J. R., & Van Petten, C. (2008). Influence of cognitive control and mismatch on the N2 component of the ERP: A review. *Psychophysiology*, *45*(1), 152–170.

Forns, J., Esnaola, M., López-Vicente, M., Suades-González, E., Alvarez-Pedrerol, M., Julvez, J., et al. (2014). The n-back test and the attentional network task as measures of child neuropsychological development in epidemiological studies. *Neuropsychology*, *28*(4), 519–529.

Fumeaux, P., Mercier, C., Roche, S., Iwaz, J., Bader, M., Stéphan, P., et al. (2016). Validation of the French version of Conners' Parent Rating Scale Revised, short version: Factorial structure and reliability. *Canadian Journal of Psychiatry*, *61*(4), 236–242.

Gevins, A., & Smith, M. E. (2000). Neurophysiological measures of working memory and individual differences in cognitive ability and cognitive style. *Cerebral Cortex*, *10*(9), 829–839.

Jaeggi, S. M., Buschkuehl, M., Jonides, J., & Perrig, W. J. (2008). Improving fluid intelligence with training on working memory. *Proceedings of the National Academy of Sciences of the United States of America*, *105*(19), 6829–6833.

Jung, T.-P., Humphries, C., Lee, T.-W., Makeig, S., McKeown, M. J., Iragui, V., & Sejnowsk, T. J. (1997). Extended ICA removes artifacts from electroencephalographic recordings. In *Proceedings of the 10th International Conference on Neural Information Processing Systems*, NIPS'97 (pp. 894–900). MIT Press.

Karatekin, C., Bingham, C., & White, T. (2009). Regulation of cognitive resources during an n-back task in youth-onset psychosis and attention-deficit/hyperactivity disorder (ADHD). *International Journal of Psychophysiology*, *73*(3), 294–307.

Kasper, L. J., Alderson, R. M., & Hudec, K. L. (2012). Moderators of working memory deficits in children with attention-deficit/hyperactivity disorder (ADHD): A meta-analytic review. *Clinical Psychology Review*, *32*(7), 605–617.

Käthner, I., Wriessnegger, S. C., Müller-Putz, G. R., Kübler, A., & Halder, S. (2014). Effects of mental workload and fatigue on the P300, alpha and theta band power during operation of an ERP (P300) brain-computer interface. *Biological Psychology*, *102*, 118–129.

Keshavan, M. S., Vinogradov, S., Rumsey, J., Sherrill, J., & Wagner, A. (2014). Cognitive training in mental disorders: Update and future directions. *American Journal of Psychiatry*, *171*(5), 510–522.

Kim, S., & Kim, M.-S. (2016). Deficits in verbal working memory among college students with attention-deficit/hyperactivity disorder traits: An event-related potential study. *Clinical Psychopharmacology and Neuroscience*, *14*(1), 64–73.

Lilienthal, L., Tamez, E., Shelton, J. T., Myerson, J., & Hale, S. (2013). Dual n-back training increases the capacity of the focus of attention. *Psychonomic Bulletin & Review*, *20*(1), 135–141.

Liu, Z.-X., Glizer, D., Tannock, R., & Woltering, S. (2016). EEG alpha power during maintenance of information in working memory in adults with ADHD and its plasticity due to working memory training: A randomized controlled trial. *Clinical Neurophysiology*, *127*(2), 1307–1320.

Lövdén, M., Bäckman, L., Lindenberger, U., Schaefer, S., & Schmiedek, F. (2010). A theoretical framework for the study of adult cognitive plasticity. *Psychological Bulletin*, *136*(4), 659–676.

Mahncke, H. W., Bronstone, A., & Merzenich, M. M. (2006). Brain plasticity and functional losses in the aged: Scientific bases for a novel intervention. *Progress in Brain Research*, *157*, 81–109.

Massat, I., Slama, H., Kavec, M., Linotte, S., Mary, A., Baleriaux, D., et al. (2012). Working memory-related functional brain patterns in never medicated children with ADHD. *PLoS One*, *7*(11), e49392.

McEvoy, L. K., Smith, M. E., & Gevins, A. (1998). Dynamic cortical networks of verbal and spatial working memory: Effects of memory load and task practice. *Cerebral Cortex*, *8*(7), 563–574.

Mesrobian, S. K. (2015). *Does working memory training affect decision making?: A neuroeconomic study*. PhD thesis, Faculty of Medicine and Biology, University of Lausanne.

Mesrobian, S. K., Lintas, A., Jacquerod, M., Bader, M., Götte, L., & Villa, A. E. (2018a). An ERP study reveals how training with dual n-back task affects risky decision making in a gambling task in ADHD Patients. In J. M. Delgado-García, X. Pan, R. Sánchez-Campusano, & R. Wang (Eds.), *Advances in cognitive neurodynamics (VI)* (Chap. 34, pp. 271–277). Springer.

Mesrobian, S. K., Villa, A. E. P., Bader, M., Götte, L., & Lintas, A. (2018b). Event-related potentials during a gambling task in young adults with attention-deficit/hyperactivity disorder. *Frontiers in Human Neuroscience*, *12*, 79.

Mies, G. W., Moors, P., Sonuga-Barke, E. J., van der Oord, S., Wiersema, J. R., Scheres, A., et al. (2018). A pilot study of behavioral, physiological, and subjective responses to varying mental effort requirements in attention-deficit/hyperactivity disorder. *Frontiers in Psychology*, *9*, 2769.

Mun, S., Whang, M., Park, S., & Park, M.-C. (2017). Effects of mental workload on involuntary attention: A somatosensory ERP study. *Neuropsychologia*, *106*, 7–20.

Oelhafen, S., Nikolaidis, A., Padovani, T., Blaser, D., Koenig, T., & Perrig, W. J. (2013). Increased parietal activity after training of interference control. *Neuropsychologia*, *51*(13), 2781–27890.

R Core Team. (2013). *R: A language and environment for statistical computing*. R Foundation for Statistical Computing.

Roberts, W., Milich, R., & Fillmore, M. T. (2012). Constraints on information processing capacity in adults with ADHD. *Neuropsychology*, *26*(6), 695–703.

Rogers, M., Hwang, H., Toplak, M., Weiss, M., & Tannock, R. (2011). Inattention, working memory, and academic achievement in adolescents referred for attention deficit/hyperactivity disorder (ADHD). *Child Neuropsychology*, *17*(5), 444–458.

Roy, R. N., Charbonnier, S., Campagne, A., & Bonnet, S. (2016). Efficient mental workload estimation using task-independent EEG features. *Journal of Neural Engineering*, *13*(2), 026019.

Salminen, T., Frensch, P., Strobach, T., & Schubert, T. (2016). Age-specific differences of dual n-back training. *Neuropsychology, Development, and Cognition. Section B, Aging, Neuropsychology and Cognition*, *23*(1), 18–39.

Schecklmann, M., Ehlis, A.-C., Plichta, M. M., Dresler, T., Heine, M., Boreatti-Hümmer, A., et al. (2013). Working memory and response inhibition as one integral phenotype of adult ADHD? A behavioral and imaging correlational investigation. *Journal of Attention Disorders*, *17*(6), 470–482.

Sonuga-Barke, E., Brandeis, D., Holtmann, M., & Cortese, S. (2014). Computer-based cognitive training for ADHD: A review of current evidence. *Child and Adolescent Psychiatric Clinics of North America*, *23*(4), 807–824.

Stroux, D., Shushakova, A., Geburek-Höfer, A. J., Ohrmann, P., Rist, F., & Pedersen, A. (2016). Deficient interference control during working memory updating in adults with ADHD: An event-related potential study. *Clinical Neurophysiology*, *127*(1), 452–463.

Venables, W. N., & Ripley, B. D. (2002). *Modern applied statistics with S*. Statistics and computing (4th ed., 498 pp.). Springer.

Vinogradov, S., Fisher, M., & de Villers-Sidani, E. (2012). Cognitive training for impaired neural systems in neuropsychiatric illness. *Neuropsychopharmacology*, *37*(1), 43–76.
Watter, S., Geffen, G. M., & Geffen, L. B. (2001). The n-back as a dual-task: P300 morphology under divided attention. *Psychophysiology*, *38*(6), 998–1003.
Wilcox, R., & Schönbrodt, F. (2016). A package of RR Wilcox' robust statistics functions. R package version 0.30. https://github.com/nicebread/WRS/tree/master/pkg.
World Medical Association. (2013). World Medical Association Declaration of Helsinki: Ethical principles for medical research involving human subjects. *JAMA*, *310*(20), 2191–2194.

Emotion Analysis Based on Multi-class Common Spatial Features of Scalp EEG

Peiyang Li, Tingyi Tan, Wenxia Qian, Gang Liu, and Yin Tian

Abstract Emotion analysis has earned much attention in affection computing and clinics.

Emotion analysis has earned much attention in affection computing and clinics (Cowie et al., 2001). Especially, major results from EEG-based emotional recognition converge to a consistent conclusion that power distribution difference of EEG signals holds close relation with different emotional states (Mantini et al., 2007), which can be served as discriminative features for emotional recognition. Previous studies mainly utilize power spectra density (PSD) to analyze different emotion states. However, PSD is hard to capture the discriminant features that represent the activation difference between different emotional states efficiently. In the essence, the discern of emotion states based on power spectra is due to the difference existing in the spatial power spectra distribution on scalp for different emotion states. Therefore, the methods which can integrate energy distribution information may further improve the recognition accuracy. Comparing with traditional power spectral analysis, common spatial pattern is capable of assigning higher weights to the channels holding powerful discriminant information between different emotional states (Winkler et al., 2010). Motivated by the above merits of CSP, we designed a hierarchical structure (one to one, one to many, etc.) based on CSP so as to extract features capable of representing the discriminative information between different emotional states from scalp EEG.

P. Li · T. Tan · W. Qian · G. Liu · Y. Tian (✉)
Bio-Information College, Chongqing University of Posts and Telecommunications, Chongqing 400065, China
e-mail: tiany20032003@163.com

A. Lintas et al. (eds.), *Advances in Cognitive Neurodynamics (VII)*, Advances in Cognitive Neurodynamics,
https://doi.org/10.1007/978-981-16-0317-4_21

1 Methods

1.1 EEG Recordings

24 healthy students were recruited to listen to 132 music clips and scored them according to their feelings. Based on the score distributions along valence dimension, nine music clips for three different emotions were selected. Each emotion has three music clips.

Five participants, different from those in the preliminary study, participated in the experiments. All of them are the students in the University of Electronic Science and Technology of China. The EEG data were recorded during the music listening. In each trial, approximately lasting 7–12 s, one of the nine music segments is randomly played for subjects. The interval between two consecutive trials is about 10 s. The experiment consists of 81 trials, with 9 trials for each music segment.

1.2 Multi-CSP for Emotional Feature Extraction

The basic idea of CSP is to find a group of spatial filters that maximize the variance of band-pass filtered EEG signals from one class (Blankertz et al., 2008; Daly & Wolpaw, 2008; De la Torre & Black, 2003), while the variance from the other class gets minimized. However, CSP is mainly designed to handle two-class problem, and it might be keenly for multi-class in emotion recognition. In this work, we exploited one-to-one strategy and expanded binary CSP to multi-CSP. The processing steps are illustrated in Fig. 1.

2 Results

2.1 Spatial Pattern for Different Emotions

Following the training procedure, three kinds of spatial filters could be generated for each concerned frequency band. In order to better understand the association between EEG activities and emotional responses, Fig. 2 illustrates the scalp distribution of spatial filters for gamma bands in three different emotional states for one subject.

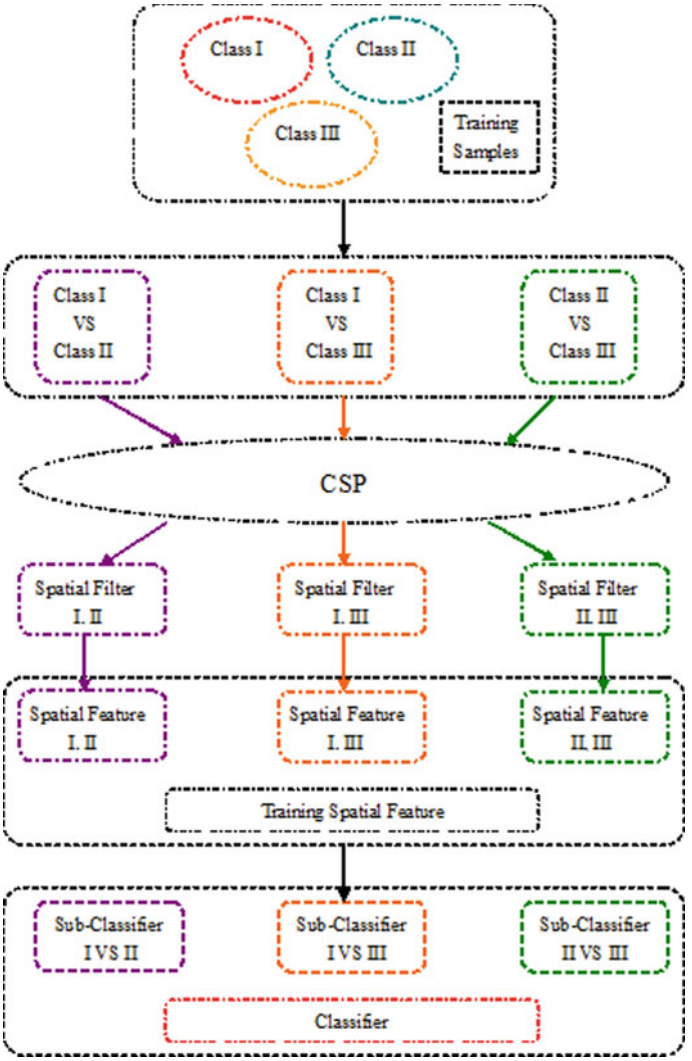

Fig. 1 Training process for CSP-based emotional feature extraction

2.2 Classification Accuracy

Table 1 integrated the average classification accuracies when both multi-CSP and PSD are used to extract features from the EEG signals mentioned in Sect. 2. Table 1 demonstrates that CSP-based approach significantly improved the emotion recognition accuracy compared with the traditional power spectrum-based approach ($p < 0.05$).

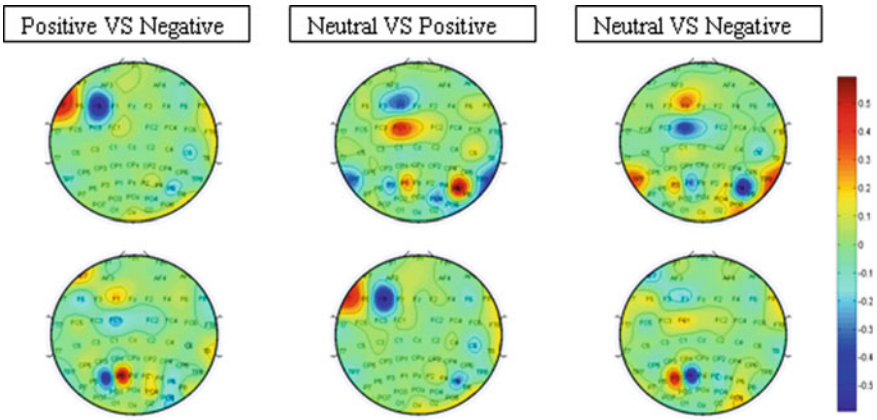

Fig. 2 Training process for multi-CSP-based emotional feature extraction

Table 1 Classification results for different features in delta band

Classification accuracy	Methods	
	PSD	Multi-CSP
Mean	0.79 ± 0.06	0.95 ± 0.07

3 Conclusion

This study developed the CSP-based emotion recognition, which can extract the common spatial information to differentiate the concerned emotions based on scalp EEG. The conducted study revealed that the significant accuracy improvement can be achieved by CSP-based recognition.

Acknowledgements This research is supported by the National Natural Science Foundation of China (#61671097); the Chongqing Research Program of Basic Science and Frontier Technology (No. cstc2017jcyjBX0007).

Conflict of Interest There is no conflict of interest.

References

Blankertz, B., Tomioka, R., Lemm, S., Kawanabe, M., & Muller, K. R. (2008). Optimizing spatial filters for robust EEG single-trial analysis. *IEEE Signal Processing Magazine, 25,* 41–56.

Cowie, R., Douglas-Cowie, E., Tsapatsoulis, N., Votsis, G., Kollias, S., Fellenz, W., et al. (2001). Emotion recognition in human–computer interaction. *Signal Processing Magazine, IEEE, 18,* 32–80.

Daly, J. J., & Wolpaw, J. R. (2008). Brain–computer interfaces in neurological rehabilitation. *Lancet Neurology, 7,* 1032–1043.

De la Torre, F., & Black, M. J. (2003). A framework for robust subspace learning. *International Journal of Computer Vision, 54*, 117–142.

Mantini, D., Perrucci, M. G., Del Gratta, C., Romani, G. L., & Corbetta, M. (2007). Electrophysiological signatures of resting state networks in the human brain. *Proceedings of the National Academy of Sciences of the United States of America, 104,* 13170–13175.

Winkler, I., Jäger, M., Mihajlovic, V., & Tsoneva, T. (2010). Frontal EEG asymmetry based classification of emotional valence using common spatial patterns. *World Academy of Science, Engineering and Technology, 45,* 373–378.

Alterations of Brain Networks Before and After Surgery in Temporal Lobe Epilepsy Patients with Hippocampal Sclerosis

Chuanzuo Yang, Guoming Luan, and Qingyun Wang

Abstract Patients with temporal lobe epilepsy (TLE) are often potential candidates for surgery. Characterizing brain networks before and after surgery can be beneficial for understanding the mechanism of seizure termination and future treatment. In this paper, electroencephalograph (EEG) recordings in the inter-ictal stage before and after surgery (IIB and IIA, respectively) and ictal stage before surgery (IB) were collected from 15 TLE patients with hippocampal sclerosis. Permutation Disalignment Index (PDI) was used to reveal the alterations of brain networks. The results suggested that the brain network in the IB had higher mean strength or lower entropy than that in the IIB, while the network in the IIA was reversed. Furthermore, the network in the IB was more regular, and the postoperative network was further away from that. This may provide potential application in the prediction of surgical outcomes.

1 Introduction

Temporal lobe epilepsy (TLE) is by far the most common type of drug-resistant epilepsy in patients referred for surgery (Asadi-Pooya & Rostami, 2017). The proportion of patients rendered seizure-free after anterior temporal lobectomy remains suboptimal, with a seizure-free rate at short-term follow-up between 66 and 70% (Zhou et al., 2018). And the prediction of surgical outcomes is significant for further strategy of treatment. In this study, we aim to investigate the alterations of brain networks before and after surgery in temporal lobe epilepsy patients with hippocampal sclerosis. It may provide additional insights into surgical effects from the network perspective.

C. Yang · Q. Wang (✉)
Department of Dynamics and Control, Beihang University, Beijing 100191, China
e-mail: nmqingyun@163.com

G. Luan
Beijing Key Laboratory of Epilepsy, Sanbo Brain Hospital, Capital Medical University, Beijing 100093, China

A. Lintas et al. (eds.), *Advances in Cognitive Neurodynamics (VII)*, Advances in Cognitive Neurodynamics,
https://doi.org/10.1007/978-981-16-0317-4_22

Electroencephalograph (EEG) is always an important clinical tool for diagnosis and treatment of epilepsy (Tatum et al., 2018). The previous research mainly focused on the frequency and duration of epileptiform discharge, which were thought to be associated with postoperative seizures (Janszky et al., 2003; Malter et al., 2016). Furthermore, multiple abrupt changes of spectral features were able to provide early warning of seizures (Mammone et al., 2017). However, epilepsy is increasingly understood to be the result of network disorder, and the evolution of epileptic process is always accompanied with alterations of brain networks. In recent years, there have been many methods proposed to quantify interactions between multi-channel recordings (Aksenova et al., 2007). Among these, Permutation Disalignment Index (PDI) was introduced to measure the nonlinear coupling, which was also robust to noise (Villa & Tetko, 2010). Herein, combined with graph theory, PDI was used to investigate the overall and local characteristics of functional brain network. To further interpret these results, random network was introduced to understand the difference in network structure.

2 Materials and Methods

2.1 Materials

Fifteen temporal lobe epilepsy patients (nine females, ages 28.2 ± 4.8 years) with hippocampal sclerosis were recruited from Sanbo Brain Hospital of Capital Medical University in Beijing. All patients underwent surgical treatment and seizure frequency during clinical follow-up 3–12 months postoperatively was significantly decreased. EEG recordings in the inter-ictal stage before and after surgery (IIB and IIA, respectively) and ictal stage before surgery (IB) were collected using a setup with 19 electrodes, which were positioned according to the 10–20 international system. These recordings were uniformly down-sampled 256 Hz and band-pass filtered between 1 and 30 Hz to remove baseline drift and reduce high-frequency artifacts. Independent component analysis (ICA) based on EEGLAB toolbox was performed to exclude additional artificial activity, namely eye movements and cardiac artifact. This study protocol was approved by the Ethics Committee of Sanbo Brain Hospital of Capital Medical University, and all subjects were written informed consent.

2.2 Permutation Disalignment Index

Permutation Disalignment Index (PDI) was developed as a symbolic descriptor to measure the nonlinear correlation between time series. Given two time series x and y both with N samples, they can be projected into an m-dimensional space:

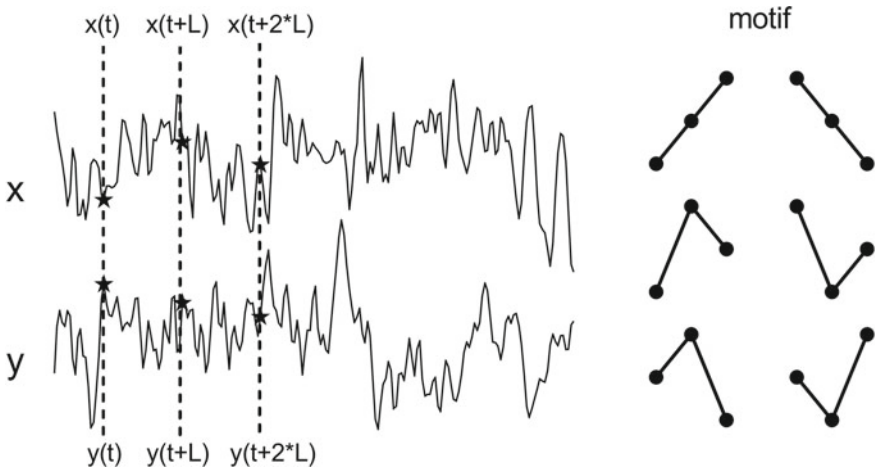

Fig. 1 Projections of the times series x and y into the motif space. When the embedding dimension m is 3, there exist six possible motifs

$$\begin{cases} X_t = [x(t), x(t+L), \ldots, x(t+(m-1)L]^T \\ Y_t = [x(t), x(t+L), \ldots, x(t+(m-1)L]^T \end{cases} \tag{1}$$

where m is the embedding dimension and L is the time lag. For a given embedding dimension m, there exist $m!$ possible motifs, as shown in Fig. 1. If X_t and Y_t have the same motif π_k ($k = 1, \ldots, m!$), the corresponding frequency $n(\pi_k)$ will be counted. By this means, a coinstantaneous occurrence rate $P_{x,y}(\pi_k)$ of each motif π_k can be defined as:

$$P_{x,y}(\pi_k) = \frac{n(\pi_k)}{N-(m-1)L} \tag{2}$$

Similar to the definition of permutation entropy, PDI can be computed as:

$$\mathrm{PDI}(x, y) = \frac{1}{1-\alpha} \log \left[\sum_{k=1}^{m!} P_{x,y}(\pi_k)^{\alpha} \right] \tag{3}$$

In order to reveal the nonlinear correlation intuitively, it can be normalized:

$$\mathrm{nPDI}(x, y) = \frac{\sqrt{\mathrm{PDI}(x, x)\mathrm{PDI}(y, y)}}{\mathrm{PDI}(x, y)} \tag{4}$$

The more coupled time series x and y are, the higher the nPDI is expected to be. In this study, the parameters $m = 3$, $L = 1$ and $\alpha = 2$ are adopted.

2.3 Brain Connectivity

Changes in brain function are often associated with the alterations of brain networks. Based on the nPDI, the relationships between multi-channel recordings can be represented by a weighted full connection network. Graph theory is further employed to reveal the characteristics of functional brain connectivity.

The average of nondiagonal elements M indicates the overall strength of connections, and information entropy E can describe the weight distribution.

$$M = \frac{1}{K(K-1)} \sum_{i \neq j}^{K} \mathrm{nPDI}(i, j) \tag{5}$$

$$E = -\sum_{i} p(i) \log_2 p(i) \tag{6}$$

where K is the number of channels and $p(i)$ is the probability of falling into the ith interval.

In order to capture the activity changes between regions in different states, the density D and clustering coefficient C of weighted networks are calculated. They can provide additional insights into the dominant alterations and involved regions.

$$D(i) = \frac{1}{(K-1)} \sum_{j, j \neq i} \mathrm{nPDI}(i, j) \tag{7}$$

$$C(i) = \frac{\sum_{j,t} \sqrt[3]{\mathrm{nPDI}(i, j)\mathrm{nPDI}(j, t)\mathrm{nPDI}(t, i)}}{(K-1)(K-2)\max(\mathrm{nPDI})} \tag{8}$$

where max(nPDI) represents the maximum elements of nondiagonal elements.

To deeply understand these network structures, it is significant to investigate their network characteristics relative to random network. However, many randomization methods for weighted networks are not convincing, and the results may be uninterpretable (Stahn & Lehnertz, 2017). As a result, we transform weighted networks into binary networks through a reasonable static threshold to further reveal relative network characteristics, such as relative shortest path and relative clustering coefficient.

3 Results

3.1 Overall Distribution

The overall characteristics of weighted networks in the IIB, IB and IIA are reflected through the comparison of the mean strength M and the entropy of weight distribu-

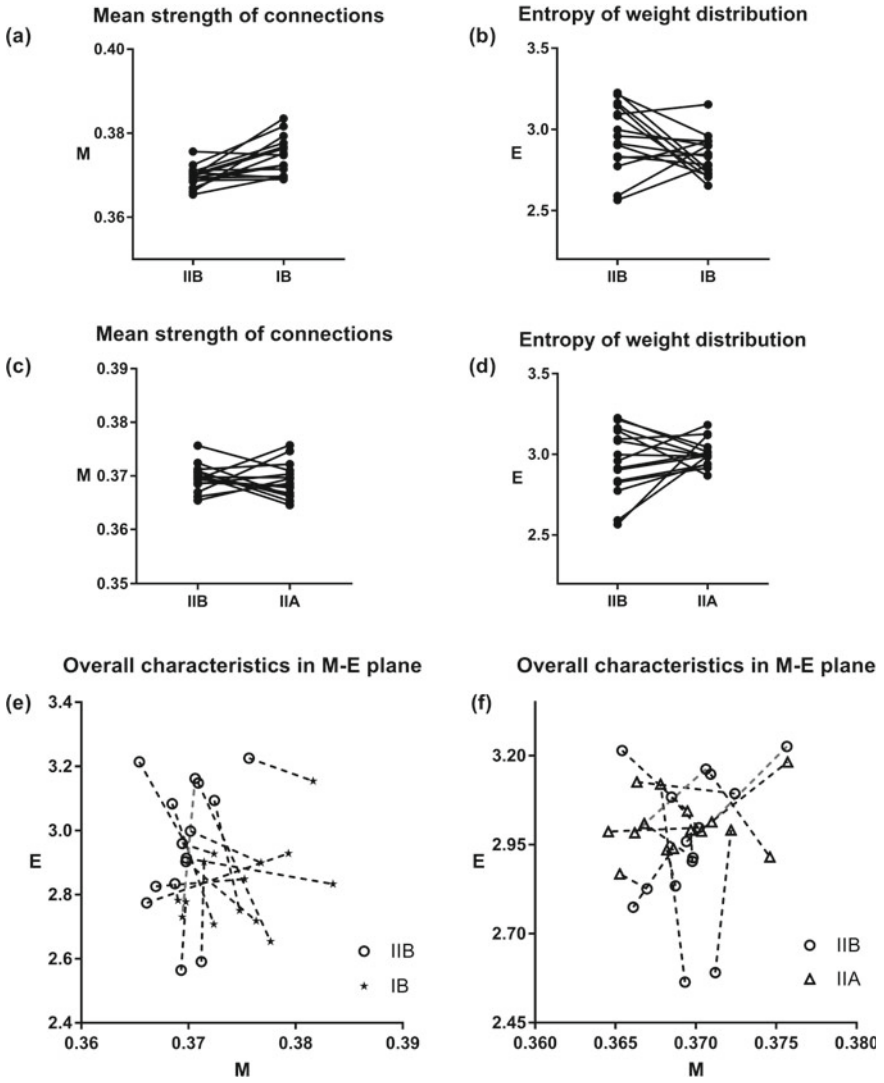

Fig. 2 Overall characteristics of weighted network. **a**, **b** The difference of mean strength and entropy of weight distribution between the IIB and IB. Characteristics from the same patient are paired. **c**, **d** The difference of mean strength and entropy of weight distribution between the IIB and IIA. **e** The distribution of overall characteristics in M–E plane during the IIB and IB. **f** The distribution of overall characteristics in M–E plane during the IIB and IIA. These exceptions are dotted in red

tion E (Fig. 2a–d). Paired t-tests were performed to identify the significant changes between stages. Compared with the IIB, the mean strength in the IB is significantly higher (p value $= 0.0014$), while the mean strength in the IIA has no significant

difference (p value > 0.05). The entropy of weight distribution cannot characterize different stages, either. However, the differences between stages can be distinguished in the $M - E$ plane (Fig. 2e, f). Compared with the IIB, the IB has higher mean strength or lower entropy (except for 1 patient), while the IIA has lower mean strength or higher entropy (except for two patients). It suggests that the alterations of brain networks between stages mainly depend on the adjustment of edge strength or the distribution of weighted edges.

3.2 Local Characteristics

Each electrode records the corresponding local activity, which plays different roles in the epileptic process. The density D and clustering coefficient C are calculated to capture the changes in local characteristics. Compared with the IIB, the number of patients with increased D and C in the IB and the number of patients with decreased D and C in the IIA are counted in Fig. 3a, b. When seizures occur, the local activity

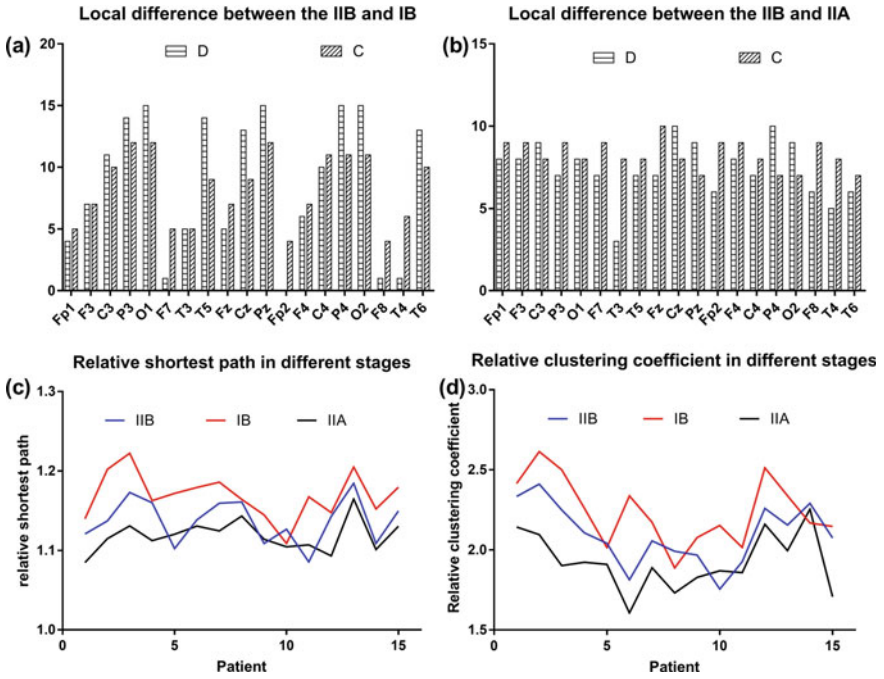

Fig. 3 **a** Compared with the IIB, the number of patients with increased density D and clustering coefficient C in the IB for each electrode. **b** Compared with the IIB, the number of patients with increased density D and clustering coefficient C in the IIA for each electrode. **c** Relative shortest path in the IIB, IB and IIA for each patient. **d** Relative clustering coefficient in the IIB, IB and IIA for each patient

in bilateral temporal, parietal and occipital lobes usually increases, while electrical activity in the frontal lobe decreases. The difference between the IIB and IIA is not significant, which may be related to individual brain network.

3.3 Relative Characteristics

To further understand the network structure, binary random networks with the same number of nodes, number of edges and degree distribution with transformed network from weighted network are introduced. Relative shortest path and clustering coefficient are used to characterize the network efficiency (Fig. 3c, d). Compared with the IIB, the IB has longer relative shortest path and higher relative clustering coefficient, indicating that brain network in the IB is more regular. It is consistent with the previous studies (Mammone et al., 2008). The postoperative network is further away from that in the IB, which may interpret the favorable surgical outcome.

4 Conclusion

Permutation Disalignment Index combined with graph theory is used to investigate the alterations of brain networks before and after surgery in temporal lobe epilepsy patients with hippocampal sclerosis. When seizures occur, the brain network has higher mean strength or lower entropy, and the increased local activity in bilateral temporal, parietal and occipital lobes plays a dominant role in the process. Furthermore, the network in the IB seems more regular. After surgical treatment, brain connectivity is further away from the epileptic network, which may provide promising application in the prediction of surgical outcomes.

Acknowledgements This research was supported by the National Science Foundation of China (Grants 11772019, 81671285), the Capital Health Research and Development of Special (2016-1-8012), Beijing Municipal Science & Technology Commission, China (Z161100000516230, Z161100002616016).

References

Aksenova, T. I., Volkovych, V. V., & Villa, A. E. P. (2007). Detection of spectral instability in EEG recordings during the preictal period. *Journal of Neural Engineering*, *4*(3), 173–178.

Asadi-Pooya, A. A., & Rostami, C. (2017). History of surgery for temporal lobe epilepsy. *Epilepsy & Behavior*, *70*(Pt A), 57–60.

Janszky, J., Schulz, R., Hoppe, M., & Ebner, A. (2003). Spikes on the postoperative EEG are related to preoperative spike frequency and postoperative seizures. *Epilepsy Research*, *57*(2–3), 153–158.

Malter, M. P., Bahrenberg, C., Niehusmann, P., Elger, C. E., & Surges, R. (2016). Features of scalp EEG in unilateral mesial temporal lobe epilepsy due to hippocampal sclerosis: Determining factors and predictive value for epilepsy surgery. *Clinical Neurophysiology*, *127*(2), 1081–1087.

Mammone, N., Bonanno, L., Salvo, S. D., Marino, S., Bramanti, P., Bramanti, A., et al. (2017). Permutation disalignment index as an indirect, EEG-based, measure of brain connectivity in MCI and AD patients. *International Journal of Neural Systems*, *27*(5), 1–19.

Schindler, K. A., Bialonski, S., Horstmann, M.-T., Elger, C. E., & Lehnertz, K. (2008). Evolving functional network properties and synchronizability during human epileptic seizures. *Chaos*, *18*(3), 033119.

Stahn, K., & Lehnertz, K. (2017). Surrogate-assisted identification of influences of network construction on evolving weighted functional networks. *Chaos*, *27*(12), 123106.

Tatum, W. O., Rubboli, G., Kaplan, P. W., Mirsatari, S. M., Radhakrishnan, K., Gloss, D., et al. (2018). Clinical utility of EEG in diagnosing and monitoring epilepsy in adults. *Clinical Neurophysiology*, *129*(5), 1056–1082.

Villa, A. E. P., & Tetko, I. V. (2010). Cross-frequency coupling in mesiotemporal EEG recordings of epileptic patients. *Journal of Physiology (Paris)*, *104*(3–4), 197–202.

Zhou, X., Yu, T., Zhang, G., Ni, D., Qiao, L., Wang, X., et al. (2018). The surgical outcome of patients with bilateral temporal lobe epilepsy. *Epilepsy Research*, *144*, 7–13.

PSO-Sub-ABLD-Based Parameter Optimization for Motor-Imagery BCI

Feiyu Yin, Yangyang Miao, Xingyu Wang, and Jing Jin

Abstract Common spatial pattern (CSP) is one of effective feature extraction algorithms, which is widely applied to motor imagery (MI)-based brain–computer interface (BCI). However, its performance is susceptible to artifacts and noise. Therefore, some researchers proposed Sub-Alpha-Beta Log-Det Divergences (Sub-ABLD) algorithm to improve the performance of BCI systems. The performance of Sub-ABLD algorithm depends on the values of hyperparameters α, β and η. In this study, a strategy named PSO-Sub-ABLD was proposed to select three hyperparameters with particle swarm optimization (PSO). Two public BCI competition datasets were used to validate the effectiveness of the proposed strategy. The results show that compared with CSP and Sub-ABLD with default hyperparameters, PSO-Sub-ABLD method gains better classification accuracy.

1 Introduction

Brain–computer interface (BCI) system is a new technology designed to create a pathway that connects the human brain and external devices without peripheral nerves and muscles (Xu et al., 2018). The BCI system provides a new means of communication for people with severe neuromuscular disorders by decoding task-related electroencephalogram (EEG) recordings and translating them into computer instructions for control and communication with external devices (Wolpaw et al., 2002; Jin et al., 2011).

So far steady state visually evoked potentials (da Cruz et al., 2015), P300 evoked potentials (Jin et al., 2015), slow cortical potentials (Mensh et al., 2004), and event-related desynchronization (ERD) (Pfurtscheller, 1977)/event-related synchronization (ERS) (Pfurtscheller, 1992) are neural response patterns commonly used in BCI systems. Motor imagery (MI)-based BCI systems, which are based on the ERD and

F. Yin · Y. Miao · X. Wang · J. Jin (✉)
Key Laboratory of Advanced Control and Optimization for Chemical Processes, Ministry of Education, East China University of Science and Technology, Shanghai, China

A. Lintas et al. (eds.), *Advances in Cognitive Neurodynamics (VII)*, Advances in Cognitive Neurodynamics,
https://doi.org/10.1007/978-981-16-0317-4_23

ERS phenomena, are widely used as it is easier to operate than other systems based on external stimulus (Qiu et al., 2016).

Common spatial pattern (CSP) has proven to be a very effective feature extraction method (Ramoser et al., 1998), and its principle is to find spatial filters, to effectively evaluate discriminant information of MI by maximizing the variances of the projected signal of one class while minimizing another (Zhang et al., 2015; Blankertz et al., 2008). Since the EEG signal is very sensitive to noise, outliers caused by noise will cause poor computation of spatial filters based on the spatial covariance matrix, which leads to poor classification accuracy (Lotte & Guan, 2011; Thiyam et al., 2017). To address this problem, a large number of improved algorithms based on CSP are proposed. Sub-ABLD algorithm is a modified algorithm of CSP, and its principle is to overcome the problem caused by the non-stationary nature of EEG data by appropriately scaling the conditional covariance matrix and using different filter selection strategies (Thiyam et al., 2017). Sub-ABLD algorithm shows a certain degree of robustness to outliers trials in EEG data (Feng et al., 2018). Three real hyperparameters α, β, and η affect the performance of Sub-ABLD (Thiyam et al., 2017), so how to choose better hyperparameters has a greater impact on improving the performance of Sub-ABLD algorithm. For the selection of hyperparameters, evolutionary algorithms (EA) such as genetic algorithm (GA) (Garrett et al., 2003) and particle swarm optimization (PSO) often have better effects. Compared with GA, PSO is widely used because of its advantages of simple programming, few parameters, and global search. Thus, this present study proposed the method of optimization hyperparameters of Sub-ABLD with PSO (PSO-Sub-ABLD) and compares it with CSP and Sub-ABLD with default hyperparameters. Two BCI competition datasets are selected to evaluate the performance.

The remainder content of this article is as follows: Sect. 2 describes the competition datasets used in this paper. Section 3 introduces the proposed method. Section 4 shows results. Finally, Sect. 5 concludes this study.

2 Description of the Data

In this paper, two competition datasets are used to evaluate the effectiveness of optimization parameters with PSO in the MI classification (Fig. 1).

(1) Dataset1 (BCI competition IV datasets I): The dataset was recorded from 4 healthy subjects (named as a, b, f, and g) at 59 electrodes with sampling rate 100 Hz, during right hand, left hand, and foot MI tasks with a total of 200 trials that two classes of three tasks would be selected (Zhang et al., 2012). Each trial started with left, right, or bottom visual cues on the screen for a duration of 4 s and the subject completed the motor imagery tasks. More details about this dataset can be seen in the following website: http://www.bbci.de/competition/IV/.

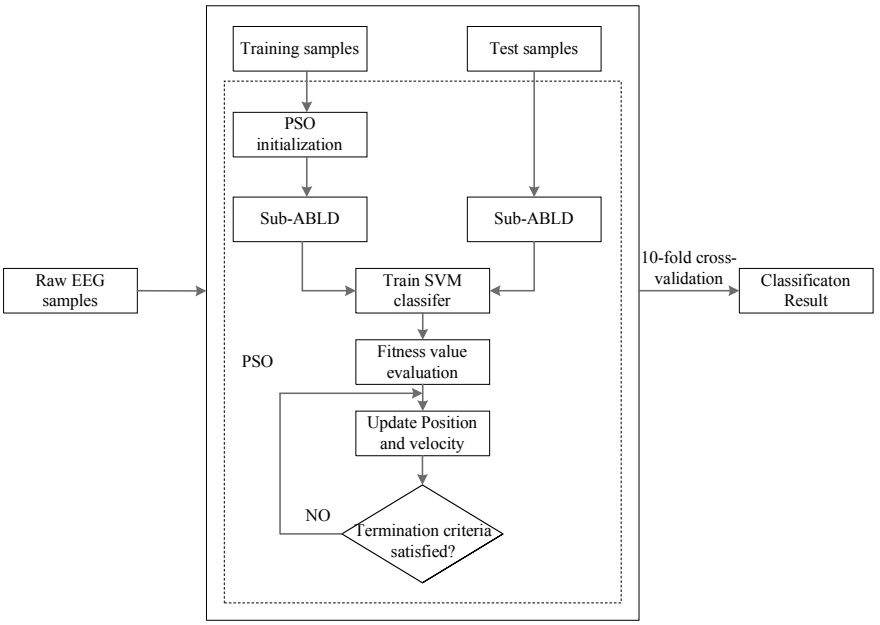

Fig. 1 Flow diagram of optimizing hyperparameters of Sub-ABLD with PSO

(2) Dataset2 (BCI competition III datasets IVa): The dataset was recorded from 5 healthy subjects (aa, al, av, aw, and ay) at 118 electrodes with down-sampling rate 100 Hz, during right hand and foot MI tasks with a total of 280 trials. The visual cue for each trial lasts for 3.5 s, in which only the right hand and right foot cues were displayed in the competition (Novi et al., 2007). More information about this dataset can be found from the following website: http://www.bbci.de/competition/iii/.

3 Method

3.1 Data Processing

For two datasets, starting from 0.5 to 2.5 s of EEG segment was selected from each trial (Song & Epps, 2007). The EEG data were third-order band-pass filtered with Butterworth band-pass filter of 8–30 Hz in this study (Sun et al., 2010).

3.2 Sub-Alpha-Beta Log-Det Divergences

Sub-ABLD is an improved method of CSP algorithm. Its main purpose is to extract d expected spatial filters to reduce the impact of outliers contained in the EEG data on feature extraction. It is mainly divided into the following two steps. First, the discriminant subspace of the spatial filters is obtained by a robust method, and then, the EEG signal is filtered by the spatial filter obtained by discriminating the subspace. In the second step, the features are extracted with CSP algorithm. The input parameters of Sub-ABLD algorithm are the covariance matrices M_j, N_j of two types of samples, hyperparameters α, β, η and the number of filters. The process of obtaining the final spatial filter matrix is as follows:

(1) Compute the prior probability $p(c_1)$, $p(c_2)$ and the average covariance matrix M, N of each class.
(2) Compute the average covariance matrix $\mathrm{Cov}(x)$ of the population (all types of stimuli) and perform eigenvalue decomposition on it.

$$\mathrm{Cov}(x) = p(c_1)M + p(c_2)N \tag{1}$$

$$\mathrm{Cov}(x) = U_1 \Delta U_1^T \tag{2}$$

(3) Compute the whitening matrix T:

$$T = \Delta^{-\frac{1}{2}} U_1^T \tag{3}$$

(4) The whitening conversion process is performed on the covariance matrix of two types of samples and the average covariance matrix of each class to obtain $\hat{M}_j$, $\hat{N}_j$, $\hat{M}$, $\hat{N}$.
(5) Compute scaling parameters k:

$$k = \begin{cases} k_{\mathrm{inf}} + \varepsilon & \text{for } k_{\mathrm{inf}} \geq 1 \\ 1 & \text{for } 1 \in (k_{\mathrm{inf}}, k_{\mathrm{sup}}) \\ k_{\mathrm{sup}} - \varepsilon & \text{for } k_{\mathrm{stup}} \leq 1 \end{cases} \tag{4}$$

(6) Initialize the iteration counter, $i = 0$;
(7) Initialize the semi-orthogonalization matrix $\Omega^{(i)} = I_{n \times d}$, where n refers to the size of the average covariance matrix of each class, and d is the number of filters;
(8) Compute robust criterion:

$$f(\Omega^{(i)}) = \eta(p(c_1)\frac{1}{N_1}\Sigma_{j=1}^{N_1} D_{AB}^{(\alpha,\beta)}((\Omega^{(i)})^T \hat{N}_j(\Omega^{(i)})||k(\Omega^{(i)})^T \hat{N}(\Omega^{(i)})))$$
$$- \eta(p(c_1)\frac{1}{N_1}\Sigma_{j=1}^{N_1} D_{AB}^{(\alpha,\beta)}((\Omega^{(i)})^T \hat{M}_j(\Omega^{(i)})||k(\Omega^{(i)})^T \hat{M}(\Omega^{(i)})))$$
$$+ D_{AB}^{(\alpha,\beta)}((\Omega^{(i)})^T \hat{M}(\Omega^{(i)})||k(\Omega^{(i)})^T \hat{N}(\Omega^{(i)})) \quad (5)$$

(9) Compute gradients $\nabla f(\Omega^{(i)})$, tangent matrices Ω_{tg}^{i+1}, and projection matrices Ω^{i+1}.

$$\nabla f(\Omega^{(i)}) = \frac{\partial f(\Omega^{(i)})}{\partial \Omega^{(i)}} - \Omega^{(i)} \frac{\partial f(\Omega^{(i)})}{\partial \Omega^{(i)}} \Omega^{(i)} \quad (6)$$

$$1.\Omega_{tg}^{i+1} = \Omega^i + \mu^{(i)} \nabla \mathrm{f}(\Omega^{(i)}) \quad (7)$$

$$\Omega^{i+1} = N_L N_R^T \quad (8)$$

$$[Q_L, D, Q_R] = svd(\Omega_{tg}^{i+1}, 0) \quad (9)$$

(10) Increase the iteration counter and determine if it converges, otherwise return to step 8.

(11) Select the maximum/minimum eigenvector of $((\Omega^{(i_{\max})})^T \hat{M}\, \Omega^{(i_{\max})}$, $(\Omega^{(i_{\max})})^T \hat{N}\, \Omega^{(i_{\max})})$.

(12) Obtain the final spatial filter matrix W^T:

$$W^T = V^T (\Omega^{i_{(\max)}})^T T \quad (10)$$

After obtaining the final spatial filter matrix W^T, the raw EEG data obtained by the time window interception is projected through the spatial filter matrix, and two new types of EEG data can be obtained by constructing corresponding features.

The total number d of expected spatial filters is 6 in this study.

3.3 PSO

PSO is a group intelligent optimization algorithm proposed by Kennedy and Eberhart to imitate bird foraging, which has been successfully applied to various optimization problems (Poli et al., 2007). The basic principle is to randomly initialize a group containing N particles in a three-dimensional space, each of which is a feasible solution to the optimization parameters. Mark the ith particle as $x_i = (x_{i1}, x_{i2}, x_{i3})$, bring it into the evaluation function, and determine the individual optimal position $p_i^t = (x_{i1}^t, x_{i2}^t, x_{i3}^t)$ and global optimal position $p_g^t = (x_{g1}^t, x_{g2}^t, x_{g3}^t)$. At the same time recording the velocity of the ith particle $v_i = (v_{i1}, v_{i2}, v_{i3})$, its position and velocity update formula is as follows:

$$v_{id}^{t+1} = wv_{id}^{t} + c_1 r_1 (p_{id}^{t} - x_{id}^{t}) + c_2 r_2 (p_{gd}^{t} - x_{id}^{t}) \tag{11}$$

$$x_{id}^{t+1} = x_{id}^{t} + v_{id}^{t+1} \tag{12}$$

where w ($w = 0.1$) is the inertia weight proposed by Shi and Eberhart; the size of w affects the ability of the particle global and local search; r_1 and r_2 are random constants in (0, 1); and $c_1 (c_1 = 1.2)$ and $c_2 (c_2 = 1.2)$ are learning factors. The velocity of particles range from -1 to 1 and the range of position is $(-2, 2)$.

4 Results

Subject f of dataset 1 and subject av of dataset 2 are respectively selected, and feature distributions of CSP, Sub-ABLD, and PSO-Sub-ABLD are compared as shown in Fig. 2. From the figure, it can be observed clearly that features extracted by PSO-Sub-ABLD are easier to classify than two other methods for two subjects.

Tables 1 and 2 present classification accuracy derived by CSP, Sub-ABLD, and PSO-Sub-ABLD for all participants with test set of two datasets. For nine subjects selected in two datasets, PSO-Sub-ABLD improves the classification accuracy compared with two other algorithms and shows good generalization performance.

Table 1 summarizes that PSO-Sub-ABLD shows better classification accuracy for four subjects compared to two other methods. The average classification accuracy

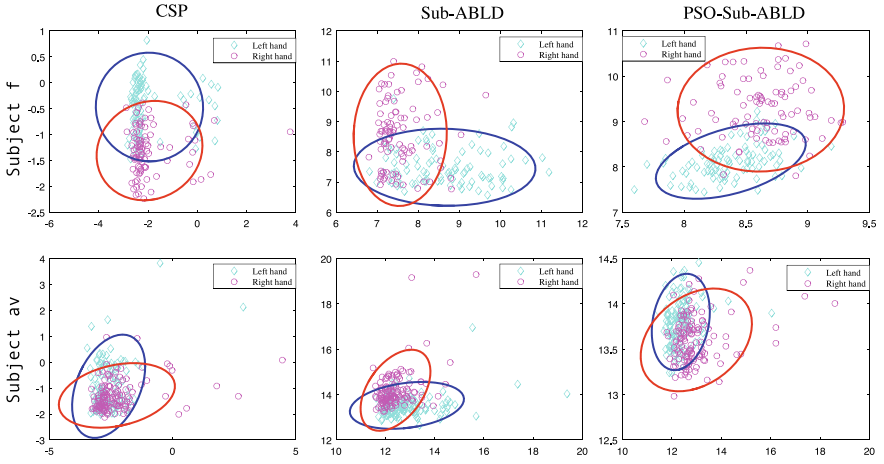

Fig. 2 Feature distribution (subject f of dataset 1 and subject av of dataset 2) of each class extracted by CSP, Sub-ABLD, and PSO-Sub-ABLD (cyan diamond represents the features of left hands, and magenta circle represents the features of right hands)

Table 1 Classification accuracy comparison of CSP, Sub-ABLD ($\alpha = \beta = 1.25$, $\eta = 0.25$), and PSO-Sub-ABLD ($\alpha = 0.9$, $\beta = 1.7$, $\eta = 0.5$) using BCI competition IV dataset I

Subject	Dataset 1 (BCI computation IV dataset I)		
	CSP (%)	Sub-ABLD (%)	PSO-Sub-ABLD (%)
a	61.5	68	78
b	51	54.5	56.5
f	45	58	74.5
g	91	88	94.5
Mean	62.1	67.1	75.9
STd	17.7	15	13.6

Table 2 Classification accuracy comparison of CSP, Sub-ABLD ($\alpha = \beta = 2$, $\eta = 0.5$), and PSO-Sub-ABLD ($\alpha = 0.6$, $\beta = 1.9$, $\eta = 1.4$) using BCI competition III dataset IVa

Subject	Dataset 2 (BCI competition III dataset IVa)		
	CSP (%)	Sub-ABLD (%)	PSO-Sub-ABLD (%)
aa	78.2	71.4	83.6
al	96.4	96.8	97.5
av	47.9	67.5	70.4
aw	86.0	82.9	90.4
ay	88.2	89.6	92.9
Mean	79.3	81.6	87.0
STd	16.8	12.2	10.5

obtained by PSO-Sub-ABLD ($\alpha = 0.5$, $\beta = 0.9$, $\eta = 1.7$) is 75.9%, 13.8% higher than CSP and 8.8% higher than Sub-ABLD, respectively.

Table 2 shows classification accuracy for five subjects of dataset 2. The average classification accuracy obtained by PSO-Sub-ABLD ($\alpha = 1.4$, $\beta = 0.6$, $\eta = 1.9$) is 87%, 7.7% higher than CSP and 5.4% higher than Sub-ABLD, respectively.

5 Conclusion

In this paper, PSO-Sub-ABLD has better robustness to outliers than CSP and Sub-ABLD to get better classification accuracy. Since default hyperparameters of Sub-ABLD result in poor generalization ability for different datasets, this study proposes PSO-Sub-ABLD algorithm, and it shows better generalization performance. In summary, compared with CSP and Sub-ABLD, PSO-Sub-ABLD obtains better classification performance based on the same classifier.

In the future work, one of the explorations is to combine channel selection and feature selection with PSO-Sub-ABLD to achieve better performance and to apply it to online systems.

References

Blankertz, B., Blankertz, B., Tomioka, R., Lemm, S., Kawanabe, M., & Müller, K.-R. (2008). Optimizing spatial filters for robust EEG single-trial analysis. *IEEE Signal Processing Magazine*, *25*, 581–607.

da Cruz, J. N., Wan, F., Wong, C. M., & Cao, T. (2015). Adaptive time-window length based on online performance measurement in SSVEP-based BCIs. *Neurocomputing*, *149*, 93–99. Advances in neural networks Advances in Extreme Learning Machines.

Feng, J., Yin, E., Jin, J., Saab, R., Daly, I., Wang, X., et al. (2018). Towards correlation-based time window selection method for motor imagery BCIs. *Neural Networks*, *102*, 87–95.

Garrett, D., Peterson, D. A., Anderson, C. W., & Thaut, M. H. (2003). Comparison of linear, nonlinear, and feature selection methods for EEG signal classification. *IEEE Transactions on Neural Systems and Rehabilitation Engineering*, *11*(2), 141–144.

Jin, J., Allison, B. Z., Sellers, E. W., Brunner, C., Horki, P., Wang, X., et al. (2011). An adaptive p300-based control system. *Journal of Neural Engineering*, *8*(3), 036006.

Jin, J., Sellers, E. W., Zhou, S., Zhang, Y., Wang, X., & Cichocki, A. (2015). A p300 brain–computer interface based on a modification of the mismatch negativity paradigm. *International Journal of Neural Systems*, *25*(03), 1550011.

Lotte, F., & Guan, C. (2011). Regularizing common spatial patterns to improve BCI designs: Unified theory and new algorithms. *IEEE Transactions on Biomedical Engineering*, *58*(2), 355–362.

Mensh, B. D., Werfel, J., & Seung, H. S. (2004). BCI competition 2003-data set Ia: Combining gamma-band power with slow cortical potentials to improve single-trial classification of electroencephalographic signals. *IEEE Transactions on Biomedical Engineering*, *51*(6), 1052–1056.

Novi, Q., Guan, C., Dat, T. H., & Xue, P. (2007). Sub-band common spatial pattern (SBCSP) for brain–computer interface. In *2007 3rd International IEEE/EMBS Conference on Neural Engineering* (pp. 204–207).

Pfurtscheller, G. (1977). Graphical display and statistical evaluation of event-related desynchronization (ERD). *Electroencephalography and Clinical Neurophysiology*, *43*(5), 757–760.

Pfurtscheller, G. (1992). Event-related synchronization (ERS): An electrophysiological correlate of cortical areas at rest. *Electroencephalography and Clinical Neurophysiology*, *83*(1), 62–69.

Poli, R., Kennedy, J., & Blackwell, T. (2007). Particle swarm optimization. *Swarm Intelligence*, *1*(1), 33–57.

Qiu, Z., Jin, J., Lam, H.-K., Zhang, Y., Wang, X., & Cichocki, A. (2016). Improved SFFS method for channel selection in motor imagery based BCI. *Neurocomputing*, *207*, 519–527.

Ramoser, H., Ramoser, H., Müller-Gerking, J., & Pfurtscheller, G. (1998). Optimal spatial filtering of single trial EEG during imagined hand movement. *IEEE Transactions on Rehabilitation Engineering*, *8*, 441–446.

Song, L., & Epps, J. (2007). Classifying EEG for brain–computer interface: Learning optimal filters for dynamical system features. *Computational Intelligence and Neuroscience*, 57180.

Sun, G., Hu, J., & Wu, G. (2010). A novel frequency band selection method for common spatial pattern in motor imagery based brain computer interface. In *The 2010 International Joint Conference on Neural Networks (IJCNN)* (pp. 1–6). IEEE.

Thiyam, D. B., Cruces, S., Olias, J., & Cichocki, A. (2017). Optimization of Alpha-Beta Log-Det divergences and their application in the spatial filtering of two class motor imagery movements. *Entropy*, *19*(3), 89.

Wolpaw, J. R., Birbaumer, N., McFarland, D. J., Pfurtscheller, G., & Vaughan, T. M. (2002). Brain–computer interfaces for communication and control. *Clinical Neurophysiology*, *113*(6), 767–791.

Xu, B., Zhang, L., Song, A., Wu, C., Li, W., Zhang, D., et al. (2018). Wavelet transform time-frequency image and convolutional network-based motor imagery EEG classification. *IEEE Access*, *7*, 6084–6093.

Zhang, H., Guan, C., Ang, K. K., & Wang, C. (2012). BCI competition IV—Data set I: Learning discriminative patterns for self-paced EEG-based motor imagery detection. *Frontiers in Neuroscience*, *6*, 7.

Zhang, Y., Zhou, G., Jin, J., Wang, X., & Cichocki, A. (2015). Optimizing spatial patterns with sparse filter bands for motor-imagery based brain–computer interface. *Journal of Neuroscience Methods*, *255*, 85–91.

Stochasticity Versus Determinacy in Neurodynamics—And the Questions of the "Free Will"

Hans Albert Braun

Abstract "We do not do what we want, we want what we do." This is the logical consequence if one accepts that all our decisions are based on processes of our brain under deterministic natural laws. In recent years, this idea has received new nourishment through spectacular neurophysiological experiments demonstrating that the subjective experience of decision-making is preceded by unconscious brain activity. In the following, these experiments and especially their conclusions will critically be examined and contrasted with other experiments that seriously question one of the foundations of the above assertion, the determinacy of neuronal information processing.

1 Introduction

Attacks against the free will have been known since ancient times. Nowadays, such attacks do not necessarily come from professional philosophers. Rather, it is renowned representatives of the neurosciences who have been repeatedly questioning the free will of humans for a number of years. Of course, it is not a surprise that the neuroscientists contribute to this discussion. In fact, it is their task to investigate the functions of the nervous system which also includes the question of the neuronal basis of higher mental and cognitive processes and their disorders as, for example, manifested in psychiatric diseases. A fundamental problem, which one inevitably encounters in such investigations, concerns the question of the connection between mind and matter, known as body-mind problem (Bateson, 1970). It is about the question in which way mental and spiritual concepts like fear and joy, aggression and love, but also thoughts—and even a will—are connected with physical processes that can be grasped materially, at least in principle. The generally accepted presupposition is, also of all experimentally based attacks against the free will, that neuronal

H. A. Braun (✉)
Institute of Physiology, Philipps University of Marburg,
Deutschhausstr. 1, 35037 Marburg, Germany
e-mail: braun@staff.uni-marburg.de

A. Lintas et al. (eds.), *Advances in Cognitive Neurodynamics (VII)*, Advances in Cognitive Neurodynamics,
https://doi.org/10.1007/978-981-16-0317-4_24

processes are at least a necessary (although not necessarily a sufficient) condition of cognitive functions. The possibility of free decisions could actually be regarded as an empirically well-proven fact if there would not be the assumption that these everyday experiences of free will are nothing more than an illusion. It is claimed that our decisions are determined before we even perceive them as our own will. Since these decisions are made in the brain whose functions are subject to deterministic laws of nature, they are determined. As far as determinacy is concerned, it has by no means been brought into play only recently by the neurosciences. One does not necessarily need the experimental findings from brain research if one wants to argue against free will assuming a universal determinism. The validity and above all the relevance of such an absolute determinism have been discussed for a long time but in specific parts, e.g., concerning Laplace's demon, ascribed to metaphysics (Russell, 1967). Often, the discussion between researchers from different fields is still characterized by many misunderstandings and mutual ignorance (Kotchoubey et al., 2016).

2 Determinacy

From the viewpoint of a neuroscientist, it is, of course, near at hand to argue from a neurophysiological basis. The following arguments against determinism refer to basic neurophysiological findings of which also neuroscientific advocates of determinism should be aware. These are experimental measurements of the opening and closing ion channels (Hille, 1978) as they have been carried out hundreds or even thousands of times since the introduction of the patch-clamp technique (Neher & Sakmann, 1976) on a wide variety of ion channels of different neurons. The neuroscientific justification of determinism refers to experiments on a completely different level which first are briefly compiled below subjected to critical examination.

2.1 Attacking the Idea of the Free Will

What has neuroscience contributed to the discussion about freedom of will with new, additional arguments? In experimental terms, it is actually only the proof of temporal delays in the conscious perception of a free decision in relation to measurable signals from the brain that can be associated with this decision. Such time delays were first proven in the famous Libet experiments with measurements of the electroencephalogram (EEG) (Libet et al., 1993). Even more significant time delays were recently demonstrated in a slightly modified experimental setup using more modern methods of functional magnetic resonance imaging (fMRI) (Soon et al., 2008).

If one assumes that arbitrary motor activity is controlled by the brain, temporal delays between brain activity and motor actions must be expected, as they have already been proven earlier in the form of readiness potentials (Kornhuber

& Deecke, 1965). The activity will spread over the motor cortex and ganglia, the spinal cord and then into the peripheral motor nerve to the innervated muscle with corresponding time delays.

The question is: How is such an arbitrary, non-reflexive movement initiated, i.e., how does the will to move arise and can a neuronal correlate be found for this? Now, indeed, one seems to have actually found such a neuronal correlate of will formation, which can be measured in the form of EEG or fMRI signals. This is spectacular, but not surprising, at least for a neurophysiologist. The really surprising thing was that the signals of will formation can be seen in the brain much earlier than the subject even becomes aware of the process of will formation. In the Libet experiments (Heisenberg, 2009; Libet et al., 1993), these were only a few hundred milliseconds, which left room for doubting the results due to possible measurement errors. Since the fMRI measurements of the Haynes group (Soon et al., 2008) this is hardly possible anymore. The so-called BOLD signals in the fMRI appear up to 7 s (!) earlier than the subject realizes that he/she has decided to press a certain button. It is even possible to predict, albeit with considerable uncertainty, which button the subject will choose.

Under the assumption that all events in this world are based on causal connections, one can argue that physical-chemical laws of nature determine the will of decision-making, which only later becomes conscious to us—and which we then erroneously regard as the result of our own free will.

2.2 Attempts to Save the Free Will

For most people, free will only as an illusion is not a particularly pleasant idea (Smith, 2011). All kinds of objections were raised against the experiments and their interpretation with both philosophically and neurobiologically justified counterarguments. From a neurophysiological point of view, the following main arguments are put forward against the interpretation of the above-mentioned experiments as signs of deterministic will formation: (1) The experiments are still far from representing real and usually far more complex situations of will formation. (2) The experiments show no more than that unconscious processes contribute to our will formation, which will not surprise anyone. The crucial factor is that we can reflect on our decisions (Heisenberg, 2009). Both lines of arguments thus refer to reflection as a necessary component of more complex processes of decision-making. But this is not necessarily the end of determinism. The above-mentioned experiments are just a beginning. Who knows whether further improved experimental techniques will soon be able to detect more complex processes of will formation in neurophysiological experiments.

The authors of the fMRI studies (Soon et al., 2008) are rather cautious and speak, at least in their scientific publications, only of unconscious determinants of will formation. Also Libet himself has tried to distance himself somewhat from his conclusions, but not always with convincing arguments. If he and several others grant

a veto right as a signature of a free will (Libet, 2005) one may ask where this veto shall come from. Is the decision to veto against a previous decision superior to brain activity? If not, why should the decision to veto be free while the previous decision is determined?

Also the Haynes' group came back to the veto issue demonstrating that pressing a button can be prevented when the beforehand already detected readiness potential lightens a red lamp (Schultze-Kraft et al., 2016). However, this veto works only outside a time window of 200 ms—which is in the range or even beyond the reaction time on a light signal.

Another repeatedly used argumentation to save the free will as, e.g., discussed in "The Volitional Brain" (Libet et al., 1999) and also addressed in Stephen M. Kosslyn's foreword refers to deterministic chaos as a possible source of fundamental uncertainties in contrast to a completely determined world. However, one should keep in mind that this is "deterministic" chaos. Also such a chaotic system, although unpredictable for the longer-term run, reacts in a fully determined way, even when it is disturbed by a signal when this comes from a deterministic world. Real uncertainties can only be introduced by really uncertain mechanisms, i.e., by stochasticity. This is the point to come back to another, already well-known source of neuronal stochasticity, the opening and closing of ion channels.

3 Stochasticity

Indeed, life seems to be full of uncertainty and stochasticity. The problem is that one never can be sure whether random events are really random or just appear to be random because of the manifold of unknown and uncontrollable influences which may lead to a seemingly random event, eventually even quite unlikely to happen.

In neurophysiology, the EEG belongs probably to most unpredictable signals, easy to explain by the billions of neurons that are involved. However, even the spike trains of a single neuron show unpredictable fluctuations, and a given neuron never reacts in exactly the same way even on an exactly defined stimulus what can be addressed to the manifold of randomly opening and closing ion channels. However, to what uncertainties can single-channel openings and closings be related? Here, we come to a point where nothing more than principle uncertainties from the physical world is needed.

3.1 Ion Channels—Harnessing Stochasticity

Already at the beginning of the 1950s, Hodgkin and Huxley introduced so-called rate constants in their groundbreaking work on the mathematical simulation of their experimental registrations of membrane potentials and ion currents (Hodgkin & Huxley, 1952), thus implicitly anticipating the statistical transition probabilities of the open-

ings and closings of ion channels. Later, by the introduction of the patch-clamp technique with the possibility to measure single channels, the inherent stochasticity of ion channel activation could be experimentally proven (Neher & Sakmann, 1976). Nowadays, knowledge of these interrelationships is basic knowledge of neurophysiology, which should not only be mastered by all neuroscientists, but also by all students of the life sciences. A tutorial on the analysis of patch-clamp data (Alvarez et al., 2002) begins with the sentence: "Ion channels open and close in a stochastic fashion, following the laws of probability. However, distinct from tossing a coin or a die, the probability of finding the channel closed or open is not a fixed number but can be modified (i.e., we can cheat) by some external stimulus, such as the voltage." The figure which here is shown to illustrate these connections is also part of a teaching software (see http://www.virtual-physiology.com, SimNeuron, Applets). It shows the opening and closing of an ion channel as a function of membrane voltage, simulated with random numbers corresponding to the rate constants already postulated by Hodgkin and Huxley.

The upper diagram Fig. 1a shows the Boltzmann function, which in this example reflects the voltage-dependent activation of an ionic current. In addition, two exponential functions are drawn, which represent the transition probabilities (rate constants) from the open to the closed and from the closed to the open state. Their parameters are chosen so that they explicitly lead to the Boltzmann function according to the equations given by Hodgkin and Huxley (Holmgren Hopkins et al., 2018) Up to this point, the whole system is still completely deterministic.

The dots in Fig. 1 indicate the percentage of the "open" states of a single channel when its transitions are simulated by random transitions according over a certain period of time as shown in Fig. 1b for selected membrane potentials. The transition probabilities are chosen according to the exponential function from Fig. 1a. Accordingly, the values of the open states follow the course of the Boltzmann function quite well—however with a certain dispersion. It is only by chance when these points exactly hit the Boltzmann function. The scattering becomes smaller the more one approaches a permanently open or permanently closed state. Also with a longer simulation time or if you sum up over a larger number of ion channels, the scatter will of course be smaller. This is basic statistics. Figure 1c shows the fluctuations of a total current, summed up over 100 and 1000 ion channels. Stochasticity is manifested as noise. All attempts elucidating certain rules of channel transitions in a given state have so far failed. This type of randomness does not need quantum uncertainty. Thermodynamics, i.e., Brownian motion, is sufficient to introduce principle uncertainty already at the lowest level of neurodynamics which is additionally supported by the pronounced temperature sensitivity of ion channel transitions (Dilger et al., 1991) and further underlined by the fact that ion channel activation can best be fitted by Boltzmann functions.

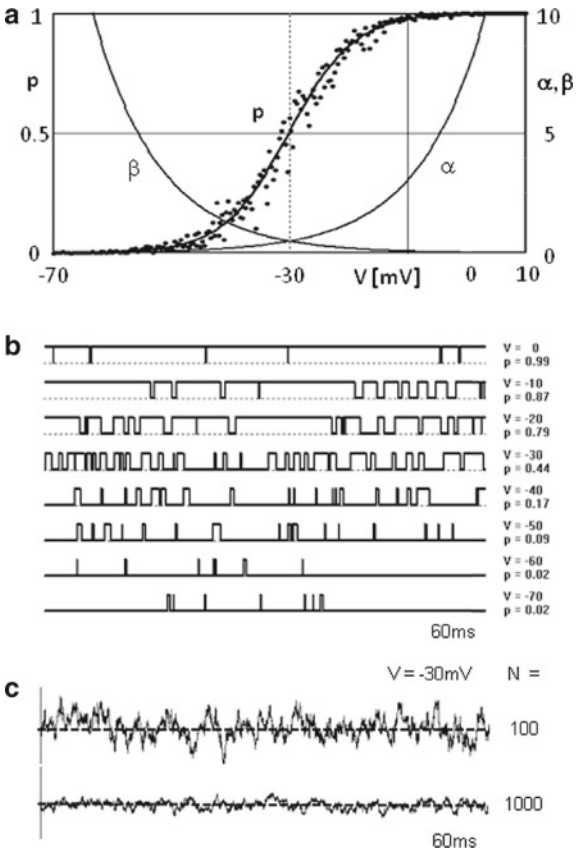

Fig. 1 **a** Curve of ion channel activation probability (p) determined by the exponential activation and inactivation curves α and β also providing the random numbers taken for computer simulations to calculate the open states at different voltages (dots). Examples are shown in (**b**) and (**c**). Fluctuations of open states (channel noise) are shown for the half activation potential on the basis of 100 and 1000 ion channels, respectively

3.2 Propagation of Ion Channel Stochasticity Toward Higher Functional Levels

Quantum uncertainty from the lowest level of physics may hardly have a macroscopic effect in the real world. One may expect that also ion channel stochasticity from the lowest level of neuronal functions is quickly averaged out toward higher functional levels. This can happen, but it can also be just the opposite, a dramatic amplification of even microscopic randomness. The decisive components for the amplification of randomness are the nonlinearities on which biological functions are built up. Co-operative effects of noise and nonlinear dynamics can lead to particular phenomena which would never be expected from a purely deterministic system, especially in the multiply meshed nonlinear feedback loops of which biological systems typically are composed.

Such co-operative effects of randomness and nonlinearities cannot only be shown by computer simulations with realistically implemented channel noise (Tchaptchet

et al., 2013) but are also manifested in a manifold of experimental data. Most well known are probably the "stochastic resonance" phenomena (Wiesenfeld & Moss, 1995), which can be detected in biology up to the levels of behavioral reactions (Russell et al., 1999). There are even neuronal transduction systems of exquisite sensitivity, the shark electroreceptors, that would not function at all without the interaction of nonlinear dynamics and noise (Braun et al., 1994).

At higher functional levels, it is becoming more and more difficult to decide whether an observed randomness is not simply due to the manifold of unknown influences. At the level of neuronal networks, synaptic transmission is often considered as a possible source of stochasticity arising from the unmanageable high number of transmitter molecules that are released (Heisenberg, 2009). This will be difficult to prove while one should not forget that also synaptic transmission is controlled by ion channel openings and closing at several points at the pre- and post-synaptic site (Postnova et al., 2010). Hence, there is principally no need to search for additional sources of randomness. Ion channel stochasticity can still be sufficient to decide whether pre-synaptic action potential can excite the postsynaptic neuron or not.

Indeed, stochasticity can play an important role in various physiological functions. For example, neuronal network synchronization should never be complete and always temporary. This means that the networks should also be able to go out of a synchronized state for which a disturbance is required, e.g., noise (Holmgren Hopkins et al., 2018; Postnova et al., 2009).

4 Summary and Conclusions

Neurophysiological experiments pretending to demonstrate that human decision is pre-determined by brain functions based on deterministic natural laws, suggesting that free will is an illusion, have critically been examined coming to the conclusion that these data cannot add significant new arguments against a free will. Several attempts to save the free will on basis of similar experiments appear even less convincing, partly exhibiting misunderstandings of fundamental concepts of theory of science. These experiments have been confronted with basic neurophysiological data demonstrating that stochasticity comes into play already at the lowest level of neuronal information processing, the opening and closing of ion channels which, transformed into noise, as the temporal aspect of stochasticity, can propagate and even can be enhanced toward higher functional levels of information processing. The background lies in co-operative effects of noise with the system's nonlinearities which seem to be much more frequent and pronounced in the animated than in the physical world.

Stochasticity, of course, is not a proof of a free will but determinism is, for sure, not a good argument against. Anyhow, neuronal stochasticity may be a main prerequisite to keeping the brain in a flexible state, also for decision-making. Stochasticity allows to "generate many possible solutions to environmental challenges" (Noble & Noble, 2018).

It seems to be omnipresent in biological systems playing a significant role also in context with other functions, e.g., in the immune system down to epigenetics (Noble & Noble, 2017). This does not need a specific form of biological stochasticity. The background is assumable of general, physical nature. Life is only compatible with temperatures far above absolute zero where molecules have kinetic energy which generates random movements, particularly well harnessed by the nonlinearities of biological function (Noble, 2017). It seems again to be the combination of chance and necessity (Monod, 1970) determining the functions of life.

Acknowledgements This work is supported by "Ingenieurbüro für Biomedizin und Technik" (BM&T), Heidelberg-Marburg (http://www.bmt-gbr.com).

References

Alvarez, O., Gonzalez, C., & Latorre, R. (2002). Counting channels: A tutorial guide on ion channel fluctuation analysis. *Advances in Physiology Education*, *26*(1–4), 327–341.

Bateson, G. (1970). A systems approach. *International Journal of Psychiatry*, *9*, 242–244.

Braun, H. A., Wissing, H., Schäfer, K., & Hirsch, M. C. (1994). Oscillation and noise determine signal transduction in shark multimodal sensory cells. *Nature*, *367*(6460), 270–273.

Dilger, J. P., Brett, R. S., Poppers, D. M., & Liu, Y. (1991). The temperature dependence of some kinetic and conductance properties of acetylcholine receptor channels. *Biochimica et Biophysica Acta*, *1063*(2), 253–258.

Heisenberg, M. (2009). Is free will an illusion? *Nature*, *459*(7244), 164–165.

Hille, B. (1978). Ionic channels in excitable membranes. Current problems and biophysical approaches. *Biophysical Journal*, 22(2):283–294.

Hodgkin, A. L., & Huxley, A. F. (1952). A quantitative description of membrane current and its application to conduction and excitation in nerve. *Journal of Physiology*, *117*(4), 500–544.

Holmgren Hopkins, N., Sanz-Leon, P., Roy, D., & Postnova, S. (2018). Spiking patterns and synchronization of thalamic neurons along the sleep-wake cycle. *Chaos*, *28*(10), 106314.

Kornhuber, H. H., & Deecke, L. (1965). Changes in the brain potential in voluntary movements and passive movements in man: Readiness potential and reafferent potentials. *Pflugers Arch Gesamte Physiol Menschen Tiere*, *284*, 1–17.

Kotchoubey, B., Tretter, F., Braun, H. A., Buchheim, T., Draguhn, A., Fuchs, T., et al. (2016). Methodological problems on the way to integrative human neuroscience. *Frontiers in Integrative Neuroscience*, *10*, 41.

Libet, B. (2005). *Mind time: wie das Gehirn Bewusstsein produziert*. Suhrkamp.

Libet, B., Freeman, A., & Sutherland, K. (Eds.). (1999). *The volitional brain: Towards a neuroscience of free will*. Imprint Academic.

Libet, B., Wright, E. W., & Gleason, C. A. (1993). *Readiness-potentials preceding unrestricted 'spontaneous' vs. pre-planned voluntary acts* (pp. 229–242). Birkhäuser Boston.

Monod, J. (1970). *Chance and necessity: An essay on the natural philosophy of modern biology*, trans. Austryn Wainhouse Vintage.

Neher, E., & Sakmann, B. (1976). Single-channel currents recorded from membrane of denervated frog muscle fibres. *Nature*, *260*(5554), 799–802.

Noble, D. (2017). Evolution viewed from physics, physiology and medicine. *Interface Focus*, *7*(5), 20160159.

Noble, R., & Noble, D. (2017). Was the watchmaker blind? Or was she one-eyed? *Biology (Basel)*, *6*(4).

Noble, R., & Noble, D. (2018). Harnessing stochasticity: How do organisms make choices? *Chaos*, *28*(10), 106309.

Postnova, S., Rosa, E, Jr., & Braun, H. A. (2010). Neurones and synapses for systemic models of psychiatric disorders. *Pharmacopsychiatry*, *43*(Suppl. 1), S82–S91.

Postnova, S., Voigt, K., & Braun, H. A. (2009). A mathematical model of homeostatic regulation of sleep-wake cycles by hypocretin/orexin. *Journal of Biological Rhythms*, *24*(6), 523–535.

Russell, B. (1967). *Probleme der Philosophie (1912)*. Suhrkamp.

Russell, D. F., Wilkens, L. A., & Moss, F. (1999). Use of behavioural stochastic resonance by paddle fish for feeding. *Nature*, *402*(6759), 291–294.

Schultze-Kraft, M., Birman, D., Rusconi, M., Allefeld, C., Görgen, K., Dähne, S., et al. (2016). The point of no return in vetoing self-initiated movements. *Proceedings of the National Academy of Sciences of the United States of America*, *113*(4), 1080–1085.

Smith, K. (2011). Neuroscience vs philosophy: Taking aim at free will. *Nature*, *477*(7362), 23–25.

Soon, C. S., Brass, M., Heinze, H.-J., & Haynes, J.-D. (2008). Unconscious determinants of free decisions in the human brain. *Nature Neuroscience*, *11*(5), 543–545.

Tchaptchet, A., Postnova, S., Finke, C., Schneider, H., Huber, M. T., & Braun, H. A. (2013). Modeling neuronal activity in relation to experimental voltage-/patch-clamp recordings. *Brain Research*, *1536*, 159–167.

Wiesenfeld, K., & Moss, F. (1995). Stochastic resonance and the benefits of noise: From ice ages to crayfish and SQUIDs. *Nature*, *373*(6509), 33–36.

From Neural Dynamics to Executive Functions: Short Papers

Temperature Effects on Action Potential Propagation in Myelinated Axons

Xinlin Song, Hengtong Wang, Yong Chen, and Yingcheng Lai

Abstract Temperature is the important factor of the activity of the biological system. Especially, temperature affects the action potential propagation along the myelinated axon. We use Hogking–Huxley-like cortical model as the node of Ravier and the internode conductance κ as the characteristic of the myelinated axon to describe the action potential propagation under temperature. The critical κ could exit to make the action potential propagate along the myelinated axon and rise with increasing temperature. Thus, the optimum of temperature exiting with different internode conductance κ is investigated to show that the information propagating on the neural system has the suitable temperature.

X. Song (✉) · Y. Chen
School of Physics and Nuclear Energy Engineering,
Beihang University, Beijing 100191, China
e-mail: xinlinsong70@buaa.edu.cn

H. Wang
School of Physics and Information Technology,
Shaanxi Normal University, Xi'an 710119, China

Y. Lai
School of Electrical, Computer, and Energy Engineering,
Arizona State University, Tempe, AZ 85287, USA

A. Lintas et al. (eds.), *Advances in Cognitive Neurodynamics (VII)*, Advances in Cognitive Neurodynamics,
https://doi.org/10.1007/978-981-16-0317-4_25

The Spontaneous Spiking in Up and Down Oscillations and Its Energy Feature

Xuying Xu, Yihong Wang, and Rubin Wang

Abstract Up and down oscillations of membrane potentials are viewed as one kind of significant spontaneous periodic activities. This kind of oscillation always shows that membrane potentials make spontaneous transitions between two preferred states called up and down states, which characterized by some features as follows in level of membrane potentials: bistability, directivity, spontaneity, synchronicity and spontaneous spikings. Here, we focus on the spontaneous spiking and its energy feature. We studied the influence of the intrinsic characteristics and synaptic transmission of spontaneous spiking during up and down activities. The simulated results showed that persistent sodium current was critical to spontaneous fluctuation without any stimulus, while the fast sodium current had the dominant position in generation of spontaneous neural firing. Considering the noise, we found the role of persistent sodium current was partially replaced by oscillation of noise. And energy consumption of neurons in spontaneous activities also shows bistable feature and bimodal distribution as same as the membrane potential, which indicated that the energy consumption can encode up and down states in this kind of activities.

Acknowledgements Supported by the National Natural Science Foundation of China (No. 11702096, 11802095) and the Fundamental Research Funds for the Central Universities (No. 222201714020, 222201814025).

X. Xu (✉) · Y. Wang · R. Wang
Institute for Cognitive Neurodynamics, East China University of Science and Technology, Shanghai 200237, People's Republic of China
e-mail: xu_xuying@126.com

Y. Wang
e-mail: wangyihong@ecust.edu.cn

R. Wang
e-mail: rbwang@163.com

A. Lintas et al. (eds.), *Advances in Cognitive Neurodynamics (VII)*, Advances in Cognitive Neurodynamics,
https://doi.org/10.1007/978-981-16-0317-4_26

Dynamic Neural Interactions Revealed by the State-Space Ising Model

Hideaki Shimazaki

Abstract Stimulus information and cognitive states of an animal are represented by correlated population activity of neurons. The maximum entropy method provides a principled way to describe the correlated population activity using much less parameters than the number of possible activity patterns. This method successfully explained stationary spiking activity of neural populations such as in vitro retinal ganglion cells. Modeling activity of cortical circuitries in vivo, however, has been challenging because both the spike rates and interactions among neurons can change according to sensory stimulation, behavior, or an internal state of the brain. To capture the non-stationary interactions among neurons, we augmented the maximum entropy model (Ising model) using a state-space modeling framework, which we call the state-space Ising model. We will demonstrate that applications of the state-space Ising model to activity of cortical neurons reveal dynamic neural interactions, and how they contribute to sparseness and fluctuation of the population activity as well as stimulus coding.

H. Shimazaki (✉)
Department of Intelligence Science and Technology School of Informatics,
Kyoto University, Kyoto, Japan
e-mail: h.shimazaki@i.kyoto-u.ac.jp

A. Lintas et al. (eds.), *Advances in Cognitive Neurodynamics (VII)*, Advances in Cognitive Neurodynamics,
https://doi.org/10.1007/978-981-16-0317-4_27

Initial Topology in Hierarchically Organized Evolvable Neural Networks Determines the Emergence of Synfire Chains

Paolo Masulli and Alessandro E. P. Villa

Abstract We investigate the effects of network topology on the dynamical activity of a hierarchically organized network of simulated spiking neurons. With a fixed basic two-by-two grid structure of processing modules each composed by almost 6000 leaky integrate-and-fire neurons and different connectivity schemes in between these modules, we study how the activation and the biologically inspired processes of plasticity on the network shape its topology using invariants based on algebro-topological constructions. By definition, a clique is a fully connected directed subnetwork that means there is one source and one sink in the subnetwork. We define 'k-clique hub cells' for a positive integer k any cell which is sink and source cell of at least k 3-cliques. We show that there is a statistically different distribution of in- and out-degrees between clique hubs and other cells. Furthermore, we show that by identifying 'clique hub cells' we can find synfire chains that are involved in spatio-temporal firing patterns. Hence, the results suggest a link exists between an initial topological structure characterized by subnetworks cliques and a functional connectivity emerging at a later stage as the outcome of synaptic plasticity mechanisms.

P. Masulli · A. E. P. Villa
NeuroHeuristic Research Group, University of Lausanne, Internef 138, Quartier UNIL-Chamberonne, 1015 Lausanne, Switzerland
e-mail: alessandro.villa@unil.ch

P. Masulli (✉)
Department of Applied Mathematics and Computer Science, Technical University of Denmark, 2800 Kgs Lyngby, Denmark
e-mail: pamas@dtu.dk
URL: http://www.neuroheuristic.org

A. Lintas et al. (eds.), *Advances in Cognitive Neurodynamics (VII)*, Advances in Cognitive Neurodynamics,
https://doi.org/10.1007/978-981-16-0317-4_28

Nonlinear Neural Dynamics of Mutual Inhibition Circuit in a Real-Life/Computer Model Hybrid System

Naoki Kogo, Felix B. Kern, Thomas Nowotny, Raymond van Ee, Takeshi Aihara, and Richard van Wezel

Abstract To process ambiguous and noisy images, often experienced in our daily life, the neural system has to actively select and organize the input signals. For a percept to emerge it has been assumed that there are selection processes of competing neural pools. Theoretical research assumed a mutually inhibiting neural circuit underlying the competition and successfully modeled bi-stable perception that occurs in response to ambiguous images. We developed an experimental system to record two real life-pyramidal neurons (in vitro) connected by modeled mutual inhibition circuit (in silica). We show that simultaneous stimulations of the two pyramidal neurons in this hybrid system evoked bi-stable activity. Furthermore, the effect of adding noise and changing stimulus strength showed similar characteristics known from bi-stable

N. Kogo (✉) · R. van Ee · R. van Wezel
Biophysics, Donders Institute for Brain, Cognition and Behaviour,
Radboud University, Heyendaalseweg 135, 6525 AJ Nijmegen, The Netherlands
e-mail: naoki.kogo@gmail.com

R. van Ee
e-mail: R.vanEe@science.ru.nl

R. van Wezel
e-mail: r.vanwezel@donders.ru.nl

F. B. Kern
School of Life Sciences, University of Sussex,
Falmer, Brighton BN1 9QG, UK
e-mail: fbk21@sussex.ac.uk

T. Nowotny
School of Engineering and Informatics, University of Sussex, Falmer, Brighton BN1 9QJ, UK
e-mail: T.Nowotny@sussex.ac.uk

T. Aihara
Brain Science Institute, Tamagawa University,
Tamagawagakuen 6-1-1, 194-8610 Machidashi, Japan
e-mail: aihara@eng.tamagawa.ac.jp

A. Lintas et al. (eds.), *Advances in Cognitive Neurodynamics (VII)*, Advances in Cognitive Neurodynamics,
https://doi.org/10.1007/978-981-16-0317-4_29

perception, suggesting a fundamental role of the non-linear dynamics in perceptual organization.

A CNN-Inspired Model for Degradation Mechanism of Retina to V1

Haixin Zhong and Rubin Wang

Abstract The visual system is under heated investigation in the field of neuroscience and computer vision (CV). In alignment with the implementation of some large brain projects across the world such as those in China, Europe, the USA and Japan, the intersection of visual system in these two fields has been promoted. Therefore, as the most important source of human perception towards the objective world, research on mechanisms of the visual information processing bears great significance for exploring biological vision and developing CV. However, there is a scarcity of soundly established and widely accepted theory that can be used to explain the mechanisms. Specifically, what remains unknown is the degradation mechanism of visual information data during the topological mapping between retina and V1. Hence, in view of the characteristics of convolutional neural network (CNN), this paper draws on the concept of convolution algorithm to propose an edge detection model based on retina to V1 (EDMRV1), which is built on the pathway of photoreceptors-ganglion cells-LGN-V1 in the functional channel of image features detection. The results not only match the neurobiological experimental data but also show that the image edge features of visual information are detected by the convolution algorithm according to the function of synaptic plasticity, when visual signals are hierarchically processed from low-level to high-level in visual cortex. Findings are expected to lay a solid foundation for revealing the mechanisms of the visual information processing in future research. In CV, applying the model to the scenes with different brightness has a better performance on the edge features detection than that in the traditional algorithms, providing an intelligent basis for breakthroughs. This research also opens up opportunities for the integration of CV and neuroscience.

H. Zhong (✉) · R. Wang
Institute for Cognitive Neurodynamics, East China University of Science and Technology, Shanghai 200237, People's Republic of China
e-mail: henry.zhx@foxmail.com

R. Wang
e-mail: rbwang@ecust.edu.cn

A. Lintas et al. (eds.), *Advances in Cognitive Neurodynamics (VII)*, Advances in Cognitive Neurodynamics,
https://doi.org/10.1007/978-981-16-0317-4_30

Mathematical Modelling for Functional Differentiation

Ichiro Tsuda

Abstract One of the most striking characteristics of the developing brain is functional differentiation, while emerging interactions develop between networking differentiated areas. To clarify the neural mechanism of functional differentiation, we constructed a mathematical model of self-organization with constraints. By casting different constraints, we investigated the mathematical structures of functional differentiation and obtained the following specific behaviors. (1) We observed the genesis of a neuron-like unit in the developmental process of networking dynamical systems. (2) We observed the genesis of neuron-like units that respond specifically to visual and auditory stimuli, respectively. (3) We observed the genesis of functional modules from randomly uniform networks of oscillations, where the modular organization can be interpreted as the differentiation of a higher cognitive area and a lower motor area interacting with the body. In all cases, the appearance of chaos and chaotic itinerancy in the whole network system brings about the generation of functional elements via an acceleration of symmetry breaking.

I. Tsuda (✉)
Chubu University Academy of Emerging Sciences, Matsumoto-cho 1200, Kasugai, Aichi, Japan
e-mail: tsuda@isc.chubu.ac.jp

A. Lintas et al. (eds.), *Advances in Cognitive Neurodynamics (VII)*, Advances in Cognitive Neurodynamics,
https://doi.org/10.1007/978-981-16-0317-4_31

The Maximum Information Principle of Place Cell Activity

Yihong Wang, Xuying Xu, and Rubin Wang

Abstract Spatial cognitive function is crucial for the animal's survival. However, the formation of place codes in different dimensional spaces cannot be uniformly explained. In this paper, a constrained optimization model based on information theory is constructed to explain the formation of place cell activity in different dimensional spaces across species. The question is proposed as, using limited amount of neural energy, how to design the place field to obtain the most efficient spatial information representation? Variational techniques are applied and the results suggest that the place field will comply with a certain centralized distribution (normally is Gaussian form) automatically to convey the largest amount spatial information per spike, under the constraint of limited neural energy. The animal's natural habitat property and locomotion experience statistics also affected the spatial codes. These findings not only answer whether the spatial codes of place cell are isotropic in different dimensional spaces, but also provide an insight about the maximum information principle of the place cell activity.

Acknowledgements Supported by the National Natural Science Foundation of China (No. 11702096, 11802095), Natural Science Foundation of Shanghai (No. 19zr1473100) and Fundamental Research Funds for the Central Universities (No. 222201714020, 222201814025).

Y. Wang (✉) · X. Xu · R. Wang
Institute for Cognitive Neurodynamics, East China University of Science and Technology, Shanghai, China
e-mail: wangyihong@ecust.edu.cn

X. Xu
e-mail: xu_xuying@126.com

R. Wang
e-mail: rbwang@163.com

A. Lintas et al. (eds.), *Advances in Cognitive Neurodynamics (VII)*, Advances in Cognitive Neurodynamics,
https://doi.org/10.1007/978-981-16-0317-4_32

Neural Coding of Reward Value in Richly Modulated Spike Patterns in Monkey Ventrolateral Prefrontal Cortex

Rossella Falcone, Mariko McDougall, David Weintraub, Tsuyoshi Setogawa, and Barry Richmond

Abstract Monkeys with lesions of the lateral prefrontal cortex lose the ability to integrate the reward value information across multiple domains. We recorded neuronal responses from the area 9/46 of ventrolateral prefrontal cortex (vlPFC) of two monkeys while they were performing a task in which in each trial was offered a reward. The reward value, signaled through its association with a visual cue, was constructed by combining one of 3 reward sizes (2, 4 or 6 drops of water) with one of 3 discounting delays (1, 5 or 10 s after the choice). The monkeys accepted or refused the offer by releasing the bar after the appearance of the go signal. They were increasingly likely to accept offers as the reward became larger and the delay became shorter. We observed that the reward values were well described by a simple reinforcement learning model for the discounted value of the rewards. In the period soon after the visual cue was presented to the animal, 69% (117/170) of the neurons modulated their firing rate according to the reward size and/or delay. We asked whether vlPFC neurons modulated their activity according to the value that the animal assigned to each offer. The estimated discounted values from the reinforcement model from the behavior were used to correlate with the mean firing rate for each offer, for each neuron. We found that 35% (41/117) of the neurons increased or reduced their firing rate linearly in relation to the discounted value measured from the behavior. The other neurons clearly showed modulation according to both reward size and delay, very few neurons were sensitive to only one factor. Some vlPFC neurons had a strong pulse after value cue appeared, others showed a strong pause, and still others showed three phase responses (small pulse followed by a pause followed by a strong pulse). Despite these striking patterns of responses, principal component analysis showed that the value-related information was encoded in the spike count. This analysis showed, however, that the period with the strong value related coding

R. Falcone · M. McDougall · D. Weintraub · T. Setogawa · B. Richmond
Section on Neural Coding and Computation, NIMH/NIH Bldg 49, Bethesda, MD 20892, USA

A. Lintas et al. (eds.), *Advances in Cognitive Neurodynamics (VII)*, Advances in Cognitive Neurodynamics,
https://doi.org/10.1007/978-981-16-0317-4_33

was restricted to a window that began and ended during cue's presence before the imperative target (a small yellow or purple spot) appeared.

Comparing Working Memory in Old World Monkeys and Humans

Barry J. Richmond

Abstract There are two types of neural phenomena that have been called working memory. The first is a selective, attention demanding process. In this first process, until the attention is interrupted, the memory trace has high fidelity over time. The second is a non-selective, non-attention demanding process where all events seem to form a memory traces each decaying with time. The first process is generally thought of as true working memory in humans. We started out to study the substrates of these working memory types in monkeys. To our surprise (frustration?) we found that monkeys rely primarily on the second type of working memory even when put in situations where it seems most efficacious to use the first type. The monkeys make large numbers of false positive responses related to the time in the past when a visual stimulus was presented in a sequential string of visual distractors. By way of comparison, humans heavily favor the first type of working memory; they make almost no false positive responses when asked to remember a single index stimulus. I will review our results and show how selective damage to different parts of the monkey brain thought important for supporting normal working memory function, prefrontal cortex, hippocampus, and different parts of lateral inferior temporal cortex, selectively interfere with different aspects of working memory. For physiologists this raises a problem: how do we study mechanisms of working memory using monkeys if monkeys use different strategies to solve working memory tasks?

.

References

Wittig, J. H., Jr., Morgan, B., Masseau, E., & Richmond, B. J. (2016). Humans and monkeys use different strategies to solve the same short-term memory tasks. *Learning and Memory, 23*(11), 644–647. https://doi.org/10.1101/lm.041764.116. PMID:27918285

B. J. Richmond (✉)
Chief Section on Neural Coding and Computation, NIMH/NIH Bldg 49,
Rm 1B-80, Bethesda, MD 20892, USA
e-mail: Barry.richmond@nih.gov

A. Lintas et al. (eds.), *Advances in Cognitive Neurodynamics (VII)*, Advances in Cognitive Neurodynamics,
https://doi.org/10.1007/978-981-16-0317-4_34

Evolution of Primate Multilevel Social Systems: Proboscis Monkey Society as Complex System

Ikki Matsuda, Ikuma Adachi, and Hiroki Koda

Abstract Great apes like chimpanzees often provide referential models to understand evolutional trajectories of human behaviour, cognition, morphology and social system as humans and chimpanzees shared a common ancestor only ∼5–7 million years ago (Mya). However, there are other lesser known non-human primates which are phylogenetically far to humans, but sharing similar traits with humans in terms of social system, i.e., multilevel societies. Among primate social systems, the multilevel society, in which smaller levels of social organization aggregate into larger units, is one of the most complex, though its origins and function are still poorly understood. Proboscis monkeys (*Nasalis larvatus*), one of the rare primate species reported multilevel social system, belong to the odd-nosed colobines, and are a large, sexually dimorphic and primarily arboreal species. We will overview what/how multilevel society in proboscis monkeys and discuss proximate mechanisms maintaining and the selective factors underlying their social system. Investigation on primate multilevel social systems would not only provide insights into the evolutionary history of human social system but also possibility develop our understanding how brain encodes the spatial position of others in such a complex society.

I. Matsuda (✉)
Chubu University Academy of Emerging Sciences, 1200, Matsumoto-cho, Kasugai-shi, Aichi 487-8501, Japan
e-mail: ikki-matsuda@isc.chubu.ac.jp

Wildlife Research Center of Kyoto University, Kyoto, Japan

Japan Monkey Centre, Inuyama, Japan

Institute for Tropical Biology and Conservation, Universiti Malaysia, Sabah, Malaysia

I. Adachi · H. Koda
Primate Research Institute, Kyoto University, Inuyama, Aichi 484-8506, Japan
e-mail: ikuma.adachi@gmail.com

H. Koda
e-mail: koda.hiroki.7a@kyoto-u.ac.jp

A. Lintas et al. (eds.), *Advances in Cognitive Neurodynamics (VII)*, Advances in Cognitive Neurodynamics,
https://doi.org/10.1007/978-981-16-0317-4_35

Social Network and Collective Intelligence Under Non-stationary Uncertain Environment

Aoi Naito, Naoki Masuda, and Tatsuya Kameda

Abstract Collective intelligence in the highly-connected, uncertain world is a topic of major interests across various social and natural-science disciplines. Here we report results of a behavioral experiment with a total of 250 human participants and a computer simulation about emergence of collective intelligence in a non-stationary uncertain environment.

1. We define "collective intelligence" as an emergent property whereby social interaction yields group-level performance superior to individual-level performance on some objectively-definable dimension.
2. Here, we focus on collective performance in a non-stationary uncertain environment. Specifically, we are interested in how well a group of people can track temporal changes in environment, the issue common in social foraging by animals where resource-levels of several patches may change over time.
3. We implemented a two-armed bandit (2AB) task in a laboratory, where the expected rewards of the two options were changing over time. We then observed how a group of 10 people could track the changes through social interaction in a centralized or decentralized network. Participants could learn how their neighbors in the network had decided in a preceding round.

A. Naito (✉) · T. Kameda
Department of Social Psychology, University of Tokyo, Bunkyo, Tokyo 1130033, Japan
e-mail: naito.aoi.94@gmail.com

T. Kameda
e-mail: tatsuyakameda@gmail.com

N. Masuda
Department of Engineering Mathematics, University of Bristol, Bristol BS8 1QU, UK
e-mail: naoki.masuda@bristol.ac.uk

A. Lintas et al. (eds.), *Advances in Cognitive Neurodynamics (VII)*, Advances in Cognitive Neurodynamics,
https://doi.org/10.1007/978-981-16-0317-4_36

4. Results confirmed that participants in the social networks could track the environmental changes more precisely than when working alone. Yet, the overall effect of network structure was minimum. Participants generally elevated reliance on individual learning, which reduced the effects of network structure. A computer simulation, incorporating parameter values from the experiment, showed that this pattern would be robust across various social network structures. Implications of these findings for network and social sciences will be discussed.

On the Neurodynamics of Intention, Decision and Free Will

Hans Liljenström and Azadeh Hassannejad Nazir

Abstract What is the role of consciousness in volition and decision making? Are our actions fully determined by brain activity preceding our decisions to act, or can consciousness instead affect the brain activity leading to action? This has been much debated ever since the famous experiments by Benjamin Libet in the 1980s, where the current most common interpretation is that conscious free will is an illusion. Intentionality, which can be seen as a precursor to conscious (free) will, is central in Freeman neurodynamics of the action-perception cycle, where intention would precede our conscious decision to act. Consciousness may be seen as an emergent property of the neural activity of the brain, but in order for consciousness to play any role in our (choice of) actions, we must also consider downward causation in the nervous system. In addition, there may be circular causation in the action-perception cycle, and hence it is crucial to study causal pathways in the brain during volition. In this presentation, I will describe a newly started project, where neuroscience, computational modeling and philosophy will be applied to elucidate the ancient enigma of free will. Computational modeling of brain parts involved in intention, decision, and action will complement experimental studies with EEG, MEG and fMRI to explore and map the causal relationships. Already, we have developed a neurocomputational model of the neurodynamics involved in decision making, involving both emotional and rational processes. In addition to individual experiential decision making, we also study the influence of the social and natural environment on human decisions. Our results so far confirm the notion that if decisions have to be made fast, emotional processes and aspects dominate, while rational processes are more time consuming and may result in a delayed decision. From some recent experiments in our consortium it appears that the readiness potential found in Libet's experiments with arbitrary choices are not found for more deliberate choices, where free will is more likely to come into play.

H. Liljenström (✉)
SLU and Agora for Biosystems, Uppsala/Sigtuna, Sweden
e-mail: Hans.liljenstrom@slu.se

A. H. Nazir
SLU and Karolinska Institutet, Uppsala/Stockholm, Sweden

A. Lintas et al. (eds.), *Advances in Cognitive Neurodynamics (VII)*, Advances in Cognitive Neurodynamics,
https://doi.org/10.1007/978-981-16-0317-4_37

Information Processing and Transmission in the Cerebral Cortex: Short Papers

Representation of Real and Imagined Actions in the Early Visual Cortex

Simona Monaco, Giulia Malfatti, Jody C. Culham, Luigi Cattaneo, and Luca Turella

Abstract Recent evidence shows that the role of the early visual cortex (EVC) goes beyond visual processing and into higher cognitive functions (Roelfsema and de Lange in Annu. Rev. Vis. Sci. 2:131–151, 2016). Further, neuroimaging results indicate that action intention can be predicted based on the activity pattern in the EVC (Gallivan et al. in Cereb. Cortex 29:4662–4678, 2019; Gutteling et al. in J. Neurosci. 35:6472–6480, 2015). Could it just be imagery? Further, can we decode action intention in the EVC based on activity patterns elicited by motor imagery, and vice versa? To answer this question, we explored whether areas implicated in hand actions and imagery tasks have a shared representation for planning and imagining hand movements. We used a slow event-related functional magnetic resonance imaging (fMRI) paradigm to measure the BOLD signal while participants ($N = 16$) performed or imagined performing actions with the right dominant hand towards an object, which consisted of a small shape attached on a large shape. The actions included grasping the large or small shape, and reaching to the center of the object while fixating a point above the object. At the beginning of each trial, an auditory cue instructed participants about the task (Imagery, Movement) and the action (Grasp large, Grasp small, Reach) to be performed at the end of the trial. After a 10-s delay, which included a planning phase in Movement trials, a go cue prompted the participants to perform or imagine performing the action (Go phase). We used standard retinotopic mapping procedures to localize the retinotopic location of the object in the EVC. Using multi-voxel pattern analysis, we decoded action type based on activity patterns elicited during the planning phase of real actions (Movement task) as well as in the Go phase of the Imagery task in the anterior intraparietal sulcus (aIPS) and in the EVC. In addition, we decoded imagined actions based on the activity pattern

S. Monaco (✉) · G. Malfatti · L. Turella
Center for Mind/Brain Sciences (CIMeC)—University of Trento, Trento, Italy
e-mail: simona.monaco@unitn.it

J. C. Culham
Brain and Mind Institute, University of Western Ontario—London, London, Canada

L. Cattaneo
Department of Neurological, Neuropsychological, Morphological, and Movement Sciences, University of Verona, Verona, Italy

A. Lintas et al. (eds.), *Advances in Cognitive Neurodynamics (VII)*, Advances in Cognitive Neurodynamics,
https://doi.org/10.1007/978-981-16-0317-4_38

of planned actions (and vice-versa) in aIPS, but not in EVC. Our results suggest a shared representation for planning and imagining specific hand movements in aIPS but not in low-level visual areas. Therefore, planning and imagining actions have overlapping but not identical neural substrates.

References

Gallivan, J. P., Chapman, C. S., Gale, D. J., Flanagan, J. R., & Culham, J. C. (2019). Selective modulation of early visual cortical activity by movement intention. *Cerebral Cortex*, *29*(11), 4662–4678.

Gutteling, T. P., Petridou, N., Dumoulin, S. O., Harvey, B. M., Aarnoutse, E. J., Kenemans, J. L., et al. (2015). Action preparation shapes processing in early visual cortex. *Journal of Neuroscience*, *35*(16), 6472–6480.

Roelfsema, P. R., & de Lange, F. P. (2016). Early visual cortex as a multiscale cognitive blackboard. *Annual Review of Vision Science*, *2*, 131–151.

Quantifying Information Dynamics in CNS Networks

Paul E. Rapp, Christopher J. Cellucci, and David Darmon

Abstract We present a generically applicable four-step process for quantifying information movement in complex networks. (1) Construction of local entropy rate and specific entropy rate. Local entropy rate is a continuous, time-dependent measure that quantifies the information gained at time t on observing $x(t)$ given the recent past. There is a statistically responsible procedure for specifying "recent". Specific entropy rate is a related time-dependent locally determined measure that gives an estimate of uncertainty at time t. (2) Construct specific transfer entropy (i.e., a time-dependent generalization of epoch-determined transfer entropy) that gives a state- and time-resolved quantification of the predictive input of a candidate input system on a candidate output system. (3) Construct a time-dependent network adjacency matrix. Specific transfer entropy can be used to populate the adjacency matrix characterizing a network. In the case of multichannel EEG/MEG recordings, the nodes are electrodes, and specific transfer entropy quantifies information movement between electrodes. In this analysis, the adjacency matrix is real, time-dependent and asymmetric. Any of a large number of measures commonly used to characterize an adjacency matrix can be used. The result $\Lambda(t)$ is a scalar function of time. (4) Identify hierarchical transition chronometries in $\Lambda(t)$. The simple directive "find transitions in $\Lambda(t)$" is unacceptably naive. Dynamically meaningful transitions are timescale-dependent. In this analysis, $\Lambda(t)$ is embedded and the structure of this embedded object is examined by quadrant scans of the corresponding recurrence diagram. A hierarchy of transitions can be identified by manipulating the embedding dimension.

P. E. Rapp (✉)
Department of Military and Emergency Medicine, Uniformed Services University, Bethesda, MD 20814, USA

C. J. Cellucci
Aquinas, LLC Berwyn, PA 19312, USA

D. Darmon
Department of Mathematics, Monmouth University, West Long Branch, NJ 07764, USA

A. Lintas et al. (eds.), *Advances in Cognitive Neurodynamics (VII)*, Advances in Cognitive Neurodynamics,
https://doi.org/10.1007/978-981-16-0317-4_39

We note that $\Lambda(t)$ can serve as the order parameter in phase transition experiments in which time is the tuning parameter.

Causal Interactions Among Cortical Regions During Sleep Based on fNIRS Recordings

Takeshi Abe, Yoshiyuki Asai, Masashi Dotare, Takahide Hayano, Stephen H. Perrig, Manon Jaquerod, Alessandra Lintas, and Alessandro E. P. Villa

Abstract Functional connectivity between cerebral cortical regions during natural sleep has attracted a keen interest from both cognitive and clinical neuroscientists because of its importance in understanding the default mode network of human brain. Multiple recordings of functional near-infrared spectroscopy (fNIRS) in several sleep phases make it possible for us to detect potential differences of directional interactions between cortical areas from healthy subjects and patients with ADHD or sleep disorders. Namely we propose a computational method to estimate

T. Abe (✉) · Y. Asai · T. Hayano
Graduate School of Medicine, Yamaguchi University, 1-1-1 Minami-kogushi, Ube, Yamaguchi, Japan
e-mail: t.abe@yamaguchi-u.ac.jp

Y. Asai
e-mail: asai@yamaguchi-u.ac.jp

T. Hayano
e-mail: thayano@yamaguchi-u.ac.jp

M. Dotare
School of Medicine, Yamaguchi University, 1-1-1 Minami-kogushi, Ube, Yamaguchi, Japan
e-mail: i907eb@yamaguchi-u.ac.jp

S. H. Perrig
Department of Medicine, Sleep Medical Center, University Hospital of Geneva, Rue Gabrielle-Perret-Gentil 4, 1205 Geneva, Switzerland
e-mail: Stephen.Perrig@hcuge.ch

M. Jaquerod · A. Lintas · A. E. P. Villa
NeuroHeuristic Research Group, University of Lausanne, Internef 138, Quartier UNIL-Chamberonne, 1015 Lausanne, Switzerland
URL: http://www.neuroheuristic.org

A. Lintas
e-mail: alessandra.lintas@unil.ch

A. E. P. Villa
e-mail: alessandro.villa@unil.ch

LABEX, HEC Lausanne, University of Lausanne, Quartier UNIL-Chamberonne, 1015 Lausanne, Switzerland

A. Lintas et al. (eds.), *Advances in Cognitive Neurodynamics (VII)*, Advances in Cognitive Neurodynamics,
https://doi.org/10.1007/978-981-16-0317-4_40

time-domain Granger causality among fNIRS time series using a Kolmogorov–Smirnov test based on F-statistics. In order to validate indication of directional interactions, we also apply convergent cross-mapping to the time series as an alternative approach to causality based on state space reconstruction of dynamical systems. Comparing the averaged heatmaps of significant causal pairs of regions, we show that the map of directional interactions varies for each sleep phase, e.g., REM, of the same subject. The observation suggests an unexplored source for non-invasive classification benchmark of the above cognitive disorders.

Unsupervised Analysis of EEG Signals Reveals Common Personality Traits During an Iterated Ultimatum Game

Qinyue Zheng, Sihao Liu, Alessandro E. P. Villa, and Alessandra Lintas

Abstract Decision-making is considered the most essential phase in volitional act, and in the "Theory of the Consumer" it is assumed that rational individuals maximize the consumption of real goods given a limited availability of nominal goods (money). The ultimatum game (UG) is a two-player game, in which Player_1 (P1) has a certain sum of money at his disposal and offers a share to Player_2 (P2). If P2 accepts the proposal, the share is done accordingly, but in case of rejection both players end up with nothing. If players were selfish income maximizers, P2 should accept any amount and P1 should offer small amounts Experimental results show that most humans do not behave like that. What happens in the brain while the game is ongoing? Decisions must be the result of a sort of calculation of costs and benefits that a human is capable of performing rather quickly. The working hypothesis is that the dynamics of the interactions within the brain network underpin decision-making and its investigation can be achieved by recordings brain signals. We study the correlation between unsupervised machine learning analysis of event-related potentials recorded during the whole decision-making process ($N = 50$ participants) with personality traits measured by the HEXACO questionnaire and with the brief mood introspection scale. Unsupervised feature extraction of ERPS found two very robust clusters

Q. Zheng (✉)
School of Artificial Intelligence and Automation, Huazhong University of Science and Technology, Wuhan, Hubei 430074, China
e-mail: qinyue.zheng@epfl.ch

S. Liu
Computer Science Department, University of California, Los Angeles, 404 Westwood Plaza, Los Angeles, CA 90095, USA
e-mail: sihao@cs.ucla.edu

A. E. P. Villa · A. Lintas
NeuroHeuristic Research Group, University of Lausanne, 1015 Lausanne, Switzerland
e-mail: alessandro.villa@unil.ch
URL: http://www.neuroheuristic.org

A. Lintas
e-mail: alessandra.lintas@unil.ch

A. Lintas et al. (eds.), *Advances in Cognitive Neurodynamics (VII)*, Advances in Cognitive Neurodynamics,
https://doi.org/10.1007/978-981-16-0317-4_41

of participants: (i) associated with emotionality, characteristic of people showing a greedy behavior; (ii) associated with honesty and agreeableness, for people expressing willingness-to-share. This approach is likely to open the way to new studies of the neural basis of where and how a “decision” is taken in the brain.

Towards the Intelligent Detection and Multimodal Rehabilitation for Cognitive Disabilities

Zengguang Hou

Abstract The ageing of the population drives the rapid increase of cognitive disorders, which cause a heavy burden for families and nations. It is important to screen and interfere with cognitive disorders at the earlier stage, but we are short of affordable and effective approaches. In this talk, we will discuss our attempt in the design of the multi-mode detection and rehabilitation methods for cognitive disorders using computational intelligence algorithms, wearable devices and rehabilitation robots.

Z. Hou (✉)
State Key Laboratory of Management and Control for Complex Systems (Key Laboratory of Complex Systems and Intelligence Science), Institute of Automation, Chinese Academy of Sciences, 95 Zhongguancun East Road, Beijing, Haidian District, China
e-mail: zengguang.hou@ia.ac.cn

A. Lintas et al. (eds.), *Advances in Cognitive Neurodynamics (VII)*, Advances in Cognitive Neurodynamics,
https://doi.org/10.1007/978-981-16-0317-4_42

Resting-State fMRI Investigation in Patients with Cervical Spondylotic Myelopathy

Guangsheng Li and Yong Hu

Abstract Cervical spondylotic myelopathy (CSM) is a common degenerative neurological disorder, usually influence on the walking ability with balance problem. The balance control during walking is a problem of motor and sensory function deficits, as well as cognitive impairs. Brian resting-state fMRI is a promising tool to investigate the cognitive-behavioral function in patients with CSM. In this study, a total of 20 CSM patients (age = 62 ± 14 years, male/female = 15/5, duration of symptom > 1 year, compression position range from C3 to C6 segment) were recruited to compare with a group of 30 healthy controls (age = 36 ± 12 years, male/female = 18/12). Most CSM patients presented walking disability if balance. Graph theory analysis of resting-state fMRI brain was performed to calculate the level of global intensity and local intensity. Results revealed that global intensity did not show significant difference between CSM patients and healthy controls. CSM patients with walking balance problem have significantly higher cerebellum local intensity than healthy controls. Furthermore, the cerebellum local intensity firstly increased, then decreased, and finally maintained at a certain level as the symptom of walking disturbance getting worse, indicating the finite ability of cerebellum functional plasticity. Findings of this study could enrich our understanding on the treatment and rehabilitation training of CSM patients with walking disturbance.

G. Li · Y. Hu
Department of Orthopaedics and Traumatology, The University of Hong Kong, Pok Fu Lam, Hong Kong, China

Spinal Division, Department of Orthopaedics, Affiliated Hospital of Guangdong Medical University, Guangdong 524001, China
e-mail: yhud@hku.hk

A. Lintas et al. (eds.), *Advances in Cognitive Neurodynamics (VII)*, Advances in Cognitive Neurodynamics,
https://doi.org/10.1007/978-981-16-0317-4_43

Training Parameters with Dual N-Back Task Affect the Outcome of the Attentional Network Task in ADHD Patients

Masashi Dotare, Yoshiyuki Asai, Sarah K. Mesrobian, Michel Bader, Alessandro E. P. Villa, and Alessandra Lintas

Abstract Patients affected by attention-deficit/hyperactivity disorder (ADHD) are characterized by impaired executive functioning and/or attentional deficits. Our study is aimed to determine whether the outcomes measured by the attentional network task (ANT), i.e., the reaction times (RT) to specific target and cueing conditions and alerting, orienting, and conflict effects, are affected by cognitive training with a dual N-Back task. We considered three groups of young adult participants: ADHD patients without medication, ADHD with medication (MADHD), and age/education-matched controls (CTL). Working memory training began the day after the pretest. Participants were asked to perform 20 trainings composed of 20 blocks during an entire month. They were told that they would have to practice the dual N-Back task for about 30 min per day during the week and to rest for two days in the weekend. Each experimental group was randomly assigned into two conditions, the first with a progressive level (PL) of difficulty training, while the second was blocked at the

M. Dotare (✉)
School of Medicine, Yamaguchi University, 1-1-1 Minami-kogushi, Ube, Yamaguchi, Japan
e-mail: i907eb@yamaguchi-u.ac.jp

Y. Asai
Department of Systems Bioinformatics, Graduate School of Medicine, Yamaguchi University, 1-1-1 Minami-kogushi, Ube, Yamaguchi, Japan
e-mail: asai@yamaguchi-u.ac.jp

M. Bader
Research Unit of the University Department of Child and Adolescent Psychiatry (SUPEA), CHUV University Hospital, 1004 Lausanne, Switzerland
e-mail: bader_m@bluewin.ch

S. K. Mesrobian · A. E. P. Villa · A. Lintas
NeuroHeuristic Research Group, University of Lausanne, 1015 Lausanne, Switzerland
e-mail: smesrobian@neuristic.org

A. E. P. Villa
e-mail: alessandro.villa@unil.ch
URL: http://www.neuroheuristic.org

A. Lintas
e-mail: alessandra.lintas@unil.ch

A. Lintas et al. (eds.), *Advances in Cognitive Neurodynamics (VII)*, Advances in Cognitive Neurodynamics,
https://doi.org/10.1007/978-981-16-0317-4_44

level 1 during the whole training phase (baseline training). We observed that PL training was beneficial with reduced RTs in all groups and reduced conflict effects. MADHD showed a positive effect already with baseline training, whereas ADHD showed no significant reduction of neither RTs nor conflict effect after baseline training. No group showed any effect of training on alerting and orienting effects.

Experimental Study on Transcranial Magneto-Acoustic Coupling Stimulation

Xiaoqing Zhou, Huiqin Wang, Ren Ma, Tao Yin, Zhuo Yang, and Zhipeng Liu

Abstract In this paper, we present a novel electrical stimulation method, which can achieve high spatial resolution electrical stimulation in the deep brain region. We name it transcranial magneto-acoustic stimulation (TMAS) method. In this study, we obtained a 2 mm spatial resolution TMAS system and applied this neuromodulation technique to hippocampal stimulation in living mice for the first time. The effect of TMAS has been evaluated and analyzed. Firstly, the magneto-acoustic (MA) coupling electric field generated by TMAS was calculated by theoretical model. The TMAS experimental system for small animals was built, and its MA electric fields were tested. The results showed that the TMAS system can obtain the spatial resolution of 2 mm both in the cortex and hippocampus of the mouse. Next, the system was used to conduct TMAS in vivo experiments in healthy and PD mice, and the stimulation location was the hippocampus. Because the transcranial ultrasonic stimulation (TUS) is inevitably involved in the TMAS process, we added the TUS group with the same parameter on the basis of the TMAS group and the control group to explore the effect of the focused ultrasound field on the TMAS. We used behavioral and electrophysiological data to assess the effects of nerve stimulation on each group of mice. The experimental results showed that the learning and memory abilities of

X. Zhou (✉) · H. Wang · R. Ma · T. Yin · Z. Liu
Chinese Academy of Medical Sciences & Peking Union Medical College Institute of Biomedical Engineering, Tianjin 300192, China
e-mail: xiaoqing-lingjun@163.com

H. Wang
e-mail: whq186235@163.com

R. Ma
e-mail: likesaber@gmail.com

T. Yin
e-mail: bme500@163.com

Z. Liu
e-mail: lzpeng67@163.com

Z. Yang
College of Medicine, Nankai University, Tianjin 300071, China
e-mail: zhuoyang@nankai.edu.cn

A. Lintas et al. (eds.), *Advances in Cognitive Neurodynamics (VII)*, Advances in Cognitive Neurodynamics,
https://doi.org/10.1007/978-981-16-0317-4_45

the healthy-TMAS group and the PD-TMAS group mice were significantly better than those of the control groups, respectively, which verified the safety and usefulness of the TMAS method. Moreover, it was found that the learning and memory abilities of the TUS group mice, include healthy and PD group, were also better than those of the control groups, but far less than those of the TMAS groups, respectively, which verified the contribution of ultrasound field in TMAS. It can be seen that TMAS is actually a compound stimulation containing two orthogonal physical fields: the MA electric fields and the ultrasound field. And the assessment of TMAS proposes should consider the bioelectric effect and the mechanical force.

Permanent Deafness. A Perfect Storm in Brain Sensory Cortex

M. A. Merchan

Abstract In order to build the perceptual scene, the brains of mammals have developed neural circuits, specialized in analyzing and mixing different sources of sensory information. This ability requires a dynamic multimodal interchange of information along all stations of the sensory pathways from the brainstem to the cerebral cortex. When one sensory system fails, the brain cortex reorganizes its neural networks to preserve intermodal processing, what is known as cross-modal plasticity. In deafened ferrets, "de novo" emerging somatosensory responses have been shown by single unit recording in the auditory cortex (AC), undoubtedly demonstrating a multimodal sensory conversion in the brain cortex after sensory deprivation (Allman et al., 2009). Since receptive fields involve inhibitory GABA interactions, as demonstrated by iontophoresis (Tremere et al., 2001), such sensory conversion may reflect imbalanced cortical multimodal neurotransmission. Our results in a model of bilateral long-term deafness indicate that hearing deprivation induces an altered functional intermodal interaction which involves increased activation of the visual cortex (VC). Also, in humans, VC overactivation after permanent and long-term deafness has been demonstrated using visual evoked potentials (Neville et al., 1983). It is known that cross-modal balance for sensory processing between primary cortices is the result of a combination of thalamic drivers' activation, horizontal polymodal connections, and intrinsic microcircuit elaboration of neuronal responses in the cortical columns. Data will be presented in this talk pointing out that after chronic and permanent deafness in the rat, a cross-modal reorganization is triggered by changes in inhibitory circuits. Such rebound of inhibition has been shown by increases in gene expression and immunoreactivity for GAD 65 and GAD 67 as well as by increases in parvalbumin positive (PV) fast-spiking interneurons. Overactivation of the VC in our model, as demonstrated by changes in activity-dependent early immediate expression genes c-Fos and Arc/Arg 3.1 and VEPs recordings (Pernia et al., 2017), is generated by imbalanced horizontal interactions as indicated by restricted changes of immunocytochemical markers in layers 2/3. However, such imbalance does not equally affect both

M. A. Merchan (✉)
Instituto de Neurociencias of Castilla y Leòn-INCyL, Universidad de Salamanca, Salamanca, Spain
e-mail: merchan@usal.es

A. Lintas et al. (eds.), *Advances in Cognitive Neurodynamics (VII)*, Advances in Cognitive Neurodynamics,
https://doi.org/10.1007/978-981-16-0317-4_46

primary cortices. Because GABA interneurons specifically increase in primary AC, greater inhibition of cortical column microcircuits could be expected (fast-spiking control). Our results also indicate that two homeostatic mechanisms actively work for a dynamic compensation of the out-of-balance bimodal relationship after deafness: (1) Increases in the expression and protein synthesis of AMPA receptors in the AC (which indicates an effort to compensate changes in its thalamic drivers' activation), and (2) the up-regulation of Arc/Arg3.1 shown by us in the VC which supports a reactive mechanism to compensate overactivation in the VC. In sum after prolonged deafness, cross-modal reorganization at long term induces the overactivation of neighboring sensory cortices (in particular VC) as a result of a dynamic compensation of the horizontal feedbacks. We have recently shown that anodal continuous current stimulation allows restricted over-activation of the AC (Colmenárez-Raga et al., 2019). A restricted stimulation with anodal currents (activation) in the AC may be able to rebalance cross-modal reaction, potentially improving cortical processing after cochlear implantation. New strategies of directional restricted neuromodulation of sensory cortices by electric fields by using the novel method of non-invasive deep brain stimulation via temporally interfering electric fields (Grossman et al., 2017) will be also discussed in this talk.

References

Allman, B. L., Keniston, L. P., & Meredith, M. A. (2009). Adult deafness induces somatosensory conversion of ferret auditory cortex. *Proceedings of the National Academy of Sciences of the United States of America*, *106*(14), 5925–30.

Colmenárez-Raga, A. C., Díaz, I., Pernia, M., Pérez-González, D., Delgado-García, J. M., Carro, J., et al. (2019). Reversible functional changes evoked by anodal epidural direct current electrical stimulation of the rat auditory cortex. *Frontiers in Neuroscience*, *13*, 356.

Grossman, N., Bono, D., Dedic, N., Kodandaramaiah, S. B., Rudenko, A., Suk, H.-J., et al. (2017). Noninvasive deep brain stimulation via temporally interfering electric fields. *Cell*, *169*(6), 1029–1041.e16.

Neville, H. J., Schmidt, A., & Kutas, M. (1983). Altered visual-evoked potentials in congenitally deaf adults. *Brain Research*, *266*(1), 127–32.

Pernia, M., Estevez, S., Poveda, C., Plaza, I., Carro, J., Juiz, J. M., & Merchan, M. A. (2017). c-Fos and Arc/Arg3.1 expression in auditory and visual cortices after hearing loss: Evidence of sensory crossmodal reorganization in adult rats. *Journal of Comparative Neurology*, 525(12):2677–2689.

Tremere, L., Hicks, T. P., & Rasmusson, D. D. (2001). Expansion of receptive fields in raccoon somatosensory cortex in vivo by GABA(A) receptor antagonism: implications for cortical reorganization. *Experimental Brain Research*, *136*(4), 447–455.

An Exception to Contralateral Dominance of Cerebral Cortex: From Abstract to Concrete

Yoshikazu Isomura

Abstract The cerebral cortex usually governs contralateral body parts in sensation and movements. The rule of contralateral dominance of cerebral cortex is well established on the basis of a long history of human and animal experiments. We also confirmed the rule for the primary (M1) and secondary (M2) motor cortices controlling unilateral forelimb movements in behaving rats. However, we found that their posterior parietal cortex (PPC) neurons preferentially represent ipsilateral forelimb movements, in contrast to the contralateral preference of M1 and M2 neurons. Moreover, our optogenetic activation of PPC neurons evoked ipsilaterally biased forelimb movements. Even weak PPC activation affected their task performance of ipsilateral forelimb movements. I will talk about our interpretation on these paradoxical observations from the point of view of an evolutional difference between rodents and primates.

Y. Isomura (✉)
Department of Physiology and Cell Biology, Graduate School of Medical and Dental Sciences, Tokyo Medical and Dental University, 1-5-45 Yushima, Bunkyo-ku, Tokyo 113-8510, Japan
e-mail: isomura.phy2@tmd.ac.jp

A. Lintas et al. (eds.), *Advances in Cognitive Neurodynamics (VII)*, Advances in Cognitive Neurodynamics,
https://doi.org/10.1007/978-981-16-0317-4_47

The Enhancement of the Reward Prediction Error Signal in the Midbrain Dopamine Neuron by the Cost Paid for the Reward

Masamichi Sakagami, Shingo Tanaka, and John O'Doherty

Abstract The midbrain dopamine (DA) neuron plays a key role in reward processing and codes signals associated with the reward prediction error (RPE) to update the value of options. Here, we examined whether these RPE signals are modulated by the cost paid to obtain the reward. After focussing a fixation point, two macaque monkeys were required to make a saccade to a condition cue, then a target appeared. In the high cost condition, long fixation to the target was required. In the low-cost condition, only a short fixation was required. After fixation on the target, the subjects made a saccade to the reward cue. Choice trials between condition cues and between reward cues were inserted randomly to test if the subjects showed a preference. Free reward and free air-puff trials were inserted randomly to determine whether each DA neuron was of a salience or motivation subtype. A cue signaling a costly action to be performed triggered less response in DA neurons with respect to a cue signaling a less costly action, but DA neuron responses to cues predicting reward and to the delivery of rewards were found to be enhanced after the monkey had performed a costly action compared to a less costly action. These findings suggest that DA neurons incorporate the cost of performing an action into the prediction error signal, and that RPEs are enhanced following the performance of a costly action. This finding suggested that monkeys would be faster to learn stimulus-reward associations after performing a costly action compared to a less costly action. A subsequent behavioral experiment confirmed this hypothesis. Information about action cost is processed in the DA

M. Sakagami (✉)
Brain Science Institute, Tamagawa University, 6-1-1, Tamagawagakuen, Machida 194-8610, Japan
e-mail: sakagami@lab.tamagawa.ac.jp

S. Tanaka
Department of Physiology, Niigata University School of Medicine, 1-757 Asahimachi Street, Chuo-ku, Niigata 951-8510, Japan
e-mail: sngtanaka@med.niigata-u.ac.jp

J. O'Doherty
Division of the Humanities & Social Sciences, Caltech, Pasadena, CA 91125, USA
e-mail: jdoherty@caltech.edu

A. Lintas et al. (eds.), *Advances in Cognitive Neurodynamics (VII)*, Advances in Cognitive Neurodynamics,
https://doi.org/10.1007/978-981-16-0317-4_48

reward system in a manner that amplifies the DA RPE signal, thereby producing more rapid learning under situations of high cost.

Cerebellar Regulation of Motor Timing and Coordination

Yifat Prut

Abstract In human and non-human primates, motor timing is considered to be dictated by cerebellar control of motor cortical activity, relayed through the cerebellar-thalamo-cortical (CTC) system. This supposition relies on studies that documented motor impairments in cerebellar patients and in animal models. However, we know very little about the way cerebellar information is integrated by cortical circuitry to affect motor cortical commands. We addressed this question by probing the CTC system in a primate model. We found that a brief activation of this pathway efficiently recruits motor cortical cells throughout the motor and premotor cortex. However, cortical response was dominated by a powerful inhibition that truncated the early excitation. At movement onset, CTC input transiently synchronized neighboring neurons. Blocking the CTC pathway produced motor impairments similar to the symptoms of cerebellar ataxia. The motor deficits were preceded by changes in neural activity that included local and global desynchronization. It is suggested that the excitation–inhibition interplay triggered by CTC input shapes the response profile of a distributed network of motor cortical neurons as required to initiate and coordinate movements.

Y. Prut (✉)
Department of Medical Neurobiology, IMRIC ELSC, The Hebrew University, Jerusalem, Israel
e-mail: yifatpr@ekmd.huji.ac.il

A. Lintas et al. (eds.), *Advances in Cognitive Neurodynamics (VII)*, Advances in Cognitive Neurodynamics,
https://doi.org/10.1007/978-981-16-0317-4_49

Multiple Control of Absence Seizures in the Brain: A Computational Study

Daqing Guo

Abstract As a typical generalized epilepsy, absence epilepsy can be easily identified during absence seizures (AS) based on the electrophysiological hallmark that synchronous 2–4 Hz spike and wave discharges (SWDs) widely observed in the clinical electroencephalography (EEG). Inspired by animal experimental studies that AS may be regulated by neural circuits within and outside the corticothalamic (CT) network, we employed computational models to further dissect the underlying biophysical mechanisms. Simulations show that in the CT network, enhancing the thalamic feedforward inhibition can effectively abate SWDs. Interestingly, the inhibitions mediated by $GABA_A$ and $GABA_B$ in the pathway from the thalamic reticular nucleus (TRN) to the specific relay nuclei of thalamus (SRN) play different roles in controlling AS. Specifically, unlike $GABA_B$ inhibition, $GABA_A$ inhibition has more influences on the dominant frequency of neural oscillations. On the other hand, the basal ganglia (BG) output pathways from the substantia nigra pars reticulate (SNr) to the TRN and SRN have been demonstrated to contribute to suppressing AS. Note that the control mechanism underlying the SNr-TRN pathway is mainly due to the collision in the TRN, whereas the weakened $GABA_B$ inhibition is responsible for the suppression of AS via the SNr-SRN pathway. More importantly, the competition between the two output pathways can induce BG bidirectionally controlling AS. Besides these observations, we further found that AS can also be terminated by the newly identified inhibitory pallido-cotrical pathway in our model. These findings highlight the neural circuits that have close associations with the CT network, including internal and external pathways, may have functional roles in regulating AS and may provide a novel insight into the treatment of absence epilepsy.

D. Guo (✉)
MOE Key Laboratory for NeuroInformation, School of Life Science and Technology, The Clinical Hospital of Chengdu Brain Science Institute, University of Electronic Science and Technology of China, Chengdu 610054, China
e-mail: dqguo@uestc.edu.cn

A. Lintas et al. (eds.), *Advances in Cognitive Neurodynamics (VII)*, Advances in Cognitive Neurodynamics,
https://doi.org/10.1007/978-981-16-0317-4_50